Systematic development of rationally designed antibodies targeting predetermined epitopes of interest and protein aggregation

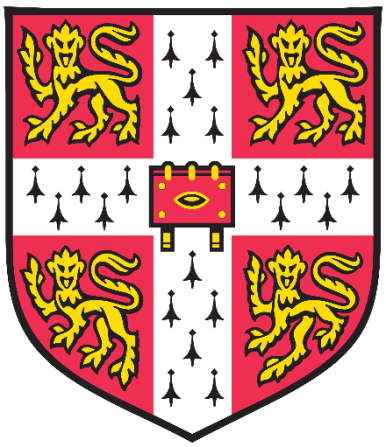

Samuel William Ness

Darwin College

Department of Chemistry

University of Cambridge

This thesis was submitted for the degree of *Doctor of Philosophy*

September 2019

Declaration

This dissertation is a summary of research carried out under the supervision of Prof. Michele Vendruscolo in the Department of Chemistry of the University of Cambridge, between October 2015 and September 2019. The work described in the dissertation is my own and contains nothing which is the outcome of work done in collaboration with others, except as specified in the text and acknowledgements. It has not, either in part, or as whole, been submitted for a degree, diploma, or other qualification at any other university. The length of this dissertation (approx. 58,000 words) does not exceed the word limit set by the Degree Committee (60,000 words).

Samuel William Ness

September 2019

Abstract

A wide range of human disorders, including Alzheimer's and Parkinson's diseases, are associated with the process of misfolding and aggregation of proteins. Therefore, modulating the aggregation pathway of disease-related proteins, in particular the Amyloid-β peptide (Aβ) in Alzheimer's disease and α-Synuclein (αSyn) in Parkinson's disease, is key to establishing therapeutics for these disorders. One promising method is the blockade of aggregation-prone regions of proteins using antibodies, but a major challenge in establishing antibodies against pre-selected epitopes is the effectiveness of the target regions to behave as antigens. To address this problem, a method of rational design was recently established in our group to construct complementary peptides in the complementarity determining regions (CDRs) of single-domain antibodies (sdAbs) towards the target regions. This was shown to bind disordered epitopes specifically and with good affinity. The binding was also shown to inhibit the aggregation of αSyn. This approach was also utilized to create multiple sdAbs binding different epitopes across the length of Aβ. It was found that systematically 'scanning' the sequence of Aβ in this way led to markedly different effects upon the Aβ aggregation pathway and the specificity of the sdAbs towards different aggregated species. To build on these advances and improve the designed sdAbs, in my work I combined this rational design method with established methods of protein evolution to improve binding affinities and specificity. The expectation was that this strategy would enable the establishment of a repertoire of high-affinity antibodies towards epitopes, which until recently, were deemed to be 'un-targetable'. Using a rationally designed αSyn antibody as a template for evolution, it was found that protein engineering via directed evolution and phage display is indeed capable of producing stable variants of the designed antibodies with improved affinity and crucially, retention of the pre-selected and poorly-immunogenic epitope that it was originally designed to bind. Next, we aimed to alter the specificity of two of the rationally designed Aβ antibodies towards maximising the inhibition of secondary protein nucleation, in order to tune the specificity of the antibodies away from binding the monomer, and towards the toxic oligomeric species. Indeed, using directed evolution and phage display with competitive selection, it was found that it is possible to further alter the inhibition of the microscopic nucleation events that govern protein aggregation, albeit with compromised sdAb thermal stability. This was likely due to both the library design strategy and the heterogeneous selection employed. Nevertheless, these results show that combining rational design and directed evolution can offer novel opportunities in antibody discovery against targets not readily accessible through existing methods.

Acknowledgements

First and foremost, I would like to take this opportunity to thank my supervisor, Professor Michele Vendruscolo for this incredible opportunity and for funding this project. Thank you for your unending enthusiasm, encouragement, trust and support, and for welcoming me into your fantastic research group. These years have been extremely special and I'll never forget everything you have done for me.

Dr. Pietro Sormanni, thank you for taking me seriously when I first approached you with the idea for this study. My flustered "I think I know how to do this" doesn't sound so convincing in my head now, but I'm grateful you could see through it and recognise my passion and drive for this field of research. I'm honoured to be your first 'guinea pig' working on the amazing legacy you have created. I could not have asked for a better collaboration and it has been thoroughly enjoyable working with you.

Dr. Francesco Aprile, thank you for sharing your exceptional scientific guidance and experience with me (or shall we say 'hand-holding' in some instances), and for making me the scientist I am today. You helped me navigate the minefield that is antibody engineering and protein aggregation. Your constant positivity kept me pushing at maximum speed, even when I couldn't see the light at the end of the tunnel, and I owe much of my accomplishments to you.

Robert Horne, thank you for the awesome year we spent together and the phenomenal effort you put into your project. Your dedication to the mind-numbing task of optimising the crude-extract screens was remarkable and I'm certain you're going to enjoy a very successful Ph.D of your own. I'm very proud to have been a part of that journey and I wish you the very best.

Dr Janet Kumita, you have been the most incredible supporter of me and everything I've done at my time in Cambridge. Without you hiring me in the first place, there would have been no Cambridge story and certainly no Ph.D thesis to write this in (whoa, meta). You've been a wonderful friend to me and were always there when I needed your help, and for that I am eternally grateful.

Dr. Erwin de Genst, thank you for your amazing crash-course in antibody evolution and phage-display. I owe much of the success of my work to your selfless guidance and expertise, and you effectively got me to hit the ground running. I will certainly miss your charming nerdiness, humour and ultra-chilled demeanour, it was exactly what I needed.

Philip Lindstedt, thank you for not only helping me with Mass-spec, fitting the $A\beta_{42}$ aggregation kinetics, sharing plate-reader runs and generally making me more efficient, but also for being a great friend and constant source of optimism. Outstanding banter.

Dr. Benedetta Mannini, Dr. Ryan Limbocker and Dr. Francesco Simone Ruggeri, thank you for helping me generate and characterise the biotinylated $A\beta_{40}$ oligomers. With your help it was painless, straightforward and easy to implement, which took a great deal of weight off my shoulders. Thank you all for a great collaboration.

Kazimir Uzwyshyn-Jones, thank you for your help setting up and optimising the ep-PCR protocol used in this study. It was a pleasure to work with you and I'm honoured that this experience helped you to secure a place to study science at Queen's college, Cambridge. I hope you have a wonderful time in Cambridge, you deserve it.

Sam Casford, thank you so much for going out of your way to help me earlier this year, I've thoroughly appreciated your assistance and it's a shame the worm experiment didn't work. I really enjoyed the time we spent in the windowless dungeon of the MPACC.

Ewa Klimont, Swapan Preet and Christian Baker, thank you all for the never-ending supply of α-Synuclein and $A\beta_{42}$. You made my work an absolute breeze and I really appreciate everything you do.

Dr. Serene Chen, Catherine Xu and Marta Castellana-Cruz, I thank each and all of you for helping me with the stuff I *really* should have known about α-Synuclein and all the annoying questions I asked. You helped me out a lot over the years and I'm very grateful.

Dr. Ana Bernardo Gancedo, being assigned as your desk-buddy was the most wonderful chance encounter. What followed was the best adventure I could hope for. Thank you for being my rock over these years and for changing my life forever.

To my wonderful family, thank you all for the infinite love and support, I love you all very much and every day you make me feel like the luckiest person in the world.

Last but certainly not least, I would like to thank the late Professor Sir Christopher Dobson. I am utterly honoured to have been a part of the remarkable legacy you created and left behind. You had an unequalled gift and talent for inspiring everyone around you, myself included. I will never forget the way you encouraged me to investigate on the basis of pure curiosity, instead of what I think people would like. A true scientist, through and through.

This thesis is dedicated to Lauren Peck.

I will never forget the way you used to go out of your way to cheer me up no matter what day you'd had. Coming home from class in my first year away from home was always the best part of the day because you would always make me feel like the most special person in the world. You brightened everyone's lives you touched and we miss you terribly.

List of abbreviations

AA	Amino acid
Ab	Antibody
AbAg	Antibody-antigen complex
AFM	Atomic-force microscopy
Ag	Antigen
ANS	8-Anilinonaphthalene-1-sulphonic acid
APP	Amyloid precursor protein
APTES	(3-aminopropyl)triethoxysilane
Aβ	Amyloid-β
BLI	Biolayer interferometry
BSA	Bovine serum albumin
CD	Circular dichroism
CDR	Complementarity determining region
cDNA	Complementary DNA
cfu	Colony-forming units
C_H	Constant heavy domain
C_L	Constant light domain
CMD	Centre for Misfolding Diseases
CNS	Central nervous system
DARPins	Designed ankyrin repeat proteins
DesAb	Designed antibody
DMSO	Dimethyl sulfoxide
DNA	Deoxyribonucleic acid
dsDNA	Double-stranded DNA
DTT	Dithiothreitol
E. coli	Escherichia coli
EDTA	Ethylenediaminetetraacetic acid
ELISA	Enzyme-linked immunosorbent assay
ep-PCR	Error-prone PCR
EvDesAb	Evolved designed antibody

Fab	Antigen-binding fragment
Fc	Crystallisable fragment
FcRn	Neonatal Fc receptor
FDC	Follicular dendritic cell
Fv	Variable fragment
HA	Hemagglutinin
HEPES	4-(2-hydroxyethyl)-1-piperazineethanesulfonic acid
HFIP	1,1,1,3,3,3-Hexafluoro-2-propanol
HRP	Horseradish peroxidase
HSQC	Heteronuclear single quantum coherence spectroscopy
IAPP	Islet amyloid polypeptide
IEC	Ion-exchange chromatography
IMAC	Immobilised metal affinity chromatography
IPTG	Isopropyl β-D-1-thiogalactopyranoside
k_+	Elongation rate constant
k_-	Fragmentation rate constant
k_2	Secondary nucleation rate constant
K_D	Equilibrium dissociation constant
k_n	Primary nucleation rate constant
k_{off}	Off-rate constant
k_{on}	On-rate constant
LB	Luria broth
LC-MS	Liquid chromatography-mass spectroscopy
mAb	Monoclonal antibody
MALDI	Matrix-assisted laser desorption/ionization
MCS	Multiple cloning site
MRE	Mean residue ellipticity
mRNA	Messenger RNA
MST	Microscale thermophoresis
MWCO	Molecular weight cut-off
NAC	Non-amyloid-β component
NEB	New England Biolabs
NGS	Next-generation sequencing

NMR	Nuclear magnetic resonance
PBS	Phosphate-buffered saline
PBS-T	Phosphate-buffered saline with Tween® 20
PCR	Polymerase chain-reaction
PDB	Protein data bank
PEG	Polyethylene glycol
PMSF	Phenylmethylsulfonyl fluoride
PPI	Protein-protein interaction
PTM	Post-translational modification
RNA	Ribonucleic acid
S. aureus	Staphylococcus aureus
SDS PAGE	Sodium dodecyl-sulphate polyacrylamide gel electrophoresis
SEC	Size-exclusion chromatography
SHM	Somatic-hypermutation
SOC	Super optimal broth supplemented with glucose
SPR	Surface plasmon resonance
TB	Terrific broth
TCEP	Tris(2-carboxyethyl)phosphine
TEM	Transmission electron microscopy
ThT	Thioflavin-T
T_m	Melting temperature
TMB	3,3',5,5'-Tetramethylbenzidine
V_H	Variable heavy domain
V_L	Variable light domain
αSyn	α-Synuclein

Contents

Chapter 1: Introduction

1.1 Antibodies as therapeutic and diagnostic tools

1.1.1 A 'magic bullet'?

Antibodies (Abs) are extremely attractive tools in biological science due to their ability to bind almost any target molecule with high affinity and specificity, and have found much success in the treatment of autoimmune disorders and cancer[1]. They are large proteins (~150 kDa), also known as immunoglobulins (Igs), and are secreted by B cells (and then later plasma cells) as part of the adaptive immune response, designed to target, neutralise and/or eliminate toxins or pathogens[2]. The fact that they are generated within living vertebrates to illicit a significant biological effect is at complete odds with small molecule drug discovery. This is because the immune system engineers Abs *in vivo* to be efficacious, non-toxic and pharmacokinetically desirable to the host organism whilst small molecule drug discovery generally requires far more research and development to address these attributes[3].

The key feature of Abs, for why they are so sought after, is their staggering specificity. Abs mediate their activity through protein-protein interactions (PPIs), which generally involve large molecular surfaces making complex contacts with their targets. This complexity often directly correlates to high affinity with very low off-target cross-reactivity compared to small molecule therapeutics[4, 5]. Because off-target cross-reactivity in drug development is commonly associated with undesired side-effects and toxicity, Abs provide pharmaceutical companies with tempting alternatives. Ab specificity can be meticulous as examples have been described that can differentiate between proteins that have or have not undergone subtle changes, such as certain post-translational modifications (PTMs), R and S enantiomers of chiral molecules and proteins differing in a single point mutation[4]. This latter point is of great significance as it is predicted that medical science is poised for a revolution towards personalised therapy where the uniqueness of patients, as unveiled by the recent developments in DNA sequencing, has revealed many new therapeutic targets[6, 7]. This potential for exceptional specificity has not gone unnoticed in the fields of research and diagnostics and Abs are now a staple in

biochemistry laboratories dependent on established techniques such as enzyme-linked immunosorbent assays (ELISA), western blotting and immunoprecipitation[8].

Reflective of their desirable properties, the rate of sales of monoclonal antibodies (mAbs) has drastically increased in recent years and the global Ab market for research, diagnostics and therapy is now the fastest growing in the biotechnology field[9]. As of 2019, 570 therapeutic Abs are in clinical development and the number of therapeutic mAbs on the market by 2020 is predicted to be ~70, with global sales at an astounding ~$250 billion[10, 11]. However, demand is only a small contributing factor to this figure. Manufacturing complexity and research and development increases the production costs of therapeutic mAbs significantly. The average price of the top nine Abs per patient was $200,000 per year in the US in 2010 and eculizumab was the most expensive drug in the world at the time at $409,500 per patient per year[12].

Another key downside to Abs is their large size, which hinders tissue penetration and buried epitope access. The former characteristic is one of the reasons Abs are usually administered at high concentrations intravenously and this can lead to formulation solubility issues that must be addressed by further development[13, 14]. Ab origins have also caused problems for therapeutic purposing as, until recently, Abs were mostly derived from animals, challenged with the target antigen (Ag). Non-human Abs have an increased risk of immune system stimulation when administered to human patients, which is known as immunogenicity[15-17]. ‘Humanising’ animal Abs to have as homologous sequences as possible to human Abs remedied the problem somewhat, but it wasn’t until the invention of synthetic Ab libraries and the establishment of mouse strains with human immune systems that standardised fully-human Ab therapeutics were finally accessible[18]. The large molecular weight of mAbs and their production costs are also being circumvented by the use of Ab fragments and the development of ‘Ab mimetics’ such as DARPins (~14-21 kDa) , Affibodies (6 kDa) and bicyclic peptides (~1-1.5 kDa). These alternatives benefit from greater tissue penetration, lower production costs and better solubility whilst mimicking the exquisite specificity of the binding sites of Abs[19-22].

Whilst Ab technology certainly has some limitations for therapy currently, the sheer scale of the growing industry and increasing interest in them and the biologicals that they have inspired indicates that the ‘magic bullet’ concept attributed to Abs, coined over one hundred years ago by Paul Ehrlich, is still very much alive in many scientist’s imaginations[23].

1.1.2 Antibody structure and function

Abs are large Y-shaped tetrameric glycoproteins, made up of an identical pair of 'heavy chains' and a pair of identical 'light chains'. The complete quaternary structure is joined and stabilised by disulphide bonds and extensive lipophilic patches that bind the heavy and light chains together. The heavy chains are made up of four immunoglobulin domains and the light chains consist of two. Each domain folds into two β-sheets that 'sandwich' together with the assistance of a disulphide bridge[24]. Each heavy and light chain is also divided into two main regions; the constant domain (C_H or C_L) and variable domain (V_H or V_L). The constant regions are completely conserved between all Abs of the same isotype (i.e. IgG) within an individual but differ from species to species. The variable regions contain the binding sites of the Abs (paratope), which are comprised of binding 'loops'. These loops commonly manifest themselves as exposed disordered polypeptides in close proximity to one another on one end of each variable domain, and are collectively known as the complementarity determining region (CDR)[25]. The CDR loops mediate reversible interactions with the target structure (epitope) via spatial complementarity and intermolecular forces (e.g. hydrophobic interactions, hydrogen bonds and electrostatics). They are hypervariable, meaning they vary in both amino acid (AA) sequence and length, and are encoded by genes that undergo somatic recombination which produces the enormous diversity of Abs that the immune system has at its disposal to target new antigens[26-28]. The full structure of an IgG Ab is explored in detail in Figure 1.1.

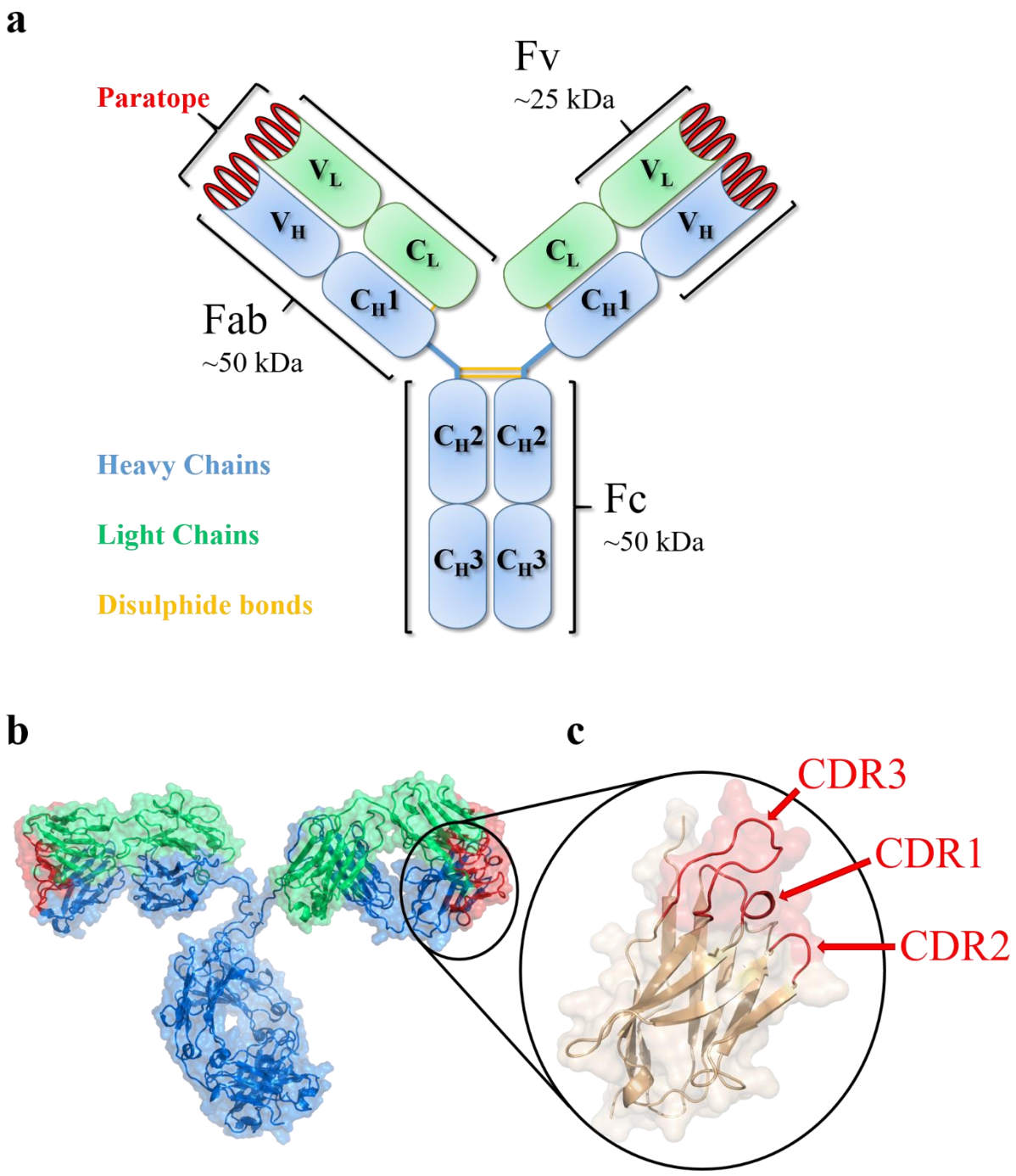

Figure 1.1. Schematic representations of an IgG Ab and a V_H immunoglobulin domain. a) Schematic diagram of the basic structure of an IgG Ab. The heavy chain (V_H/C_H) is coloured in blue and the light chain (V_L/C_L) is coloured green. Disulphide bonds joining the chains together are coloured in yellow. The paratopes, made up of the CDR loops are shown in red. The 'arms' of the Ab are called the antigen-binding fragment (Fab) region and the 'stem' of the Ab is known as the crystallisable fragment (Fc) region. The variable domain region is often referred to as the variable fragment (Fv). b) X-ray crystal structure of an IgG Ab with matching colours to (a) (PDB entry 1IGT)[29]. c) X-ray crystal structure of the variable heavy immunoglobulin domain (V_H). The immunoglobulin domain with the classic β-sheet 'sandwich' folds are coloured in tan and its three individual CDR loops are clearly shown in red. The structures were produced using PyMOL (PyMOL, Molecular Graphics System, Version 2.2.0, Schrödinger, LLC).

The Fc region regulates the immune function of Abs by signalling to immune cells, such as phagocytes, and by co-localising cell and antigen for phagocytosis. This 'marking' of targets for immune clearance is termed 'Ab opsonisation'. For example, binding of the Fc region to Fc receptors on the membrane surface of phagocytes signals for cellular ingestion (phagocytosis) and destruction of the pathogen[30]. The Fc region signalling is regulated by levels of glycosylation, which alter the interaction with the Fc receptor by modifying the binding affinity of the interaction[31, 32]. Abs can also function independently as neutralising agents, for example by binding to and blocking a region of a pathogen that is crucial for the biological effect (such as the cellular entry receptors on a virus)[33]. As full-length Abs contain more than one paratope, it is possible for them to bind more than one pathogen simultaneously. This can result in pathogen agglutination which inhibits pathogen spread, localises them for efficient immune clearance and can even precipitate them from solution[34]. The functions of Abs are visualised in Figure 1.2.

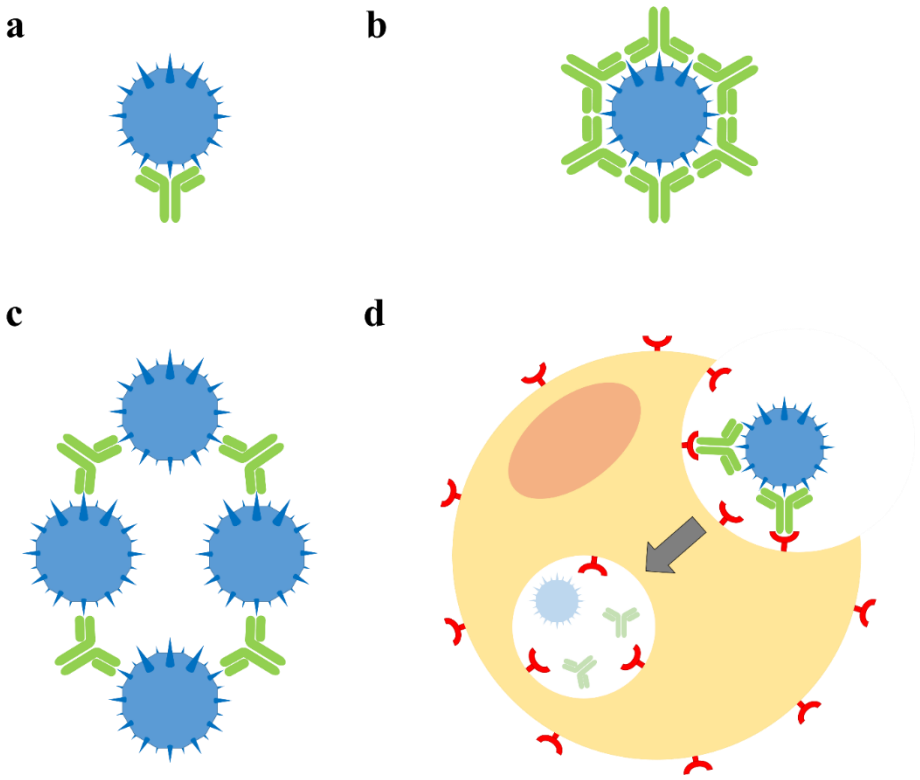

Figure 1.2. Comparisons of Ab function. Abs are depicted in green and pathogens destined for immune clearance are coloured in blue. a) Opsonisation occurs when Abs 'label' immunogenic material as 'pathogens' to the immune system. b) Neutralisation is the result of Abs completely coating and blocking a part of a pathogen vital to its pathogenicity. c) Precipitation/agglutination is caused by the multi-avidity of full-length Abs binding more than one pathogen. d) Ab-mediated phagocytosis. Surface membrane Fc receptors (red) bind to the Fc region of Abs bound to pathogens, stimulating phagocyte (yellow) engulfment and destruction of the enveloped material.

Ab neutralisation can be retained with the use of smaller fragments containing the paratope but lacking the Fc region. They include: Fab region fragments, single-chain variable fragments (scFv) and single-domain antibodies (sdAb), and they can be engineered from human IgG Abs and can be produced in bacteria[35]. As mentioned in Chapter 1.1.1, these smaller fragments are beneficial due to the reduced cost of prokaryote expression and their smaller size, but also share favourable biophysical characteristics with full-length Abs[36]. Lacking the Fc region means they will not likely recruit the immune response and associated inflammation and this can be useful in targeting the brain and central nervous system (CNS) as neuroinflammation has been implicated in some recent high-profile failures of brain/CNS targeting Ab therapeutics[37-39].

There are two distinct classes of protein epitope: conformational (discontinuous) and linear (continuous). Conformational epitopes have a clearly-defined three-dimensional structure such as a protein secondary or tertiary structure, are discontinuous in sequence and display rigidity. Linear epitopes are continuous in sequence, such as a peptide or any disordered protein region and can inhabit many conformational ensembles. Once bound, many linear epitopes become efficient binding partners as their flexibility bestows easier access to intermolecular interactions with the paratope than rigid epitopes[40]. However, due to the many conformational ensembles of unbound linear epitopes, Abs must couple the folding of the disordered epitope with the binding to the paratope and therefore the binding event may be associated with a significant loss of entropy[41]. Ab binding affinity generally suffers as a result and this correlation may partially explain why disordered epitopes are frequently associated with poor immunogenicity[42]. Ab binding with linear and conformational epitopes is displayed in Figure 1.3.

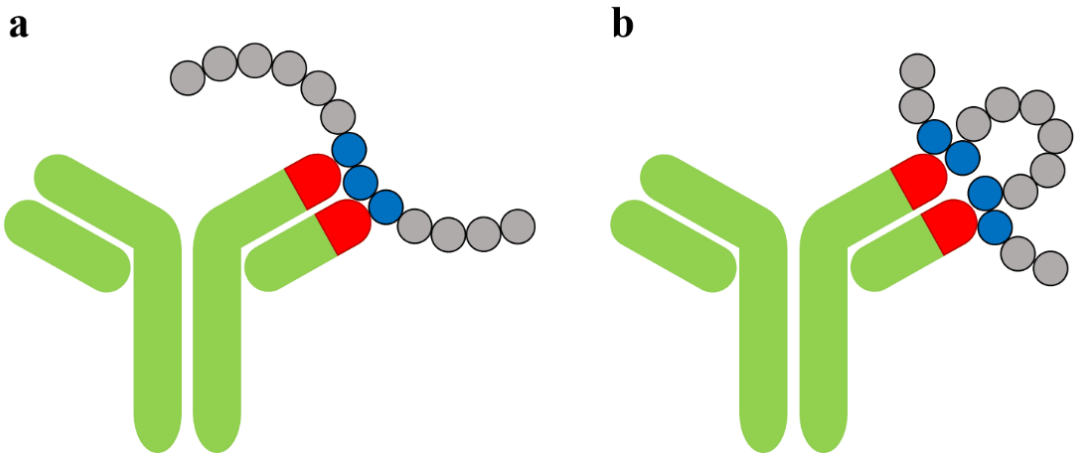

Figure 1.3. Comparison of protein epitope types. Abs are depicted in green with one of their paratopes coloured red. The target protein epitope is highlighted in blue with the non-bound regions greyed out. a) Linear epitope. b) Conformational epitope.

Obtaining Abs against pre-selected disordered linear epitopes within proteins such as that in $A\beta_{42}$, a key protein in the pathology of Alzheimer's disease (AD), still represents a significant challenge to Ab drug discovery and these are attractive targets for creating therapeutics against disease-related intrinsically disordered proteins (IDPs).

1.2 Protein misfolding and aggregation in health and disease

1.2.1 Intrinsically disordered proteins and protein misfolding diseases

IDPs do not have a stable three-dimensional structure and have challenged old theories on protein function being entirely dependent on a rigid tertiary structure. Indeed, many proteins with unstructured regions, or which are fully unstructured, have been shown to contribute to biological processes across the diversity of life[43]. Due to their high flexibility and ability to form many structural ensembles, IDPs have been found in the centre of PPI networks[44]. Interactions between proteins are extremely common in cells and it is now estimated that over eighty percent of all known protein functions are dependent upon some form of protein complex[45].

Many IDPs have been implicated in human diseases such as type II diabetes, cancer, neurodegeneration and amyloidoses[46]. The failure of protein homeostasis networks is thought to allow for the pathological accumulation and deposition of misfolded proteins into toxic aggregates, which are the hallmarks of many debilitating diseases such as AD and Parkinson's disease (PD)[47]. Owing to their increased flexibility with comparison to 'structured' proteins, many IDPs have a higher chance of 'misfolding' and those with a large hydrophobic content have an increased aggregation likelihood. Native-state or misfolded proteins can self-assemble into structured or unstructured aggregates via many pathways[48, 49]. A summary of the unified view of these pathways is shown in Figure 1.4.

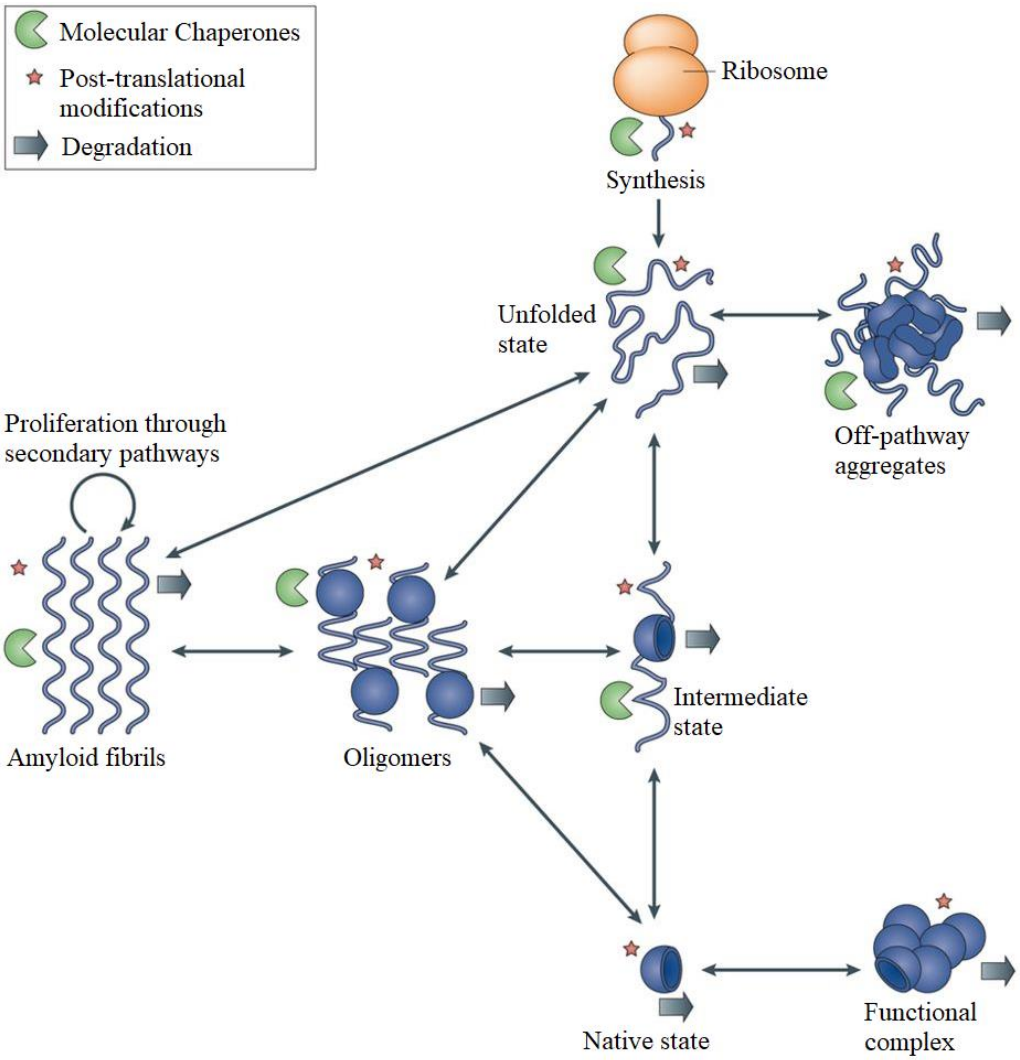

Figure 1.4. Overview of the various fates of a newly translated polypeptide or protein. Multiple folding routes can result in many monomeric or multimeric structures. These pathways are governed by the species' relative thermodynamic and kinetic properties and are also regulated by the cellular state (e.g. synthesis, PTMs, chaperone interactions and degradation). Figure adapted with permission from reference [49].

The pathological accumulation and deposition of toxic aggregates into body tissues are termed as 'deposition diseases' and due to unhealthy lifestyles and an increase in average lifespans thanks to improved medicine, the world population is spending more average time with a compromised protein homeostasis network and as a result the rate of deposition diseases is rapidly rising[49-54]. Deposition diseases are clustered into three categories; neuronal cell deposition (neurodegenerative diseases), multiple organ deposition (non-neuropathic systemic amyloidosis) and single-organ deposition (non-neuropathic localised amyloidosis)[49, 50]. A list of some known amyloid-associated diseases and their respective aggregating proteins is shown in Table 1.1.

Table 1.1. Examples of human diseases known to be associated with protein misfolding and amyloid aggregation. Adapted from reference [49].

Disease	Aggregating protein or peptide	Number of residues	Native structure
Neurodegenerative diseases			
Alzheimer's disease	Amyloid-β peptide	37-43	Intrinsically disordered
Spongiform encephalopathies	Prion protein or its fragments	230	Intrinsically disordered and α-helical
Parkinson's disease	α-Synuclein	140	Intrinsically disordered
Amyotrophic lateral sclerosis	Superoxide dismutase 1	153	β-sheet and Ig-like
Huntington's disease	Huntingtin fragments	Variable	Mostly intrinsically disordered
Familial amyloidotic polyneuropathy	Transthyretin variants	127	β-sheet
Non-neuropathic systemic amyloidosis			
Amyloid light chain (AL) amyloidosis	Immunoglobulin (Ig) light chains or its fragments	~90	β-sheet and Ig-like
Amyloid A (AA) amyloidosis	Serum amyloid A1 protein fragments	76-104	α-helical and unknown fold
Senile systemic amyloidosis	Wild-type transthyretin	127	β-sheet
Haemodialysis-related amyloidosis	β2-microglobulin	99	β-sheet and Ig-like
Lysozyme amyloidosis	Lysozyme variants	130	α-helical and β-sheet
Non-neuropathic localised amyloidosis			
Apolipoprotein A1 (Apo A-1) amyloidosis	Apo A-1 fragments	80-93	Intrinsically disordered
Type II Diabetes	Amylin	37	Intrinsically disordered
Injection-localised amyloidosis	Insulin	21 and 30	α-helical and insulin-like

Protein folding is governed by intramolecular forces that can be highly sequence and environment dependent and the process is readily perturbed by mutations, oxidative stress, temperature and pH change[51]. Such disruptions to the normal folding process can allow exposure of the hydrophobic regions to the hydrophobic regions of other proteins (self or non-self). This can result in protein aggregation, whereby intermolecular forces begin to dominate[55, 56]. Depending on the degree of protein folding, distinct morphologies of aggregates result. Amorphous aggregates have no distinct structure and are the result of the initial aggregation of highly disordered or unfolded proteins[57]. The aggregation of partially folded proteins can give rise to oligomeric aggregates, which are more ordered than amorphous aggregates and have been generally found to be the most toxic morphology to cells[58-70]. Proteins and their aggregates can convert between different forms of aggregates as they traverse their 'free energy landscape' towards more thermodynamically stable species. The most thermodynamically stable aggregate species are amyloid fibrils and they thus represent the energy minima for protein aggregation pathways[71-74].

1.2.2 Amyloid fibrils and the mechanisms of their formation

Amyloid disorders are most famously associated with the formation of stable amyloid fibrils, which are highly ordered thread-like aggregates of misfolded monomers. These become highly problematic for cellular function as the proteins that form the fibrils undergo loss of function and also, as mentioned in Chapter 1.2.1, many of the intermediates and oligomeric aggregates involved in their assembly have been found to be toxic. They can be formed by many types of protein, regardless of their primary sequence or native state. They are primarily composed of flat layers of monomers, arranged on top of one-another in β-sheets to give rise to long proteinaceous filaments[75, 76]. Amyloid fibrils from different proteins share many similar characteristics such as red shift upon binding to Congo red, green birefringence under polarised light and increased fluorescence upon binding with Thioflavin-T (ThT)[77-79]. A typical amyloid fibril structure is depicted in Figure 1.5.

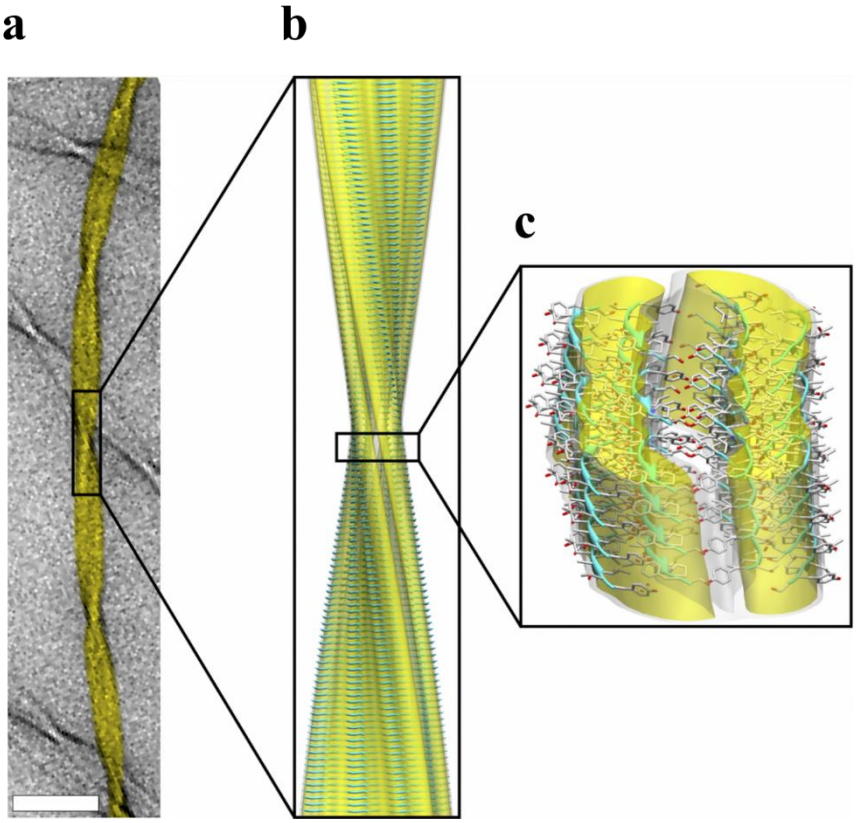

Figure 1.5. Amyloid fibril structural features. Fibril surface is highlighted in yellow in all images. a) Transmission electron microscopy (TEM) image of transthyretin fibrils (Scale bar, 50 nm). b) Solid-state nuclear magnetic resonance (NMR) atomic-resolution structure of the amyloid fibril, fitted into a cryo-electron microscopy (cryo-EM) reconstruction. c) Close-up image showing the molecular structure with the β-sheets shown as pale blue ribbons. Figure adapted with permission from reference [80].

The mechanisms of amyloid fibril formation can be categorised into three main growth phases and four microscopic kinetic processes. The three growth phases are; an initial lag phase where nucleation first occurs, an elongation phase where fibrils rapidly form with the addition of monomer to the fibril ends and finally a growth plateau, where available monomer is exhausted and mature amyloid fibrils are formed[81]. These growth phases can be significantly altered by the environmental conditions such as temperature, pH and the presence of other molecules. The microscopic kinetic processes involved in amyloid fibril formation were recently defined in detail through the analysis of precisely controlled aggregation experiments[82-86]. The individual microscopic events and their corresponding rate constants (k_x) are; Primary nucleation, where soluble protein monomers interact to form new aggregates (k_n); Elongation, which involves the addition of monomers to the fibril ends (k_+); Dissociation, which is the reverse of elongation as it defines the rate in which monomers dissociate from the fibril ends (k_{off}); Fragmentation, which is the generation of new aggregates from the splitting of existing fibrils (k_-); Monomer dependent secondary nucleation, such as surface-catalysed nucleation on the body of the fibrils as opposed to the ends, which is dependent on the concentrations of both the free monomer and the aggregates (k_2)[85, 87, 88]. A visualisation of the growth phases and the contributing microscopic steps are shown in Figure 1.6.

The common attributes between amyloid fibril formation of different proteins has allowed this form of kinetic analysis to study the aggregation of many proteins in detail. These have included disease-related aggregation-prone IDPs such as Amyloid-β (Aβ)[87, 89], tau[90-92], α-Synuclein (αSyn) [93, 94] and the Islet amyloid polypeptide (IAPP)[95, 96]. The detailed information produced from this strategy has allowed understanding about the way other molecules interact and modulate the aggregation pathways, such as small molecules, Abs and chaperones[96-105]. This may be crucial for the development of therapeutics against disease-related aggregation-prone proteins and the aforementioned proteins are implicated in two of the largest growing global epidemics, dementia (Aβ/ tau/ α-Syn)[54, 106] and type II diabetes (IAPP)[107-109]. In this thesis, the focus will be on the interactions of novel Abs with Aβ and α-Syn.

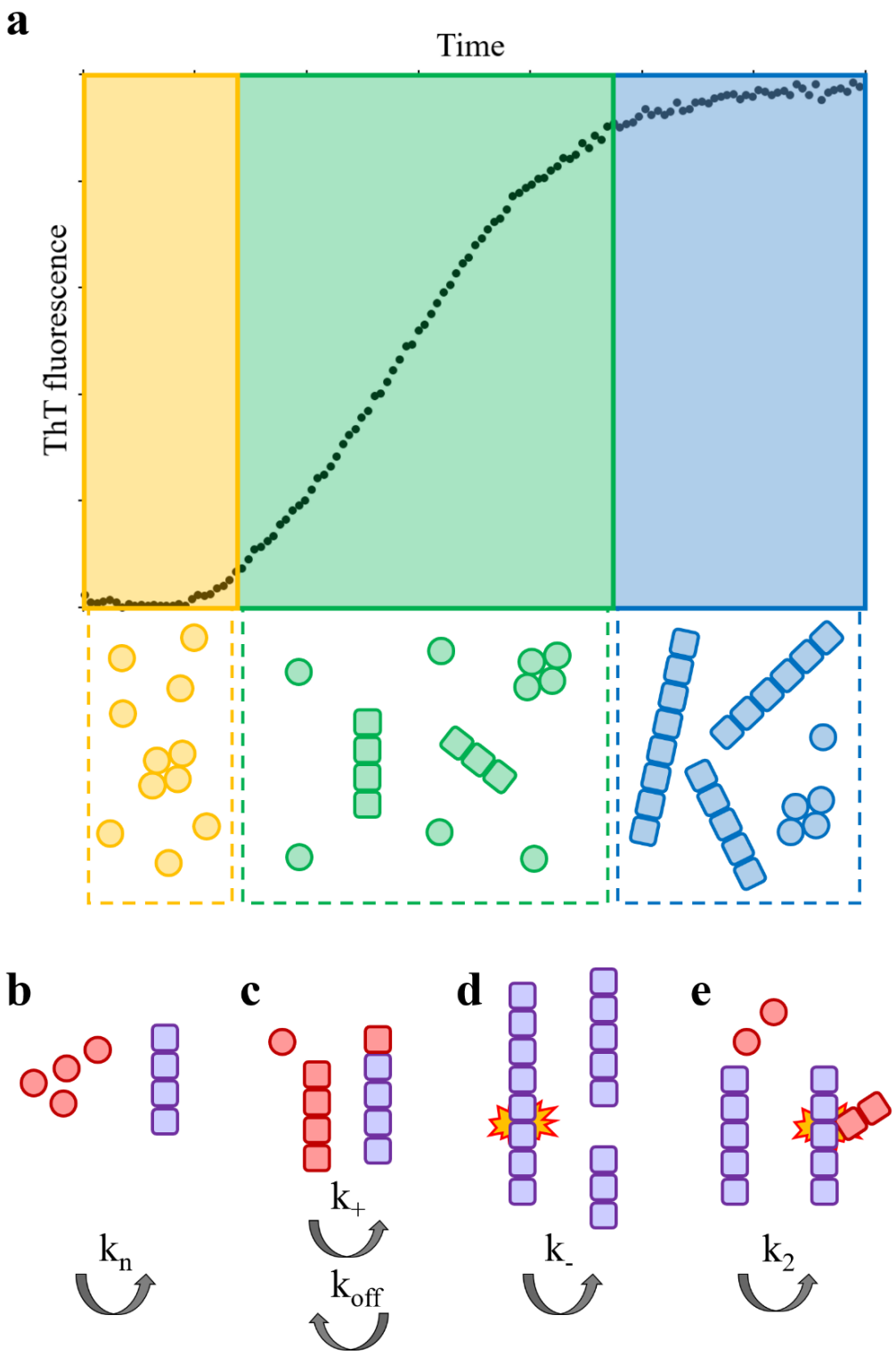

Figure 1.6. Schematic of the different growth phases and kinetic processes involved in amyloid fibril formation. a) A typical amyloid aggregation curve, as followed by the increase in ThT fluorescence over time, which is proportional to the concentration of fibrils. The initial lag phase, elongation phase and growth plateau are shown in orange, green and blue respectively. The dashed boxes below show the bulk average species present in each of the growth phases and are shown in the same colours. Monomers are depicted as circles, oligomers are depicted as four joined circles and fibrils are depicted as lines of rounded squares. b) Primary nucleation (k_n); c) Elongation (k_+) and dissociation (k_{off}); d) Fragmentation (k_-); e) Secondary nucleation (k_2). Figure modified from reference [88].

1.2.3 Amyloid-β

AD is a chronic neurodegenerative disease and is the leading cause of dementia globally, making up of 60-70% of cases[110]. Symptoms include disorientation, mood swings, language difficulties, behavioural problems and the inability to self-care. Eventually, bodily functions decline until lost, resulting in death[110]. One of the hallmarks of AD is the accumulation of amyloid plaques and neurofibrillary tangles in the brain of patients[111]. Amyloid plaques are extracellular proteinaceous deposits that consist primarily of aggregated Aβ and neurofibrillary tangles are intracellular deposits of hyperphosphorylated tau[112, 113]. Aβ is a disordered peptide that has its origins in a protein called the amyloid precursor protein (APP). APP is a membrane-bound protein that is expressed in multiple tissues but is mostly abundant in neuronal synapses. It is believed to play an important role in synapse formation, although this function is widely debated[114]. APP is cleaved by two enzymes, β-secretase and γ-secretase, which liberates soluble Aβ from the membrane into the extracellular space. Aβ can exist in differing lengths, between 30-51 residues[115]. The most common forms are $A\beta_{40}$ and $A\beta_{42}$, with $A\beta_{42}$ being the most aggregation prone and making it a prime target in AD therapeutics research. Recent research has indicated that it is the oligomers, rather than the plaques themselves, that are the toxic agents responsible for the disease[61, 116]. The structure of Aβ peptides are shown in Figure 1.7.

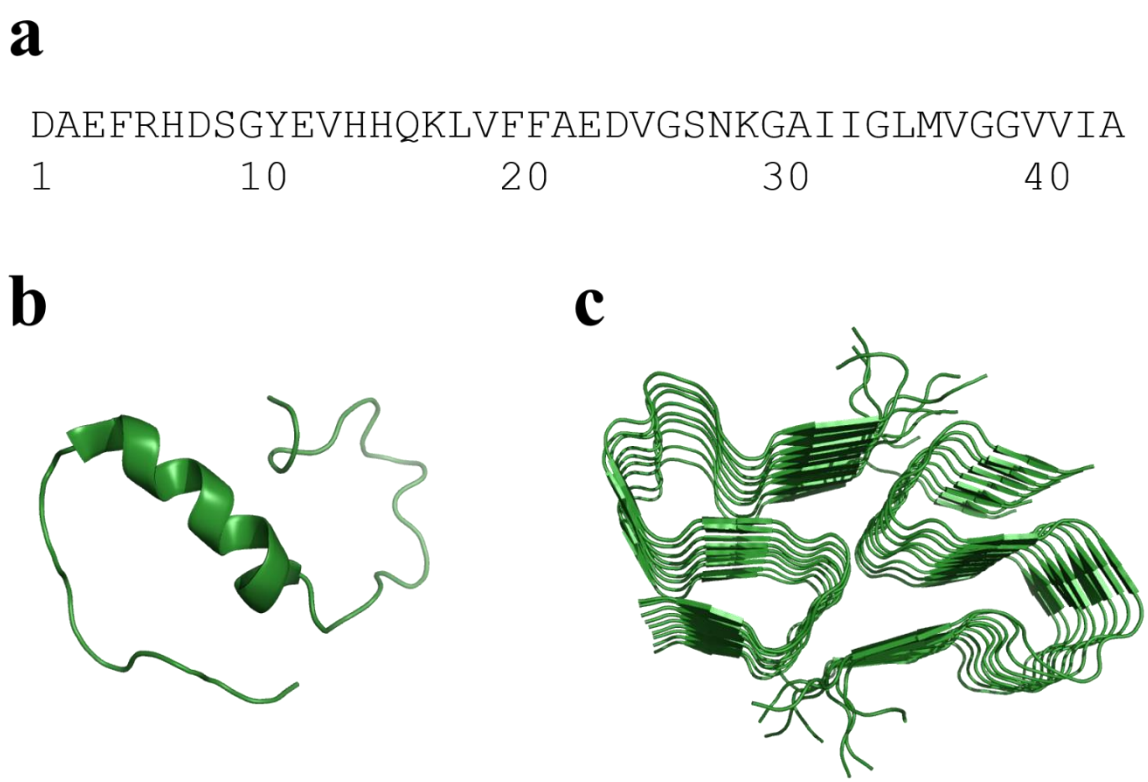

Figure 1.7. Structures of the Aβ peptide. a) AA sequence of the $A\beta_{42}$ peptide. b) Solution NMR structure of a partially folded $A\beta_{40}$ monomer (PDB entry 2LFM)[117]. c) Solid-state NMR structure of a short $A\beta_{42}$ amyloid fibril. The fibril is arranged as two independent stacks of monomers arranged in β-sheets (PDB entry 5KK3)[118]. The structures were produced using PyMOL (PyMOL, Molecular Graphics System, Version 2.2.0, Schrödinger, LLC).

1.2.4 α-Synuclein

αSyn is a 140-residue long IDP and is found in abundance at presynaptic terminals, located at the tips of neurons, and its function is poorly understood. It is postulated to be involved with regulating neurotransmitter release by inhibiting synaptic vesicle recycling[119-121]. αSyn can aggregate into amyloid fibrils and the products of its aggregation are found in Lewy bodies[122, 123]. Lewy bodies are proteinaceous deposits like amyloid plaques, but unlike amyloid plaques they form intracellularly. Its aggregation and deposition into Lewy bodies are one of the hallmarks of a range of diseases called synucleinopathies. These include Lewy body dementia, multiple system atrophy and Parkinson's disease, the latter being the second most common form of dementia[122, 124]. Parkinson's disease is a slow, debilitating neurodegenerative disorder that can also cause shaking, mobility difficulties, rigidity, depression, anxiety and typically

results in death, 7-15 years after diagnosis[125]. The primary sequence of αSyn is divided into three main domains. Residues 1-60 form an amphipathic region that readily forms α-helices and behaves similarly to the binding domains of apolipoproteins[126]. Residues 61-95 are mostly hydrophobic and these contain the non-amyloid-β component (NAC) region which is the most responsible driver of αSyn aggregation[127]. Residues 96-140 form a mostly acidic residue region containing many prolines, and is inherently highly disordered. The structure of αSyn is shown in Figure 1.8.

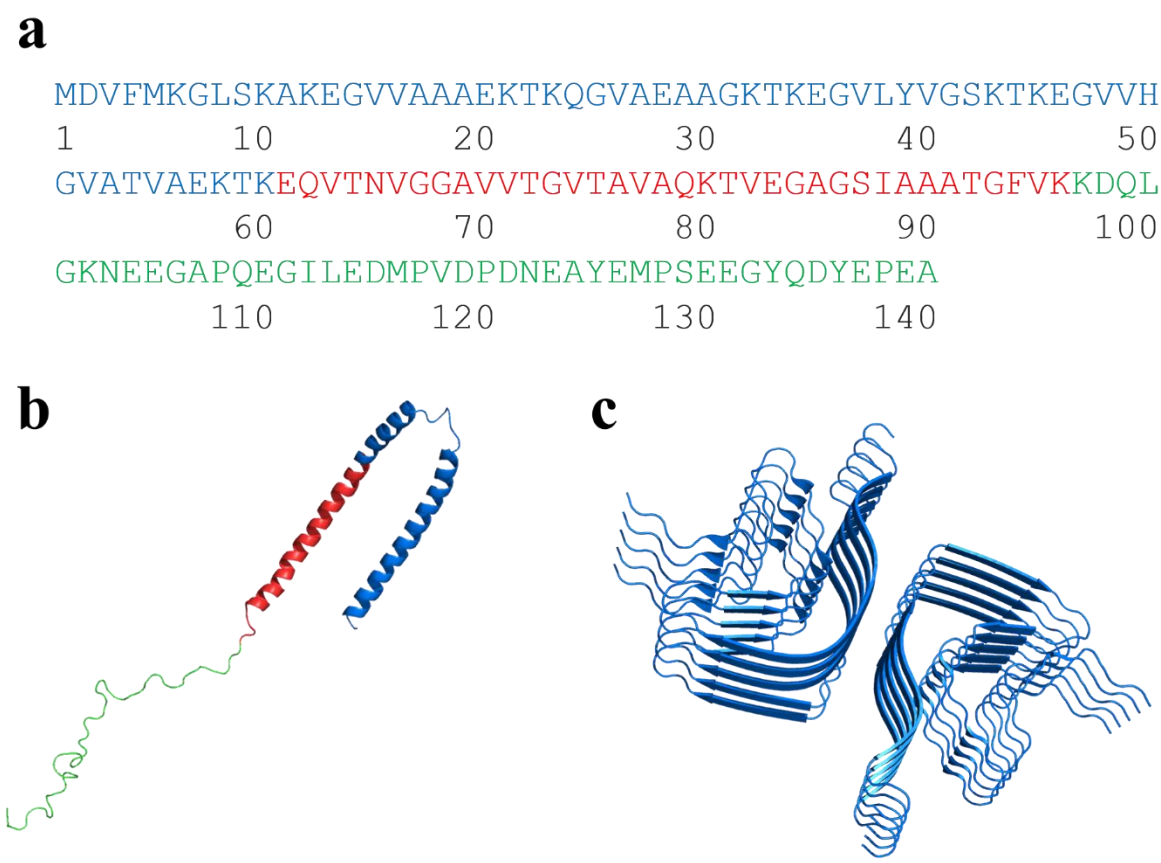

Figure 1.8. Structures of αSyn. a) AA sequence of αSyn. The amphipathic region is shown in blue, the NAC region is shown in red and the acidic region is shown in green. b) Solution NMR structure of a micelle-bound αSyn monomer. The amphipathic (blue) and NAC (red) regions are folded into α-helices whilst the acidic region (green) remains disordered (PDB entry 1XQ8)[128]. c) Electron microscopy resolved structure of a short section of an αSyn amyloid fibril with individual monomers wholly depicted in blue. Like $A\beta_{42}$ (Figure 1.7 c), the fibril is arranged as two independent stacks of monomers arranged in β-sheets (PDB entry 6CU7)[129]. The structures were produced using PyMOL (PyMOL, Molecular Graphics System, Version 2.2.0, Schrödinger, LLC).

1.3 Antibodies targeting misfolding disease-related proteins

1.3.1 Aggregation inhibition using specific antibodies

Abs and Ab fragments have been discovered against a vast range of native-states, transition-states and aggregates involved in protein misfolding diseases[130-136]. They have given structural insights into the nature of different species involved in the aggregation pathways[104, 136]. Abs that can bind to different epitopes within a protein can show which regions play important roles in the misfolding process and the formation of aggregates[104, 136]. Some Abs and combinations of Abs have been shown to inhibit the formation of different types of aggregates, including amyloid fibrils. For example, in one study, a series of camelid sdAbs, called 'nanobodies', were raised against different epitopes within a disease-related variant of human lysozyme, which undergoes amyloidosis, and each one inhibited the formation of fibrils, irrespective of the specific epitope[136]. However, the individual microscopic nucleation steps can be significantly altered by Ab binding to different epitopes of a protein[104]. Using the same aggregation inhibition kinetics as introduced in Chapter 1.2.2, one can discern the individual nucleation events that are inhibited upon Ab binding and, in theory, understand which type of aggregating species they bind to[85, 104, 137]. This process is visualised in Figure 1.9.

It is important to understand which aggregating species is being targeted and inhibited as one cannot simply assume that inhibition of amyloid formation will also inhibit the generation of the more toxic intermediates. In fact, recent studies on aggregation kinetics have shown that in some cases the inhibition of fibril formation can actually increase the concentration of toxic oligomers[85, 104]. Therefore, the development of Abs targeting aggregation, as a therapy to limit the generation of disease-related aggregates, must incorporate microscopic kinetic characterisation as a 'screening' method to ensure only the pathological species are specifically inhibited[85, 104, 137]. Targeting surface-catalysed secondary nucleation has emerged as one of the most attractive strategies to inhibit the formation of oligomers. This is because whilst both primary nucleation and secondary nucleation are responsible for the production of oligomers, secondary nucleation forms several orders of magnitude more oligomers than primary nucleation[138]. Furthermore, the binding of Abs to monomers (implicated in the inhibition of primary nucleation) can be undesirable in the case when the exact function of the monomer is unknown[85].

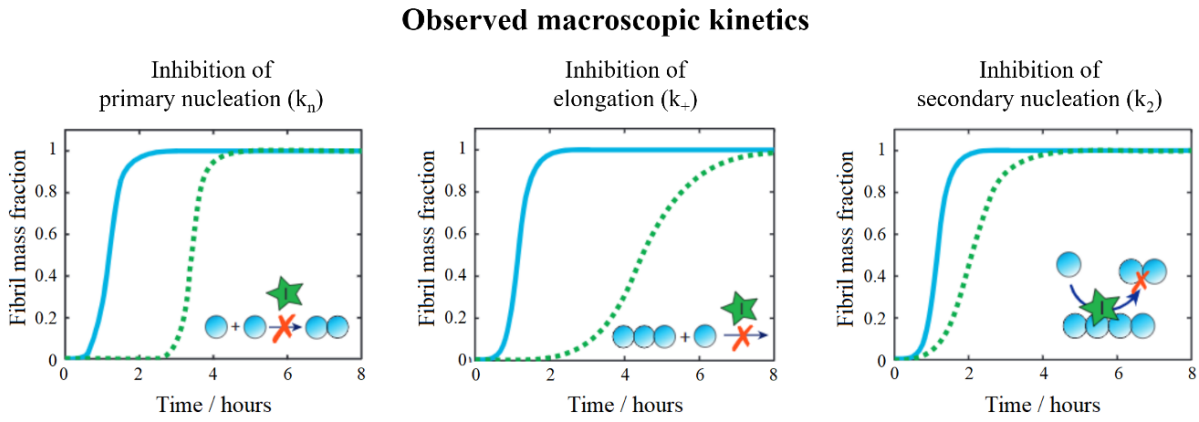

Figure 1.9. Model simulations of the microscopic time-course of amyloid fibril formation[85]. Shown is the microscopic kinetic profile of an aggregating protein (blue) and the effect of the presence of an aggregation inhibitor (dashed, green). Simplified schematics depicting the different effects of an aggregation inhibitor (green) on the aggregating protein (blue) are also shown next to each profile. Inhibition of primary nucleation (left) sees an increase in the lag phase time with no effect on the slope of the elongation phase. Inhibition of elongation (centre) results in an increase in the lag phase time and an increase in the elongation phase time. Inhibition of secondary nucleation (right) causes an increase in the elongation phase time with a negligible effect on the lag phase time. Figure modified with permission from reference [85].

Experimental aggregation inhibition data, such as a ThT fluorescence time course of different concentrations of Ab in an aggregation reaction, can be rapidly fitted by applying this mathematical method[85, 139]. This allows many Ab candidates to be 'ranked' against one another, not by binding but by biological effect. In this thesis, this methodology is used in Chapters 3.7 and 3.12 and will be described in more detail in Chapter 5.9. Ab binding to aggregating monomers or aggregates can be thought of as a 'blockade' and is analogous to Ab neutralisation of a pathogen, introduced in Chapter 1.1.2.

1.3.2 Antibody clearance of aggregates

Research into the use of Abs as therapeutics to treat AD has been marred by the clinical failures of some high profile treatments[140-144]. Ab candidates such as Solanezumab (Eli Lilly), Crenezumab (Roche) and Aducanumab (Biogen Inc.) brought hope to the scientific community and the general public, showing great promise in pre-clinical studies[145-147]. They were all raised against Aβ and targeted different aggregated species. Solanezumab preferentially bound

to soluble monomeric Aβ and Crenezumab and Aducanumab were found to mainly bind the lateral fibril surface and oligomeric species[148, 149]. All three Abs, which are all full-length IgGs, demonstrated clearance of aggregates *in vivo*, although it has remained unclear as to what mechanisms are responsible. In the case of Aducanumab, it was postulated that the Fc region-mediated recruitment of microglia, the macrophages of the CNS, was inducing clearance by phagocytosis[147].

Despite demonstrating plaque reduction, all three Abs failed in mid-to-late stage clinical trials due to lack of efficacy in patients with AD. Promising results, in the form of a reduction in the rate of cognitive decline, were seen upon treatment of patients with mild symptoms, indicating that early treatment is of the most benefit to patients[141]. Despite the encouraging results, the hope of a complete cure has proven to be elusive to many involved in AD therapy research and development, and a better understanding of the disease is necessary. As mentioned in Chapter 1.1.1, the current price of research and development is extremely high and pharmaceutical companies risk to lose vast sums of money with every failed project. This discouragement has led Pfizer, one of the biggest pharmaceutical companies in the world, to pull out of neuroscience research entirely[150]. Recent encouraging clinical studies[141] show the necessity of treating AD before symptoms actually develop (preventative therapy). This requires extensive research into diagnostics to identify patients at highest risk of developing AD[151, 152]. In the case of Abs, it would also require an overhaul in the way Abs are discovered. Solanezumab, Crenezumab and Aducanumab were all identified as pre-clinical 'leads' based on their ability to bind Aβ, not their ability to induce a biological effect. If a drug's biological effect can be identified earlier in the discovery process, then failures may be identified before significant amounts of money, resources and time are wasted[9, 153]. Efforts in reducing the costs and time of Ab research and development may yet be enough to reassure hope and prevent further exodus of pharmaceutical companies from neurodegenerative disease research.

1.4 Classical antibody discovery and the advent of in silico engineering

1.4.1 Limitations of the antibody discovery process

In the case of biopharmaceutical companies, research and development is a lengthy process and it is common for successful Ab drug candidates to require ~10-15 years to reach approval. Of this, screening using animal models or 'naïve' gene libraries can take years and requires extensive planning and development for each individual target[154]. Screening traditionally involves selecting Abs that bind the desired antigen from vast libraries or 'repertoires' which can range in size up to tens of trillions of variants ($1x10^{13}$)[155]. These libraries can be provided by animals through the use of hybridoma technology, where spleen cells of immunised animals are fused with myeloma cells and the resulting immortalised hybridoma cells are screened for the production of desired mAbs[156]. The libraries can also be provided by *in vitro* selections such as B cell reverse transcription and synthetic libraries. B cell reverse transcription also involves immunising an animal with the desired antigen, but the selection is through the use of cDNA from removed B cells in a blood sample by reverse transcription. The Abs are then selected using a recombinant *in vivo* selection such as yeast or bacterial display, or *in vitro* selection such as phage display, ribosome display or mRNA display[157, 158]. Synthetic naïve libraries do not come from animals, or involve any immunisation of any kind, but are derived from carefully selected desirable human Ab 'scaffolds' that have genetic diversity introduced into their structures via random mutagenesis or recombination of human V gene repertoires[159, 160]. These large libraries mimic the vast Ab diversity of a human immune system, without challenging it with an antigen, and the same libraries can be applied to multiple antigens. Selection of these libraries also involves the use of the aforementioned recombinant display technologies[161, 162].

Each of these traditional Ab discovery platforms have their advantages and pitfalls. Hybridoma technology and B cell reverse transcription both harness the power of the immune system's inherent ability to engineer and optimise Ab properties such as affinity and stability, and as a result, the Abs produced by these methods are of high quality[163]. However, as they both rely on an immunisation procedure, antigens are usually limited to highly-immunogenic non-toxic species and in the case where animals are immunised, the resulting Abs need to be humanised which can result in losses of binding affinity and further development is often required[164-166].

The reverse is true for the advantages and disadvantages of synthetic naïve libraries, as whilst they are fully human by design and can be immediately selected against toxic antigens, they cannot rely on the immune system for optimisation and the resulting Abs frequently require time-consuming affinity maturation and stability/solubility engineering[166, 167]. In recent years, considerable effort has been made to shift the approach of discovering Abs towards incorporating computational *'in silico'* modelling and design as a method of assisting with development constraints[36, 168-170]. The timescale in which *in silico* design can be implemented during Ab drug discovery is shown in Figure 1.10.

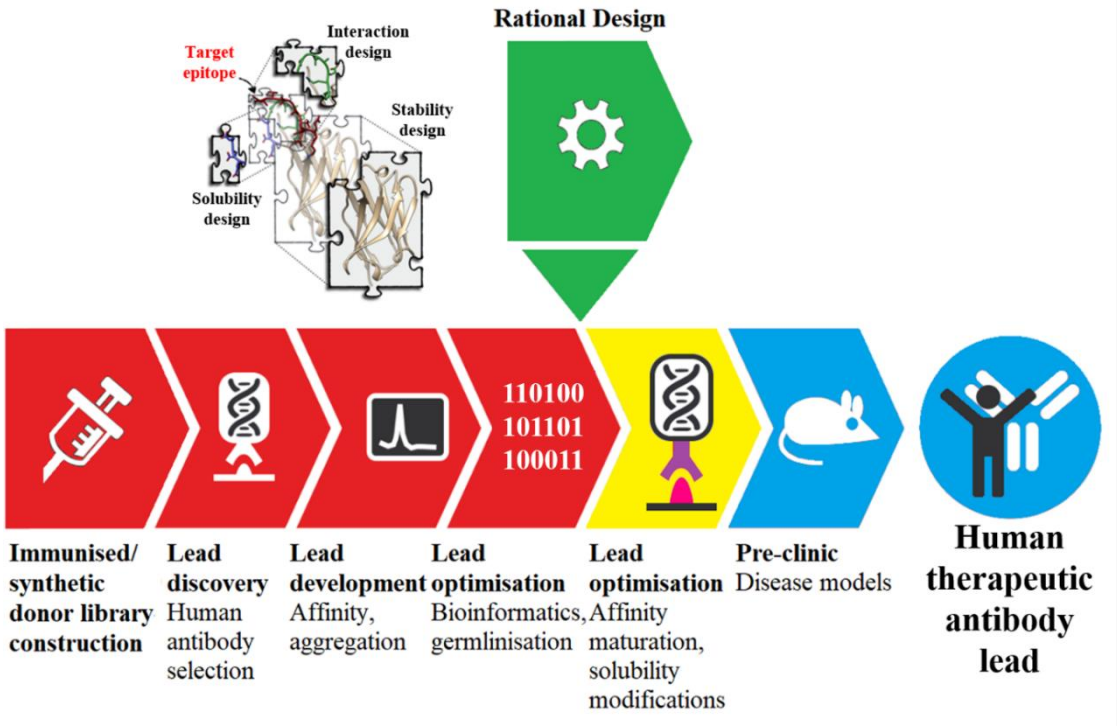

Figure 1.10. Overview of the stages involved in Ab development for biopharmaceutical companies, from Ab discovery to approval. *In silico* design (green) may provide an opportunity to accelerate the process and significantly reduce labour and cost.

Even though *in silico* design is still in its infancy, the ever-expanding Ab structural database with Ab-target complexes and Illumina next-generation sequencing (NGS) has allowed the development of many promising computational techniques[171-176]. Computational Ab design carries with it the advantage of being able to rapidly produce fully human Ab leads *de novo* and as computers become more powerful and as high-quality structural data becomes more accessible, this will only get faster. Another key advantage has been the demonstration of *in silico* design to target poorly-immunogenic linear epitopes, insufficiently accessible to classical methods[176].

1.4.2 Rational design of antibody paratopes

Whilst obtaining mAbs against most antigens with hybridoma technology and naïve Ab libraries has proved very successful in Ab discovery, targeting epitopes of interest within proteins has proved challenging for these established techniques. These techniques are almost entirely reliant on the ability of the target to behave as an antigen and as a result, Abs are usually obtained against the most 'immunogenic' locations[177]. This is a problem if the target is a protein as it is not a general strategy to simply immunise an animal model or screen a naïve Ab library against a peptide representing a pre-selected epitope as the tertiary structure of the epitope, if conformational, may not be retained as it would be on the full-length protein[178]. Also, the physicochemical properties may be significantly different to that of the full-length protein and many peptides may suffer drastic solubility problems.

Computational design methods for Abs have frequently been used to modify the paratopes to alter the binding activity and specificity for antigens[171-176]. If successful, Abs may be discovered without ever having to screen against the target. As mentioned in Chapter 1.1.2, the antigen binding site of an Ab lies within the variable region and is polygenic in nature, being encoded by multiple genes –V, D and J, which undergo random recombination and random mutation to create significant variation in the paratope[28]. One rational design strategy which has seen frequent applications in directing Ab specificity has been the replacement of regions of the CDR loops with peptide sequences, known as grafting, which are complementary to the target epitope[36, 104, 176, 179-183]. If a well characterised protein-protein interaction is to be disrupted, such as a receptor-ligand, then it is possible to graft a small portion of the ligand into one of the CDR loops to initially direct the specificity towards the receptor and then design other portions of the Ab to assist with improving the binding affinity[179, 180].

This approach was recently used by researchers in an attempt to create good Ab leads targeting the inhibition of $A\beta_{42}$ aggregation by grafting short sequences (10 AA) of $A\beta_{42}$ into the CDR3 loops of different sdAbs and then observing the effect on protein aggregation. The 'grafted amyloid-motif domain antibodies' (gammabodies) obtained against $A\beta_{42}$ did bind the target epitopes specifically but had a propensity to destabilise and aggregate with $A\beta_{42}$[181, 182]. Recently, efforts have been made to block aggregation-prone regions of proteins with sdAbs grafted with non-homologous designed complementary sequences in an effort to induce binding but prevent Ab destabilisation in the presence of aggregates[104, 176].

1.5 Rationally designing stable single-domain antibodies towards aggregation-prone targets

1.5.1 Single-domain antibodies

As introduced in Chapter 1.1.1, smaller antigen-binding fragments are desirable as they can access buried epitopes within structured proteins that are not accessible to larger Abs and can be equally specific. They suffer less solubility issues than larger formats, penetrate tissues more rapidly, are simpler to develop and significantly cheaper to produce as they can be synthesised in bacteria and are not reliant on mammalian cell culture. Whilst antigen-binding sdAbs derived from full-length Abs were first described in 1989, they were far from applicable due to poor biophysical properties resulting from the exposed V_H/V_L interface[184]. It was not until the discovery of naturally occurring Abs devoid of light chains, derived from camels, that isolated V_H fragments were perceived as viable for research, medicine and biotechnology[185]. Seeking a fully-human alternative to nanobodies, researchers solved the problematic hydrophobic V_H/V_L interface through the use of compensatory mutations that gave solubility and stability to the isolated sdAbs[186, 187]. Since then, sdAbs have enjoyed much attention due to their ease of isolation and use, and already have shown therapeutic potential for the treatment of cancer, blood disorders and neurodegenerative diseases[103, 188, 189]. Owing to their folding simplicity, mostly due to a single disulphide bond in the V_H domain, sdAbs are particularly well suited to cytosolic expression and hence are suitable for phage display and have even been reported for *in vitro* expression for ribosome display[190, 191].

However, there are drawbacks associated with the smaller size of sdAbs. Having only one binding domain results in lower binding avidity, meaning that the high affinity commonly achieved by larger fragments is more challenging to obtain[192]. Their reduced size (~12.5 kDa) also translates to a shorter serum half-life because their size is significantly lower than the 60 kDa renal threshold[193]. Lacking an Fc region may be advantageous when recruitment of the immune system is undesirable, but it also means sdAbs are not rescued by binding to the neonatal Fc receptor (FcRn)[194]. Another disadvantage is that, whilst full-length Abs have evolved to be fairly stable with such a large variation in the sequences that make up the antigen-binding site, restricting the size to only ~120 residues places more 'weight' on each residue and sdAbs are more sensitive to destabilising mutations as a result[191]. Their paratopes are also

usually convex, which is more suitable for binding conformational epitopes rather than linear epitopes, meaning that significant engineering is usually required to accommodate linear targets[36, 158, 191]. Regardless, sdAbs still represent one of the most attractive approaches for targeting neurodegenerative disorders due to the requirement for specificity and small-size enhanced tissue penetration. Stable single-domain human Ab scaffolds are becoming increasingly available and if the binding regions can be engineered to be specific, then they represent significantly better starting points for smaller Ab-based therapeutic discovery. The structure of a sdAb is shown in Figure 1.11.

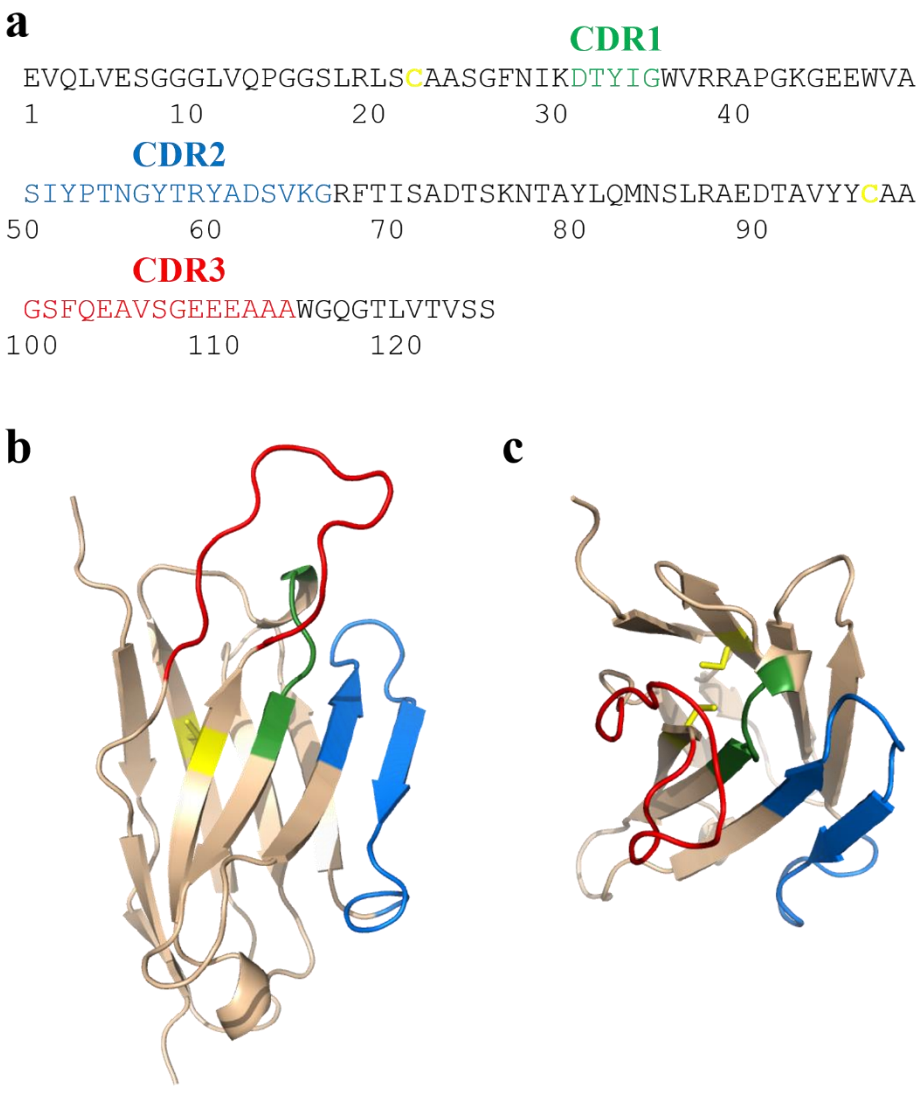

Figure 1.11. Structures of DesAb-F, a human sdAb[176]. The non-conserved (variable) regions forming the CDR loops (as defined by Kabat) are shown in green (CDR1), blue (CDR2) and red (CDR3). The conserved region, or scaffold, is shown in black (a) and tan (b, c) with the single disulphide-bond shown in yellow. a) AA sequence of DesAb-F. b) X-ray crystal structure of DesAb-F, viewed from the side. c) X-ray crystal structure of DesAb-F, viewed from the top. The structures were provided by P. Sormanni and F. A. Aprile and produced using PyMOL (PyMOL, Molecular Graphics System, Version 2.2.0, Schrödinger, LLC).

1.5.2 *in silico* design of antibodies directed towards pre-selected linear epitopes

A rational design method was recently described that was successful in directing sdAb specificity towards pre-selected disordered epitopes[36, 104, 176, 195]. As an initial proof of concept, six sdAbs were designed with grafted designed complementary peptides in the CDR3 loop towards epitopes within αSyn, $A\beta_{42}$ and IAPP. The design strategy (known as Modular), first involves the Cascade method, which involves assembling 7-residue complementary peptides towards a selected epitope from smaller fragments in β-sheet conformations with the same hydrogen bonding pattern from the protein data bank (PDB), with matching sequences to the target. The method accounts for promiscuity, i.e. the cross-reactivity of the fragments with other sequences, and the least promiscuous fragments are selected to enhance the epitope specificity. It also accounts for parallel or anti-parallel H-bonding patterns. The principle of the design is that once the peptide is assembled into an Ab, then the ability of each fragment to form β-sheet conformations with the epitope is additive and each residue will contribute towards a larger β-sheet[36, 176]. The second strategy involves the CamSol method, which computationally screens variants to identify residues with the largest impact on the target protein's solubility, assuming that the native state and biological activity are to remain unchanged. This is combined with the Cascade method to identify complementary peptides with desirable solubility and also to engineer the stems of the grafted CDR loops[36, 195]. An illustration of Modular is shown in Figure 1.12.

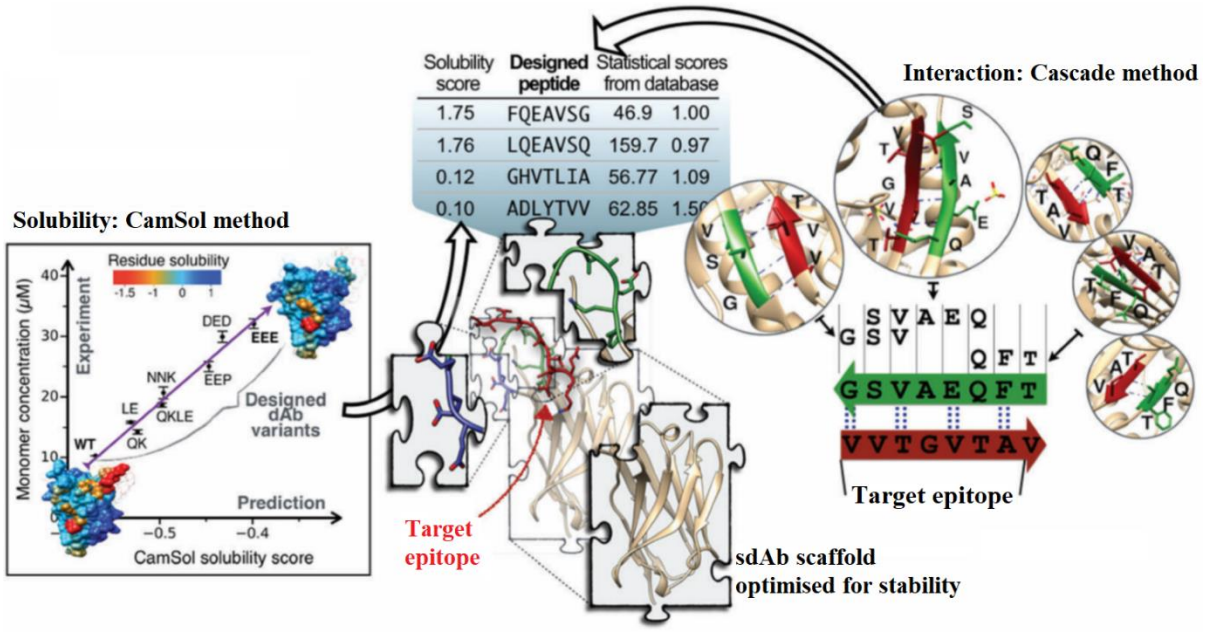

Figure 1.12. Overview of Modular[36]. The CamSol method (left) is used to optimise the solubility of the designed Ab (DesAb) by ranking the potential complementary peptides (top middle) and engineering the CDR3 stem (bottom middle, blue). The scatter plot (left) shows a correlation example between predicted (*x*-axis) and experimentally measured (*y*-axis) solubility[195]. The Cascade method (right) designs sequenced-based complementary peptides. The shown example is the design of the complementary sequence (green) for DesAb-F, a sdAb that was designed to bind residues 70-77 of αSyn (red) with the predicted hydrogen bonds shown as dashed lines. The structures enclosed in circles are the fragments (green) that would be used to assemble the complementary peptide, interacting with fragments that represent the target epitope (red)[36, 176]. The structures shown are from other proteins in the PDB database. Figure adapted with permission from reference [36].

One of the designed Abs, DesAb-F was characterised in detail in their study[176]. It's binding affinity, specificity towards the epitope and effect on αSyn aggregation were all quantified and found to be satisfactory[176]. The techniques and results are highlighted in Figure 1.13.

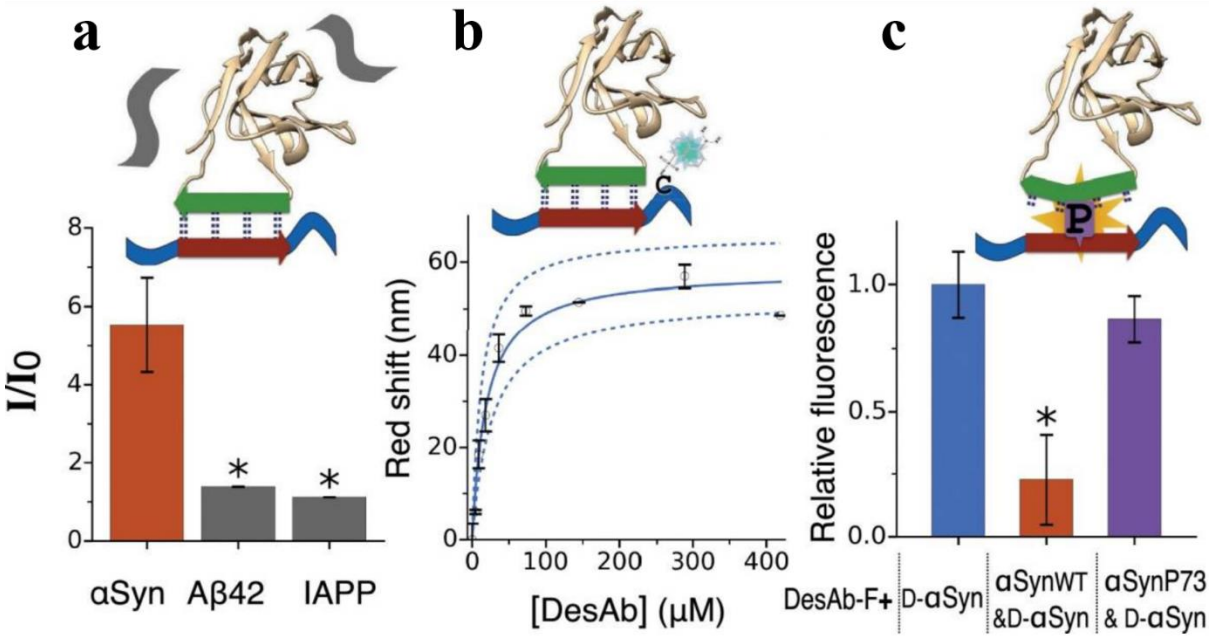

Figure 1.13. Characterisation results of DesAb-F[176]. a) ELISA signal comparison at Abs_{490nm} for the binding of DesAb-F to αSyn (designed/much stronger) and $Aβ_{42}$/IAPP (not designed/weaker). Dot blot assays were also performed in cell-lysates with and without αSyn expression and the signal intensity was significantly different (not shown). b) Binding affinity calculation using dansylated αSyn in a fluorescence titration of increasing concentrations of DesAb-F. The binding affinity (K_D) of the single binding model was calculated to be ~18 μM. c) Fluorescence competition assay to confirm selected epitope binding. Insignificant binding was observed for αSyn 73P, which has a flexibility-disrupting proline inserted in the centre of the epitope, which indicates correct intermolecular Ab specificity. Figure adapted with permission from reference [176].

Another DesAb was also generated against the same target epitope with two grafted complementary peptides, one in the CDR3 loop and one in the CDR2 loop. The rationale in this design was that Abs frequently bind their targets with more than one CDR loop and that two binding interfaces would hopefully produce a higher affinity Ab. The two-loop DesAb was found to bind αSyn in the mid- to low-nanomolar range, which is more desirable for Ab applications, but the stability of the scaffold was compromised and the purification became very challenging. This two-loop DesAb did show that more than one CDR loop could be involved in a designed Ab binding and improve the binding affinity[176]. The two-loop DesAb design, structure and affinity characterisation are shown in Figure 1.14.

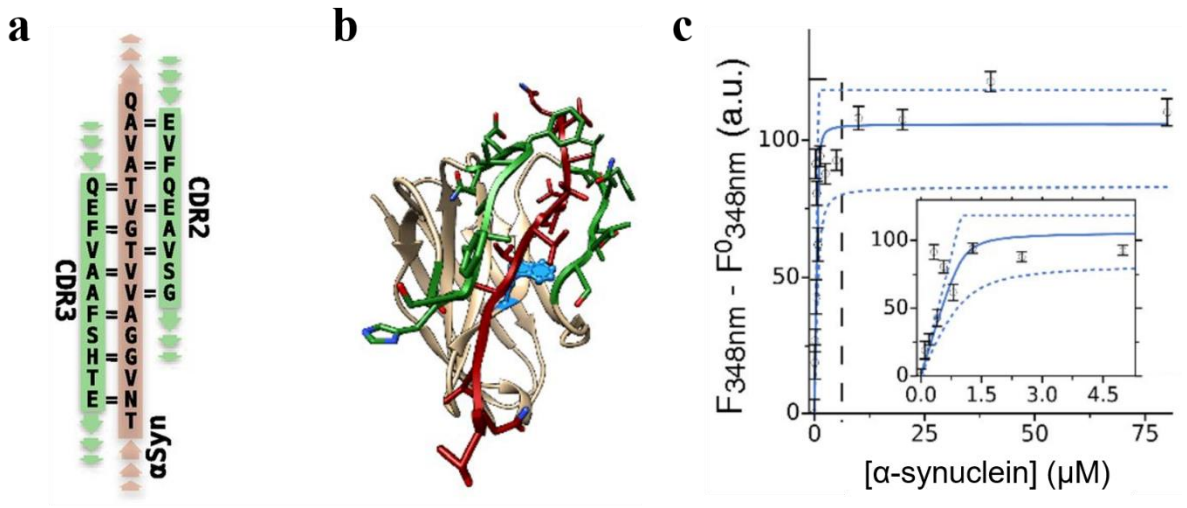

Figure 1.14. Design, structure and affinity characterisation of the two-loop DesAb[176]. a) Representation of the grafted designed complementary peptides (green) in a 'sandwich' anti-parallel β-sheet-like interaction with the target epitope (red). Arrows denote the N to C terminus direction and double lines mark residue pairs predicted to contribute backbone-backbone hydrogen bonding. b) Simulated structure of the interaction of the grafted complementary peptides (green) and the target epitope (red). The sdAb scaffold (tan) is shown with Trp-47 shown in light blue. c) Intrinsic fluorescence (Trp) titration assay at a static concentration of two-loop DesAb (1 μM) and a variable concentration of αSyn (*x*-axis). The line of best fit (solid, blue) indicates a binding affinity of ~45 nM. (*Inset*) Zoom of the dashed-black line region for clarity. Figure modified with permission from reference [176].

Sormanni and co-workers showed that the design of multiple Abs to be specific towards disordered epitopes was indeed impressive; however none of the stable Abs were immediately viable for typical therapeutic, diagnostic and research applications due to their low binding affinity[176].

1.5.3 *in silico* design of antibodies to selectively target protein aggregation nucleation pathways

After the establishment of Modular, it was then utilised to study the role that different disordered polypeptide regions play in the aggregation of $A\beta_{42}$. A panel of five DesAbs were designed and generated against five separate epitopes covering the majority of the length (81%) of $A\beta_{42}$[104]. The $A\beta_{42}$ 'scanning' DesAbs and their target epitopes are illustrated in Figure 1.15 and Table 1.2.

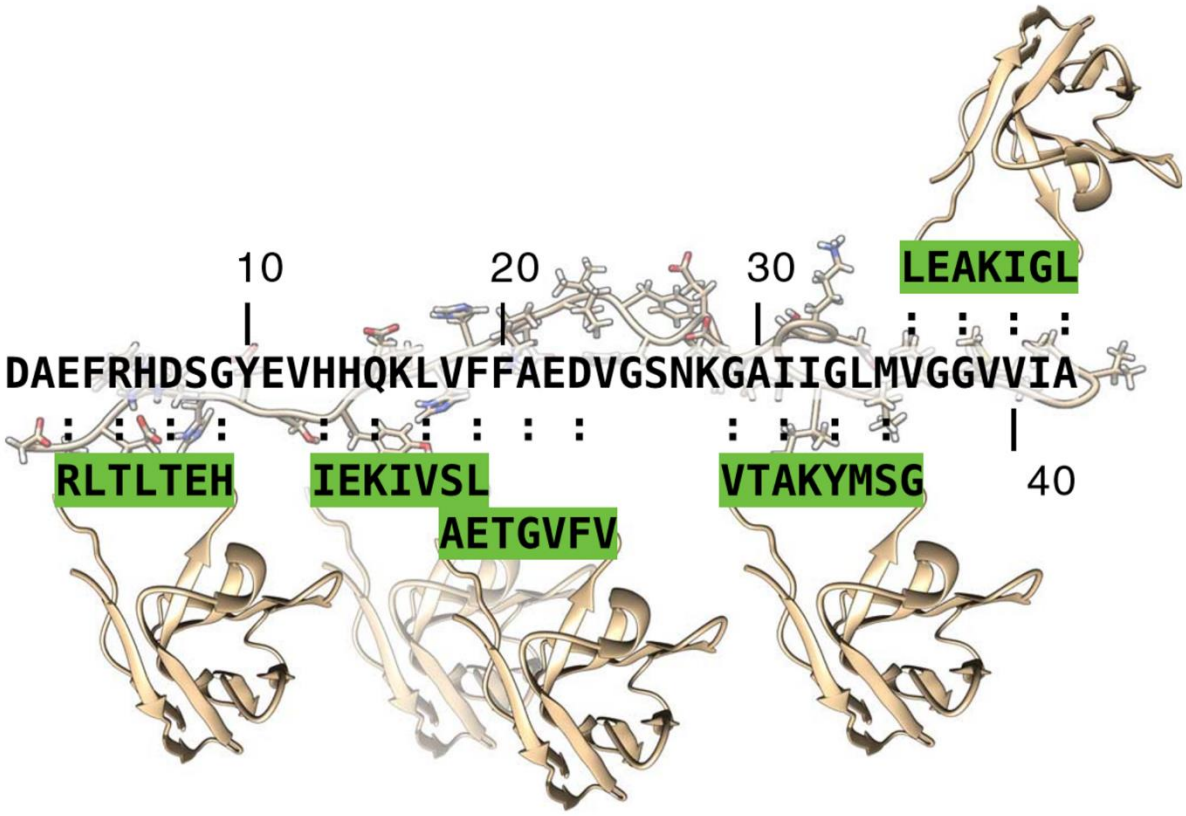

Figure 1.15. Schematic representation of DesAb scanning of the Aβ$_{42}$ sequence. The Aβ$_{42}$ peptide is shown in the centre (N-C terminus shown as left to right) with its full sequence and side chains shown as stick models. The five DesAbs are shown with their CDR3-grafted complementary sequences highlighted in green. Predicted backbone-backbone hydrogen bonds are indicated by dashed lines. Figure adapted with permission from reference [104].

Table 1.2. Names, associated target epitopes and grafted sequences of the scanning DesAbs against Aβ$_{42}$. Table modified with permission from reference [104].

Antibody	Grafted sequence	Target sequence
DesAb$_{3\text{-}9}$	**HETLTLR**	EFRHDSG
DesAb$_{13\text{-}19}$	**LSVIKEI**	HHQKLVF
DesAb$_{18\text{-}25}$	**VFVGTEA**	VFFAEDVG
DesAb$_{29\text{-}36}$	**GSMYKATV**	GAIIGLMV
DesAb$_{36\text{-}42}$	**LGIKAEL**	VGGVVIA

The five DesAbs were characterised based on their ability to inhibit the aggregation of Aβ$_{42}$ using the ThT fluorescence-monitored time course measurements introduced in Chapter 1.2.2. It was found that Ab binding to different epitopes across the length of Aβ$_{42}$ has a profoundly different effect on the microscopic nucleation steps in Aβ$_{42}$ aggregation[104]. The findings are summarised in Figure 1.16.

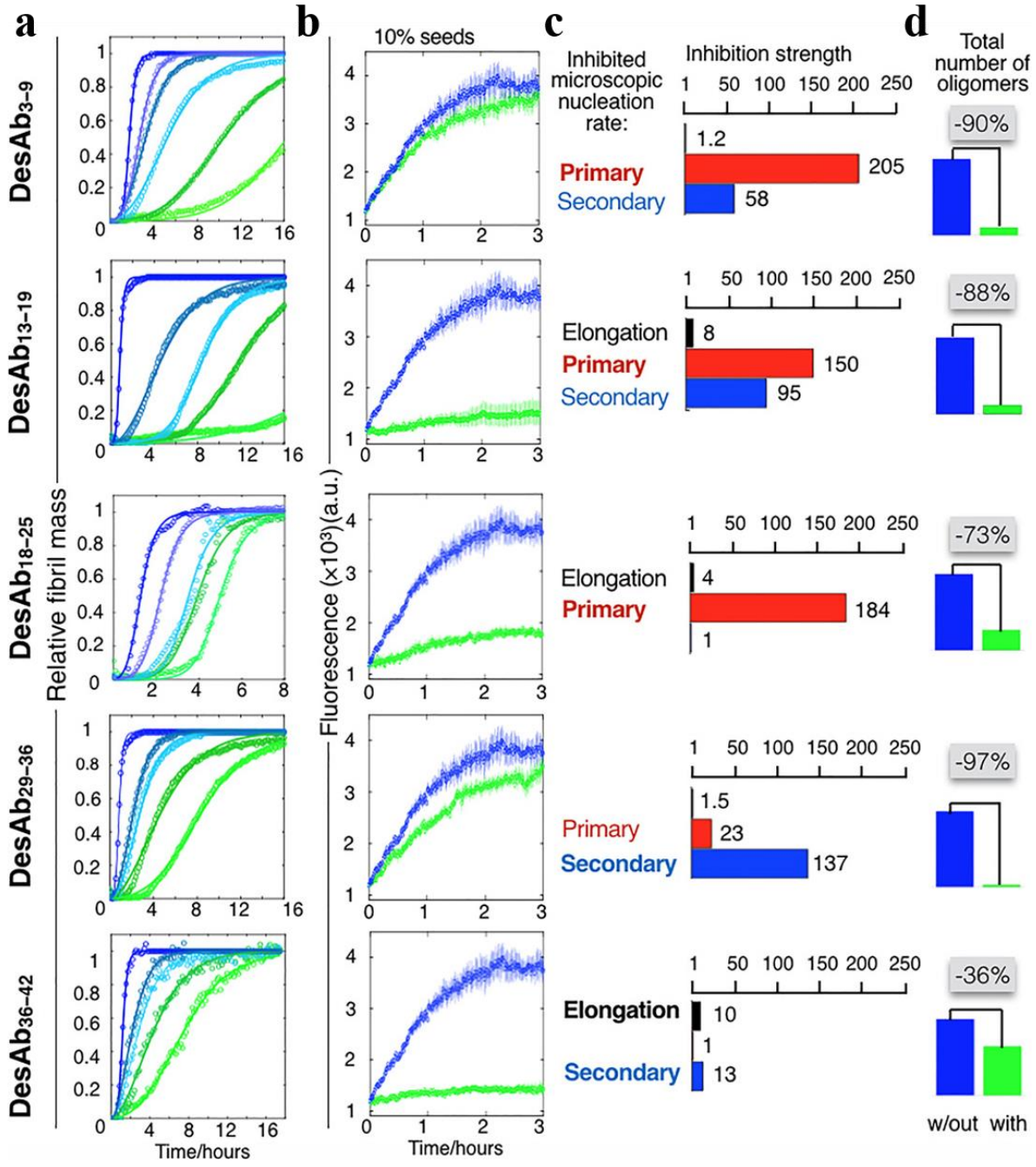

Figure 1.16. Measured effects of the DesAb binding to different Aβ$_{42}$ epitopes on the macroscopic time-course of amyloid fibril formation and the microscopic nucleation events. a) Macroscopic time courses of Aβ$_{42}$ aggregation as followed by ThT fluorescence, in the presence of varying amounts of DesAbs. The aggregation of Aβ$_{42}$ alone is shown in blue and Aβ$_{42}$ with increasing monomer equivalents (blue to green) of corresponding DesAb are shown up to 2:1 molar equivalents of Aβ$_{42}$:DesAb (bright green). Continuous lines represent the fits of the data[85, 139]. b) Seeded aggregations of Aβ$_{42}$ in the presence of 10% preformed fibrils to observe the effect of 1:1 Aβ$_{42}$:DesAb (green) on the elongation rate against Aβ$_{42}$ alone (blue). c) Comparison of the calculated inhibition strengths on the k_+ (black), k_n (red) and k_2 (blue) rate constants. d) Calculated numbers of oligomers formed in the absence (blue) and presence (green) of a 1:2 DesAb-to-Aβ$_{42}$ monomer ratio. Figure adapted with permission from reference [104].

These results indicate that different epitopes of a protein may be responsible for different microscopic mechanisms of aggregation. This information is extremely important when developing inhibitors of aggregation. The analysis also provides a foundation for new methods of screening Abs for their specificities towards different aggregate species which could be an extremely attractive feature for Ab diagnostics. For example, $DesAb_{3-9}$ and $DesAb_{29-36}$ both had the most profound effect on the reduction of oligomer formation but had very different inhibition strengths of primary and secondary nucleation. As oligomers are produced by both primary and secondary nucleation, it appears that both Abs have different affinities for the species responsible for these microscopic nucleation steps. Primary nucleation inhibition suggests affinity for the monomers/oligomers and secondary nucleation suggests affinity for the fibril lateral surfaces and also oligomers[85, 104]. By increasing the ratio of one type of nucleation inhibition to another, the ratio of affinity towards one species over another should theoretically also increase. This is partially reflected in the $DesAb_{3-9}$ and $DesAb_{29-36}$ binding affinities towards $A\beta_{42}$ monomers with the former having a calculated binding affinity of 5 nM and the latter 5 μM[104].

It was postulated that the stable but low-affinity designed Ab (DesAb-F) may still become an attractive candidate by applying currently used methods of *in vitro* 'affinity maturation' to it. It was also believed that affinity maturation could change the ratios in affinity towards different aggregate species of $DesAb_{3-9}$ and $DesAb_{29-36}$ to make them more specific to certain species. *in vitro* affinity maturation is a standard technique in Ab development to improve the binding affinities of specific but affinity-poor Abs towards their targets without losing their specificity[196-201]. If affinity maturation can be successfully applied to these designed Abs and the binding affinities and specificities can be improved, then Modular may provide a rapid and cheaper alternative to traditional Ab discovery.

1.6 Affinity maturation of antibodies

1.6.1 *in vivo* affinity maturation by somatic hypermutation and B cell selection

In immunology, affinity maturation of Abs occurs as part of the adaptive immune response in a diverse range of vertebrates. It is a short-term but rapid evolutionary process, confined to an individual organism's immune system. It occurs during the immune response to infection with a foreign agent and is initiated by the capture and presentation of the antigen by follicular dendritic cells (FDCs) inside compartments called germinal centres. Ab paratope diversity is then naturally selected by the B cells that express and present them. Ab diversity is created during B cell proliferation by V(D)J recombination and somatic-hypermutation (SHM) which introduces a large amount of diversity into the CDR loops by targeted error-prone DNA replication. The selection of binders is possible as the antigen is presented on the FDCs in limiting concentrations and competition between B cells for binding results in the most specific and highest affinity binders becoming bound to the FDCs. Selection of binders is achieved by induced apoptosis of non-bound B cells, thus removing non/low-binding diversity from the Ab 'library'. B cells bound to the FDCs proliferate further and more SHM occurs to the specific Abs, increasing the evolutionary potential of their binding affinities. Once the binding affinity is optimal, selected B cells become memory B cells which secrete large quantities of high-affinity Abs to assist the immune response in clearing the foreign agent/infection and rapidly protect against re-exposure[202]. This process is visualised in Figure 1.17.

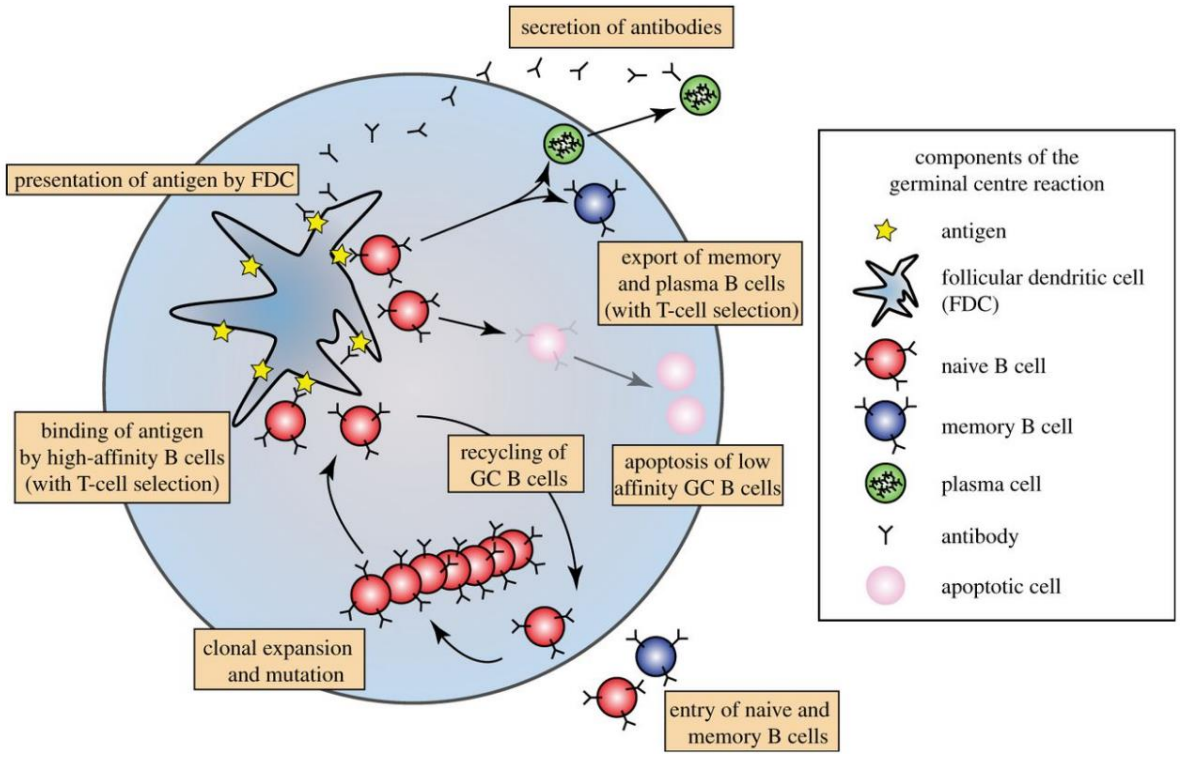

Figure 1.17. Schematic of natural *in vivo* Ab affinity maturation. Ab diversity is selected for high-affinity and specific binders by the controlled competition of B cells (red) within the germinal centre of the lymph nodes. Figure adapted with permission from reference [202].

In pharmaceutical or diagnostic Ab discovery, 'hits' are first obtained by selecting binders from libraries simultaneously using cell screens or display systems, such as phage display. Ab affinity maturation *in vitro* closely resembles that of natural B cell evolution and is widely used to optimise sub-optimal Abs and Ab fragments. It is a directed evolution technique and can be achieved using a variety of strategies. It usually involves taking the Ab hits from animal B cell cDNA or naïve synthetic DNA libraries and subsequently synthetically mimicking SHM[196-201, 203].

1.6.2 *in vitro* directed evolution of binding affinity

Directed evolution is a high-throughput laboratory technique that mimics Darwinian evolution and is used to engineer proteins with new or improved functions[198, 204]. It has been successfully applied to a diverse range of proteins to create new reagents, therapeutics and biocatalysts[205-209]. It involves the rapid diversification of a selected protein's coding DNA to suit a laboratory

time scale to create a DNA library of mutants. The protein chosen to evolve is usually a naturally-occurring protein that already has some of the characteristics of the desired product, such as a similar substrate or thermo-stability in the case of biocatalysts for industrial synthesis[207-211]. The resulting protein variants are then all expressed simultaneously and screened or selected until the most desirable proteins in the library are found. If desired, the evolved protein can then be diversified again if further improvements are sought after. This is only possible through the use of a phenotype-genotype linkage during translation, which can either be covalent or by the use of compartmentalisation such as water in oil micro-droplets or single cell organisms[198]. The directed evolution cycle is illustrated in Figure 1.18.

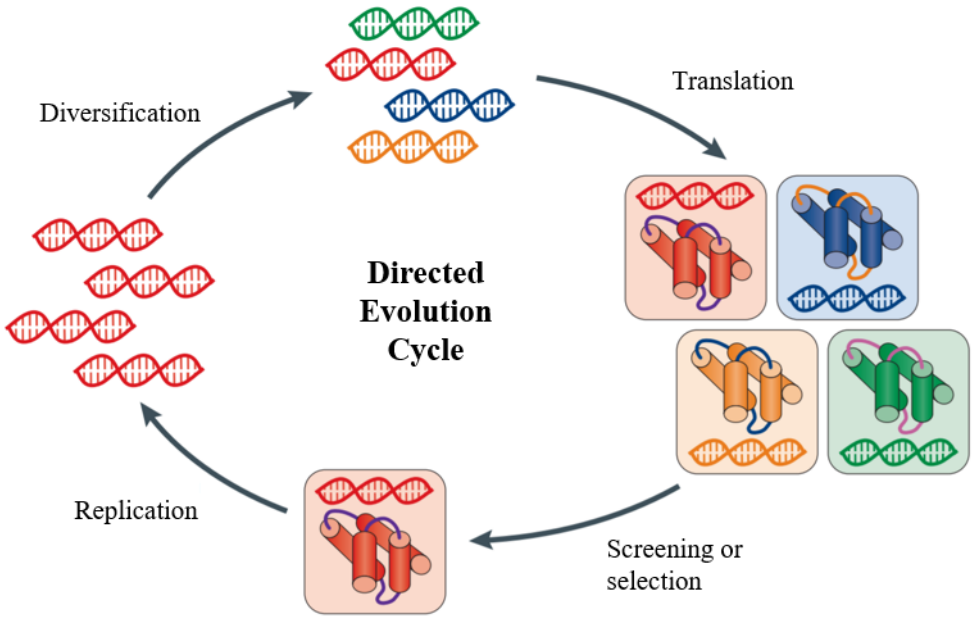

Figure 1.18. The directed evolution cycle. Proteins are evolved through DNA diversification and translation to give a gene product library with variation in protein 'fitness'. Through the linkage of genes and gene products, proteins are selected or screened for improved fitness and the DNA of the most improved functional proteins can be isolated, replicated and diversified further if needed. Figure modified with permission from reference [198].

Binding affinity of Abs is a straightforward property to select for and improve, and multiple techniques exist. The most commonly used are the display systems and each have their own strengths and weaknesses. In display systems, Ab libraries are expressed and linked to their encoding DNA and then exposed to an immobilised target antigen. After competitive binding has been allowed to occur, poor-affinity and non-binding Abs are washed away and high-affinity Abs are selected and sequenced[198]. Yeast-surface display can be used for affinity maturation of larger Abs such as IgGs more effectively than bacterial display as eukaryotic

cells have access to better quality control machineries for stability and protein-folding, although yeast display libraries are the most limited in size[212]. Phage display is partly *in vitro* and is more suitable for smaller Ab fragments as expression takes place in bacterial hosts, and can be used to sample larger libraries. Both yeast and phage display are very straightforward and widely used for Abs, but their library size coverage is limited by the transformation efficiency of cells and phage display reaches a limit of 10^9-10^{10} variants[198, 212]. Ab libraries as large as 10^{13} members can be sampled by entirely *in vitro* display methods such as mRNA display and ribosomal display. These formats do not rely on cellular transformation but require more specialised conditions per type of protein due to the lack of folding control systems. Displayed proteins by *in vitro* systems have been more limited in their size and the most successful examples have been with polypeptides[198]. The *in vitro* display systems are illustrated in Figure 1.19.

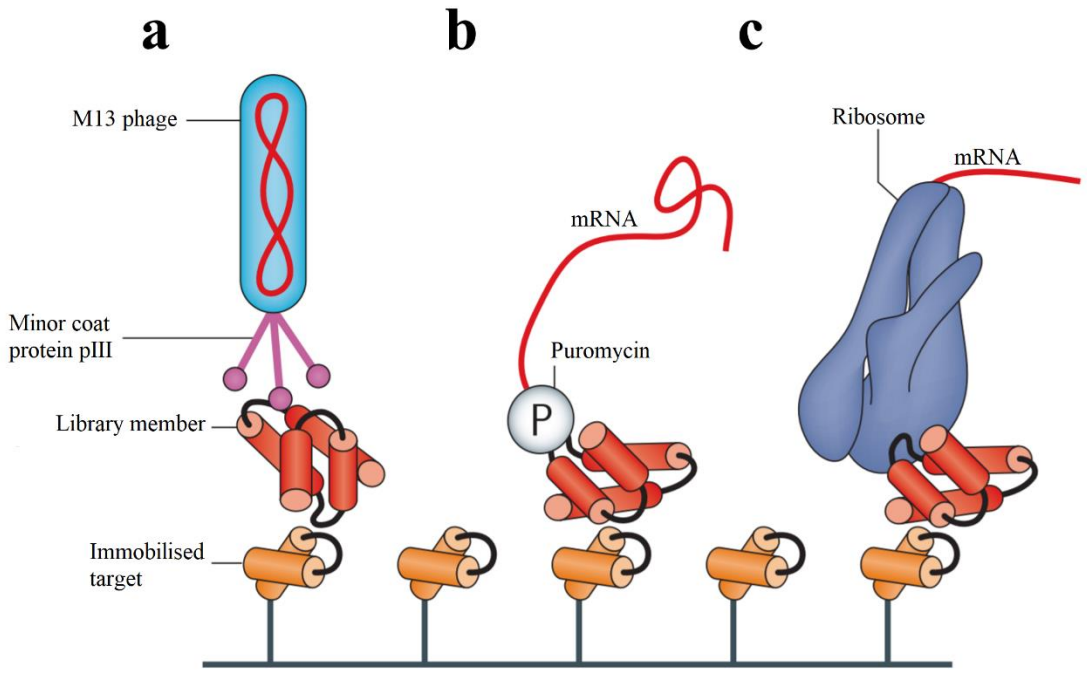

Figure 1.19. Comparison of the *in vitro* display types. a) Phage display utilises proteins synthesised and folded in *Escherichia coli* (*E. coli*), which are then packaged into bacteriophage along with their encoding DNA and are selected *in vitro*. b) In mRNA display, the protein and its encoding mRNA are covalently linked via puromycin following translation and the complex is released by the ribosome. c) Ribosome display uses specialised conditions to halt the ribosome, preventing the release of the protein and its encoding mRNA. Figure modified with permission from reference [198].

1.7 Optimal DNA library construction strategies for antibody evolution

1.7.1 Whole protein scanning mutagenesis

In order to perform *in vitro* affinity maturation, each display format requires the construction of a synthetic Ab DNA library. Diversification strategies typically require careful consideration depending on the structural knowledge available for the protein of interest and it should never be underestimated how challenging it can be to predict protein function at the AA level. When information is scarce, the scanning mutagenesis technique, error-prone PCR (ep-PCR) is commonly used. It is fairly simple to implement, with PCR being performed with a non-proofreading polymerase such as *Taq* and then adjusting the conditions such that the natural error rate of replication is increased. This technique is useful for determining which regions of a protein contribute most to the desired activity and these regions can then be subjected to more focussed diversification. These 'hotspots' are found as ep-PCR mutates AA locations at random. Once found, the mutated AA and neighbouring residues can be simultaneously randomised using site-directed saturation mutagenesis which, if desired, can include combinations of all twenty naturally occurring AAs. Saturation mutagenesis is commonly used when the protein structure has been more thoroughly characterised. It is beneficial to randomise multiple residues simultaneously as it allows better exploration of epistatic interactions. Many single mutations created during ep-PCR may result in 'silent' phenotypes as the substituted residues may only be beneficial in the presence of certain combinations not present in the original gene[198, 213, 214]. A comparison of ep-PCR and the methods of site-directed saturation mutagenesis is shown in Figure 1.20.

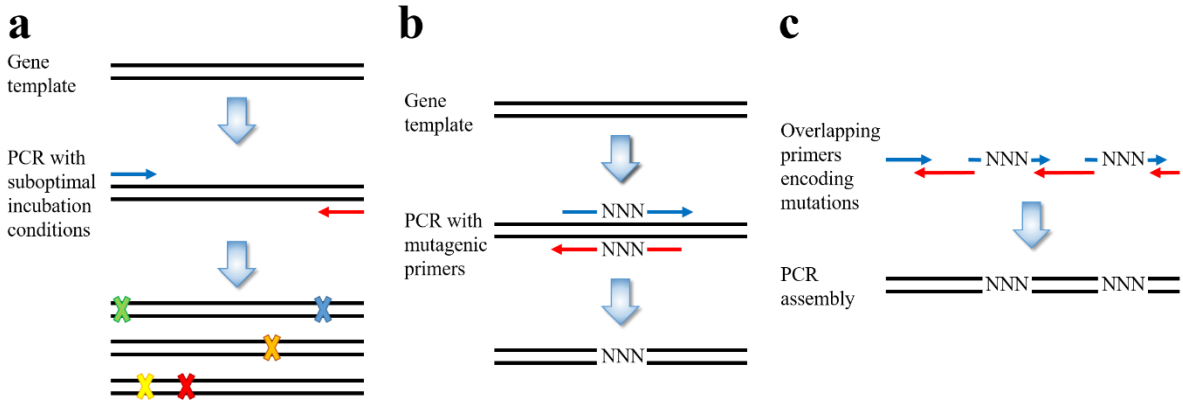

Figure 1.20. Comparison of ep-PCR and site-directed saturation mutagenesis. a) ep-PCR introduces a small number of mutations (coloured crosses) anywhere on the gene between two primers (red and blue arrows). Diversity introduced is large but the extent of mutated residues is low. b) Site-directed saturation mutagenesis. c) *de novo* gene synthesis. Both b) & c) are methods of creating targeted saturated mutations. Primers replace whole 'wild-type' codons with random mixtures of nucleotides (N) to explore all possible AA combinations at the chosen locations. Figure modified with permission from reference [213].

1.7.2 Focussed mutagenesis

Saturation mutagenesis is particularly well suited to the evolution of Abs as B cells naturally target their homologous recombination towards the CDR loops and the structural data available for Abs is vast. Homologous recombination can be used *in vitro* for diversifying Ab genes, however controlled saturation mutagenesis can explore more combinations of phenotypes without having to sample as many genotypes and thus higher diversity libraries can be sampled[198, 213, 215].

The genotype to phenotype ratio can be problematic in library sampling and arises due to the degeneracy of the genetic code. For example, serine is encoded by six codons whilst tryptophan is encoded by one. This means that as the number of simultaneously randomised residues increases, codon bias is exacerbated and it becomes exponentially more difficult to sample the rarest codon combinations in a given library[216-218]. Codon bias can be reduced in saturation mutagenesis by fine-tuning the mutagenic codon used. For example, NNN randomises all bases in a codon equally (N=A/T/C/G) whilst NNK randomises the first two bases fully and the third base is restricted (K=T/G). This is known as NNK 'doping' and it decreases the numbers of all possible codons by half for each AA, whilst still encoding all twenty AAs. The three stop codons are also cut to only TAG, which is not utilised as a stop codon in amber-suppressor

strains of *E. coli*. The use of NNK codons in assembling saturation libraries significantly reduces codon bias but more specialised degenerate and non-degenerate codons exist[213, 216-218]. Some of these are shown in Table 1.3.

Table 1.3. Examples of used codons in saturation mutagenesis for the construction of DNA libraries. Table modified with permission from reference [213].

Degenerate codon	Mixed base sequence	Encoded codons	Stop codons	Encoded AAs	Properties
NNN	(A,T,G,C) (A,T,G,C) (A,T,G,C)	64	TAA, TAG, TGA	All	Fully randomised codon
NNK	(A,T,G,C) (A,T,G,C) (G,T)	32	TAG	All	All 20 AAs
NNS	(A,T,G,C) (A,T,G,C) (G,C)	32	TAG	All	All 20 AAs
NDT	(A,T,G,C) (A,T,G) T	12	No	Phe, Leu, Ile, Val, Tyr, His, Asn, Asp, Cys, Arg, Ser, Gly	Mixture of polar, nonpolar, positive and negative charge (Reetz 2008)
NTN	(A,T,G,C) T (A,T,G,C)	16	No	Met, Phe, Leu, Ile, Val	Nonpolar residues
NAN	(A,T,G,C) A (A,T,G,C)	16	TAA, TAG	Tyr, His, Gln, Asn, Lys, Asp, Glu	Charged, larger side chains
NCN	(A,T,G,C) C (A,T,G,C)	16	No	Ser, Pro, Thr, Ala	Smaller side chains, polar and nonpolar residues
RST	(A,G) (G,S) T	4	No	Ala, Gly, Ser, Thr	Small side chains

Saturation mutagenesis libraries can be created via many strategies, the simplest and cheapest of which are cassette or PCR assembly. Both use randomised oligonucleotide primers with homologous ‘arms’ to target specific locations for diversification. Cassette assembly involves creating dsDNA from randomised primers and then ligating them in place of the target gene. Cassette-based assembly avoids another library bias: thermodynamic amplification bias. Amplification bias can arise during PCR with randomised primers as each primer will have a different degree of homology to the target gene and will result in different annealing temperatures. Those with the highest degrees of homology will outcompete those with less, and diversity may be restricted. Cytosine and Guanine-rich sequences are also biased for due to their stronger hydrogen bonding pattern[219, 220]. This phenomenon is also exacerbated by the exponential nature of PCR replication. The homology bias created in early cycles will be exponentially amplified as the cycles continue and the library diversity will proportionally suffer[221].

Cassette assembly’s main disadvantage is that the strategy is limited by the effectiveness of the ligation step and overall DNA yield and quality can be poor. This is problematic for display technologies that rely on cellular transformation, as high concentrations of high-quality circular DNA are a necessity[222]. A PCR saturation library assembly method was recently described

that showed thermodynamic amplification bias to be minimal. It uses inverse-PCR, which is a whole-plasmid amplification using 5'-phosphorylated primers that do not overlap, and only one of the primers contains the saturation randomisation. By placing the randomised codons between the centre and the 5' end of the primer, Jain and co-workers found little evidence of thermodynamic amplification bias[223]. The amplified whole plasmids are then circularised by ligation, which is a significantly more efficient ligation than cassette mutagenesis, resulting in excellent library size and quality[223]. The procedure is shown in Figure 1.21.

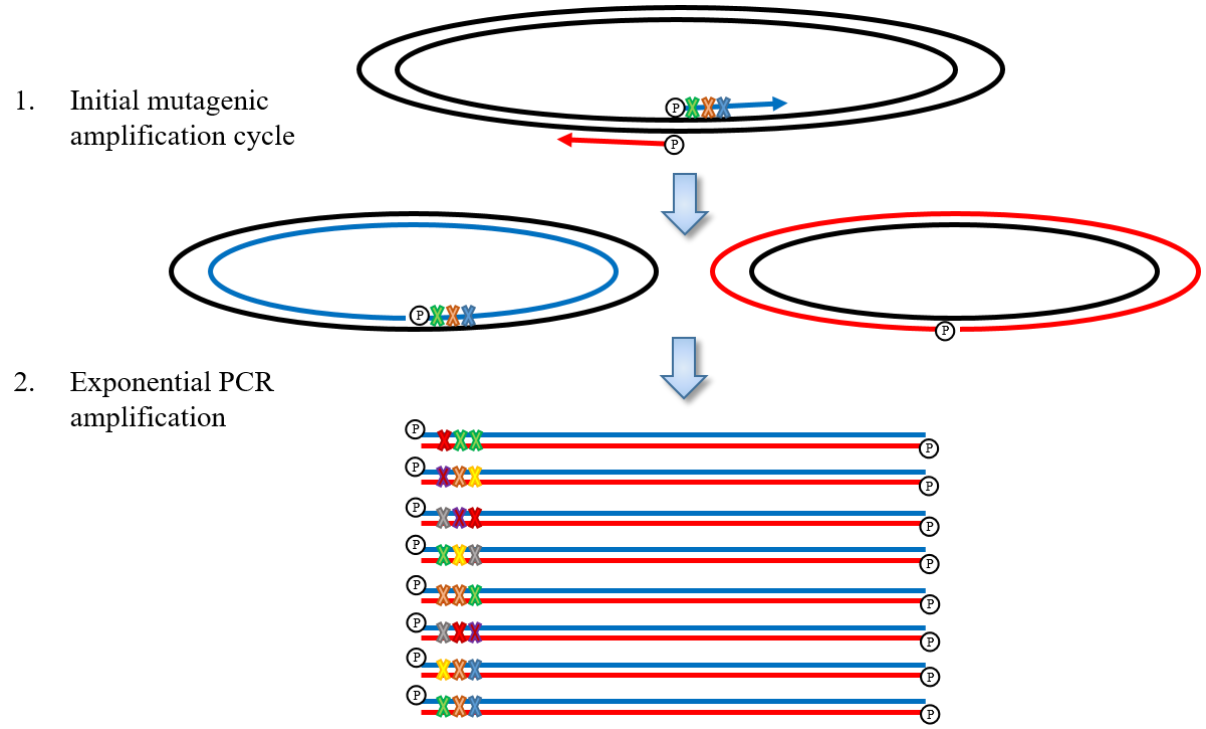

Figure 1.21. Inverse-PCR saturation library generation. Non-overlapping phosphorylated primers are used to amplify the whole plasmid whilst simultaneously installing random mutations (coloured crosses). This generates linear full-length library DNA with phosphorylated 5' ends for 'blunt-end' re-circularisation. Figure modified with permission from reference [223].

1.8 Binding affinity selection

1.8.1 Phage display

Phage display has been widely successful in the discovery and affinity maturation of Abs, and has seen widespread use in the study of protein and peptide interactions[161, 224, 225]. The early development of phage display can be traced back to the generation of fully-human monoclonal Abs[226]. It was first pioneered by George P. Smith in 1985 where he described the display of peptides on the surface of filamentous bacteriophage[227]. Phage display is advantageous over hybridoma technology using animal models as it allows the discovery of Abs against virtually any target, including toxic and self-antigens[226]. It is an ideal choice for discovering smaller Ab fragments such as scFvs and sdAbs, although it is unsuitable for large Abs due to their requirements for eukaryotic post-translational processing. Smaller Ab formats discovered by phage display can allow the reverse engineering of larger Abs to mimic the paratope found[228].

Bacteriophage are natural viruses of bacteria and they are very attractive for the display of Abs as they are highly resistant particles. They are very resistant to thermal denaturing, acid treatment and proteolysis which means that equally resistant Abs can also be selected for[229]. Specially-engineered strains of phage package the encoding 'phagemid' DNA of Abs preferentially over their own and the library size they can sample is fairly large (10^9-10^{10}). The most commonly used format for phage display is the use of filamentous M13 or fd strains. The Ab fragment can be theoretically displayed on any of the virus' coat proteins, however the most common is the low-copy number and essential pIII protein. The pIII protein is required for phage attachment and entry to bacterial cells and phage display is possible by linking the Ab fragment gene to the N-terminus of the pIII gene (geneIII or 'gIII'). This orientation allows display without severely disrupting the function of pIII[226]. M13 phage display of a sdAb is illustrated in Figure 1.22.

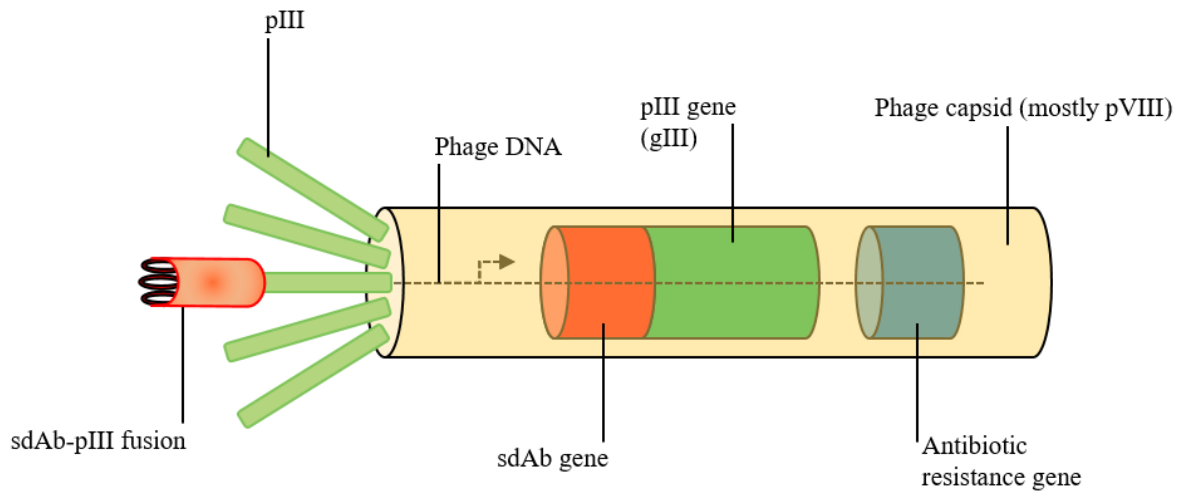

Figure 1.22. Monovalent M13 phage display of a sdAb (orange) on the pIII coat protein (green). The phagemid (dashed lines and red, green and blue cylinders) is packaged within the phage capsid (pale yellow cylinder). Fusion of the sdAb gene (dark orange cylinder) with gIII (dark green cylinder) allows sdAb-pIII display on the surface of the M13 phage capsid. The phage capsid is comprised mostly of the major coat protein, pVIII (not shown). Only *E. coli* containing sdAb-library DNA produce phage due to antibiotic selection (blue cylinder).

Phage display is performed by introducing the Ab-gIII fusion gene to *E. coli*, allowing expression of the protein fusion, and then infecting the culture with phage. As new phage particles are produced in the infected *E. coli*, the Ab-pIII fusion is assembled into the viral capsid and the Ab-gIII DNA is packaged inside. The *E. coli* survive and secrete many copies of Ab-displaying phage. Once enough Ab-displaying phage are produced, they are purified from the bacterial culture and selected against the Ag *in vitro*[226].

For Ab affinity maturation, it is desirable for the Ab to be present in one-copy on the phage. This is because with more than one copy, there is a likely possibility that the Ab-phage will bind more than one antigen due to higher avidity. This makes washing away low-affinity Abs more difficult as the whole particle will have a higher total affinity than one Ab alone. Monovalent phage display allows the whole particle to have the same binding affinity as the displaying-Ab and this is ideal for selecting between affinities, especially when the library is derived from a known binder. This is complicated by the fact that filamentous phage have five copies of pIII. The solution is to use 'helper phage' rescue, which utilises modified wild-type M13/fd to provide the coat protein genes including wild-type pIII. Helper phage are modified so that they preferentially package the Ab-gIII DNA, meaning they cannot themselves replicate, and they provide wild-type pIII which competes with Ab-pIII for incorporation into

the new phage particles. The expression is controlled such that there is significantly more wild-type pIII present than Ab-pIII and that means the vast majority of phage have, on average, zero (bald) or one copy of the Ab displayed (monovalent). This is desirable, as in theory the bald phage will not bind the target and will be lost from the selection[226]. Helper phage rescue and multivalent vs monovalent display is visualised in Figure 1.23.

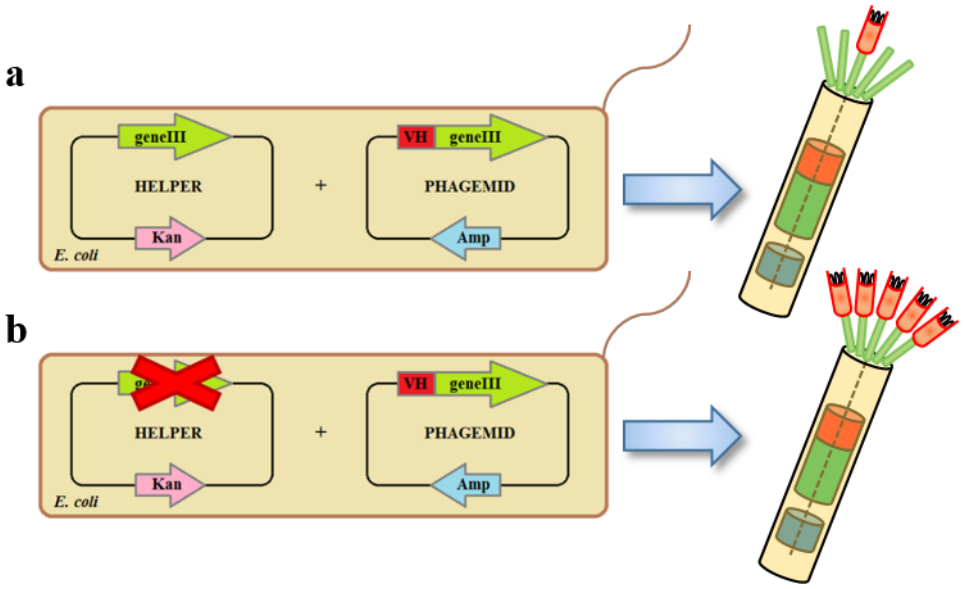

Figure 1.23. Methods of altering levels of Ab display on M13 phage. a) Monovalent phage display. *E. coli* expressing V_H-pIII fusions (red) are infected with helper phage carrying wild-type pIII (green). Dual antibiotic selection with kanamycin and ampicillin ensures only bacteria with both Ab and helper phage DNA produce new phage particles. b) Multivalent phage display. Helper phage with a wild-type pIII knock-out ensure there are only 5-copy multivalent phage particles produced. This is useful for phage display Ab discovery from naïve/immunised libraries but not for affinity maturation.

Binding affinity selection is achieved using a technique known as ‘biopanning’. Purified Ab-displayed phage are incubated with immobilised antigen on a ‘solid’ support such as plastic plates, magnetic beads or even the surfaces of cells. Stringent washing is performed to wash away low-affinity binders and non-specific binders (background binding), leaving high-affinity specific binders. The remaining binders are eluted with either low-pH or Ab proteolysis and the eluted ‘output’ phage are used to infect fresh *E. coli* to screen surviving clones or recover more phage for further rounds of selection. It is desirable to perform multiple cycles of selection as this ‘enriches’ the library towards the highest affinity binders by further increasing the ratio of high-affinity binders to low-affinity binders. Enrichment, put simply, increases the chance of finding the best binders from the library during subsequent clonal screening by decreasing

the overall diversity of the library. A library with decreased diversity but increased proportions of high-affinity binders has been successfully evolved and is the real purpose of phage display. Desirable Abs must still be found manually via e.g. ELISA, and phage display decreases the screening effort[230]. Selection cycles and binding enrichment are displayed in Figure 1.24.

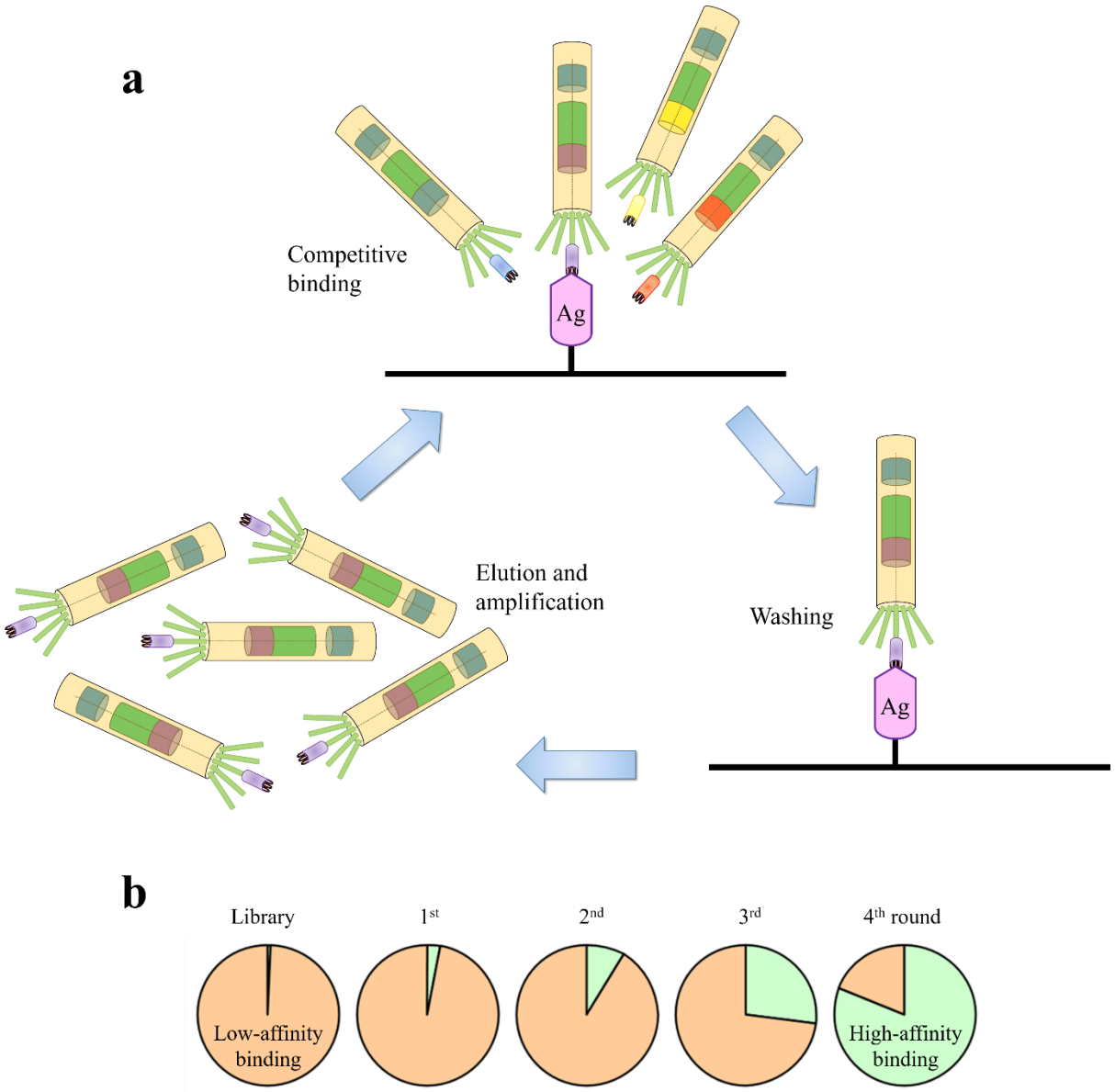

Figure 1.24. Binding affinity enrichment through biopanning. a) Schematic of biopanning technique. Cycles of washing are performed following competitive Ab-phage library binding with immobilised antigen (Ag) and the remaining binders are eluted, recovered and amplified in fresh *E. coli*. b) Relative library composition of binding affinity before and after multiple rounds of biopanning.

1.8.2 Selection conditions

Careful considerations must be made when designing a binding affinity selection as the choice of equipment and conditions will drastically effect the outcome of library enrichment. This becomes clear when taking into account the kinetic parameters of Ab-Ag interactions. Binding affinity is generally measured and reported as the equilibrium dissociation constant (K_D). As introduced in Chapter 1.1.2, Ab-Ag binding is in equilibrium as their interaction is governed by weak reversible intermolecular forces such as hydrophobic interactions, hydrogen bonds, electrostatics and van der Waals forces. K_D is calculated for Abs with one binding site using the following equation

$$K_D = \frac{[Ab][Ag]}{[AbAg]} = \frac{k_{off}}{k_{on}} \quad \text{(Eq. 1.1)}$$

where [Ab], [Ag] and [AbAg] are the concentrations of antibody, antigen and the antibody-antigen complex respectively. The off-rate constant is termed k_{off} and the on-rate constant is termed k_{on}. The smaller the K_D, the higher the overall binding affinity, however two Abs with the same K_D can have very different k_{on} and k_{off} rates. Whilst the k_{off} constant is independent of Ab and Ag concentrations (first order), the reverse is true for k_{on} (second order). This can have drastic implications for binding affinity selection as considerations need to be made depending on what k_{on} and k_{off} rates are desired in the evolved Abs, as they are very sensitive to the selection conditions. For example, biopanning procedures with short incubation times will select for the fastest binding Abs (high k_{on}) but will have less effect on k_{off}. Allowing binding equilibrium with longer incubation times will select for Abs with a low k_{off} but selection based on high k_{on} is essentially negated. Washing stringency, i.e. duration and number of wash steps, greatly affects the k_{off} selection, as more stringent washes removes the displayed Abs with higher k_{off} rates. As k_{on} is also dependent on the concentration of the Ag, conditions with lower concentrations of Ag will select for Abs with high k_{on}. For an affinity maturation experiment with multiple rounds of selection, it is desirable to start with an Ag concentration close to the K_D of the 'parental' Ab (i.e. the Ab that was diversified into the library) and then decreasing the Ag concentration every round whilst simultaneously increasing the washing stringency. Starting with milder conditions allows enough of the rarer higher-affinity Abs to survive selection to enrich the library and ensure there are enough clones for later rounds with increased high k_{on} and low k_{off} selection[231].

It is extremely important to ensure maximum binding affinity enrichment as there are two major competing forces against affinity selection which can enrich the library for low-affinity or non-specific Abs. The first is non-specific binding, primarily arising from charged and hydrophobic interactions. This can be minimised by altering the solution composition with the use of salts and detergents, such as polysorbate 20 (Tween® 20), and protein blocking agents such as bovine serum albumin (BSA) or skimmed milk. The second competing selection, and arguably the most troublesome, is expression enrichment. As almost all Abs will differ in genetic sequence and as cellular codon usage can be significantly different, Ab variants will propagate at different rates. This can lead to significant expression bias as highly-abundant low-affinity Abs will have a higher chance of surviving stringent selection and if more of them are recovered than high-affinity Abs, then their enhanced expression will begin to dominate the amplified libraries and skew enrichment towards increased propagation[218, 231]. Both undesired competing enrichments are known as the 'background' and are quantified by performing control selections in the absence of target Ag and measuring the 'titres' of eluted phage. Monitoring rounds of biopanning in this way, by comparing the titres in the presence and absence of target Ag, can indicate if specific binding affinity enrichment is progressing as desired. If the ratio of Ag:background titres are <10-fold, it is worth considering optimising the selection conditions as the library most likely contains significant non-specific binding/expression enrichment[231].

Binding affinity selection *in vitro* requires the use of an immobilised target Ag in order to isolate bound Ab-displayed phage from the unbound. The choice of immobilisation strategy can also significantly affect the outcome of selection. The simplest and cheapest of which to implement is Ag adsorption onto a solid surface. This is beneficial as it requires no prior labelling of the Ag, however any conformational change induced upon adsorption or the presence of even tiny amounts of impurities will compromise desired binding enrichment. The use of biotinylated-Ag, for capture with pre-immobilised Streptavidin or NeutrAvidin, solves these problems somewhat as adsorption is no longer required and the biotinylated-Ag can be 'pulled down' from solution and its impurities. Selection against immobilised Ag is sufficient for discovery of Ab binders from a library of non-binders but is less desirable for affinity maturation as greater emphasis is placed on discriminating between a range of binding affinities. Selecting for k_{on} requires precise control of Ag concentration and immobilised Ag is at an effective concentration of zero in solution and an extremely high local concentration on the solid surface. It is very difficult to estimate the effective Ag concentration on a surface and

the close proximity of Ags to one another preferentially selects for Ab-phage with higher avidity (i.e. displaying more than one Ab) rather than high affinity[231, 232]. Close proximity of Ags to one-another or to the capturing proteins/blocking agents also increases the local steric hindrance, disfavouring binding. To alleviate these issues, it is preferable to use selection in solution, whereby the Ab-phage are pre-incubated with biotinylated-Ag and then the bound complexes of phage-Ab-Ag-biotin are captured using Streptavidin or NeutrAvidin. The most efficient and rapid method of capture is the use of Streptavidin or NeutrAvidin-coated magnetic beads as, being small (~2.8 μm) and spherical, they have an extremely high surface area and motility for fast binding kinetics, which is crucial when short incubations for high k_{on} are desired[231, 232].

Binding specificity (i.e. low cross-reactivity) and low k_{off} can both be selected for using competitive selection. Competitive selection involves the use of an additional unlabelled binding competitor molecule that will bind to Abs displaying less desirable qualities and due to its lack of biotinylation, both competitor and undesirable Ab-phage will be lost during washing. If the competitor is an excess of unlabelled Ag (introduced after incubation with labelled Ag), then quickly dissociating Abs (high k_{off}) will likely bind the unlabelled Ag and be removed. It can also be used to remove cross-reactive Abs when the competitor is a different species such as an Ag in a non-desirable conformation or a mixture of non-desirable proteins like a cell-lysate[231, 233]. Care must be taken during multiple rounds of selection due to the presence of the multiple proteins in the incubation step. Blocking and capture proteins are theoretically potential sources of unwanted binding enrichment and, left unchecked, Abs can be selected for these proteins rather than the desired Ag. The solution to this is to simply alternate between different blocking and capture proteins between rounds so that the only consistent target is the Ag itself[231].

1.9 Screening for antibodies with improved binding affinity

1.9.1 Crude-extract ELISA

ELISA is a widely-used sensitive technique for the detection and quantification of molecules of interest, and can function with complex mixtures and at extremely low concentrations[234, 235]. ELISA typically works by generating and using immune-complexes, which are detected with the use of an enzyme/fluorescently conjugated specific molecule, such as an Ab. All ELISAs initiate with one of the immune-complex members being adsorbed onto a solid surface, such as a well of a microtiter plate. The immune-complex is then formed sequentially, with washing in between, until the enzyme/fluorescently conjugated molecule joins the complex. The conjugate on the detection molecule is then responsible for the generation of a quantifiable signal, such as a visible colour change or fluorescence, the intensity of which is proportional to the concentration of the immune-complex. There are multiple ELISA formats and a few of these are displayed in Figure 1.25[236].

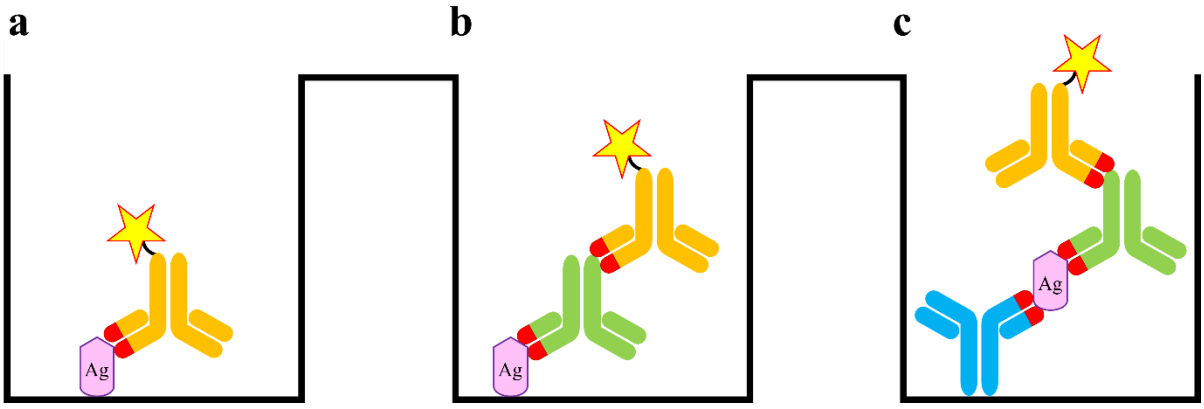

Figure 1.25. Common ELISA formats. Black half boxes represent solid wells of a typical microtiter plate. The detection molecule is shown here as a conjugated Ab (orange) and the target molecule is designated as an Ag (pink). a) 'Direct' ELISA involves adsorption of the desired target molecule to the solid surface, followed by immediate detection with a specific conjugated Ab. b) 'Indirect' ELISA functions similarly to direct ELISA, with an additional Ag-specific Ab in between, known as a primary Ab (green). The detection Ab is specific for the primary Ab and is known as a secondary Ab. c) 'Sandwich' ELISA is useful when it is undesirable for adsorption of the desired target molecule and it is instead presented to solution using an adsorbed capture Ab (blue). This then proceeds like an indirect ELISA but for it to work, both the capture and primary Abs must bind different epitopes on the target molecule.

Once phage display selection is complete, improved-affinity Abs must still be identified and isolated from the enriched library. ELISA is a suitable screen for this task as it is a fairly high-throughput technique and it does not require prior Ab purification. The eluted phage from the

final round of affinity-selection are used to infect fresh *E. coli* and these can be grown on selective growth plates to separate the individual library members as bacterial colonies. These colonies are then picked, grown separately and the expressed Abs are extracted in a crude lysate[158, 226, 232]. This Ab-containing cell-lysate can be analysed by ELISA to ensure Ab expression and simultaneously rank Abs against one-another based on their relative binding signals[232, 234]. Expression bias can also be identified by ELISA, which is crucial when ranking Ab binding affinities against one-another in crude lysates as more abundant low-affinity Abs will exaggerate their detection signal compared to less abundant high-affinity Abs. To do this, firstly a direct ELISA is performed by immobilising the cell-lysate contents and detecting the expression levels of the library Abs with a detection Ab specific for the library Abs. Then, an indirect ELISA is carried out with immobilised target Ag and cell-lysate from the same library clones is tested for binding against the Ag. Here, the library Abs act as primary Abs and are detected by the same conjugated secondary detection Ab. By performing and comparing these two ELISAs simultaneously, binding signals can be corrected for expression levels which identifies false positives and provides a rough, yet useful, relative affinity ranking. Improved Ab binding can be rapidly identified in this way and the isolated clones can immediately be sequenced and expressed for further characterisation[158, 226, 232].

1.9.2 Microscale Thermophoresis

In this thesis, accurate Ab binding affinity characterisation was performed using microscale thermophoresis (MST). MST is an immobilisation-free biophysical technique that measures the change in fluorescence of fluorescently-labelled biomolecules, subjected to a temperature gradient from an infra-red laser. The change in fluorescence is attributed to the directed movement of molecules away from the laser and this motility is dependent on the size, charge and hydration shell of the labelled biomolecule. This means that any changes to these physical characteristics, induced by the binding of one biomolecule to another, can be quantified and binding affinities can be calculated[237]. Ab binding affinities are calculated by performing a serial dilution and incubating each Ab concentration with a constant concentration of fluorescently labelled target ligand. An advantage of MST is that each sample measurement is carried out in a small glass capillary (~10 μL), which results in very little required material and up to 16 different concentrations can be run simultaneously, which is enough to obtain an accurate binding-curve in a period of only ~15 minutes. MST is illustrated in Figure 1.26.

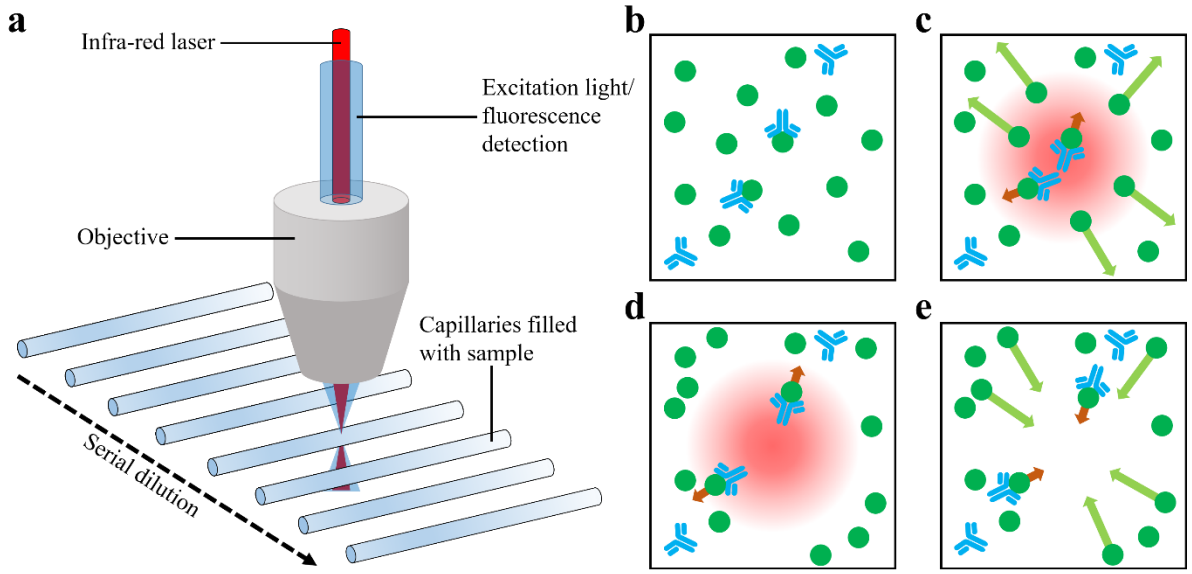

Figure 1.26. Schematic of the microscale thermophoresis technique. a) Overview of the MST set-up. Capillaries are filled with samples containing a fluorescently-labelled target ligand and different concentrations of an Ab. Fluorescence is induced by excitation through a dichroic mirror (not shown) from an LED, focussed through an objective, towards a capillary. Thermophoresis then occurs when an infra-red laser penetrates the sample and the fluorescence change is recorded. b), c), d) & e) Microscopic schematics of the effect of binding on thermophoretic motility. b) Capillary contents of a mixture of fluorescently-labelled ligand (green) and unlabelled Ab (blue) at equilibrium. c) As the laser is switched on it induces a temperature gradient, and directed movement of molecules occurs away from the laser at different rates. Here, unbound ligand migrates rapidly, whilst ligand-Ab complexes move more slowly. d) After some time has passed, the majority of labelled ligand has left the temperature gradient and the system enters the 'steady state'. Larger complexes, such as Ab-ligand, may still be moving. e) As the laser is switched off, the fluorescence changes again as labelled ligand and Ab-ligand complexes diffuse back to the vacated region. Figure modified with permission from reference [238].

A disadvantage of MST is that in order to get accurate K_D measurements, the system must be performed at binding equilibrium[237]. This means that the kinetic parameters, k_{on} and k_{off} cannot be individually obtained. For the purposes of this thesis however, only improvements to K_D were required for proof of concept, as it is the most commonly cited point of reference for binding affinity.

1.10 Thesis aims

This research was designed to show proof of principle that Modular, the rational design strategy introduced in Chapters 1.5.2 & 1.5.3, is suitable for generating Ab hits that are comparable to those discovered by classical methods. The projects undertaken aim to use simple directed evolution, through the use of affinity selection via phage display, to address the limitations of the *in silico* method by increasing the affinity or selectivity of the DesAbs towards their targets. Chapter 2 will cover the affinity maturation of DesAb-F, the low-affinity yet stable sdAb, that was rationally designed to bind residues 70-77 of αSyn, and ascertain the viability of non-immunogenic epitope pre-selection[36, 176]. Chapter 3 will investigate the effect of competitive affinity selection, to alter the specificity of rationally designed Abs towards certain aggregate species, on the inhibition of microscopic nucleation kinetics. This will involve the evolution of two Abs, $DesAb_{3\text{-}9}$ and $DesAb_{29\text{-}36}$, which were rationally designed to bind the N-terminus and C-terminus of $A\beta_{42}$, respectively[36, 104]. The findings and implications of these projects will be discussed in detail in Chapter 4 and any future work required will also be presented.

Chapter 2: Affinity maturation of a rationally designed antibody targeting a pre-selected linear epitope

2.1 Introduction

2.1.1 Lessons from two single-domain antibodies against linear epitopes

The affinity maturation strategy of DesAb-F was inspired by two sdAbs, both binders of αSyn with intermediate affinity[176, 239]. The first was the two-loop DesAb, the result of Modular rational design, introduced in Chapter 1.5.2[176]. The second was NbSyn2, a nanobody derived from a camelid immune library against the C-terminus (135-140) of αSyn. Unlike the two-loop DesAb, NbSyn2 is stable (T_m = 67 ± 1 ºC) whilst retaining a nanomolar binding affinity. The crystal structure of the interaction of NbSyn2 and a peptide representing the target epitope (N-GYQDYEPEA-C) was obtained, revealing the contribution of the CDR loops[239]. The crystal structure and interaction is illustrated in Figure 2.1

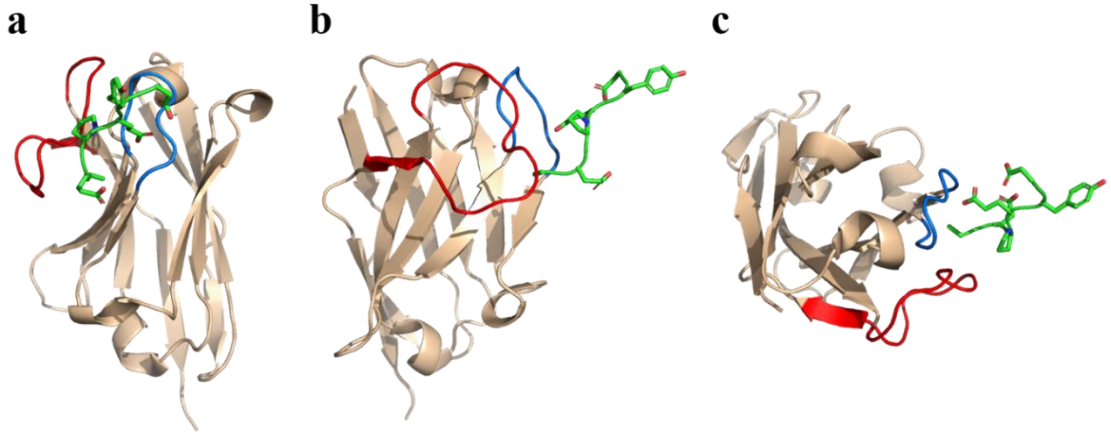

Figure 2.1. X-ray Crystal structure of NbSyn2 in a complex with peptide N-GYQDYEPEA-C. The peptide is shown with side chains (green) and NbSyn2 (tan) is shown with highlighted CDR2 (blue) and CDR3 (red) loops. Of the peptide, only residues DYEPEA are displayed. Of these, residues EPEA are situated between the CDR2 and CDR3 loops (PDB entry 2X6M)[239]. a) Frontal view of the interaction. b) Side view of the interaction. c) Top view of the interaction. The structures were produced using PyMOL (PyMOL, Molecular Graphics System, Version 2.2.0, Schrödinger, LLC).

It is clear from the structure of NbSyn2 that it is possible to form a binding interaction between a sdAb and an intrinsically disordered linear epitope, utilising the space between the CDR2 and CDR3 loops to yield an Ab with desirable binding affinity[239]. Of course, NbSyn2 was obtained utilising an immune library with limited control of epitope choice and the acidic C-terminus may represent a relatively easier target for immunological Ab generation. Weakly immunogenic epitopes remain challenging targets for raising Abs via immune stimulation and in the case of protein misfolding diseases, these can be desirable targets[104]. With the two-loop DesAb in mind, it is possible to achieve decent-affinity sequence-directed epitope targeting towards non-immunodominant epitopes, such as residues 70-77 of αSyn[176]. As the more stable DesAb-F targets the same epitope, it was hypothesised that it might be more straightforward to evolve the CDR2 loop into a synergistic interaction towards the epitope with the designed CDR3 loop than to reengineer the poor stability of the two-loop DesAb. The CDR1 loop was considered for randomisation, however it has been shown that V_H fragments are sensitive to mutations in aggregation 'hotspots' and the CDR1 has been implicated as a risky region[14, 240].

2.1.2 Chapter aims

The challenging feature of this experiment was that DesAb-F's affinity was to be improved whilst retaining the epitope that is was originally designed to bind. The use of a peptide to represent the linear epitope was not to be used for selection as this does not represent a general strategy for pre-selected epitope Ab generation (see Chapter 1.4.2). This means the library was to be selected against full-length protein, which carries an inherent risk of epitope 'spread'[241]. Therefore, the method of library design was chosen to be minimal to reduce the risk of epitope-switching. Site-directed saturation mutagenesis using NNK doping was decided as the most suitable method of diversification and the location was decided on the tip of the CDR2 loop (3 adjacent residues). The rational here is that we wished to emulate the two-loop synergistic antiparallel β-sheet-like binding that was achieved with the two-loop Ab grafting, and obtain stable high-affinity sdAbs. DesAb-F's evolution was compared with that of a 'non-designed' Ab, DesAb-IAPP, to act as a suitable control. DesAb-IAPP was also rationally designed using the Cascade method, but targeted IAPP, not αSyn. The evolution strategy is shown in Figure 2.2.

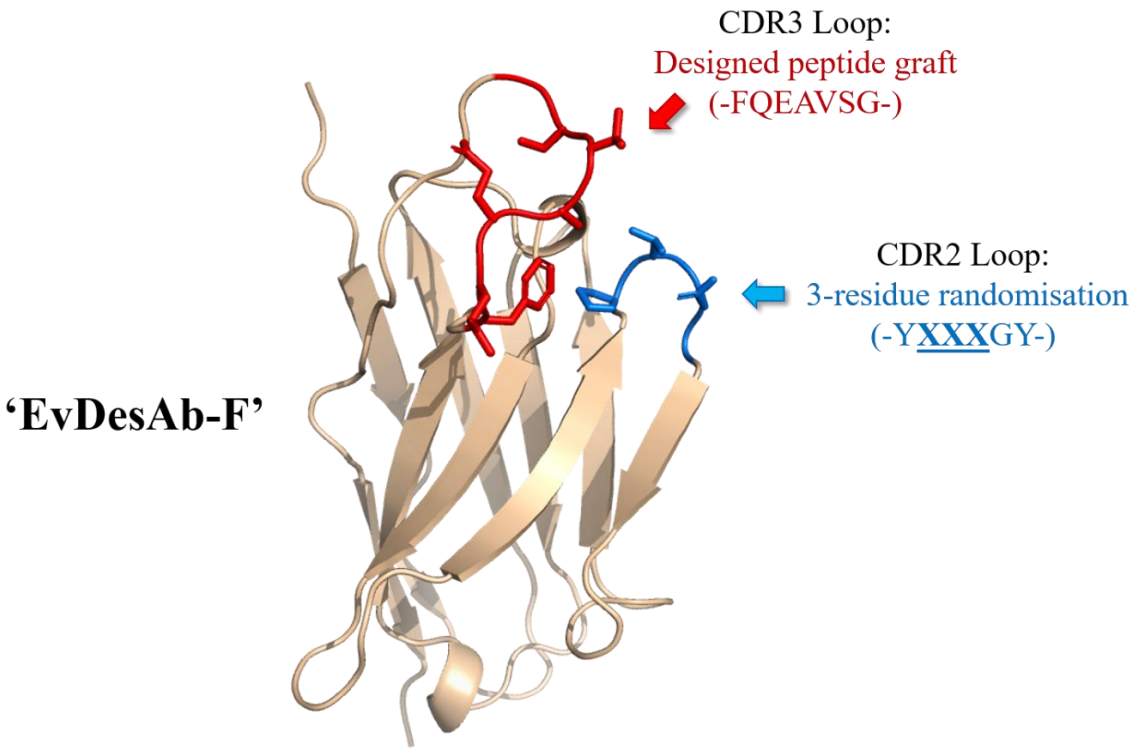

Figure 2.2. Structure of the proposed DesAb-F evolution and partial sequences of the CDR2 and CDR3 loops. The designed peptide graft, complementary to an epitope on human αSyn, is highlighted with side chains in red. Three residues on the tip of the CDR2 loop (blue) were chosen for saturation mutagenesis (Residue X is any of the 20 possible naturally occurring AAs). Abs yielded from these studies shall henceforth be called 'EvDesAbs' in this thesis. The structure was provided by P. Sormanni and F. A. Aprile and produced using PyMOL (PyMOL, Molecular Graphics System, Version 2.2.0, Schrödinger, LLC).

As DesAb-F was the primary DesAb in this study, evolution was performed to target full length αSyn monomer, as the Ab was designed against an epitope within the NAC region (residues 70-77). As three NNK codons were used, the library diversity is quite small, at just 8000 phenotypes and 32,768 genotypes. This meant that only a small affinity gain was expected to be obtained, as more diverse libraries are more likely to yield Abs with higher affinities[242]. However, the main aim of the study was to simply show that affinity maturation was possible, and that the resulting EvDesAbs displayed other desirable characteristics such as good expression and stability. Phage display using M13 phage was chosen as this is a standard technique for affinity maturation in Ab lead development. Phage display can be performed against Ag adsorbed to a solid support but this can mask the sequence of a large proportion of the αSyn monomer. With this in mind, selection in solution was deemed more appropriate as it enables greater control of the total epitope presentation. Finally, pre-selected epitope retention characterisation will be shown for the most desirable EvDesAbs.

2.2 Results: DNA library construction using CDR2 focussed mutagenesis

As with any protein directed evolution experiment, the first step is the diversification of the parental protein's encoding DNA. Described in this Chapter is the simultaneous DNA library construction and evaluation of DesAb-F and the control, DesAb-IAPP. For the control evolution to be comparable, the exact same diversification strategy and materials were used. NNK doping into adjacent residues along the CDR2 loop requires only one mutagenic primer and therefore can easily be assembled using inverse-PCR site-directed saturation mutagenesis, introduced in Chapter 1.7.2. As this method is a whole plasmid amplification which terminates in a self-circularisation ligation step, which can be a cellular transformation bottleneck, it was more logical to clone the DesAbs into a phage display 'phagemid', from their pET17-b plasmid used in previous studies, prior to library construction[176, 182]. The DesAbs used in the previous studies were also encoded with an N-terminal PelB leader sequence for periplasmic expression, three C-terminal FLAG tags (DYKDDDDK) and a C-terminal 7xhistidine tag for nickel agarose affinity chromatography purification. It was decided to retain these tags, as they would prove useful following affinity selection when purification of soluble Abs would be required for characterisation. The N-terminal PelB leader sequence is essential for phage display as pIII is directed and assembled into the viral capsid at the periplasmic membrane, so it was also retained[243]. The phagemid chosen for this study was pMESy4, which is a pHEN derivative that was developed for the phage display of camelid nanobodies and will be described in more detail in Chapter 5.1.1[158].

2.2.1 Cloning of designed single-domain antibodies into pMESy4

A requirement of pIII phage display is the use of an amber stop codon (TAG) at the C-terminus of the displayed protein, if subsequent soluble protein expression is desired without the need for re-cloning. This is because pIII phage display requires the displayed protein gene to be linked to the N-terminus of pIII, as its C-terminus is buried within the virion[227]. In amber-suppressing strains of *E. coli*, the amber stop codon is instead translated as an AA and phage display of the protein-pIII fusion is possible. If soluble protein expression without the pIII fusion is desired, then the phagemid encoding the protein-pIII fusion can simply be isolated and transformed into a non-amber-suppressing strain of *E. coli*, which translates TAG into a

stop codon. For cloning of the DesAbs into pMESy4, it was decided that replacement of their TAA stop codons with TAG would be an efficient way of introducing a unique restriction site given its usefulness in phage display. It would involve insertion of a SpeI restriction site (5'-ACTAGT-3') into both the DesAb genes and pMESy4. As pMESy4 already contains an NcoI restriction site (5'-CCATGG-3') in its own PelB leader sequence, then a 'silent' insertion of NcoI into the same position of the DesAb's PelB leader sequence would provide the means to easily clone the DesAb genes with their tags into pMESy4. pMESy4 also contains two additional tags before the pIII gene (gIII), a CaptureSelect™ tag preceding the amber stop codon, and a hemagglutinin (HA) tag between the amber stop codon and gIII[158]. The CaptureSelect™ tag was deemed unnecessary for this work and was to be deleted in the SpeI insertion mutagenesis of pMESy4. A detailed schematic of the genetic fusion design of the DesAb genes to gIII is illustrated in Figure 2.3.

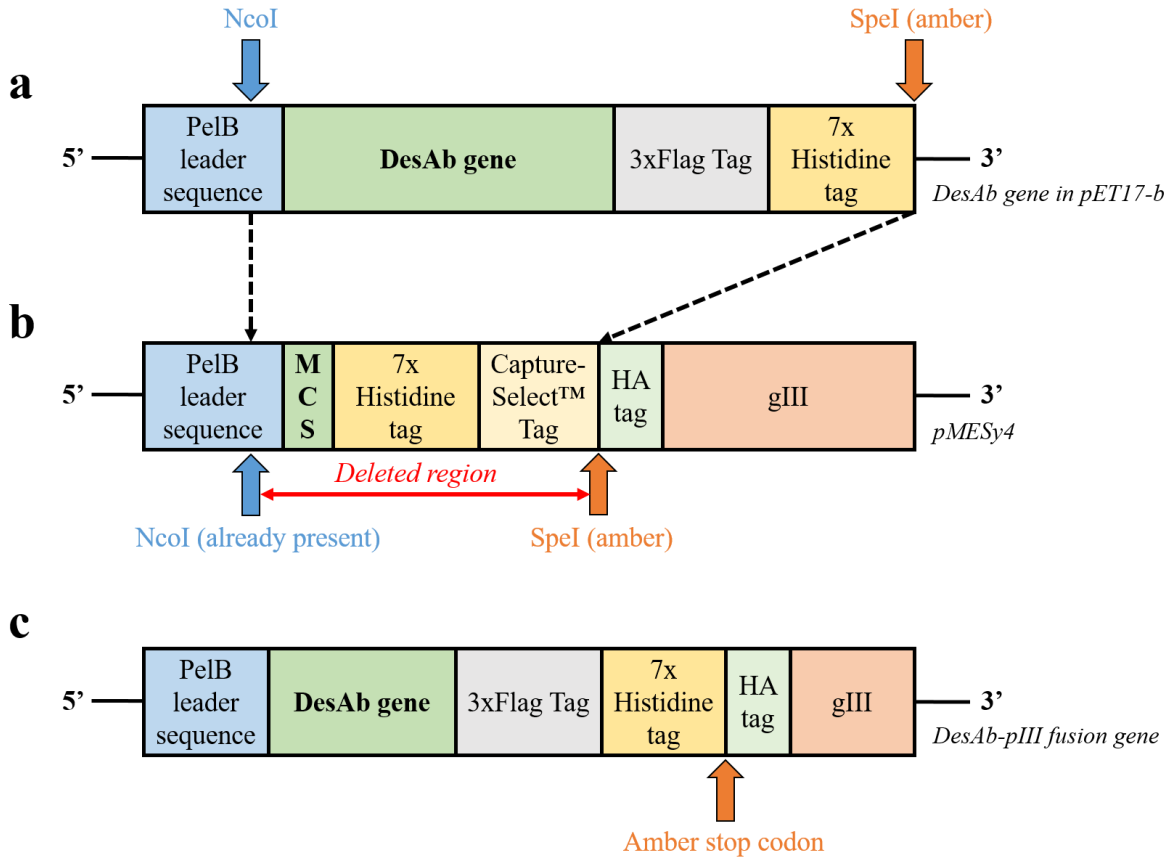

Figure 2.3. Design for the genetic fusion of a DesAb with pIII. Dashed arrows indicate which region of a) will be inserted into b). Genes are not drawn to scale. a) Expression gene of a DesAb in pET17-b. Both NcoI and SpeI restriction sites were planned for restriction cloning into pMESy4. b) pMESy4 phage display pIII-fusion gene. NcoI is already present but SpeI required inserting. The multiple-cloning site (MCS), 7xhistidine and CaptureSelect™ tags were to be deleted and replaced with the restriction digests of a). c) DesAb-pIII fusion gene.

The NcoI and SpeI restriction sites were inserted into the DesAb expression genes with the use of PCR involving two mutagenic primers, amplifying only the sequence between the restriction sites. 7-10 bases were left beyond the restriction sites, to allow space for the restriction enzymes to attach to the DNA. pMESy4 SpeI insertion was carried out with the use of inverse-PCR with adjacent 5'-phosphorylated primers, amplifying the whole phagemid, with only one of the primers carrying the mutation. The pMESy4 phagemid carrying the SpeI insertion was self-circularised, transformed into XL10-gold *E.* coli and sequenced. Following confirmation of correct sequencing of SpeI-inserted pMESy4, both it and the NcoI and SpeI-inserted DesAb expression genes were digested with NcoI and SpeI. The results of both of these mutageneses and double restriction digests are shown in Figure 2.4.

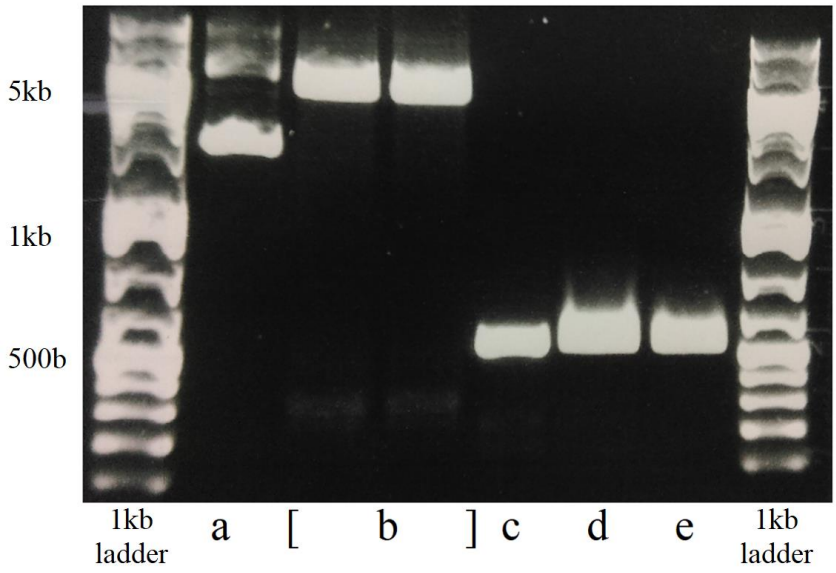

Figure 2.4. Agarose gel electrophoresis of the SpeI and NcoI double-digests of pMESy4 (b), the DesAb-F gene (d) and the DesAb-IAPP gene (e). The pre-digested pMESy4 (a) and DesAb-F gene (c) were ran for comparison. The GeneRuler^{TM} 1 kb Plus DNA Ladder did not migrate smoothly, however the sizes were correct (~5 kb for digested pMESy4 and ~550 b for the DesAb gene digests).

The double-digested DesAb genes and pMESy4 were excised from the agarose gel, purified and ligated separately to yield pMESy4+DesAb-F-pIII and pMESy4+DesAb-IAPP-pIII. The DesAb-containing phagemids were amplified in XL10-gold *E. coli* and their sequences were confirmed.

2.2.2 Eliminating parental antibody prevalence with an intentional frameshift

One issue with the construction of DNA libraries for directed evolution is the inherent risk of functional wild-type protein contamination. Most mutagenesis strategies are not completely effective at eliminating wild-type DNA and even small contaminations can end up being enriched in selections, especially if the wild-type is functional and expresses well. If possible, it is recommended to eliminate the wild-type gene, prior to the construction of a DNA library, by removing its functionality and then having the library construction restore the functionality so that only the mutant 'offspring' have a chance of selection. There are many effective means to do this and two were considered; one is the introduction of premature stop codons in the wild-type sequence; the other is to introduce a frameshift, which results in a nonsense wild-type gene[244, 245]. For focussed mutagenesis, a premature stop codon or frameshift can be inserted into the region chosen for randomisation, eliminating the wild-type sequence, and the full gene can then be restored with the mutagenic oligonucleotide/s.

For this experiment it was decided that a frameshift would be the best approach, as some premature stop codons are not entirely effective and can occasionally give rise to read-through protein expression[246]. Frameshifts (upstream of gIII) also have the added advantage of frameshifting and scrambling the sequence of pIII, meaning that phage display of the wild-type DesAb or failed mutant is impossible and they are removed from selection automatically. The frameshift (-2 bases) was inserted into the CDR2 loop, in the middle of the three-residue region targeted for randomisation, via inverse-PCR with 5'-phosphorylated primers spaced by two bases, amplifying the whole phagemid except for those two bases. The frameshift and subsequent frame-restoring mutagenic strategy is illustrated in Figure 2.5. The result of the frameshift mutagenic PCR is shown in figure 2.6.

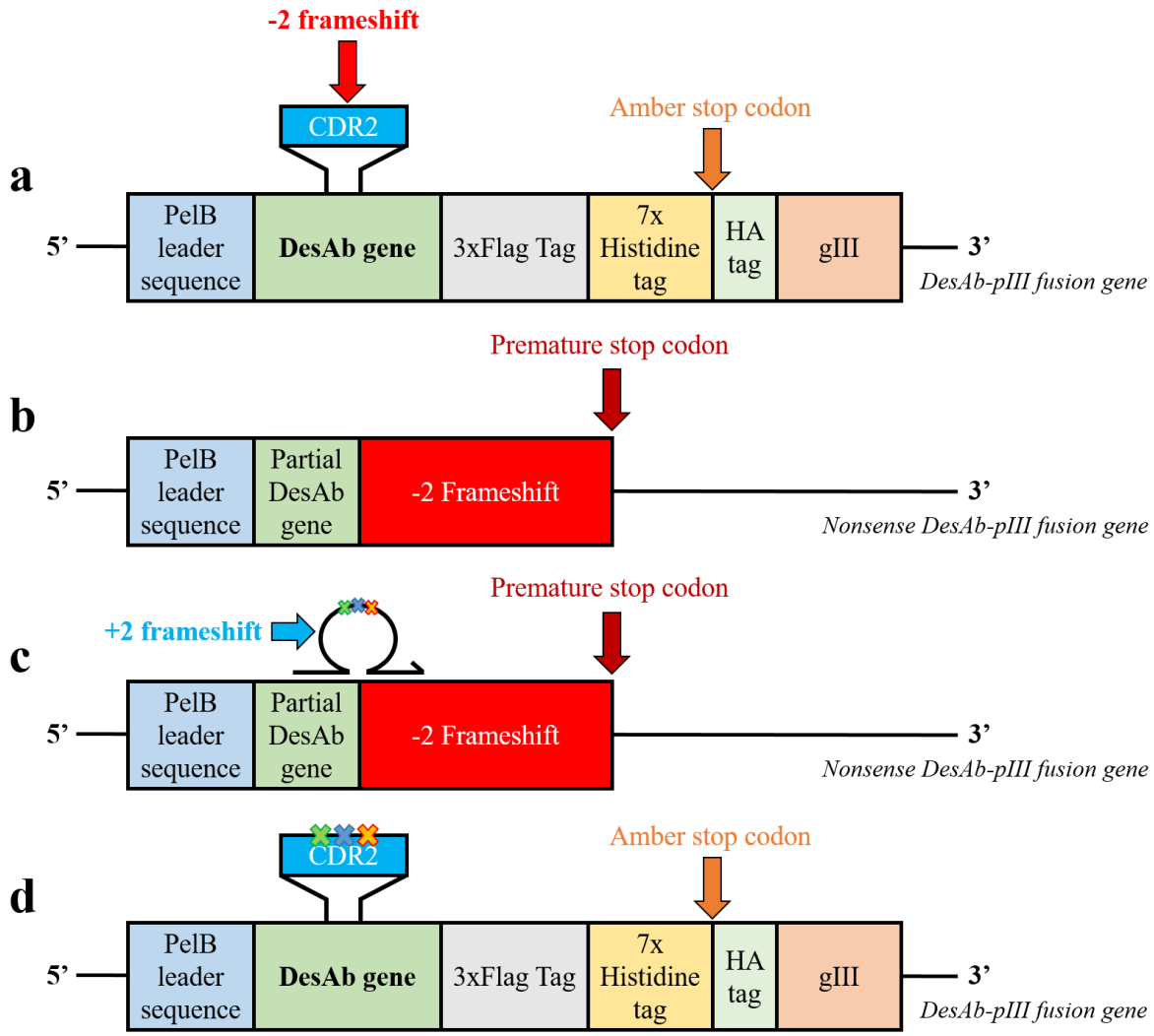

Figure 2.5. Design for 'wild-type' gene elimination from subsequent DNA via frameshift incorporation. Genes and oligonucleotides are not drawn to scale. a) 'Wild-type' DesAb-pIII fusion gene with the CDR2 location shown. The -2 frameshift was introduced into the centre of the CDR2. b) Resulting frameshift of the wild-type DesAb-pIII fusion gene. The pIII fusion cannot be expressed as the frameshift results in nonsense protein sequence (red) and a premature stop codon. c) A large oligonucleotide containing both the randomised codons (coloured crosses) and a +2 frameshift simultaneously creates the DNA library and restores the reading-frame. d) Mutant DesAb-pIII fusion gene with restored reading frame and simultaneously randomised codons in the CDR2 loop.

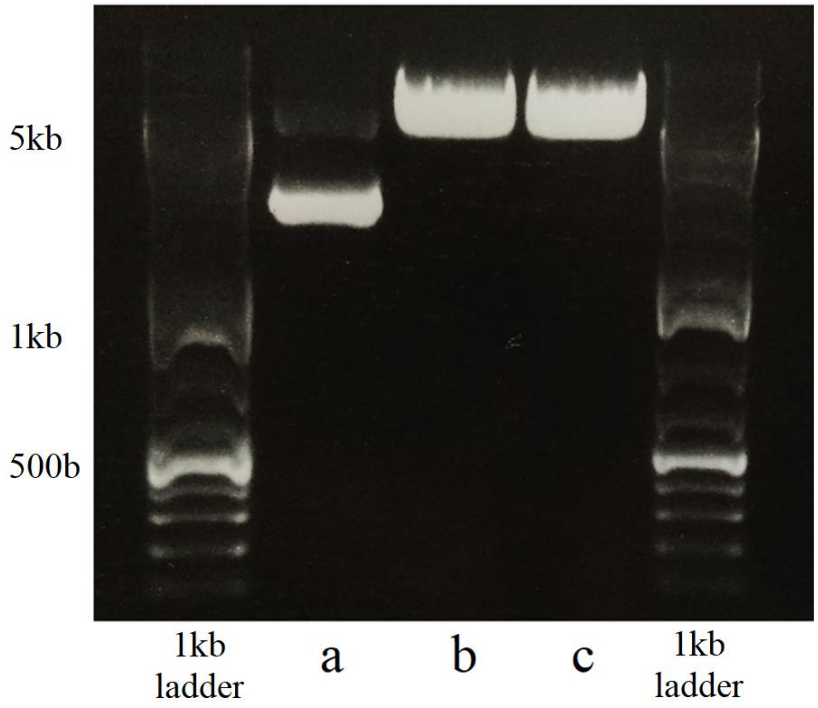

Figure 2.6. Agarose gel electrophoresis of the PCR products resulting from the introduction of -2 frameshifts. a) pMESy4+DesAb-F-gIII construct for comparison. b) pMESy4+DesAb-F-gIII (-2) PCR product. c) pMESy4+DesAb-IAPP-gIII (-2) PCR product. The GeneRuler^{TM} 1 kb Plus DNA Ladder did not migrate smoothly, however the sizes were correct (~5.5 kb for frameshifted DesAb-gIII in pMESy4).

The frameshifted DesAb-containing phagemids were self-circularised, amplified in XL10-gold *E. coli* and their sequences were confirmed.

2.2.3 CDR2 saturation mutagenesis with a two-step inverse PCR

As inverse-PCR whole plasmid amplification was selected as the method of choice for DNA library construction, thermodynamic amplification bias was still a concern due to the small size of the library. As the library was extremely small, even small thermodynamic amplification biases may have resulted in significant overrepresentation of any already prevalent mutants created through degenerate codon bias[245]. In an effort to minimise this potential problem, the inverse-PCR was redesigned to involve as few mutagenic amplification cycles as possible. This would not be desirable when attempting to generate a very large library, as the number of mutagenic cycles would be proportional to library size. However, given that only ~$3.3x10^4$ genotypes were required to completely cover the NNK doping of three residues, a mutagenic

PCR with only a few cycles was hypothesised to establish ample coverage. The next requirement was a high-yield for the DNA library to ensure a large enough bacterial transformation to cover and sample the rarest sequences. One potential method was to use large quantities of the frameshifted 'wild-type' as the template, which would drastically increase the yield over a small number of cycles. However, whilst the 'wild-type' sequence was frameshifted and non-functional, an increased starting quantity would also increase the wild-type sequence contamination, lowering the functional library percentage. An alternative method is to use small quantities of 'wild-type' template and perform a two-step PCR with a small number of mutagenic cycles, followed by a large amplification using 5'-phosphorylated non-mutagenic primers which will induce no thermodynamic amplification bias and allow self-circularisation. To implement this into inverse-PCR whole plasmid amplification, long mutagenic primers (≥60b) would be required as the non-mutagenic primers would have to completely fit between 5' end and the mutagenic NNK codons of the mutagenic primers. The further away from the 5' end the NNK codons are placed, the worse the efficiency of the mutagenesis[223]. Therefore, a long complementary 3' arm was required to centre the NNK codons and anchor the mutagenic primer to the template DNA, further increasing the length. The design methodology is illustrated in Figure 2.7.

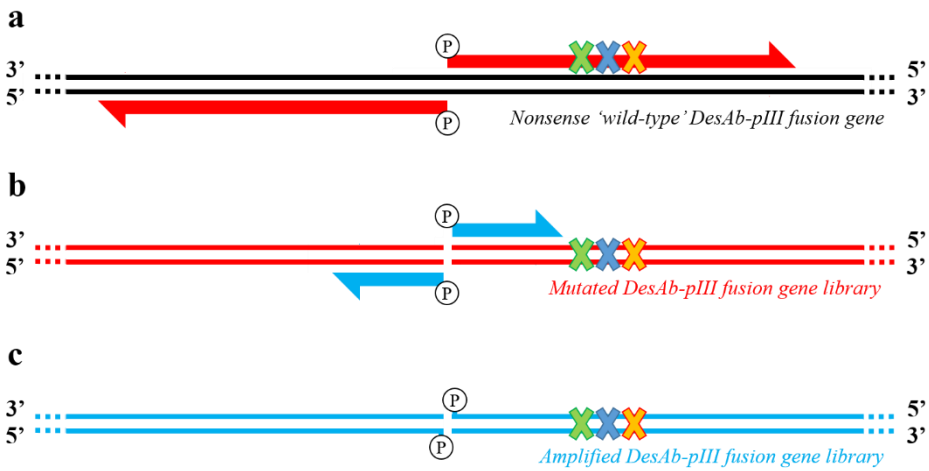

Figure 2.7. Primer design for the two-step inverse-PCR DNA library construction. Dashed lines indicate continuous circular DNA. Oligonucleotides are not drawn to scale. a) Schematic of the mutagenic PCR. Long adjacent 5'-phosphorylated primers (red), one of which contains the NNK mutations (coloured crosses), incorporate the mutations and amplify whole plasmid for a low number of cycles to establish the library. b) Schematic of the non-mutagenic amplification PCR. Short 5'-phosphorylated primers (blue) anneal to the ends of the now linear DNA and, unlike the mutagenic PCR, are completely complementary to the target and impose no thermodynamic amplification bias. The 5'-phosphorylation of the linear DNA (red) is not shown. c) After a high number of amplification cycles, the DNA library (blue) can be self-circularised thanks to the 5'-phosphorylated PCR products and is sufficiently high yield for bacterial library transformation.

Before the two-step inverse-PCR DNA library construction could be implemented, the annealing temperatures needed to be optimised to accommodate primers of significant variance in length. Care needed to be given to the temperature selection as the sensitivities of each PCR are different. The mutagenic PCR required the lowest temperature that would produce the fewest amount of impurities. Lower temperatures can result in non-specific annealing of primers but in this case, higher temperatures would significantly enhance thermodynamic amplification bias. The resulting impurities from non-specific primer annealing was also concerning as they could compromise the yield of the non-mutagenic amplification PCR, and the product of the mutagenic PCR would be too low for gel-extraction purification. It was decided that a compromise between the two issues was best and the lowest annealing temperature that yielded the 'cleanest' PCR product would be selected. Gel-extraction purification is possible for the non-mutagenic amplification PCR and as the primers involved are completely complementary to the template DNA, the highest temperature that could produce the most amount of the correct PCR product, with or without impurities, would be selected. Trial PCRs for both steps were set up individually, across a range of annealing temperatures to determine the optimal conditions for the two-step inverse-PCR. The number of cycles used for the trial mutagenic PCR were significantly higher than that which was used for the final library generation, to produce enough PCR product to analyse in agarose-gel electrophoresis. The results of the trial PCRs are shown in Figure 2.8.

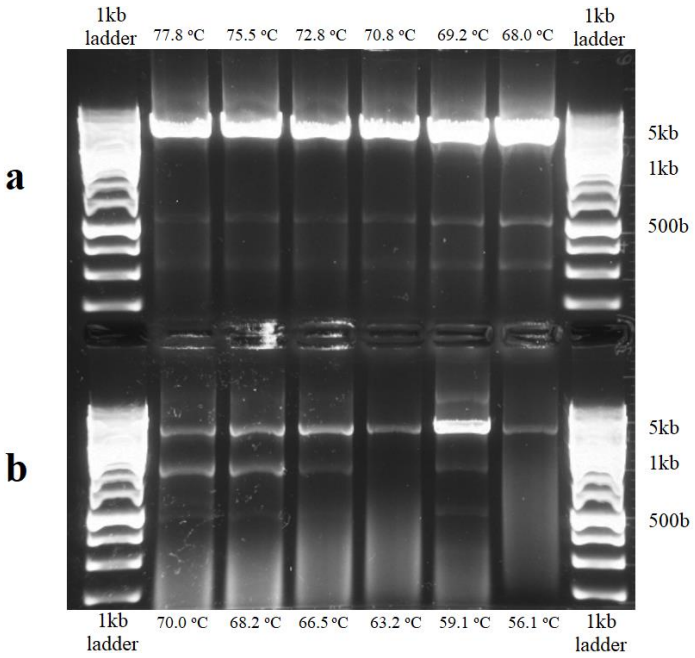

Figure 2.8. Agarose gel electrophoresis of the library test PCRs using a temperature gradient. a) Mutagenic PCR test. The annealing temperature chosen was 70.8 ºC as it was the lowest temperature that gave the smallest yield of impurities. b) Amplification PCR test. The selected annealing temperature was 59.1 ºC as it gave the highest yield of the correct product.

Once the optimal annealing temperatures had been calculated, the full two-step inverse-PCR DNA library construction was performed on both pMESy4+DesAb-F-gIII and pMESy4+DesAb-IAPP-gIII. Henceforth, the resulting DNA libraries of DesAb-F and DesAb-IAPP will be termed DesAb-F pLib and DesAb-IAPP pLib respectively. The number of mutagenic cycles was chosen to be five and the number of amplification cycles was thirty-five. After the mutagenic PCR, the frameshifted 'wild-type' templates were digested and the mutagenic PCR product was briefly purified by spin column to remove the mutagenic primers and was used immediately in the amplification PCR. The results of the two-step inverse-PCR DNA library construction for both DesAb-F and DesAb-IAPP are shown in Figure 2.9.

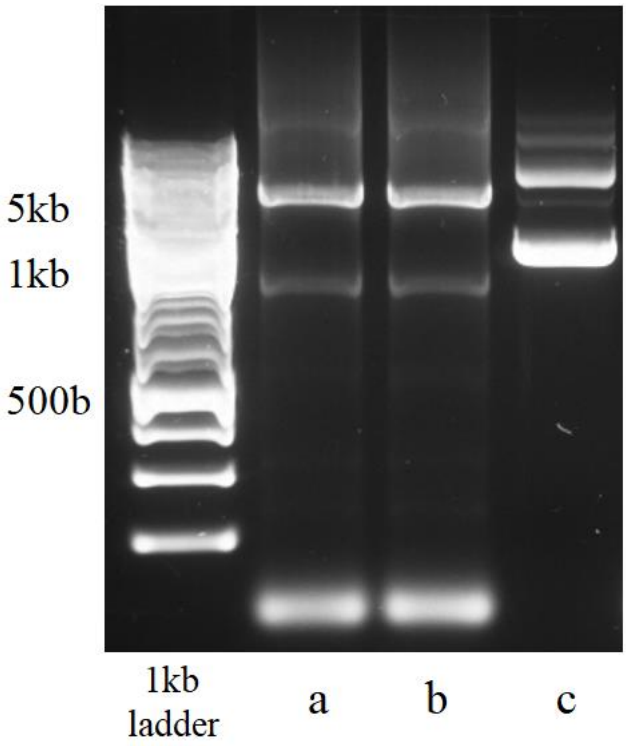

Figure 2.9. Agarose gel electrophoresis of the constructed DNA libraries. a) DesAb-F pLib. b) DesAb-IAPP pLib. c) pMESy4+DesAb-F-gIII construct for comparison. There were two significant impurities present in both libraries, however gel-extraction purification was performed to remove them prior to self-circularisation. The GeneRuler^{TM} 1 kb Plus DNA Ladder did not migrate smoothly, however the sizes were correct (~5.5 kb for both DesAb-F pLib and DesAb-IAPP pLib).

Both DNA libraries were constructed, purified successfully and were self-circularised in yields suitable for bacterial library construction (~1 μg/DNA library). The true quality of the DNA libraries would only become apparent on the analysis of the diversity of the clones generated upon bacterial transformation.

2.2.4 Bacterial library generation and CDR2 diversity evaluation

Before binding affinity selection with phage display can be performed, a DNA library must be introduced into *E. coli.* Apart from the requirement of *E. coli* for production of phage, they also offer an opportunity to assess the quality of DNA libraries by the ability to isolate individual clones in the form of colonies. DNA libraries can also be thoroughly assessed, without the use of *E. coli*, in the form of NGS which can characterise entire libraries, provided the read-length is relatively short (maximum ~700b)[247, 248]. The main drawback to NGS is the cost, with one analysis per DNA library costing thousands of pounds. As the libraries for this experiment were small, it was decided that single-clone Sanger sequencing would be ample for the assessment and a small group of 50 clones would be analysed as a representative sample. In order to ensure the entire DNA library was represented for selection, special attention needed to be placed on the number of transformed bacterial colonies. As mentioned in Chapter 1.6.2, very large DNA libraries (10^{11}-10^{13}) diminish in size when transformed into *E. coli* as the maximum realistic transformation yield achievable is 10^{9}-10^{10}, representing a significant loss in library coverage[198, 249]. For this experiment this problem was not an issue, due to the small library size, but it is important to be aware of the need to over-represent a DNA library where possible to ensure the likeliest probability of sampling the rarest codon combinations[216, 222]. NNK doping produces 32 possible codon combinations per residue and the resulting genetic diversity for a simultaneous 3-residue randomisation is 32^3 (32,768 genotypes). A Poisson distribution can be used to calculate the number of clones required to sample the entire DNA library with 99% confidence. This increases the size for the required number of transformants by ~4.5-fold, and for this experiment ~$1.5x10^5$ colonies were required[222].

DNA library transformation of TG_1 *E. coli* by electroporation was performed, which resulted in ~$1x10^6$ colonies. TG_1 is an amber-suppressing *E. coli* strain which translates the TAG stop codon to Glutamine (Q) and are very susceptible to M13 phage infection, making them suitable for phage display. 50 colonies were picked and their DNA was amplified using colony-PCR and submitted for Sanger sequencing. The nucleotide proportions of the randomised positions are shown in Figure 2.10.

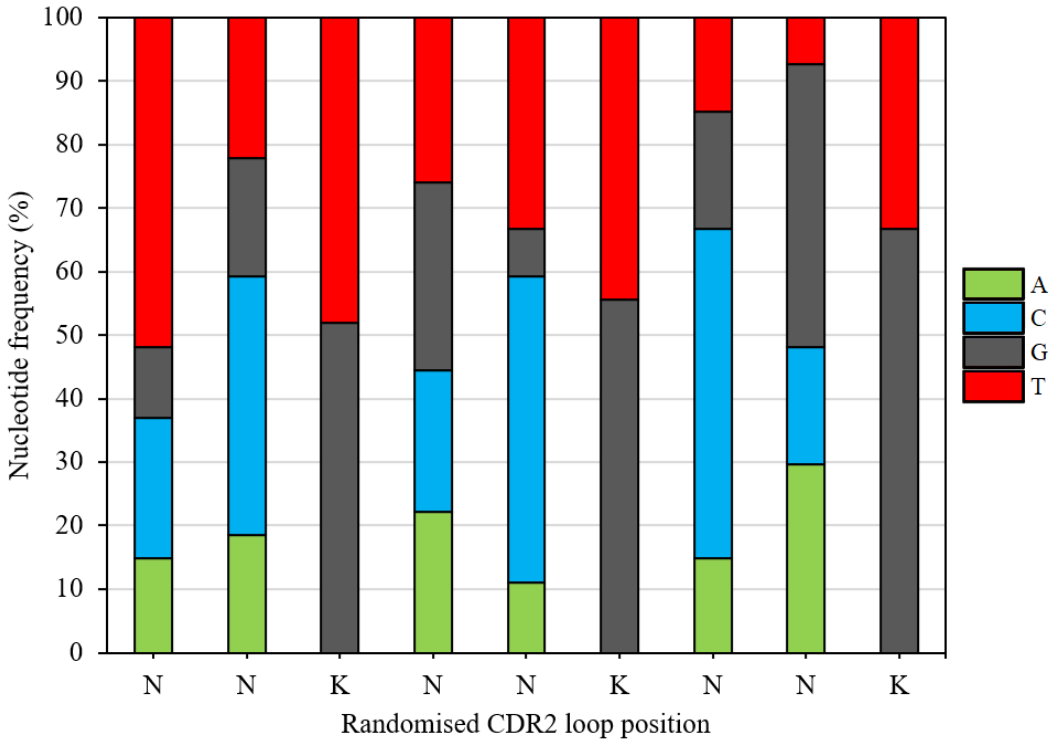

Figure 2.10. Nucleotide percentage at the randomised base positions of the CDR2 loop. The positions from left to right represent the randomised adjacent codon region (5' to 3') of the resulting saturation mutagenesis of the CDR2 loop. In the mutagenic oligonucleotide, nucleotide mixture 'N' is an equal mixture of Adenine (A, green), Cytosine (C, blue), Guanine (G, grey) and Thymine (T, red). Nucleotide mixture 'K' is an equal mixture of Guanine and Thymine.

The combinations of nucleotides present at each position in the CDR2 loop is correct for the 'N' & 'K' positions but not distributed as evenly as was designed. The sample-size is small as only 46 were successfully sequenced and only 27 were positive for the mutagenesis (~60% correct mutants and ~40% PCR errors or frameshifted wild-type) so an accurate analysis is difficult. Fortunately this is not much of a concern with a small library but to determine the extent of any possible thermodynamic amplification bias, the distributions for all 'N' and 'K' base mixtures were averaged to analyse the overall mutagenic content of the DNA library. The result is shown in Figure 2.11.

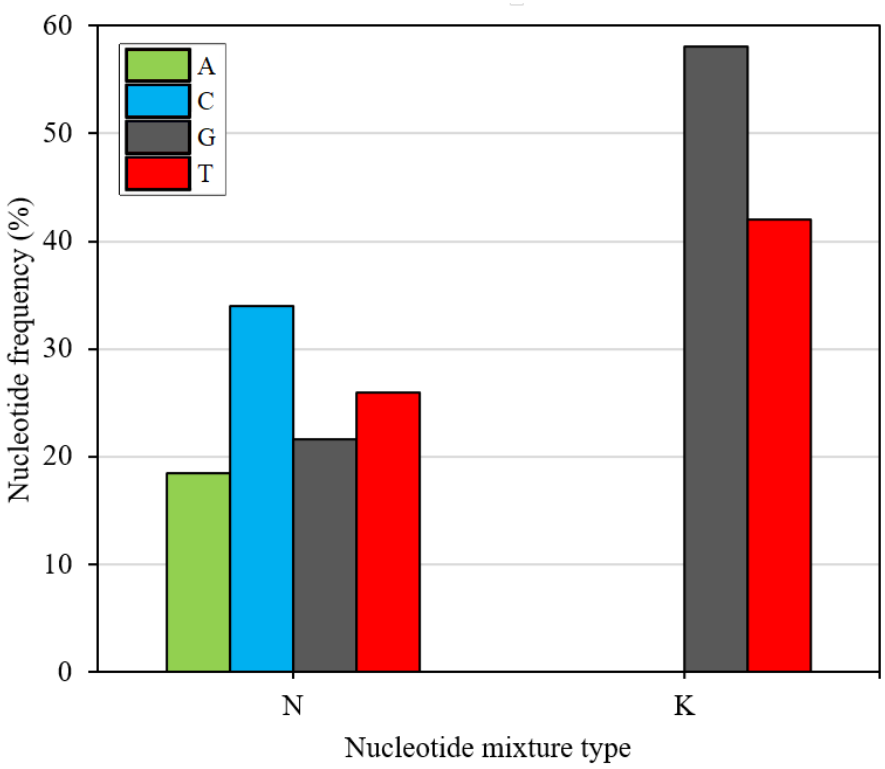

Figure 2.11. Average nucleotide incorporation for the N and K mixture types. 'N' is a mixture of Adenine (A, green), Cytosine (C, blue), Guanine (G, grey) and Thymine (T, red). Nucleotide mixture 'K' is a mixture of Guanine and Thymine. When no bias is present, 'N' is expected to consist of 25% of each nucleotide and 'K' should be a 50% mixture of Guanine and Thymine.

The increased proportions of Cytosine (34%) in 'N' and Guanine (58%) in 'K' in the library sample imply possible evidence of thermodynamic amplification bias, however in thermodynamic amplification bias the frequency of Guanine in the 'N' positions should be similarly proportional to the frequency of Cytosine[219, 220]. Instead, in the 'N' mixture, Thymine is the second most abundant nucleotide (26%), whilst Guanine is underrepresented (21%). This suggests the library sample sent for sequencing may be too small for this kind of analysis and would benefit most from high-throughput NGS sequencing. The codons of each correctly mutated library member were identified and analysed to further ascertain any biases in the resultant codon distribution. The results are shown in Figure 2.12.

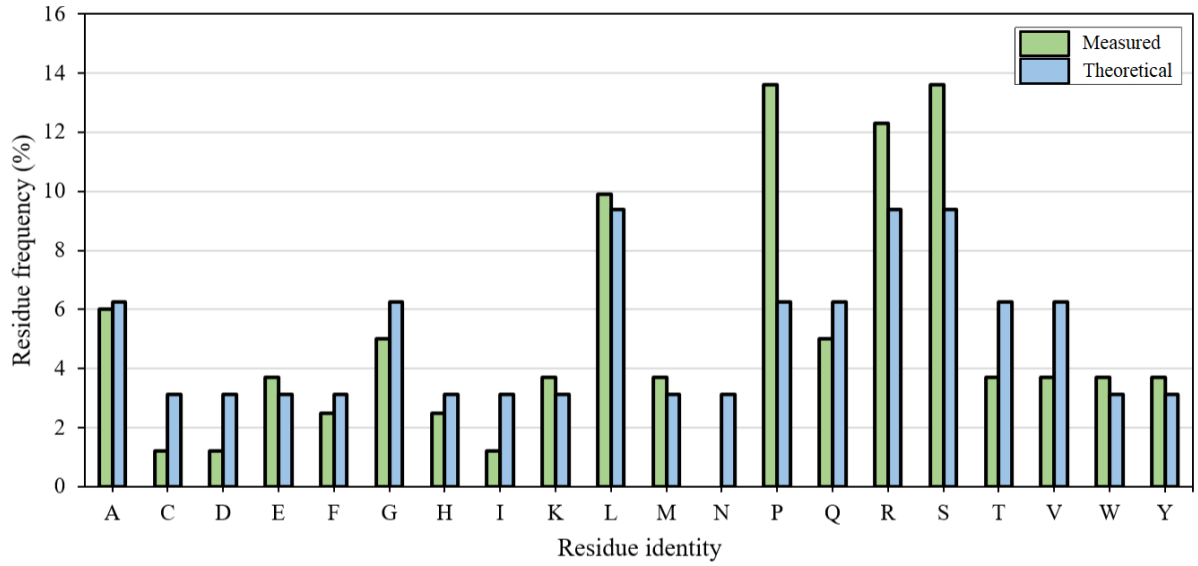

Figure 2.12. AA abundance in the CDR2 loops of the library sequencing samples. Measured codon frequencies (green) are shown for each residue with their theoretical frequency (blue) for comparison. Stop-codons are not shown due to their restriction by NNK saturation to the amber stop-codon. The TG_1 *E. coli* strain used suppresses the amber stop-codon (TAG) and instead encodes Glutamine (Q). The TAG codon correspondingly contributes to the measured and theoretical Glutamine frequency.

The frequency of codons in even the small library sample is generally as expected with NNK saturation mutagenesis, although there are some anomalies. The expected codon bias is shown as the theoretical codon frequency and any deviations will be caused by small sample size error or thermodynamic amplification bias. The significantly increased prevalence of Proline (P) is interesting as it is encoded by only two codons using NNK saturation, whilst Leucine (L), Arginine I and Serine (S) are encoded by three. As thermodynamic amplification bias occurs with sequences partially homologous to the 'wild-type' sequence, and codons rich in Cytosine and Guanine, the analysis of significantly over/underrepresented residues could provide insight into whether any bias has occurred. The increased abundance of Proline may be attributed to the homology of the mutated 'wild-type' sequence (PTN), however the Prolines were equally distributed across all three target residues. The reduced prevalence of Threonine (T) and complete absence of Asparagine (N) also suggests that homology may not be a significant source of bias. However, when analysing the Cytosine and Guanine content of the over/underrepresented codons, there is some evidence of thermodynamic amplification bias. Asparagine and Isoleucine (I) are encoded by only AAT and ATT respectively in NNK doping, which have a Cytosine and Guanine content of 0% and are significantly underrepresented. Proline on the other hand has a Cytosine and Guanine content of 83% and is clearly

overrepresented. Anomalies to this hypothesis exist as well, as Serine has a Cytosine and Guanine content of 44% and is significantly overrepresented whilst Glycine (G) is underrepresented and has a Cytosine and Guanine content of 83%. These inconsistent findings imply that the sample size is indeed too small and would benefit from significant expansion before any accurate analysis should be attempted. As the DNA library size was modest, any introduced thermodynamic amplification bias was most likely not as diversity constraining as it would be with a large library, and the diversity analysis indicates that the library was constructed with sufficient quality for affinity selection with phage display.

2.3 Results: Experimental preparation for phage display

2.3.1 α-Synuclein single-labelling with biotin (Maleimide)

As mentioned in Chapter 2.1.2, the disadvantages of solid-phase adsorption of αSyn, especially epitope masking and poor concentration control was deemed unsuitable for affinity maturation biopanning. Instead, affinity selection in solution, followed by 'pull-down' of the phage-DesAb-αSyn complexes would be performed with the use of biotinylated-αSyn and Streptavidin/NeutrAvidin coated magnetic beads. In order to achieve this, αSyn would need to be specifically labelled with biotin, ideally far from the target epitope (70-77) to prevent steric hindrance which ruled out Lysine labelling with (+)-Biotin N-hydroxysuccinimide ester as there is a Lysine at position 80. Instead, the specific biotinylation of the C-terminal Cysteine of the A140C mutant of αSyn with EZ-link^{TM} Maleimide-$(PEG)_2$-Biotin was chosen as it would result in single-labelling of a position far from the target epitope. Labelling was performed in the presence of tris(2-carboxyethyl)phosphine (TCEP) and was successfully verified by Matrix-assisted laser desorption/ionization (MALDI) mass-spectroscopy. The resulting mass spectra is shown in Figure 2.13. αSyn mutant A140C was provided by the Centre for Misfolding Diseases (CMD), University of Cambridge.

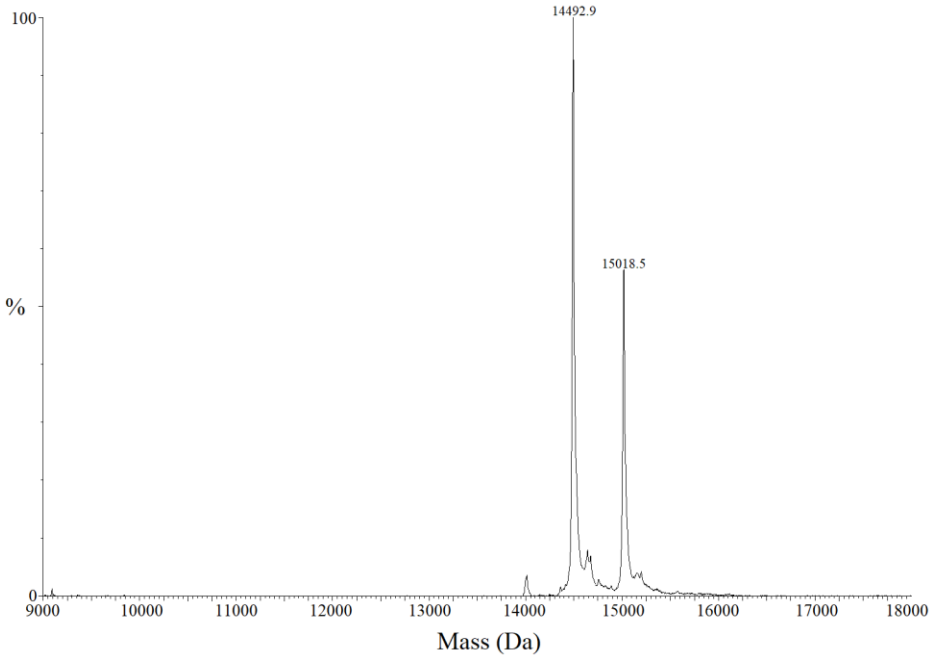

Figure 2.13. Mass-spectra of the biotinylation of A140C. The peak at 15018.5 Da corresponds to biotinylated αSyn A140C. It is at roughly 50% of the abundance of the remaining unlabelled αSyn A140C (14492.9 Da). This equates to ~33% labelling efficiency.

The MALDI mass-spectra analysis indicated significant unlabelled αSyn A140C was present, which would almost certainly interfere with biopanning due to the exposed Cysteine and non-reducing environment. Therefore, purification of the biotinylated-αSyn A140C was performed using monomeric Avidin agarose to remove the contaminating unlabelled αSyn A140C.

2.3.2 Confirmation of single-domain antibody display with Protein A

Before committing both libraries to affinity maturation, it was deemed prudent to confirm the correct display of the DesAbs on the surface of the phage[231]. A straightforward method to achieve this is to perform a 'mock' binding selection against Protein A as target 'Ag'. Protein A is a 45 kDa cell-surface protein of *Staphylococcus aureus* (*S. aureus*) which strongly binds the heavy chain, in both the Fc and Fab regions, of human Abs and Abs of some other species[250, 251]. In the V_H domain, Protein A binds a conformational 'epitope' on the surface of the core of the domain, across multiple β-sheets[252]. This gives Protein A additional specificity towards folded V_H domains and makes it an excellent choice for determining whether the DesAbs are displayed on the surface of the phage and also, if they are folded correctly. Display confirmation was achieved by performing one round of phage display affinity selection against Protein A-coated magnetic beads and comparing the eluted phage titres against beads coated

with Streptavidin. Only DesAb-F pLib was used in this instance as it was assumed one library could be representative for both libraries as they were constructed in identical conditions. The results of Protein A biopanning are shown in Figure 2.14.

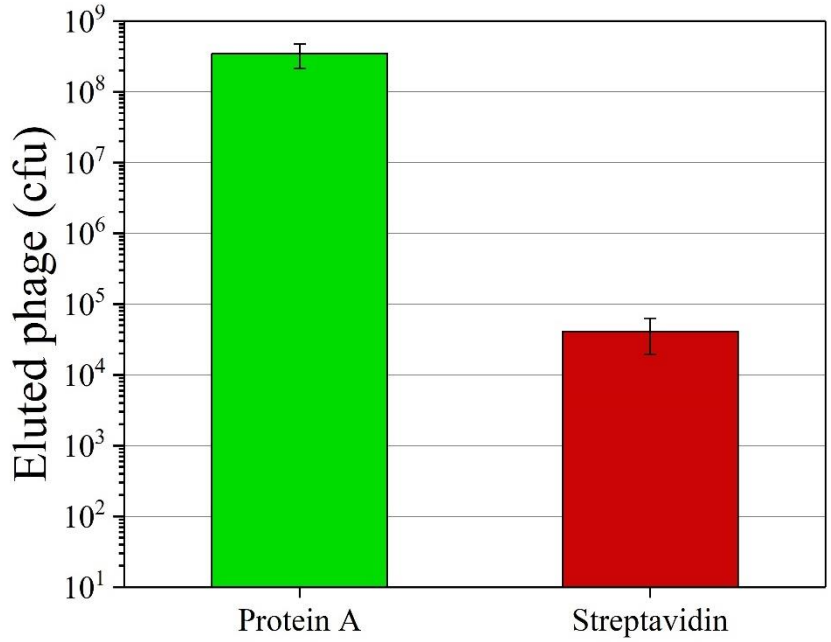

Figure 2.14. Output phage titre for DesAb-F pLib binding to Protein A. Streptavidin coated-beads were used as a control non-binding protein. The biopanning round showed significant enrichment of DesAb-F pLib towards Protein A (green), ~2,000-fold higher than the beads coated in a non-binding protein (red, streptavidin). The eluted phage are quantified as the bacterial colony-forming units (cfu) resulting from phage infection of fresh *E. coli* on antibiotic-selective agar. Bars represent the mean average and error bars represent the standard deviation of three repeat measurements.

Due to the strong binding preference towards Protein A over Streptavidin, it was clear that the DesAbs were displayed correctly and present in significant quantity. Phage input titres into all selections described in this thesis were standardised to $1x10^{11}$ cfu and this result (~$3.4x10^{8}$) represents the theoretical total of DesAb-displaying phage in this experiment. Taking the ~60% library success rate and the fact that a large proportion of phage are secreted from E. coli without the displayed protein (bald), this indicates that a significant proportion of the library remains correctly displayed[253, 254]. As the library only encodes ~$3.3x10^{4}$ clones, this means that each member is roughly estimated to be present in ~3,000 copies (ignoring expression bias). Whilst it was possible to use this Protein A-enriched library for full affinity maturation against αSyn, expression enrichment bias was also selected for, so the Protein A-enriched library was discarded and the first round of binding selection of the libraries would be against αSyn to maximise binding enrichment.

2.4 Results: Affinity selection against full-length α-Synuclein

Following confirmation of DesAb display, affinity selection of both libraries began in earnest. Selection conditions were optimised and the concentrations of biotinylated α-Syn were reduced by a factor of ten between rounds (round one: 1 μM, round two: 100 nM, round three: 10 nM). The concentration of capture protein-coated magnetic beads was also reduced by a factor of ten accordingly between rounds so as to mitigate any unwanted enrichment. Unwanted enrichment was also mitigated by alternating between Streptavidin and NeutrAvidin-coated beads between rounds and alternating the blocking agents between BSA and skimmed-milk. Further to this, the phage libraries were pre-incubated with the capture protein-coated magnetic beads, which were then discarded, to remove any non-specific binders prior to affinity selection. The buffer system chosen was phosphate-buffered saline (PBS) in the presence of 2% w/v BSA or skimmed milk and the optimised concentration of Tween® 20 was found to be 0.05% v/v. DesAb-phage incubations with biotinylated α-Syn were for 2 hours and each round included ten washing steps. The resulting phage titres of each library for each round of selection are shown in Figure 2.15.

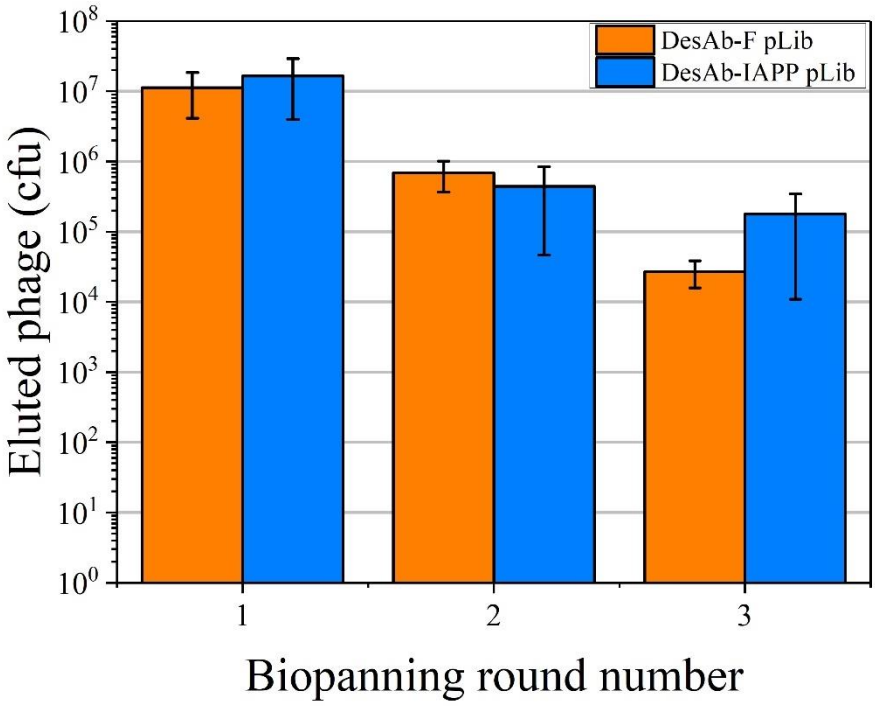

Figure 2.15. Mean average output phage titres for the affinity selections of DesAb-F pLib and DesAb-IAPP pLib. DesAb-F pLib phage titres are shown in orange and DesAb-IAPP phage titres are shown in blue. Bars represent the mean average and error bars represent the standard deviation of three repeat measurements. Rounds one, two and three were selections against 1 μM, 100 nM and 10nM αSyn respectively.

A clear decrease can be seen in the measured output phage titres of both libraries, roughly ten-fold per round, indicating strong restriction in diversity. It should be noted that output phage titres merely indicate the progression of the selection and it is difficult to ascertain qualitative information on the types of enrichment taking place. The decrease in overall titres suggests that the selection conditions may be rather stringent and that the libraries likely contained very few, if any, high-affinity binders (low-nanomolar K_D). In order to visibly observe specific binding enrichment, keeping the concentration of biotinylated αSyn the same between rounds would have allowed the enriched Abs to propagate and result in higher titres the following round. However, maintaining the concentration between rounds also allows expression bias an improved chance to compete and does not enforce any additional binding selection pressure to further select the highest-affinity variants. In Ab discovery from large libraries of non-binders, it is especially important to observe an increase in phage titres, as the proportion of binders starts extremely low. For affinity maturation it can be assumed that a high proportion of the library already binds to the target, so it is more important to rapidly increase the stringency of selection[231].

The drop in phage titres could also be the result of other factors such as the simultaneous decrease in the concentration of the capture-protein beads. A lower concentration of capture-protein beads will result in reduction of the kinetics of phage-DesAb-αSyn complex capture and as a result, some phage-DesAb-αSyn were probably not captured. Longer incubations with the capture-protein beads could have been used to mitigate this, however these resulted in an increase in the background phage titres (not shown) and therefore it was decided to retain the short (30 minute) incubation time. Both libraries appeared to yield the same phage titres for the first and second rounds, but for the third round, the DesAb-IAPP pLib phage titres decreased significantly less than those of DesAb-F pLib. This was unexpected, as DesAb-IAPP pLib was expected to be a library containing a significantly lower proportion of binders due to DesAb-IAPP showing negligible binding to αSyn[176]. It was postulated that in the absence of binding affinity enrichment for the early rounds of DesAb-IAPP pLib αSyn affinity selection, expression and non-specific binding enrichment and had been significantly selected for and was allowing rapidly propagating DesAb-IAPP mutants to survive in increasingly stringent conditions. Of course, this information cannot be reasonably deduced from phage titres alone, especially as the titres for each round were within one-another's error, and would have to be obtained during screening and characterisation.

2.5 Results: Screening for evolved antibodies against α-Synuclein

2.5.1 EvDesAb-expressing cell-lysate screening via ELISA

Following phage display affinity selection against αSyn, the eluted phage from round three were used to infect fresh TG_1 *E. coli*, which were plated on antibiotic-selection agar in their entirety to recover the libraries and allow colony picking to isolate individual clones for screening. As the EvDesAbs were screened in crude cell-lysates from amber-suppressing TG_1 cells, they were expressed and screened as DesAb-gIII fusions. Once screened, ranked and sequenced, they would then be transformed into non-amber-suppressing WK.6 *E. coli* for purification of soluble sdAbs. Screening was performed on the EvDesAb-containing crude extracts using ELISA as introduced in Chapter 1.9.1, with expression signals measured by direct coating of cell-lysate to the microwells and binding signals quantified using an indirect ELISA of the cell-lysate against αSyn-coated microwells. The results of the screening for both DesAb-F pLib and DesAb-IAPP pLib are shown together for comparison in Figure 2.16.

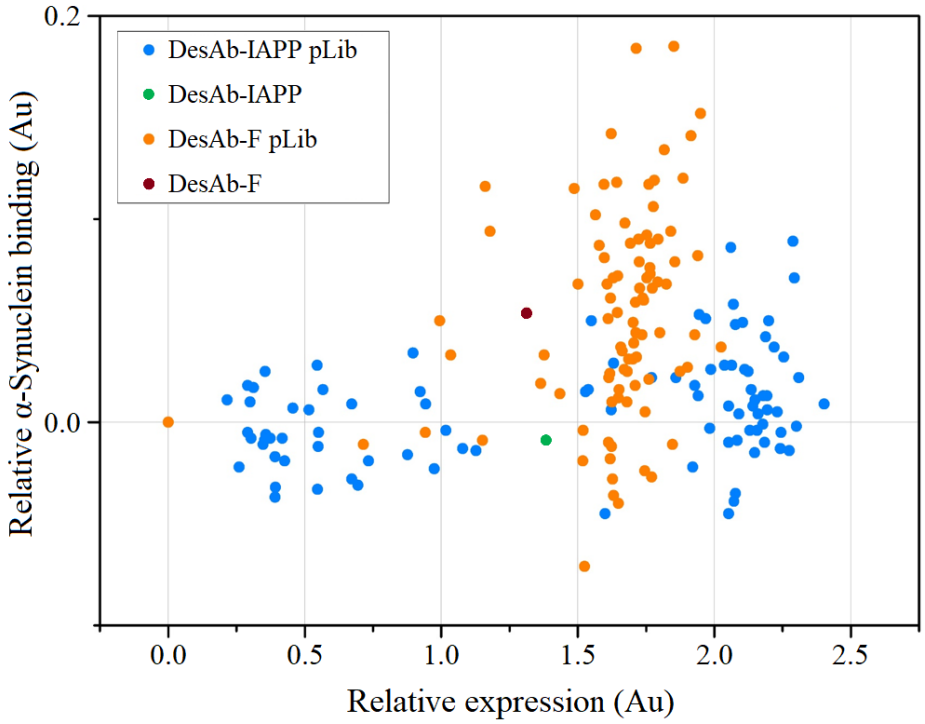

Figure 2.16. Crude extract screening of individual EvDesAbs from DesAb-F pLib and DesAb-IAPP as measured by ELISA. DesAb-F pLib EvDesAbs are shown in orange and DesAb-IAPP pLib EvDesAbs are shown in blue. For comparison with the parental DesAbs, DesAb-F is shown in dark red and DesAb-IAPP is shown in green. Values are the measurements of the 450 nm absorbance (Au) change produced by the oxidation of 3,3',5,5'-Tetramethylbenzidine (TMB), which is proportional to the presence of the screened Abs.

The ELISAs used to generate the screening signals were all performed in parallel, using equal volumes of cell-lysate of each isolated clone and the control parental DesAbs. Binding values are the result of measured binding signals subtracted by the background signals, which is the signal produced upon clones interacting with microwells coated in cell-lysate of non-transformed *E. coli* in a separate ELISA (not shown). The commercial 'secondary' Ab for signal generation was a horseradish peroxidase (HRP)-conjugated Ab that binds Histidine-tags (Anti-His), such as the one at the C-terminus of the screened clones. HRP oxidises the chromogenic substrate TMB into a diimine, which produces a colour change; the intensity of which is proportional to the concentration of the HRP-conjugated Ab remaining in the microwell. This Ab was selected for its high-specificity (low background) and expression values are the result of the measured expression values subtracted by the background signal produced by the HRP-conjugated Anti-His Ab interacting with *E. coli* cell-lysate alone.

After screening analysis of 94 clones per library, a clear set of trends could be observed. There was immediate evidence of the expression enrichment of the DesAb-IAPP pLib during affinity selection as the average relative αSyn binding measurements for the population was much lower than DesAb-F pLib and a large proportion of clones displayed higher expression scores than all of the DesAb-F pLib library members. A significant proportion of the DesAb-IAPP library displayed reduced expression with respect to DesAb-IAPP itself. An explanation could be the result of high non-specific binding during selection, indicated by a large proportion of these mutants giving negative or close-to-zero binding values as a result of their high background signal. It appears that extensive characterisation of this population would be required to understand the phenomenon at work, however as this was not the primary focus of this study it was not prioritised.

As expected, the screening of DesAb-F pLib showed strong enrichment towards improved αSyn binding with respect to DesAb-F but it is also clear that expression was also selected for as well, as almost half of the screened clones showed enhanced expression, with no gain or even a decrease in αSyn binding. Nevertheless, screening revealed subpopulations of both libraries suitable for further characterisation. Clones were selected for further characterisation based on improvements to binding scores and expression scores, with priority being given to binding improvements as more highly expressing mutants will have exaggerated binding scores. Sequencing analysis was then performed to analyse the compositions of the CDR2 loops of the EvDesAbs with improved characteristics.

2.5.2 Sequencing analysis of evolved antibody populations

DNA sequencing analysis was performed on a small selection of EvDesAbs displaying apparent αSyn binding affinity improvements, as measured during crude-extract screening. The resulting sequences of the mutated regions of the CDR2 loops of eleven EvDesAbs from each library are shown in Table 2.1.

Table 2.1. Mutated CDR2 sequences of EvDesAbs from DesAb-F pLib and DesAb-IAPP pLib displaying improved binding to αSyn with respect to their parental DesAbs. Sequences found in more than one clone are denoted with an asterisk (*).

DesAb-F pLib	DesAb-IAPP pLib
CLQ	ALF
DGT	ARG
HSV	GAQ
LSH	GLF*
NLS	GLF*
RHR	GQG
RQH	PLG*
RSQ	PLG*
SSL	QVI
TDQ	RFW
WSR	WAP

As expected, all sequences obtained for the analysed group were mutated and in-frame due to the ‘wild-type’ elimination design. As the purpose of phage display is to restrict library diversity, the chance of observing multiple clones with identical sequences drastically improves after selection. This can be observed with the repeated occurrences of ‘GLF’ and ‘PLG’ in the clones sequenced for DesAb-IAPP pLib. This phenomenon was not observed in the clones sequenced in the DesAb-F pLib group, indicating that possibly a larger diversity of the selected library displayed good binding affinity. Of course, the sequencing sample size is again very small, and such an assumption cannot be made without a significantly larger sample size. What can be immediately observed in the sequences between the two libraries is a large difference in the types and classes of residues selected for. An analysis of these residue distributions is shown in Figure 2.17.

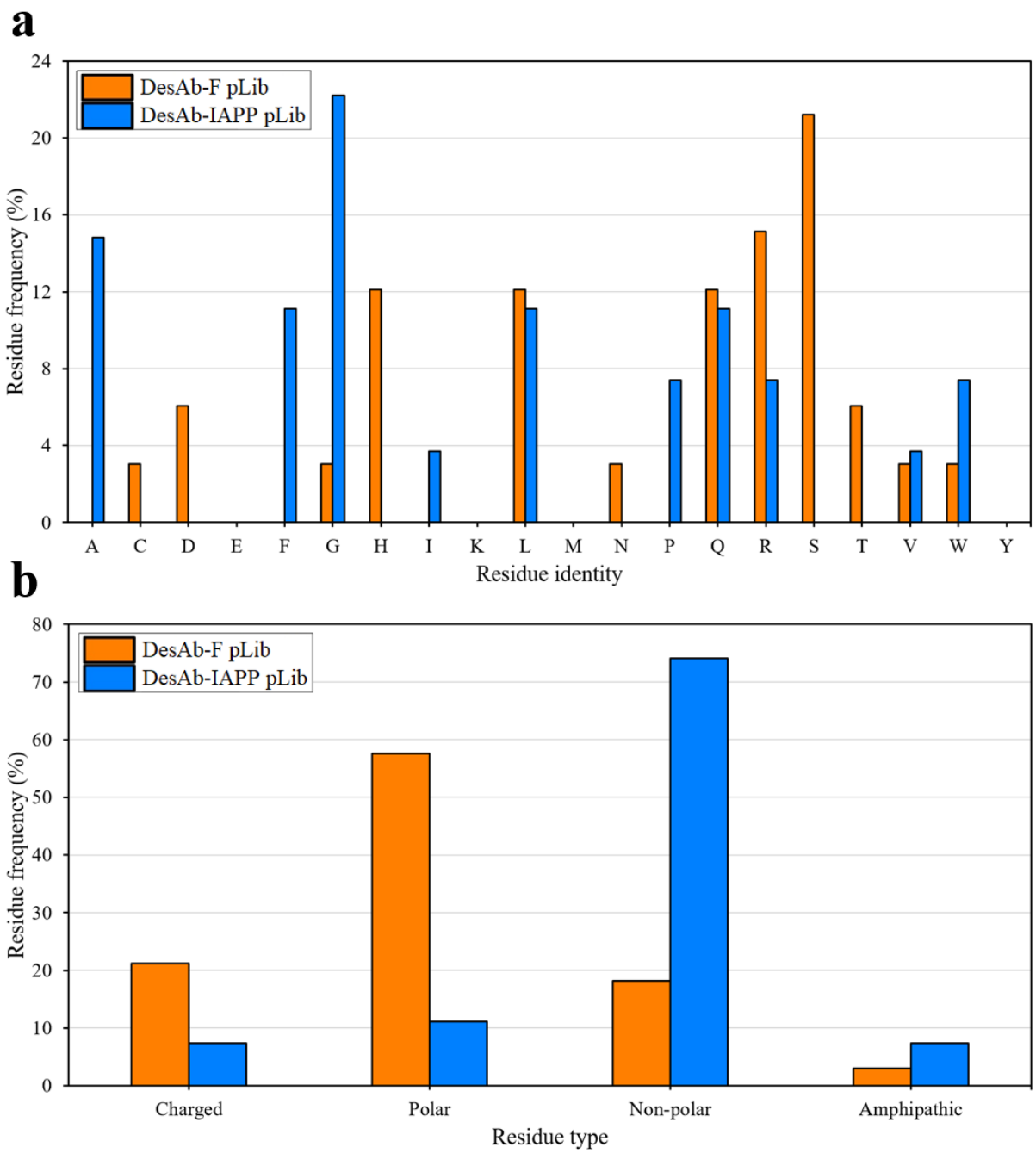

Figure 2.17. CDR2 residue identities and classes found in improved affinity clones of DesAb-F pLib and DesAb-IAPP pLib post-selection. DesAb-F pLib clone mutant residues are shown in orange and DesAb-IAPP pLib clone mutant residues are shown in blue. a) Residue identities of sequenced clones and their percentage frequency. b) Residue class types of sequenced clones and their percentage frequency. Residue class types are: charged residues (D, E, K, R), polar residues (C, H, N, Q, S, T), non-polar (A, F, G, I, L, P, V) and amphipathic (M, W, Y).

Upon analysis of the CDR2 sequences for both libraries, the difference in enriched residues is large. Affinity maturation of DesAb-F yielded significant enrichment of polar residues whilst the same selection for DesAb-IAPP pLib enriched for non-polar residues. This is supported by

the additional enrichment of hydrophilic charged residues for DesAb-F pLib and the amphipathic, but highly hydrophobic, Tryptophan for DesAb-IAPP pLib. This may imply that the EvDesAbs of DesAb-IAPP pLib may have survived selection through the formation of large hydrophobic interactions with the most hydrophobic regions of αSyn, such as the NAC region. The enrichment of DesAb-F pLib towards hydrophilic residues may potentially increase the risk of switching epitope towards the acidic C-terminus of αSyn and therefore it was imperative that the epitope of each affinity-improved EvDesAb was characterised.

2.5.3 Expression and purification of soluble evolved antibody fragments

Before EvDesAb characterisation could commence, each selected clone would require large-scale expression and purification. At this stage it was not desired to express the EvDesAbs with their pIII fusion and therefore their encoding DNA was directly transformed into non-amber-suppressing WK.6 *E. coli*, which would express the soluble ~18 kDa sdAbs (cf. 62 kDa sdAb-pIII fusions). The PelB leader sequence on the N-terminus directs the expressed EvDesAbs to the bacterial periplasm, where it is cleaved from the sdAb. Cellular periplasmic extraction of the sdAbs was performed through the use of osmotic shock with a high concentration of sucrose and a two-step sdAb purification was then carried out, firstly by immobilised metal affinity chromatography (IMAC) and then by size-exclusion chromatography (SEC). IMAC purification involved an immobilised Nickel resin that chelates and binds with the C-terminal 7xhistidine tag, removing the majority of impurities, and SEC would serve as a final 'polishing' step to remove the remaining impurities and completely buffer-exchange the EvDesAbs into their experimental working buffer. All EvDesAbs from both libraries expressed in good yields (~10 mg/L of liquid culture) and purification was consistent with minimal issues. A representative purification comparison of a DesAb and one of its EvDesAbs is illustrated in Figure 2.18.

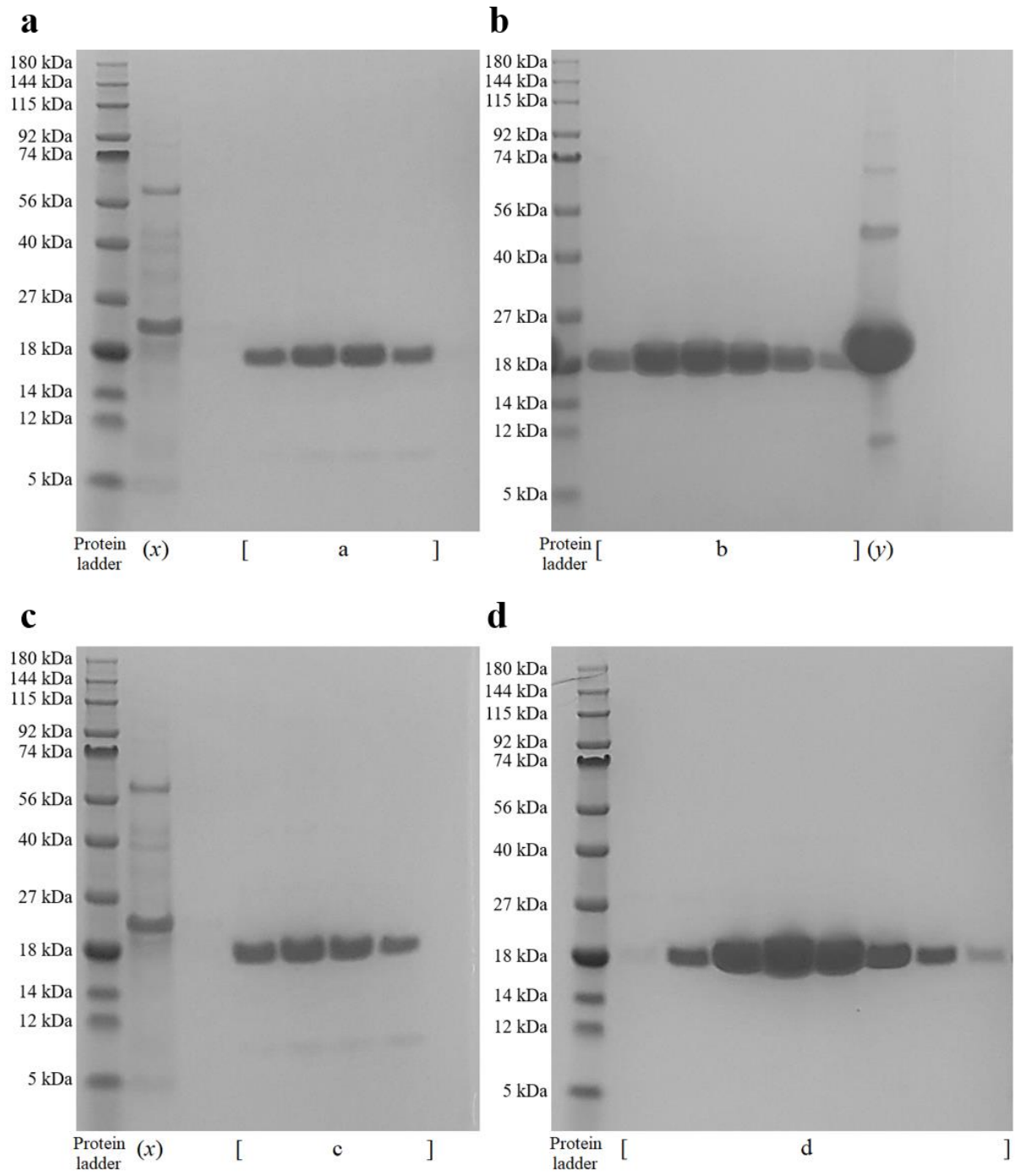

Figure 2.18. Sodium dodecyl-sulphate polyacrylamide gel electrophoresis (SDS PAGE) analysis of the purifications of DesAb-F and one of its mutants (EvDesAb-LSH). a) IMAC purification of DesAb-F (~18 kDa). b) SEC purification of DesAb-F. c) IMAC purification of EvDesAb-LSH (~18 kDa). d) SEC purification of EvDesAb-LSH. (*x*) Discarded *E. coli* periplasmic extract flow-through. (*y*) Concentrated pre-SEC DesAb-F sample for comparison.

2.6 Results: Affinity characterisation by microscale thermophoresis

2.6.1 α-Synuclein single-labelling with Alexa488

Due to the fact that many clones would be characterised for their αSyn binding affinity by MST, it was deemed more appropriate to fluorescently label αSyn instead of labelling each clone for efficiency purposes. This dictated that the concentration of αSyn remain constant whilst the EvDesAbs would be titrated against it. Alexa488 (A488) was chosen as the fluorescent label, due to its high emission and resistance to photobleaching[255]. Single labelling was also required to ensure a uniform ligand fluorescence for accurate MST-induced fluorescence changes. αSyn mutant N122C was chosen for labelling with A488-Maleimide. The purification of αSyn N122C is the same for all Cysteine-containing variants of αSyn (described in Chapter 5.3.1) and the purification is shown in Figure 2.19.

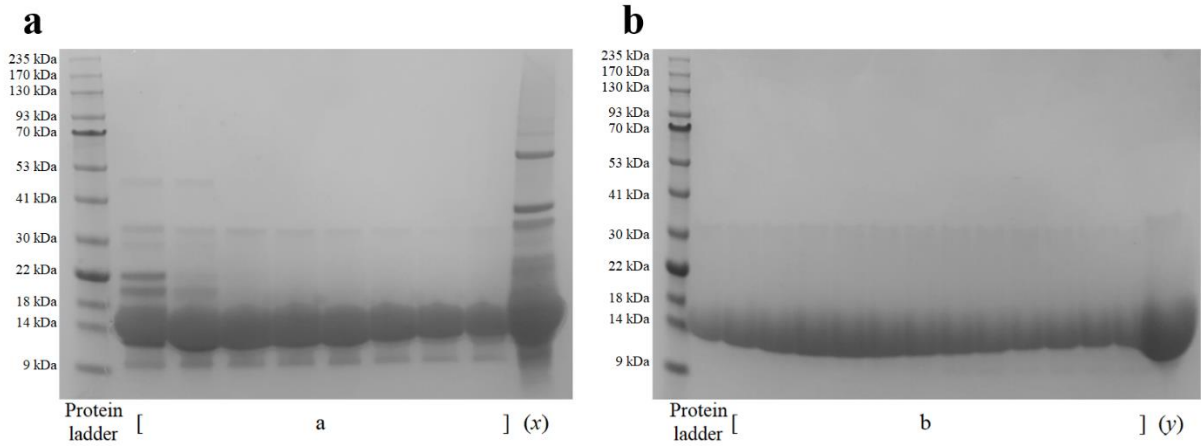

Figure 2.19. SDS-PAGE analysis of the purifications of αSyn N122C. a) Ion-exchange chromatography (IEC) purification of αSyn N122C (~14 kDa). b) SEC purification of αSyn N122C. (*x*) Discarded pre-IEC sample of αSyn N122C. (*y*) Concentrated pre-SEC αSyn N122C sample for comparison.

A488 single labelling of αSyn N122C was performed and verified by liquid chromatography-mass spectroscopy (LC-MS). The resulting mass-spectra is shown in Figure 2.20.

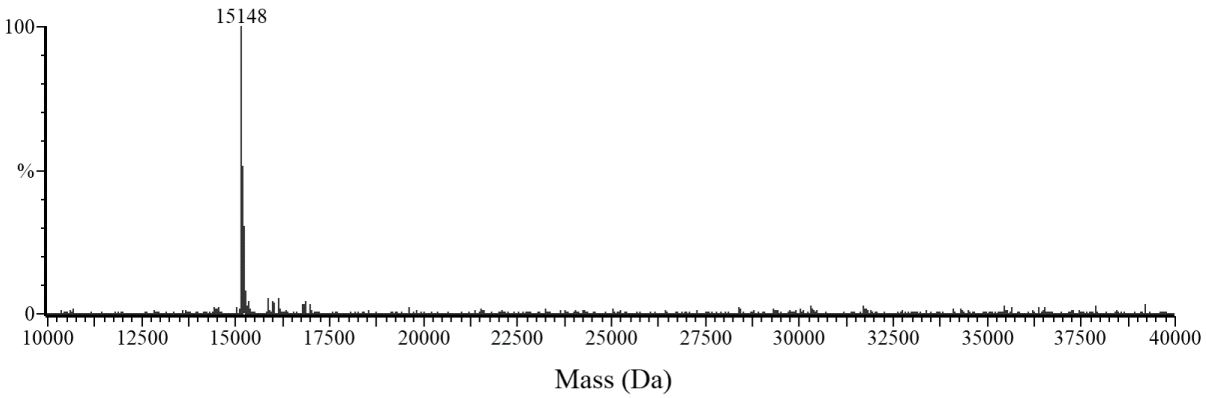

Figure 2.20. Mass-spectra of the A488 single labelling of αSyn N122C. The 15148 Da peak corresponds to the single-labelling of αSyn N122C (14449.19 Da) with A488-Maleimide (698.67 Da).

The LC-MS mass-spectra analysis indicated that the A488 labelling efficiency of αSyn N122C was essentially ~100%, due to the sample appearing to be devoid of unlabelled αSyn N122C. Purification with SEC was performed to remove the excess A488-Maleimide labelling reagent.

2.6.2 EvDesAb binding affinity characterisation

Binding affinity characterisation of the purified EvDesAbs with αSyn was carried out using MST with comparison to the measurements of the parental DesAbs. Conditions were optimised and the final concentration of αSyn-A488 used in all experiments was 50 nM. Abs were diluted 1:1 in a series covering concentrations of ~5 orders of magnitude. Binding equilibrium was achieved with 2-hour incubations of αSyn-A488 with different concentrations of EvDesAb, followed by MST binding measurements. Most of the sequenced EvDesAbs shown in Table 2.1 (Chapter 2.5.2) were characterised and the MST results of the three highest-affinity EvDesAbs found from each library are shown in Figure 2.21 and Figure 2.22.

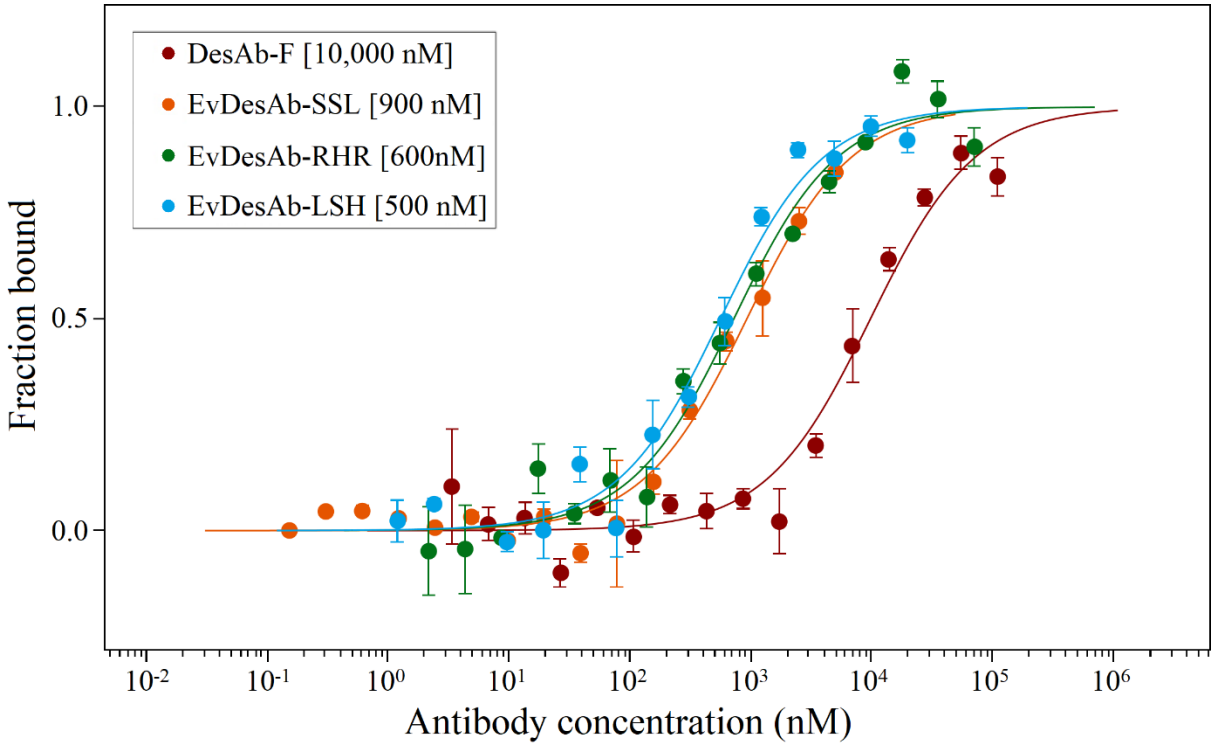

Figure 2.21. Normalised binding curves of DesAb-F and its three highest affinity EvDesAbs as measured by MST. DesAb-F (dark red) was measured by MST as having a K_D of 10 μM (cf. 18 μM from reference [176]). The binding curves of EvDesAb-SSL (orange), EvDesAb-RHR (green) and EvDesAb-LSH (blue) yielded K_D values of 900 nM, 600 nM and 500 nM respectively. Error bars represent the standard deviation from three independent experiments. The binding curves were normalised into bound/unbound fraction (*y*-axis) and were plotted against Ab concentration (*x*-axis). Binding curve fitting is described in Chapter 5.6.2.

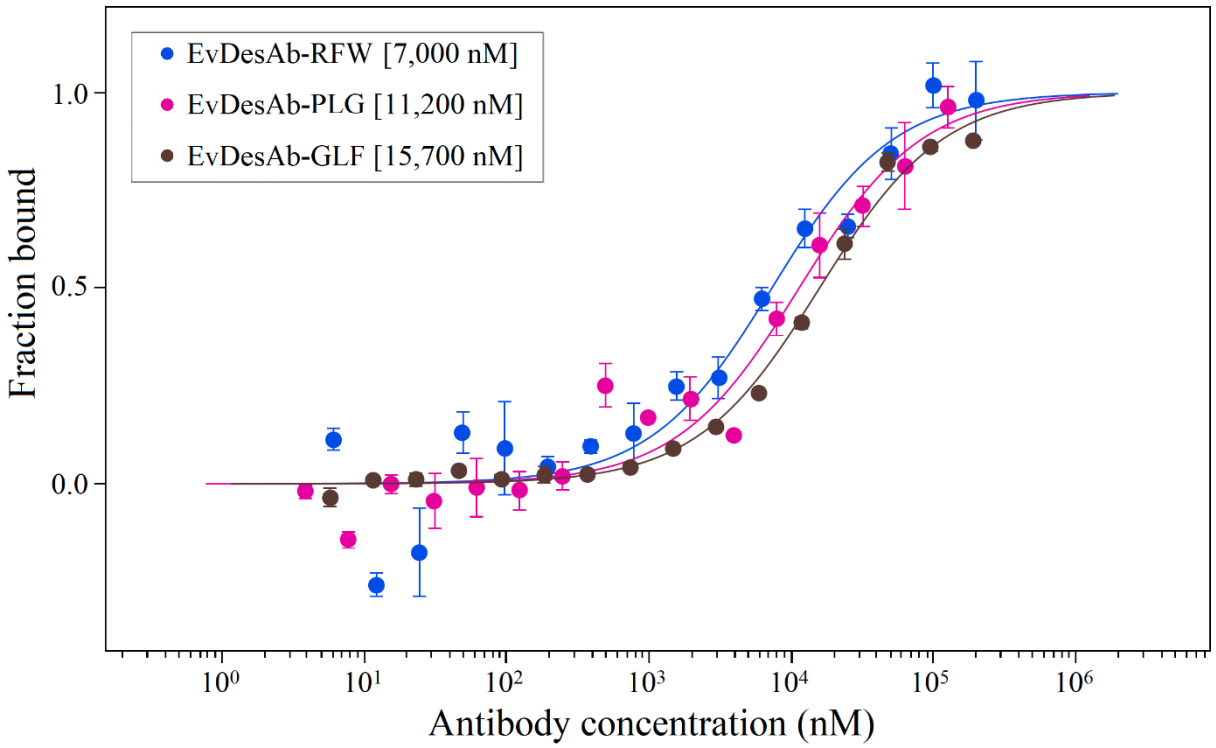

Figure 2.22. Normalised binding curves of the three highest affinity EvDesAbs found from DesAb-IAPP pLib as measured by MST. DesAb-IAPP is not shown for comparison as a binding signal could not be obtained and fitted due to the non-binding nature of this control. The binding curves of EvDesAb-GLF (dark brown), EvDesAb-PLG (pink) and EvDesAb-RFW (dark blue) yielded K_D values of 15,700 nM, 11,200 nM and 7,000 nM respectively. Error bars represent the standard deviation from three independent experiments. The binding curves were normalised into bound/unbound fraction (*y*-axis) and were plotted against Ab concentration (*x*-axis). Binding curve fitting is described in Chapter 5.6.2.

The binding affinities obtained from MST suggest that the crude-extract ELISA screen signals appear to be reliable for clonal selection. These results show that the affinity maturation strategy was successful in yielding EvDesAbs with improved binding affinities to αSyn with respect to their parental DesAbs. For DesAb-F, affinity maturation yielded a maximum αSyn affinity gain of ~20-fold (as measured by MST) and an average of ~10-fold. As was predicted in Chapter 2.1.2, the affinity gain is modest, but this was expected with such a small DNA library. The DesAb-IAPP library yielded EvDesAbs with weaker binding affinities, comparable to the initial affinity of DesAb-F. This was also expected as they did not have the αSyn specificity-directing designed CDR3 loop to assist with binding and their binding affinities may indicate the potential binding contribution of the CDR2 loop in the DesAb-F EvDesAbs. This assumption cannot be relied upon however, as the residue types are significantly different between the libraries and the binding orientation of the CDR2 loops is, at this point, unknown. In order to characterise whether the improved-affinity DesAb-F mutants

had retained their original epitope, their αSyn-WT MST binding curves would be compared to their binding to an αSyn mutant with a disrupted epitope caused by a Proline insertion at position 73 (αSyn 73P). When inserted into the centre of a protein secondary structure, Proline disfavours its formation and as the complementary-sequence CDR3 loop graft was designed to form an antiparallel β-sheet-like interaction, the insertion of a Proline into the target epitope sufficiently inhibits the binding of DesAb-F to αSyn[176, 256]. If the MST-measured αSyn binding affinities were inhibited by the Proline-insertion, then it could be concluded that EvDesAb binding was still taking place in the 70-77 sequence that they were originally designed to bind.

2.6.3 α-Synuclein 73P construction and single-labelling with Alexa488

αSyn 73P also required A488 single-labelling to be used as the fluorescent ligand for MST and therefore it was mutated from αSyn N122C. The Proline-insertion was created by a single site-directed mutagenic inverse-PCR of the αSyn N122C gene. The result of the mutagenesis is shown in Figure 2.23.

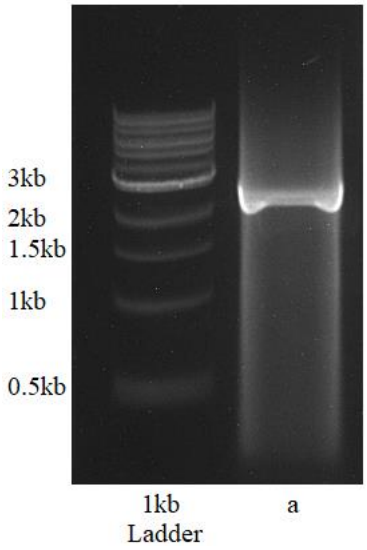

Figure 2.23. Agarose gel electrophoresis of the PCR product of the 73P insertion mutagenesis of αSyn N122C. a) 73P insertion PCR product. Inverse-PCR amplifies the entire plasmid (αSyn 73P+N122C in pT7-7 ~ 2.9 kb).

The 73P insertion was confirmed by DNA sequencing and αSyn 73P+N122C was purified using the standard Cysteine-containing αSyn purification protocol (described in Chapter 5.3.1). The results of the purification are shown in Figure 2.24.

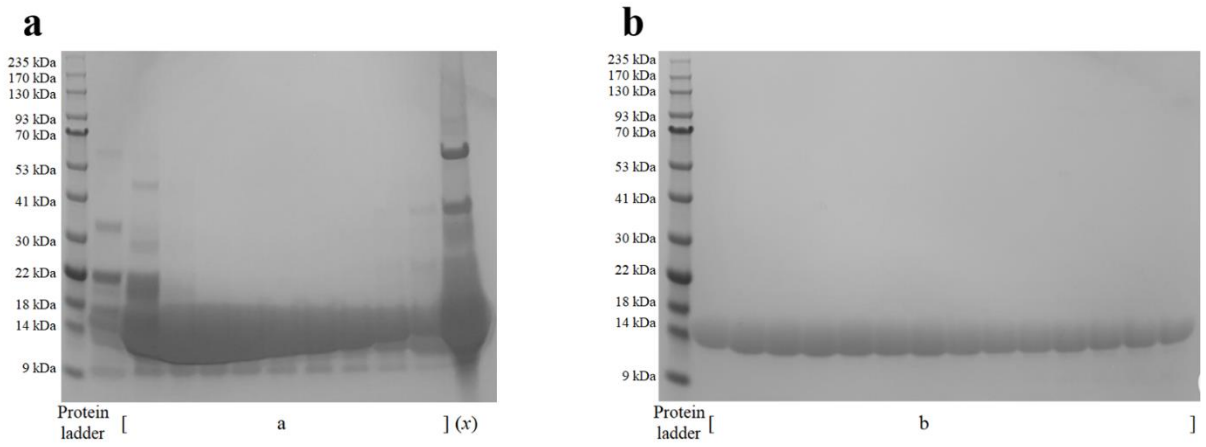

Figure 2.24. SDS-PAGE analysis of the purifications of αSyn 73P+N122C. a) IEC purification of αSyn 73P+N122C. b) SEC purification of αSyn 73P+N122C (~14 kDa). (*x*) Discarded pre-IEC sample of αSyn N122C.

A488 single labelling of αSyn 73P+N122C was performed and verified by liquid chromatography-mass spectroscopy (LC-MS). The resulting mass-spectra is shown in Figure 2.25.

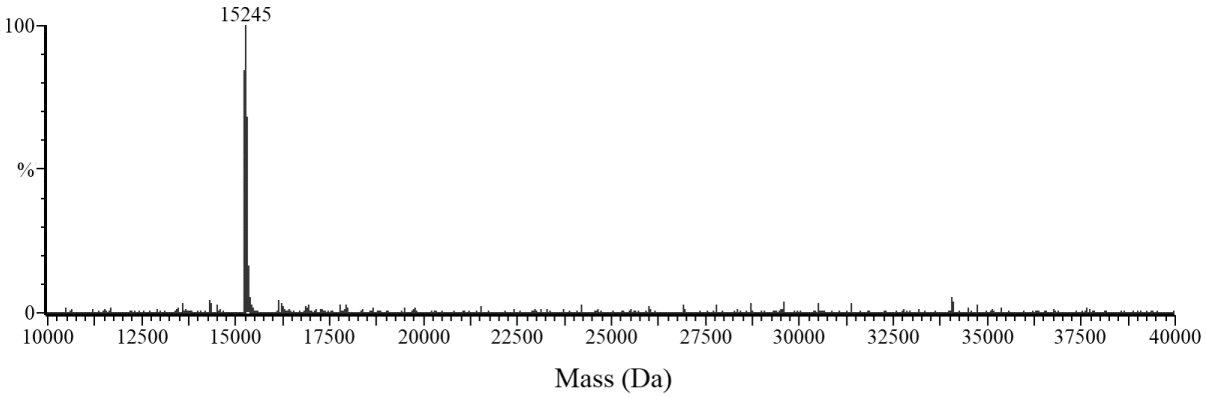

Figure 2.25. Mass-spectra of the A488 single labelling of αSyn 73P+N122C. The 15245 Da peak corresponds to the single-labelling of αSyn 73P+N122C (14546.31 Da) with A488-Maleimide (698.67 Da).

The LC-MS mass-spectra analysis indicated that the A488 labelling efficiency of αSyn 73P+N122C was essentially ~100%. Purification with SEC was performed to remove the excess A488-Maleimide labelling reagent.

2.6.4 EvDesAb epitope retention characterisation

Pre-selected epitope retention was performed using MST with the same optimised conditions as utilised for the binding affinity characterisations of the EvDesAbs against αSyn WT. Comparisons were made between the binding curves of the EvDesAbs against αSyn N122C A488 (αSyn-'WT') and αSyn 73P+N122C-A488 (αSyn-73P) as measured by MST. As the Proline-mediated binding disruption was previously only quantified by a competition assay for DesAb-F, it was important to confirm that the binding disruption of DesAb-F by αSyn 73P could also be observed in MST[176]. The binding curve comparison of DesAb-F against both αSyn-WT and αSyn-73P are shown in Figure 2.26.

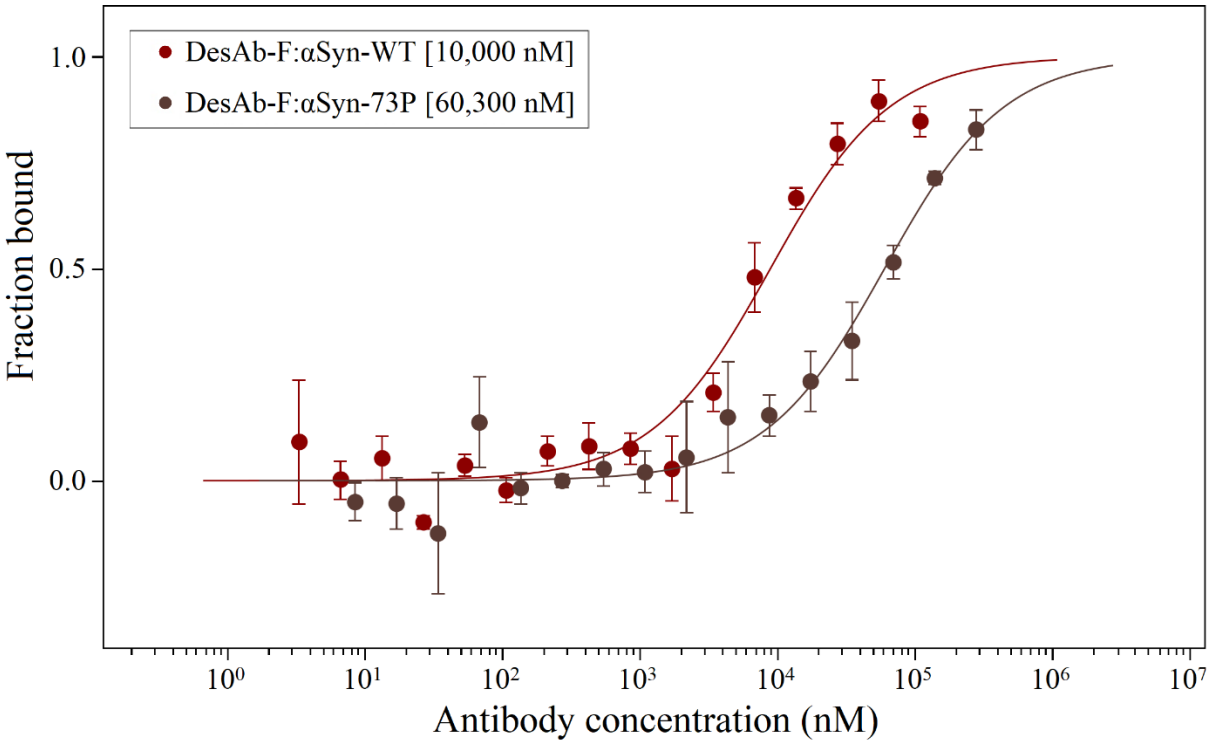

Figure 2.26. Normalised binding curves of DesAb-F to αSyn-WT and αSyn-73P, as measured by MST. The binding curves of DesAb-F to αSyn-WT (dark red) and αSyn-73P (dark brown), yielded K_D values of 10,000 nM and 60,300 nM, respectively. Error bars represent the standard deviation from three independent experiments. The binding curves were normalised into bound/unbound fraction (*y*-axis) and were plotted against Ab concentration (*x*-axis). Binding curve fitting is described in Chapter 5.6.2.

The MST results of DesAb-F binding comparison to both αSyn-WT and αSyn-73P show a large difference in affinity (~6-fold), indicating that MST is appropriate for characterising pre-selected epitope retention. Therefore, the characterised EvDesAbs of DesAb-F were also tested for αSyn-73P binding via MST to elucidate whether their epitopes had changed during affinity maturation. The MST results of EvDesAb-LSH, EvDesAb-RHR and EvDesAb-SSL binding to αSyn-WT and αSyn-73P are shown in Figure 2.27, Figure 2.28 and Figure 2.29 respectively.

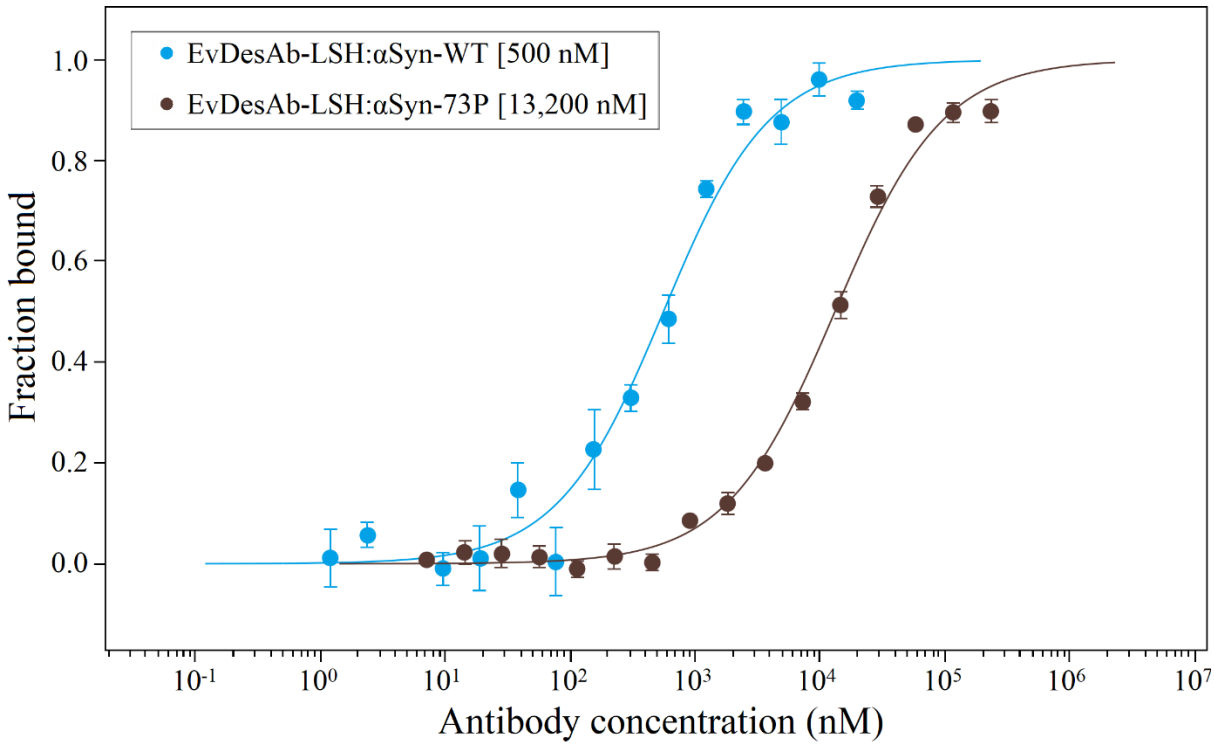

Figure 2.27. Normalised binding curves of EvDesAb-LSH to αSyn-WT and αSyn-73P, as measured by MST. The binding curves of EvDesAb-LSH to αSyn-WT (blue) and αSyn-73P (dark brown), yielded K_D values of 500 nM and 13,200 nM, respectively. Error bars represent the standard deviation from three independent experiments. The binding curves were normalised into bound/unbound fraction (*y*-axis) and were plotted against Ab concentration (*x*-axis). Binding curve fitting is described in Chapter 5.6.2.

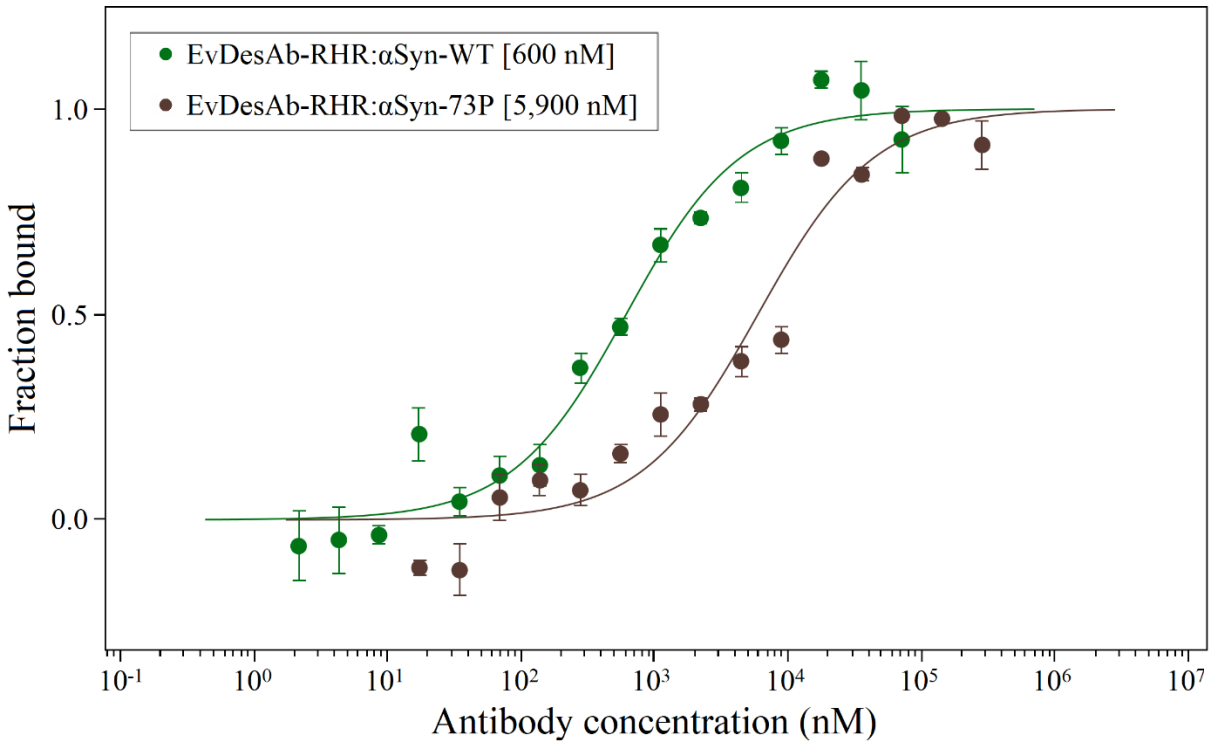

Figure 2.28. Normalised binding curves of EvDesAb-RHR to αSyn-WT and αSyn-73P, as measured by MST. The binding curves of EvDesAb-RHR to αSyn-WT (green) and αSyn-73P (dark brown), yielded K_D values of 600 nM and 5,900 nM, respectively. Error bars represent the standard deviation from three independent experiments. The binding curves were normalised into bound/unbound fraction (*y*-axis) and were plotted against Ab concentration (*x*-axis). Binding curve fitting is described in Chapter 5.6.2.

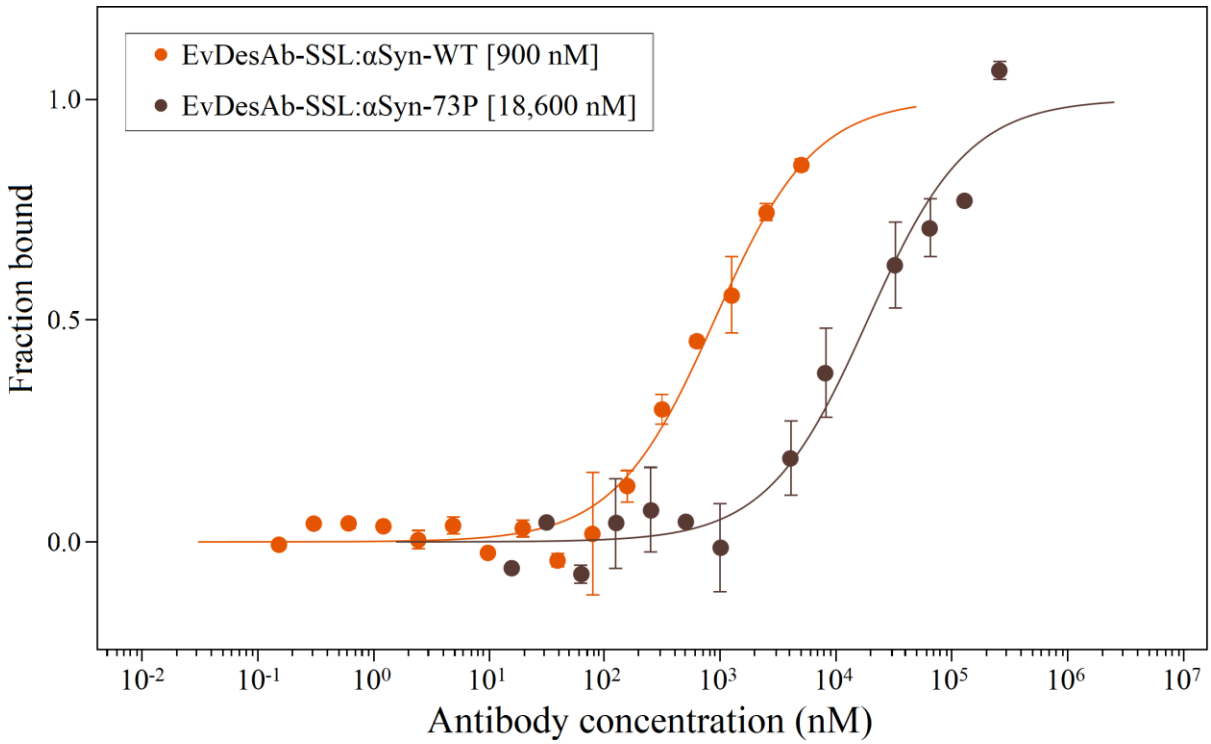

Figure 2.29. Normalised binding curves of EvDesAb-SSL to αSyn-WT and αSyn-73P, as measured by MST. The binding curves of EvDesAb-SSL to αSyn-WT (orange) and αSyn-73P (dark brown), yielded K_D values of 900 nM and 18,600 nM, respectively. Error bars represent the standard deviation from three independent experiments. The binding curves were normalised into bound/unbound fraction (*y*-axis) and were plotted against Ab concentration (*x*-axis). Binding curve fitting is described in Chapter 5.6.2.

The MST binding curves of EvDesAb-LSH, EvDesAb-RHR and EvDesAb-SSL all showed clear inhibition in the presence of the Proline-disrupted epitope, indicating that the pre-selected 70-77 epitope was likely retained for these clones. The difference in affinity is more pronounced than for DesAb-F (~6-fold) with EvDesAb-RHR showing ~10-fold, EvDesAb-SSL showing ~20-fold and EvDesAb-LSH showing ~26-fold lower affinity for αSyn-73P than αSyn-WT. There was concern that randomising a second loop may yield EvDesAbs that bind two or more distant epitopes simultaneously (one with each loop) due to the highly flexible nature of the αSyn disordered sequence. In this case Proline-disruption could simply inhibit the binding of designed CDR3 loop, resulting in a lower perceived affinity due to only the CDR2 loop binding another epitope. However, in this case one might expect a smaller, not larger, decrease in binding affinity than for DesAb-F.

2.7 Results: Stability characterisation by circular dichroism spectroscopy

2.7.1 Evolved designed antibody structure characterisation

It is important to evaluate the impact of protein evolution on the secondary structure content and stability of Abs yielded by affinity maturation, as altering the structure through mutation frequently impacts other biophysical characteristics in a trade-off[36, 257-259]. In this thesis, circular dichroism (CD) was chosen for EvDesAb secondary structure and stability characterisation as it provides the fraction of secondary structures of proteins, making it relatively easy to identify any changes in conformation[260, 261]. To characterise any changes in EvDesAb secondary structure, the CD spectra was recorded between 200-250 nm for each EvDesAb and its parental DesAb for comparison. The analysis of the EvDesAb secondary structure comparisons are shown in Figure 2.30 and Figure 2.31.

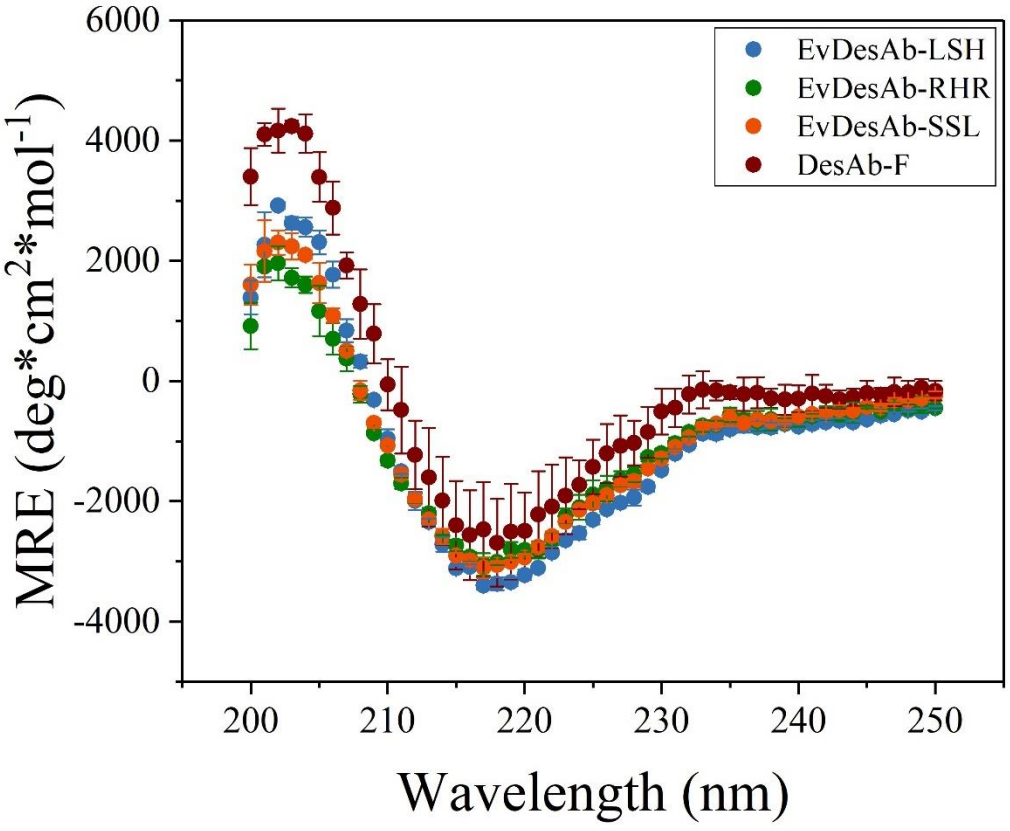

Figure 2.30. Analysis of DesAb-F and its EvDesAbs with highest binding affinity as measured by CD in the far-UV region. Secondary structure analysis for all Abs are in terms of mean residue ellipticity (MRE) at a given wavelength. DesAb-F (dark red), EvDesAb-LSH (blue), EvDesAb-RHR (green) and EvDesAb-SSL (orange) are shown for comparison. The data is shown as the mean average and error bars represent the standard deviation of three independent experiments.

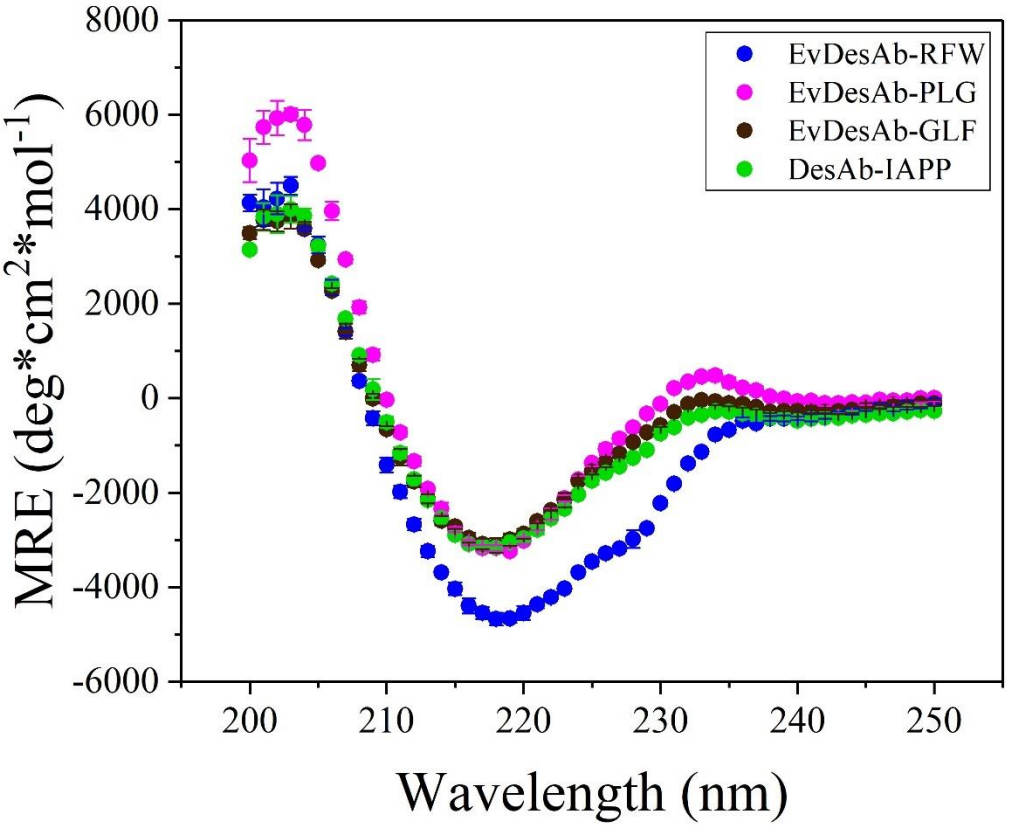

Figure 2.31. Analysis of DesAb-IAPP and its EvDesAbs with highest binding affinity as measured by CD in the far-UV region. Secondary structure analysis for all Abs are in terms of MRE at a given wavelength. DesAb-IAPP (green), EvDesAb-RFW (dark blue), EvDesAb-PLG (pink) and EvDesAb-GLF (dark brown) are shown for comparison. The data is shown as the mean average and error bars represent the standard deviation of three independent experiments.

The analyses of the EvDesAb CD spectra from both the DesAb-F and DesAb-IAPP libraries appear to generally show minimal change in the β-sheet content of the EvDesAbs with respect to their parental DesAbs, with the exception of EvDesAb-RFW which has a distorted MRE between 210-235 nm. This suggests that their folding and secondary structure content is largely the same, with possibly some conformational changes in the stem of the CDR2 loop and the loop itself. However, this information imparts no knowledge of the overall stability of the observed EvDesAb tertiary structures.

2.7.2 Evolved designed antibody stability characterisation.

CD was also used to assess the thermal stability of the EvDesAbs by following the MRE signal generated at 207 nm across a temperature gradient to determine the sdAb melting temperature (T_m). T_m for proteins is the midpoint temperature in which they completely unfold, which in

the case of Abs is the point in which the proportion of β-sheet content has half-converted to random coil, as measured by CD. 207 nm was selected as the followed wavelength as it is a good compromise between observing a large signal change, due to the transition between β-sheet and random coil, and avoiding high-noise generated by the large high-voltage (HV) values associated with measurements at smaller wavelengths. The melting temperature (T_m) is calculated as the mid-point between the folded and unfolded fractions by fitting the thermal denaturation curves to a two-state model, which is described in Chapter 5.7. The comparison of the thermal denaturation curves of DesAb-F and its EvDesAbs is shown in Figure 2.32 and their calculated melting temperatures (T_m) are shown in Table 2.2.

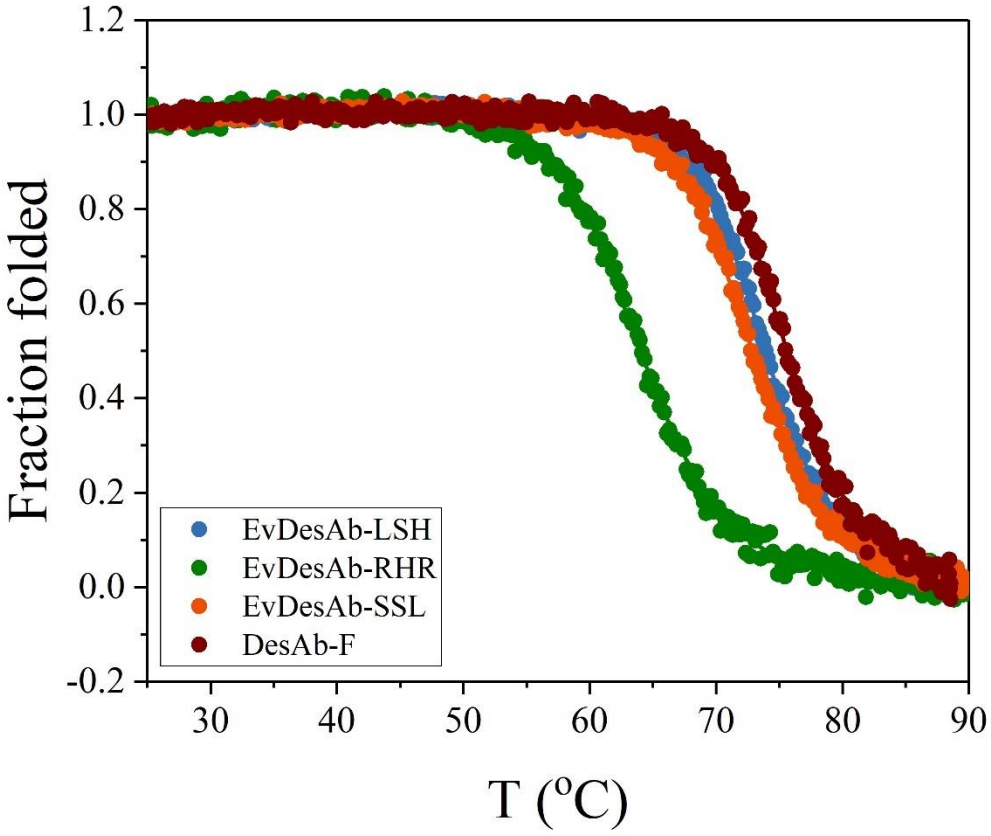

Figure 2.32. Comparison of the thermal denaturation curves of DesAb-F and its EvDesAbs as monitored in the far-UV region (207 nm) by CD. The thermal denaturation curves of DesAb-F (dark red), EvDesAb-LSH (blue), EvDesAb-RHR (green) and EvDesAb-SSL (orange) are shown as the folded fraction with their two-state model fittings. Values shown the mean averages of three independent experiments.

Table 2.2. Calculated melting temperatures (T_m) for DesAb-F and its EvDesAbs.

Antibody	T_m (°C)
DesAb-F	75.8 ± 0.2
EvDesAb-LSH	73.9 ± 0.1
EvDesAb-SSL	72.9 ± 0.1
EvDesAb-RHR	64.0 ± 0.1

The thermal denaturation curves for DesAb-F and its EvDesAbs showed a slight decrease in melting temperature for EvDesAb-LSH (1.9 ºC) and EvDesAb-SSL (2.9 ºC). A much larger decrease in melting temperature was observed for EvDesAb-RHR (11.8 ºC), indicating that its dense positively-charged CDR2 loop may have a largely destabilising effect on the sdAb framework. The comparison of the thermal denaturation curves of DesAb-IAPP and its EvDesAbs is shown in Figure 2.33 and their calculated melting temperatures (T_m) are shown in Table 2.3.

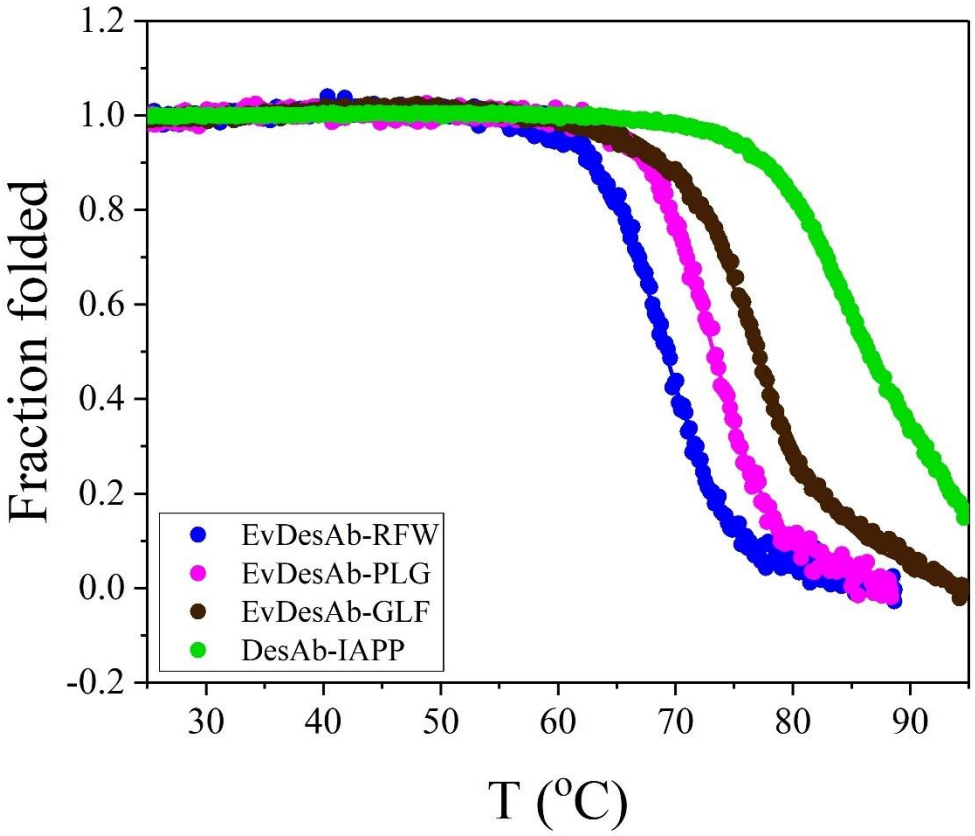

Figure 2.33. Comparison of the thermal denaturation curves of DesAb-IAPP and its EvDesAbs as monitored in the far-UV region (207 nm) by CD. The thermal denaturation curves of DesAb-IAPP (green), EvDesAb-RFW (dark blue), EvDesAb-PLG (pink) and EvDesAb-GLF (dark brown) are shown as the folded fraction with their two-state model fittings. Values shown the mean averages of three independent experiments.

Table 2.3. Calculated melting temperatures (T_m) for DesAb-IAPP and its EvDesAbs.

Antibody	T_m (ºC)
DesAb-IAPP	86.7 ± 0.4
EvDesAb-GLF	77.0 ± 0.2
EvDesAb-PLG	73.2 ± 0.1
EvDesAb-RFW	69.1 ± 0.1

The thermal denaturation curves for DesAb-IAPP and its EvDesAbs showed a larger average decrease in melting temperature for all EvDesAbs. The melting temperature for DesAb-IAPP is 10.9 ºC higher for DesAb-F, meaning that its EvDesAbs actually have comparable melting temperatures to the EvDesAbs of DesAb-F. Nevertheless, the consistently observed decrease in melting temperature implies that CDR2 loops with high hydrophobic content may also have a largely destabilising effect on the sdAb framework

2.8 Conclusion

In this chapter we explored the potential of combining rational design with affinity maturation by directed evolution to demonstrate if DesAbs yielded by Modular are suitable for immediate development via lead optimisation strategies employed during typical Ab discovery. The steps taken were modelled as close as possible to standard *in vitro* Ab affinity maturation, with the only exception being the conservative approach to sequence randomisation in an attempt to minimise the risk of losing the pre-selected epitope. The work involved the successful generation of high-quality DNA libraries using a novel two-step inverse-PCR focussed mutagenesis to minimise thermodynamic amplification bias. It also involved the use of sdAb phage display affinity selection and an optimised crude-extract screen, with the use of three simultaneous ELISAs, to produce affinity and expression scoring for reliable clonal selection. The EvDesAbs selected by screening generally showed not only improved binding affinity, but also desirable expression, folding and stability characteristics. This is extremely desirable as when systematic development of Abs is required in lead development, the frequent trade-offs in biophysical characteristics frequently yields Abs with improved characteristics, at the cost of other critical traits[36, 257-259]. Most importantly, the pre-selected epitope was shown to be retained in the characterised DesAb-F EvDesAbs with the use of a Proline-disrupted epitope in MST. This indicates that Modular is a suitable alternative for Ab discovery, especially when targeting disordered and poorly-immunogenic linear epitopes. This study also vindicates the conservative approach to CDR diversification and opens up the potential for further affinity maturation with the use of more intensive diversification and larger libraries. This would be desirable as, whilst this work improved the binding affinity of DesAb-F to the nanomolar range, Abs typically require low-nanomolar binding affinities or greater for therapeutic and diagnostic applications. Next, we sought to apply some of the optimised procedures to identify Abs with

improvements in desired activity through modulating their specificity towards the microscopic steps involved in protein aggregation.

Chapter 3: Selectivity development of rationally designed antibodies targeting aggregation inhibition

3.1 Introduction

3.1.1 Towards antibody activity selection

As mentioned in Chapter 1.3.2, the failures of recent high-profile therapeutic Ab candidates have highlighted the need for an overhaul in the way that Abs are discovered and developed for therapy. For neurodegenerative diseases, focus has begun to shift away from traditional Ag-binding Ab discovery towards isolating leads with potent anti-aggregation properties, rather than simply high binding affinity[85, 104, 137]. The rationale behind this is partly to do with the failures of drugs targeting AD to elicit positive responses in patients already displaying severe symptoms of the disease and the indication that early treatment to prevent the formation of the most toxic aggregates may represent the best therapeutic strategy, given the current understanding of the disease[140-144]. With early diagnosis rapidly becoming a priority in neurodegenerative research, the need for accurate and sensitive diagnostics development is crucial. This may require the generation of exquisitely specific Abs that can identify the early signs of toxic aggregate accumulation whilst being minimally cross-reactive with the soluble monomeric proteins. The same requirement may be essential for preventative therapy, targeting the generation of only the most toxic species whilst interfering as little as possible with the monomers, the functions of some are still poorly understood[114].

The creation of toxic oligomer-specific Abs has remained challenging in therapeutic Ab development due to the heterogeneity of oligomeric conformations, resulting in a requirement of conformation specificity rather than sequence specificity, although this requirement is still widely debated[61, 262]. For example, a camelid nanobody called KW1 was discovered in a study using a synthetic naïve library which was found to have tantalising specificity for certain $A\beta_{40}$ oligomers and displayed negligible binding to monomers and fibrils[133]. Further studies revealed that not only was KW1 binding to the hydrophobic core of certain conformations of oligomers with hydrophobic CDR loops and this conformational specificity prevented KW1 from binding any forms of $A\beta_{42}$ oligomers, but it also increased their *in vivo* toxicity[263].

Another study generated multiple Abs through immunisation using different types of oligomeric forms of $A\beta_{42}$, however whilst some Abs were more specific towards some aggregated species than others, none were found to bind only the oligomeric forms[134]. Abs have recently been described that are both sequence and conformation-specific in the study mentioned in Chapter 1.4.2, where regions of $A\beta_{42}$, grafted into the CDR3 loops of sdAbs, directed the sequence specificity towards linear epitopes in $A\beta_{42}$ and some were completely specific to the conformations of these epitopes in amyloid fibrils of $A\beta_{42}$. However, none of the Abs produced in the study by Perchiacca and co-workers could recognise conformational epitopes present in only oligomeric species[182]. The lengthy Ab discovery process coupled with the unreliable selection of conformation-specific Abs using oligomers as targets in immunisation or affinity selection suggests that generating and screening therapeutic Abs for the specific aggregation inhibition of toxic-oligomers may be a better alternative.

3.1.2 Chapter aims

The aims of the work described in this Chapter were to engineer $A\beta_{42}$ binding Abs into selective inhibitors of surface-catalysed aggregation and in the process, potentially generate Abs with greater selectivity for oligomeric forms of $A\beta_{42}$. The sequence scanning DesAbs produced using Modular against $A\beta_{42}$ provided a valuable starting point for altering aggregation inhibition characteristics because their effects on the microscopic nucleation steps of $A\beta_{42}$ aggregation were known[104]. The recently established 'kinetic selection' of Abs would be employed to identify variants with altered ratios of primary nucleation (k_n) and surface-catalysed secondary nucleation (k_2) inhibition[85, 137]. The primary objective was to select Abs with significantly improved ratios of k_2:k_n as our reasoning was that, by reducing k_n inhibition, oligomer formation inhibiting Abs with lower cross-reactivities towards $A\beta_{42}$ monomers should be isolated. To achieve this, directed evolution and selection by phage display was used again to maximise the protein-engineering potential with the use of vast numbers of mutants. In order to achieve the increased discrepancy between k_2 and k_n, it was hypothesised that affinity selection could be used to improve or retain an Ab's K_D towards $A\beta_{42}$ oligomers whilst significantly weakening its K_D towards $A\beta_{42}$ monomers. The selection strategy used was inspired by the competitive selection used in the generation of KW1, whereby oligomer-selective Ab-displaying phage are selected with the use of biotinylated Aβ oligomers and unlabelled Aβ monomer is then added to act as 'bait' for the binding of Abs with strong K_D for

the monomer[133]. As the monomer is unlabelled, Ab-displaying phage bound in complex to the monomer are removed via washing and the library is enriched for Abs with strong oligomer-binding K_D and weak monomer-binding K_D. This selection strategy is illustrated in Figure 3.1.

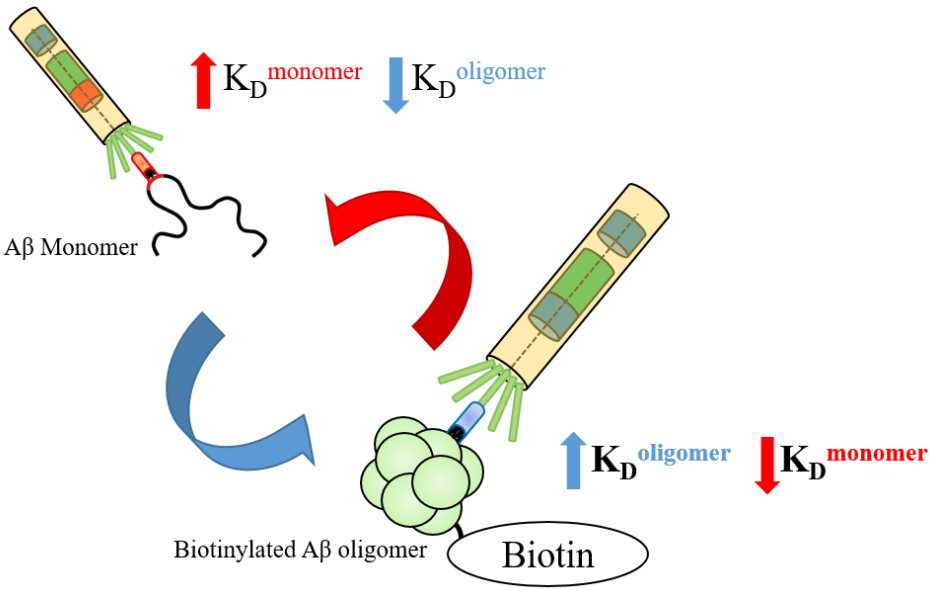

Figure 3.1. Schematic of competitive affinity selection to alter the selectivity of Abs towards different aggregate species of Aβ. Ab-displaying phage are incubated with biotinylated Aβ oligomers and then Aβ monomer is added as a binding competitor. Abs with strong K_D for oligomeric species (blue) are selected using the biotin-Avidin system when in complex with the biotinylated Aβ oligomers after washing. Abs with weak Aβ oligomer-binding K_D and those with strong monomer-binding K_D (red) are removed with stringent washing.

As mentioned in Chapter 1.5.3, the DesAbs selected for selectivity evolution were $DesAb_{3\text{-}9}$ and $DesAb_{29\text{-}36}$ due to their already significant secondary nucleation inhibition and oligomer generation reduction. Unlike the evolution of DesAb-F, which involved increasing the affinity towards a desired specific sequence, the goal of this work was to increase the complexity with which $DesAb_{3\text{-}9}$ and $DesAb_{29\text{-}36}$ interact with their target epitopes, in the hope that the increased contribution of epitope conformation would drive selection away from the intrinsically disordered Aβ monomer. A challenging feature of this selection was that, whilst unlabelled Aβ fibrils could have also been used as a binding competitor to drive oligomer specificity, fibril lateral surfaces are also significant secondary nucleation sites and removing fibril-binding Abs may also deplete a large proportion of secondary nucleation-inhibiting variants in the libraries. Therefore, fibrils would not be used as competitor and the risk of obtaining many fibril cross-reactive Abs would have to be accepted.

As the objective of this work was the directed evolution of the complexity of the epitope interaction, rather than absolute binding affinity, the DNA library generation strategy was designed more towards changing the orientation and presentation of the specificity-directing grafted CDR3 loop. This would hopefully yield Abs that complement conformational epitopes of the same sequence, rather than the disordered epitopes they were designed to bind. Significantly changing the orientation and presentation of the CDR loops is more readily achieved through mutations to the V_H framework, rather than focussed mutations to the CDR loops themselves[264, 265]. Knowing which framework regions to mutate for this purpose is extremely challenging, however these regions or 'hotspots' can be identified through whole-protein scanning mutagenesis[198]. The method chosen to identify and mutate these hotspots was ep-PCR, which has been shown to be successful in altering CDR loop presentation to enhance and stabilise Ab-Ag interactions[266]. The evolution strategy is shown in Figure 3.2.

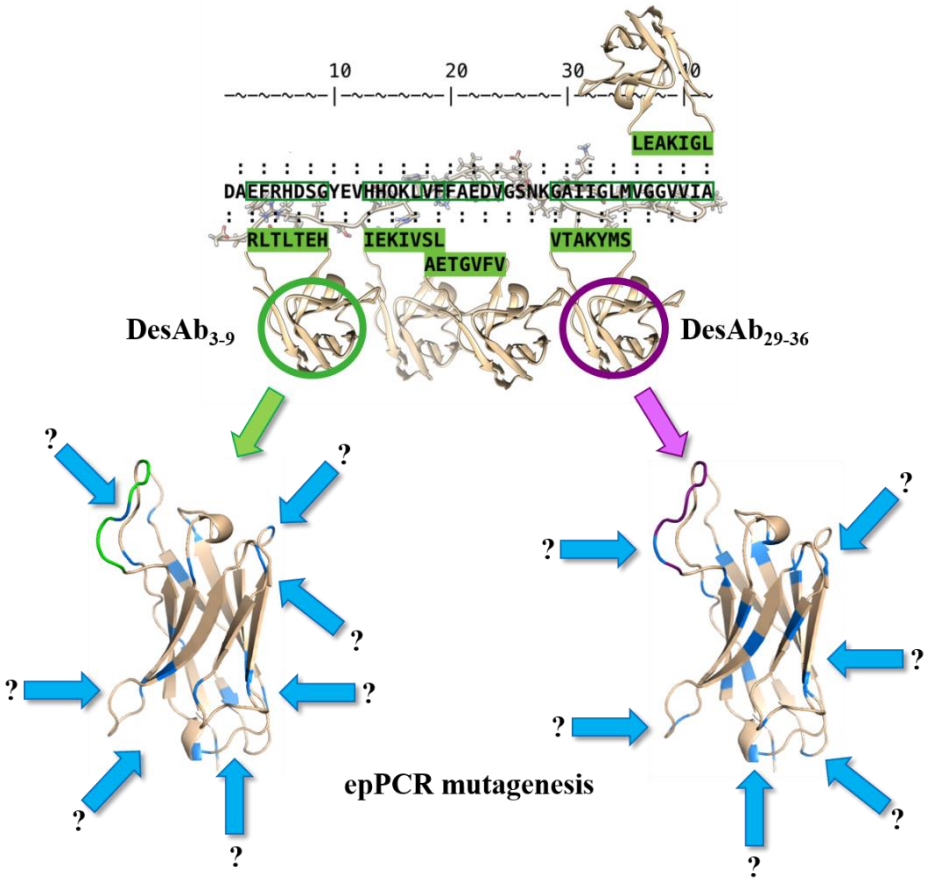

Figure 3.2. Structure of the proposed DesAb$_{3-9}$ and DesAb$_{29-36}$ ep-PCR diversification. The Aβ N-terminal binding DesAb$_{3-9}$ (green) and C-terminal binding DesAb$_{29-36}$ (purple) were selected for selectivity evolution. ep-PCR introduces random mutations at random locations of a protein (blue). The structure is that of DesAb-F and was provided by P. Sormanni and F. A. Aprile and produced using PyMOL (PyMOL, Molecular Graphics System, Version 2.2.0, Schrödinger, LLC).

3.2 Results: Whole protein scanning mutagenesis using error-prone PCR

3.2.1 DesAb-F CDR3 replacement for changing target antigen

For $DesAb_{3\text{-}9}$ and $DesAb_{29\text{-}36}$ insertion into pMESy4 for DNA library construction and phage display, it was deemed simpler to use the already constructed pMESy4+DesAb-F-gIII and replace the designed CDR3 loop (N-FQEAVSG-C) with those of $DesAb_{3\text{-}9}$ (N-HETLTLR-C) and $DesAb_{29\text{-}36}$ (N-GSMYKATV-C). This would remove the requirement of inserting SpeI into the $DesAb_{3\text{-}9}$ and $DesAb_{29\text{-}36}$ genes and the use of restriction digestion. Once again, inverse-PCR was used to replace the designed CDR3 loops with adjacent 5'-phosphorylated oligonucleotides, each with overhangs containing half of the sequence to be substituted. The use of inverse-PCR allowed the mutagenesis and construct generation to be performed in a single step for immediate DNA library generation. The result of the CDR3 replacement is shown in Figure 3.3.

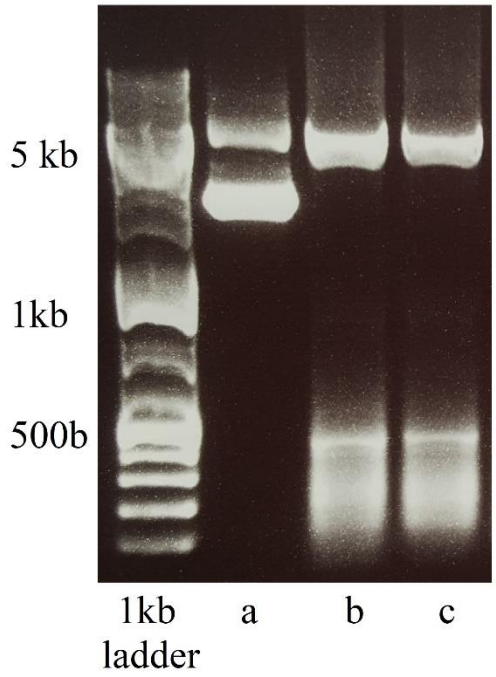

Figure 3.3. Agarose gel electrophoresis of the separate CDR3 replacement of pMESy4+DesAb-F-gIII with the CDR3 loops of $DesAb_{3\text{-}9}$ and $DesAb_{29\text{-}36}$. a) unmodified pMESy4+DesAb-F-gIII for comparison. b) pMESy4+$DesAb_{3\text{-}9}$-gIII. c) pMESy4+$DesAb_{29\text{-}36}$-gIII. The GeneRuler^{TM} 1 kb Plus DNA Ladder did not migrate smoothly, however the sizes were correct (~5.5 kb for pMESy4+$DesAb_{3\text{-}9}$-gIII and pMESy4+$DesAb_{29\text{-}36}$-gIII).

The CDR3-replaced $DesAb_{3\text{-}9}$ and $DesAb_{29\text{-}36}$-containing phagemids were gel-extraction purified, self-circularised, amplified in XL10-gold *E. coli* and their sequences were confirmed.

3.2.2 Error-prone PCR DNA library construction

As ep-PCR was selected for the generation of the $DesAb_{3-9}$ and $DesAb_{29-36}$ framework region diversification, care needed to be taken to ensure high-quality DNA libraries were produced. Unlike focussed mutagenesis, explored in Chapter 2, eliminating the 'wild-type' DesAb sequence from the resulting library using frameshifts or premature stop codons is not realistically feasible. If used, random mutagenesis would have to restore the reading frame or substitute the premature stop codon by complete chance and the resulting small proportion of functional mutants would heavily restrict the DNA library diversity. Instead, generating libraries with some level of 'wild-type' contamination would have to be accepted. This level can be minimised with careful design, optimisation and also the inherent nature of ep-PCR. Mutation frequency, i.e. the number of mutations per mutated clone, can be controlled by both the initial amount of 'wild-type' DesAb sequence used as template, and also the number of amplification cycles. Decreasing the concentration of 'wild-type' DesAb sequence template and increasing the number of cycles results in an increased mutation frequency[245]. Increasing the mutation frequency decreases the level of 'wild-type' sequence contamination as ep-PCR DNA library mutations follow a Poisson distribution[267]. Increasing the mutation frequency is also desired to decrease the proportion of silently mutated 'wild type' sequences that arise due to codon redundancy.

Along with codon bias, ep-PCR comes with its own unique biases; error bias and amplification bias. Error bias is the result of uneven nucleotide substitution rates and these are unique to the types of non-proofreading DNA polymerase used. By using specialised mixtures of DNA polymerases with different nucleotide substitution rates, the error biases of each DNA polymerase on the resulting ep-PCR can be mitigated to a large extent. The GeneMorph II random mutagenesis kit (Stratagene) was used for the $DesAb_{3-9}$ and $DesAb_{29-36}$ ep-PCRs to reduce mutation bias, which is an optimised mixture of different *Taq* DNA polymerase variants with opposite mutational spectra[268]. Amplification bias is the result of mutations accumulating from early cycles of PCR amplification, which can become highly prevalent in comparison with mutations introduced in later cycles due to the PCR products in early rounds acting as templates for further amplification. This can be problematic for framework mutation hotspot-analysis because it can be challenging to identify which mutations are genuinely conserved between improved mutants and which are the result of amplification bias[245]. In practice however, when considering a number of template molecules such as 10^9, the number of

amplification biases from the first cycle of PCR would be ~1 in 10^9 which may be undetectable in libraries produced using ligation and bacterial transformation as these result in diversity bottlenecks and are typically smaller than 10^9 in sequence diversity[269].

The genetic region mutated by ep-PCR is defined by the amplified sequence between the PCR primers and for these libraries the primers were designed to include the entire DesAb V_H framework region (E1-S124) in the amplified sequence. As this was a standard PCR amplification of only the $DesAb_{3-9}$ and $DesAb_{29-36}$ genes, subsequent re-cloning into a freshly NcoI and KpnI-digested pMESy4+DesAb-gIII phagemid was required. The DesAb V_H framework region is flanked by two restriction sites; an upstream NcoI (as used in Chapter 2) and a downstream KpnI (5'-GGTACC-3') and each was incorporated into the PCR primers. ~6-19 bases were left beyond the restriction sites, to allow space for the restriction enzymes to attach to the DNA. The ep-PCR design strategy is illustrated in Figure 3.4.

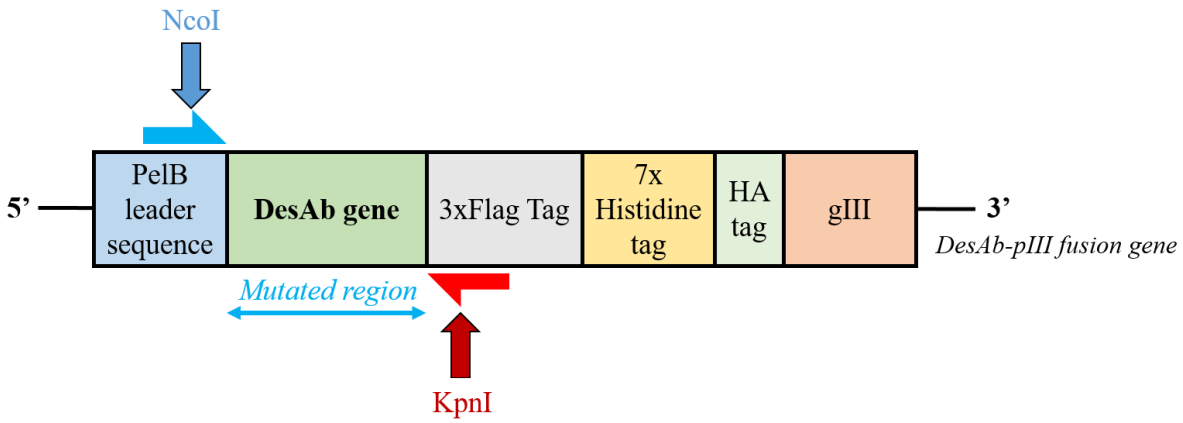

Figure 3.4. Design for the diversification of $DesAb_{3-9}$ and $DesAb_{29-36}$ using ep-PCR. Genes and oligonucleotides are not drawn to scale. The region randomly mutated by ep-PCR (blue double arrow) was defined by the sequence between the forward (blue half arrow) and reverse (red half arrow) PCR primers. These also contained the unique restriction sites, NcoI and KpnI, for subsequent re-cloning into freshly NcoI and KpnI-digested pMESy4+DesAb-gIII phagemids.

The conditions for the ep-PCR diversification of the $DesAb_{3-9}$ and $DesAb_{29-36}$ genes were optimised to yield the desired mutation spectra (described in Chapter 3.2.3) and the full DNA library construction was performed with identical conditions for both $DesAb_{3-9}$ and $DesAb_{29-36}$. The results of the separate ep-PCRs of the $DesAb_{3-9}$ and $DesAb_{29-36}$ genes are shown in Figure 3.5.

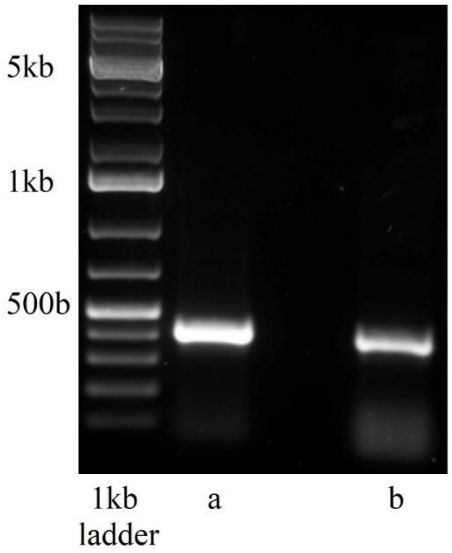

Figure 3.5. Agarose gel electrophoresis of the ep-PCR DNA libraries of DesAb$_{3-9}$ and DesAb$_{29-36}$. a) DesAb$_{29-36}$ ep-PCR product. b) DesAb$_{3-9}$ ep-PCR product. There were two small impurities (~100 b) present in both libraries, however gel-extraction purification was performed to remove them prior to restriction digestion and ligation. The sizes of both DesAb ep-PCR products were correct (~400 b).

Both DNA libraries were constructed, purified successfully by gel-extraction and were ligated into NcoI and KpnI-digested pMESy4+DesAb-gIII in yields suitable for bacterial library construction (~1 μg/DNA library).

3.2.3 Bacterial library generation and error-prone PCR mutation frequency analysis

As the number of mutations introduced by ep-PCR into each variant is mostly random, the 99% confidence calculation (introduced in Chapter 2.2.4) for sampling the majority of the library was not applicable. Assuming a mutation rate of 3 for the DesAb gene (124 AA), one would need to obtain at least $1.8x10^7$ transformants to even have a chance of covering the entire diversity, if codon bias was to be ignored completely. In reality, samplable ep-PCR DNA library coverage is tiny in comparison to theoretical diversity due to codon bias. Therefore, to sample the largest amount of DNA library diversity as possible, TG$_1$ electroporation was scaled up 10-fold. DNA library transformation of TG$_1$ *E. coli* by electroporation was performed, which resulted in ~$1.5x10^7$ colonies for each library. 50 colonies were picked (25 from each library) as representative samples and their DNA was amplified using colony-PCR and submitted for Sanger sequencing. The average nucleotide and AA mutation frequencies are analysed in Figure 3.6.

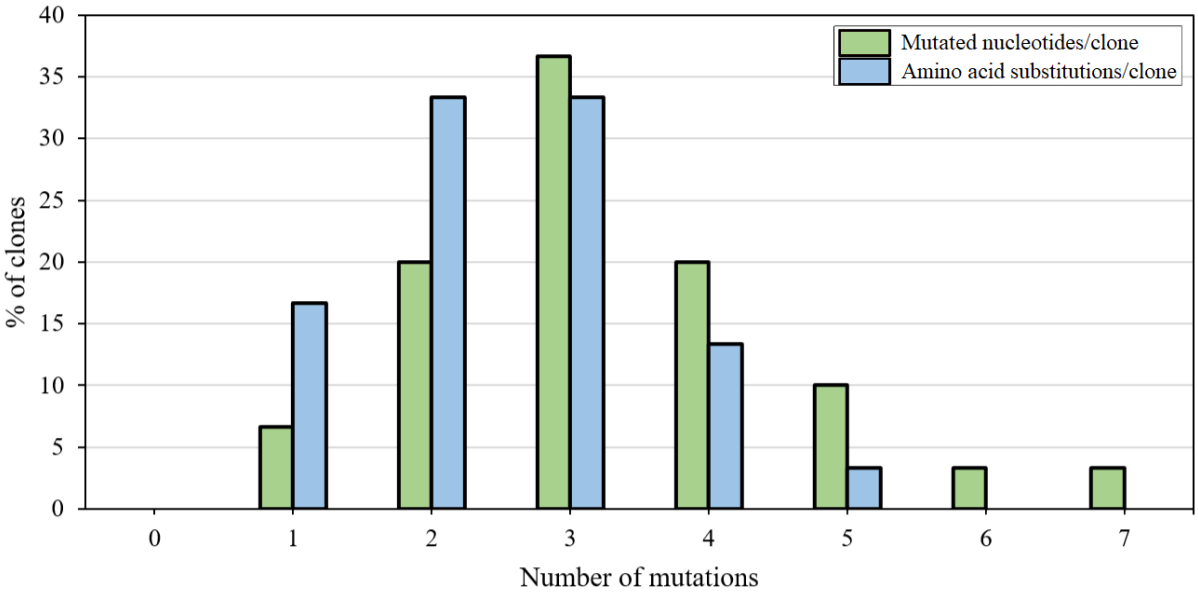

Figure 3.6. DesAb$_{3-9}$ pLib and DesAb$_{29-36}$ pLib ep-PCR mutation frequency analysis. The DNA sequences of the 50 representative library clones were analysed and the number of mutated nucleotides (green) per clone was compared with the number of AA substitutions (blue) per clone to yield the average mutation frequency in terms of the percentage of sequenced clones. Both nucleotide and AA mutations follow a Poisson distribution and the discrepancy between the two distributions is the result of silent mutations, whereby nucleotide mutations result in different codons for the same AA. No clones were found with no nucleotide or AA mutations ('wild-type' sequence).

Once again, the sampled library diversity was modest in comparison to the theoretical diversity, however it was encouraging that the 'wild-type' DesAb$_{3-9}$ and DesAb$_{29-36}$ sequences were not observed. Of the 50 clones sampled, only 30 contained functional genes as the remaining 20 showed evidence of premature stop codons and frameshifts. This placed further restriction on the diversity of the bacterial libraries as only 60% of the library was predicted to be functional. These clones with premature stop codons and frameshifts would be removed during phage display due to the lack of pIII expression (excluding those with TAG amber stop codons). The ep-PCR library mutation frequency observed was as expected with a Poisson distribution for both nucleotide and AA substitutions, and a higher average nucleotide substitution rate than AA substitution rate due to silent mutations. The average AA mutation frequency was 2-3 residues per clone, which was targeted in the ep-PCR optimisation to reduce the levels of 'wild-type' sequence contamination. Due to the predicted 40% loss of functional clones, the resulting bacterial library diversity was estimated to be $9x10^6$ which was certainly not enough to sample the entire ep-PCR DNA library diversities. Nevertheless, the DesAb$_{3-9}$ and DesAb$_{29-36}$ TG$_1$ libraries were deemed of sufficient size and quality for affinity selection by phage display. Due

to the identical phagemid sequence construction, as that described in Chapter 2, confirmation of DesAb display with Protein A was not believed to be necessary.

3.3 Results: Experimental preparation for phage display

3.3.1 $A\beta_{40}$ labelling with biotin (NHS-ester)

As Aβ oligomers were to be used for affinity selection in solution, they would require biotinylation prior to use. Different strategies were possible and all were considered as they each have advantages and disadvantages. Biotin labelling could take place before or after the formation of oligomers and could be achieved via specific labelling via a mutated Cysteine residue (such as that explored in Chapter 2.3.1) or non-specific labelling of the Lysine residues. As the formation of aggregate species was required, introducing a Cysteine into Aβ was not desirable in case the mutation had a significant effect on the morphology of the generated oligomers. Therefore, Lysine labelling using (+)-Biotin N-hydroxysuccinimide ester was chosen for this purpose. There are two Lysines present in Aβ (K16, K28), and there would be effectively no control over which would be labelled. Neither position is in the epitopes of the two DesAbs, however K28 neighbours the epitope of $DesAb_{29\text{-}36}$ so some steric hindrance may be expected. The level of labelling was an important consideration as well as it was believed that the biotin labels on the surface were potentially significant sources of steric hindrance. Labelling the oligomers post-formation would create two problems; the first would be the lack of control of labelling and the result would almost certainly be oligomers with high degrees of labelling; the second was the requirement for the removal of excess (+)-Biotin N-hydroxysuccinimide ester as its presence would interfere with the Avidin capturing of the phage-DesAb-oligomer complexes. This additional purification step following the Aβ oligomer formation was undesirable due to the short-lived nature of Aβ oligomers. Therefore, labelling of the monomer was selected and it would have to be used to form the Aβ oligomers, however the oligomers would not have to be formed entirely from labelled monomer as only one biotin molecule is required to capture the phage-DesAb-oligomer complex. It was decided that oligomers would be formed from a 1:10 molar ratio of biotinylated Aβ monomer to unlabelled Aβ monomers.

It was decided that $A\beta_{40}$ would be used to generate the oligomers, rather than $A\beta_{42}$. This was because the aggregation of $A\beta_{42}$ is too rapid for the timescale in which competitive affinity selection was to be employed. Another benefit to the use of $A\beta_{40}$ is that its oligomers can be stabilised during aggregations in the presence of Zn^{2+} in much higher yields than those of $A\beta_{42}$. Zn^{2+} enhances the aggregation of Aβ and kinetically traps the intermediate species before they can form amyloid fibrils[270]. Labelling was performed and was successfully verified by LC-MS. The mass-spectra is shown in Figure 3.7. $A\beta_{40}$ was provided as the recombinantly expressed variant, containing an additional N-terminal Methionine, by the Centre for Misfolding Diseases (CMD), University of Cambridge.

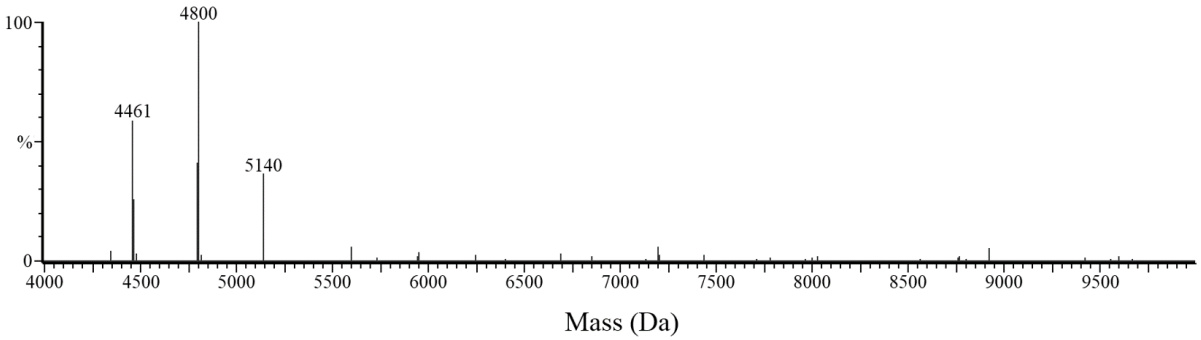

Figure 3.7. Mass-spectra of the biotinylation of Aβ40. 4 species were produced as a result of Biotin-labelling of $A\beta_{40}$ and these fell under 3 distinct molecular weights. 4461 Da corresponds to unlabelled $A\beta_{40}$ (4461.05 Da), 4800 Da corresponds to singly-labelled $A\beta_{40}$ (at either K16 or K28) and 5140 Da corresponds to labelling at both K16 and K28. The molecular weight of (+)-Biotin N-hydroxysuccinimide ester label is 340 Da.

Following the labelling reaction, it was decided that purification using monomeric Avidin agarose was not necessary as the unlabelled $A\beta_{40}$ monomers could be used in the aggregation reaction. This would have been necessary had the use of Cysteine mutants been implemented. Excess (+)-Biotin N-hydroxysuccinimide ester was removed by SEC and the purified labelled $A\beta_{40}$ monomers were buffer exchanged into 50 mM ammonium acetate pH 8.5 and lyophilised.

3.3.2 Zn^{2+} stabilised $A\beta_{40}$ oligomer generation and characterisation

Biotin-labelled Zn^{2+} stabilised $A\beta_{40}$ oligomers were generated using the method described in Chapter 5.3.3. It was important to characterise these oligomers to ascertain whether the formation of Zn^{2+} stabilised $A\beta_{40}$ oligomers from biotinylated $A\beta_{40}$ monomer significantly affects their structure. Firstly, 8-Anilinonaphthalene-1-sulphonic acid (ANS) was used to probe

the hydrophobic content of the oligomer's surface. ANS is a fluorescent molecular probe and its emission intensity is proportional to the size of exposed hydrophobic surfaces[271]. The turbidity of the oligomers was also quantified and the results of the ANS fluorescence and turbidity measurements are shown for both unlabelled and biotinylated $A\beta_{40}$ oligomers in Figure 3.8

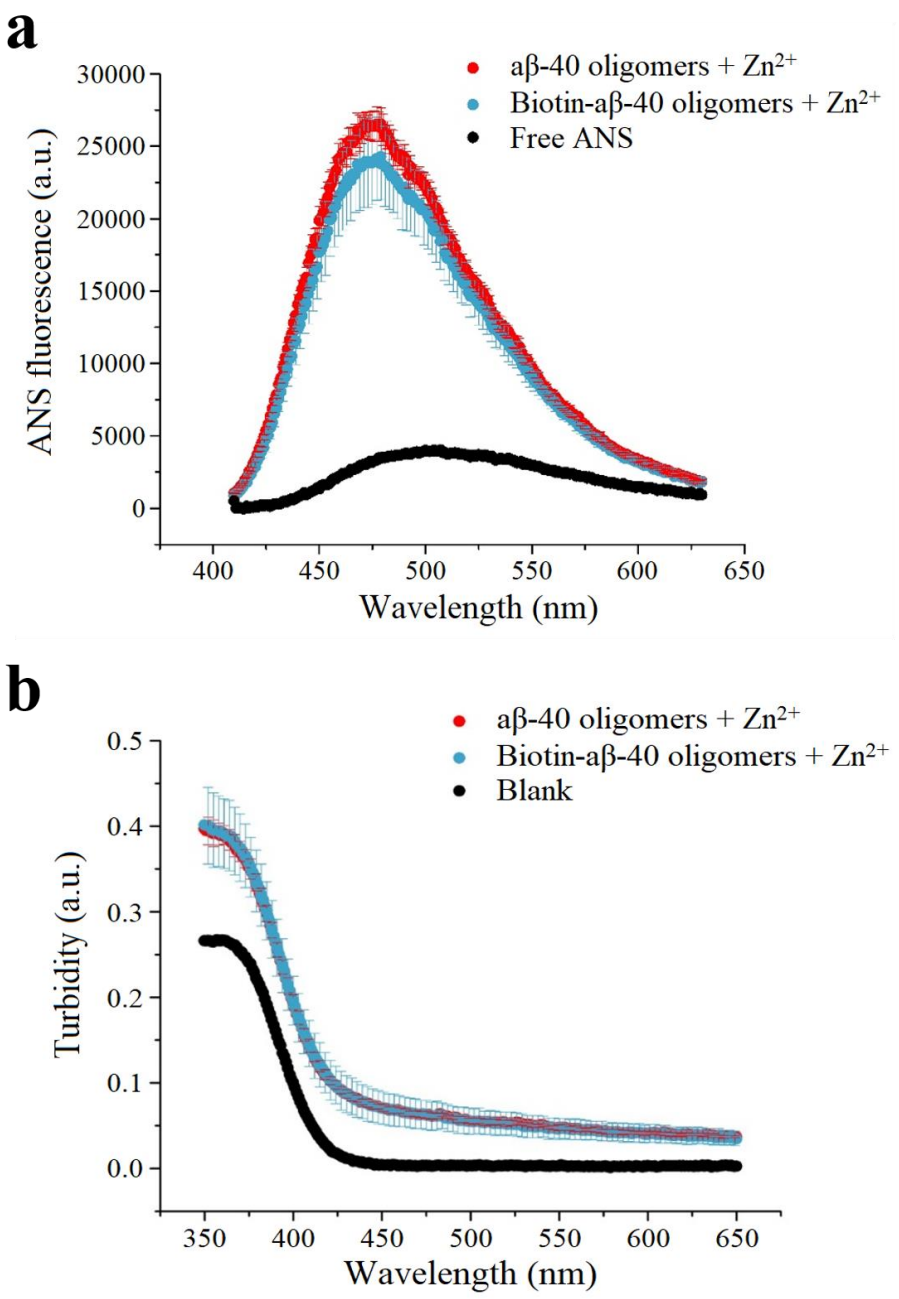

Figure 3.8. ANS binding fluorescence and turbidity measurements for unlabelled and biotinylated $A\beta_{40}$ oligomers. a) ANS fluorescence with unlabelled $A\beta_{40}$ oligomers (red), biotinylated $A\beta_{40}$ oligomers (blue) and free ANS in solution for comparison. b) Turbidity measurements of unlabelled $A\beta_{40}$ oligomers (red), biotinylated $A\beta_{40}$ oligomers (blue) and PBS buffer (black) for comparison. Error bars represent the standard deviation from three independent experiments.

The ANS binding fluorescence and turbidity measurements showed no significant differences in the hydrophobic surface or turbidity of the biotinylated $A\beta_{40}$ oligomers with respect to the unlabelled $A\beta_{40}$ oligomers. The small discrepancy for the ANS fluorescence measurement is within the error, most likely due to errors in the biotinylated $A\beta_{40}$ oligomer concentration. The same error pattern can be observed in the biotinylated $A\beta_{40}$ oligomer turbidity measurement. The ANS fluorescence and turbidity measurements were performed in collaboration with Dr. Benedetta Mannini and Dr. Ryan Limbocker. To characterise the morphology of the oligomers, i.e. to confirm they were of classical globular shape as opposed to the elongated shapes of protofilaments, protofibrils and mature fibrils, atomic-force microscopy (AFM) was used to determine their shape and size. The AFM images of both biotinylated $A\beta_{40}$ oligomers and unlabelled $A\beta_{40}$ oligomers are shown in Figure 3.9.

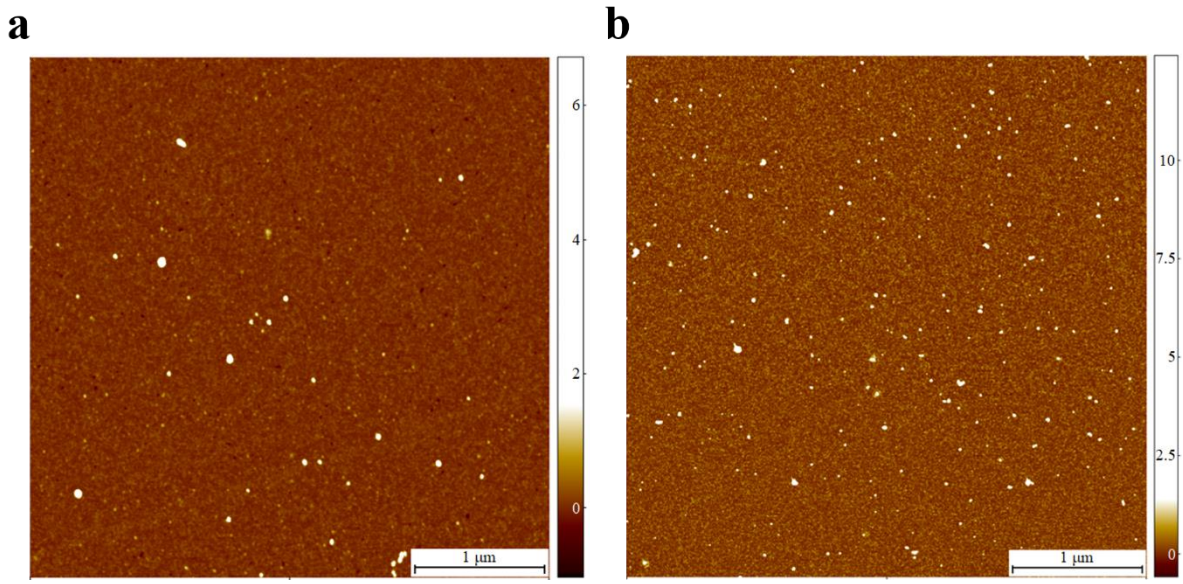

Figure 3.9. AFM morphology maps of biotinylated $A\beta_{40}$ oligomers and unlabelled $A\beta_{40}$ oligomers. Scale bar is 1 µm for both images and the height bars on the right of each image are given in nm. a) Unlabelled $A\beta_{40}$ oligomers as imaged by AFM. b) Biotinylated $A\beta_{40}$ oligomers as imaged by AFM.

The AFM images appear to show that Zn^{2+} stabilisation of biotinylated $A\beta_{40}$ oligomers also arrests aggregation after the generation of oligomers as they also display the characteristic globular shape and size. The AFM slide preparation and image analysis was performed in collaboration with Dr. Francesco Simone Ruggeri and Dr. Ryan Limbocker. It was desired to investigate any changes in the secondary structure content of forming $A\beta_{40}$ oligomers from biotinylated Aβ monomer by attenuated total reflection Fourier transform infrared (ATR-FTIR) spectroscopy, however access was not available in the timeframe required.

3.4 Results: Competitive affinity selection against Aβ$_{40}$ oligomers and monomers

Competitive affinity selection was performed under the same conditions as the affinity selection against αSyn, mentioned in Chapter 2.4, with some notable exceptions. Following the 2-hour incubation of the DesAb-phage libraries with biotinylated Aβ$_{40}$ oligomers, unlabelled Aβ$_{40}$ monomer was added and the competition mixture was incubated at room temperature under quiescent conditions before Avidin-capture. Aβ$_{40}$ monomer concentrations were kept low to minimise the risk of aggregation during the incubation, although some aggregation was expected to occur. The concentrations of biotinylated Aβ$_{40}$ oligomers and unlabelled Aβ$_{40}$ monomer was kept the same between rounds one and two in order to attempt to observe Aβ$_{40}$ oligomer binding enrichment through an increase in the output phage titres. Following round two, all subsequent rounds would involve a ten-fold decrease in biotinylated Aβ$_{40}$ oligomer concentration and a ten-fold increase in unlabelled Aβ$_{40}$ monomer. The inverted concentration changes of Aβ$_{40}$ oligomers and monomers was chosen to keep the bulk average concentration of Aβ$_{40}$ low to avoid aggregation complications. The increase in concentration of Aβ$_{40}$ monomers between rounds was also used to maximise the negative selection of Aβ monomer-binding DesAb-phage in the late rounds. A total of five rounds of competitive affinity selection were performed, with biotinylated Aβ$_{40}$ oligomers and unlabelled Aβ$_{40}$ monomer being freshly prepared prior to each selection. The concentrations of Streptavidin or NeutrAvidin coated-beads were not decreased between rounds this time in order to maximise the kinetics of phage-DesAb-oligomer complex capture. Any binding enrichment towards the Streptavidin or NeutrAvidin coated-beads was deemed to be minimal due to pre-incubation of the DesAb-phage libraries with the beads and the alternating between capture proteins between rounds. The resulting output phage titres of all five rounds of competitive affinity selection are shown in Figure 3.10.

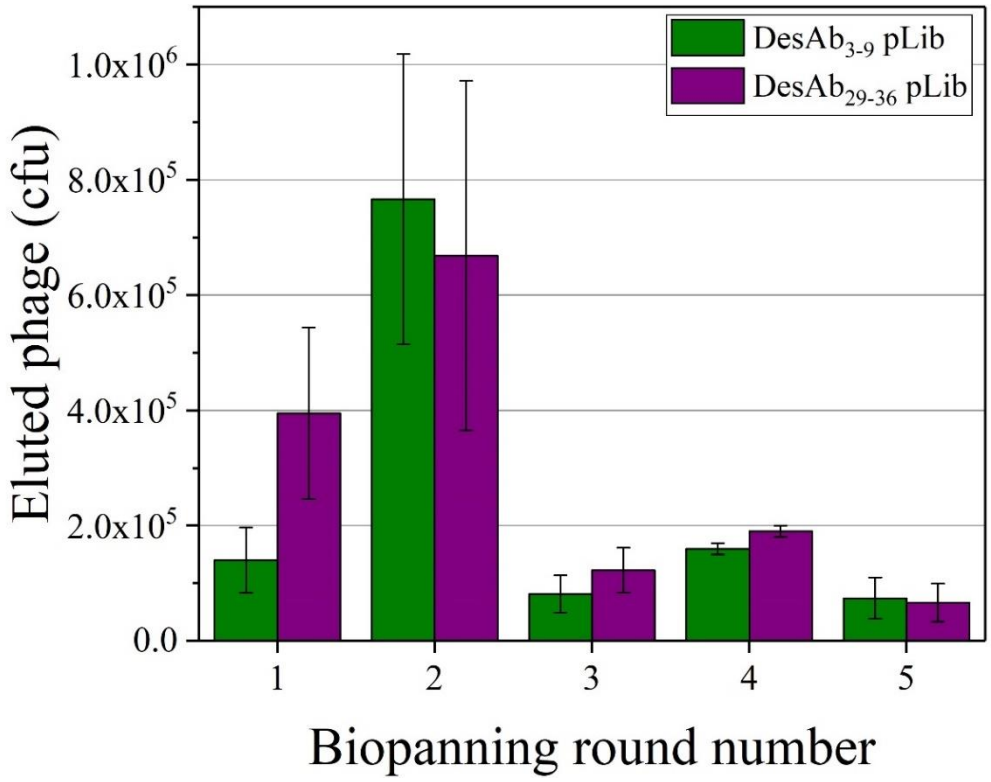

Figure 3.10. Mean average output phage titres for the competitive affinity selections of DesAb$_{3-9}$ pLib and DesAb$_{29-36}$ pLib. DesAb$_{3-9}$ pLib output phage titres are shown in green and DesAb$_{29-36}$ pLib output phage titres are shown in purple. Rounds one and two were selections against 5 μM biotinylated Aβ$_{40}$ oligomers and 1 nM Aβ$_{40}$ monomers. Round three was a selection against 500 nM biotinylated Aβ$_{40}$ oligomers and 10 nM Aβ$_{40}$ monomers, round four was a selection against 50 nM biotinylated Aβ$_{40}$ oligomers and 100 nM Aβ$_{40}$ monomers and round five was a selection against 5 nM biotinylated Aβ$_{40}$ oligomers and 1 μM Aβ$_{40}$ monomers. Bars represent the mean average and error bars represent the standard deviation of three repeat measurements.

As expected, the output phage titres for both DesAb$_{3-9}$ pLib and DesAb$_{29-36}$ pLib increased between rounds one and two of competitive affinity selection when the concentrations of target and competitor were kept the same. The apparent biotinylated Aβ$_{40}$ oligomer-binding enrichment was much greater for DesAb$_{3-9}$ pLib (~5.5-fold) than for DesAb$_{29-36}$ pLib (~1.7-fold) between rounds one and two. This supposed Aβ$_{40}$ oligomer-binding enrichment of DesAb$_{3-9}$ pLib was then not reflected in round three, as the concentrations were decreased, as the output phage titres decreased more dramatically for DesAb$_{3-9}$ pLib than for DesAb$_{29-36}$ pLib. The output phage titres for both DesAb$_{3-9}$ pLib and DesAb$_{29-36}$ pLib then increased (~1.7-fold) between rounds three and four, even though the concentration of biotinylated Aβ$_{40}$ oligomers was decreased a further 10-fold, suggesting that significant Aβ$_{40}$ oligomer-binding enrichment had taken place. The output phage titres for both DesAb$_{3-9}$ pLib and DesAb$_{29-36}$ pLib then decreased again between rounds four and five, suggesting a significant decrease in

the population of lower-affinity Aβ$_{40}$ oligomer-binders. The output phage titres appeared to decrease marginally more for DesAb$_{29-36}$ pLib than for DesAb$_{3-9}$ pLib during the fifth round, but due to both measurements being within one-another's errors, it is not possible to derive any comparisons about the performances of both libraries from this observation.

3.5 Results: Screening for evolved antibodies against Aβ$_{40}$ oligomers

3.5.1 EvDesAb-expressing cell-lysate screening via ELISA

Crude-extract EvDesAb screening for binding to Aβ$_{40}$ oligomers was performed using the same methodology as described in Chapter 2.5.1, with the only difference being the binding screen being performed against unlabelled Aβ$_{40}$ oligomers adsorbed to the surface of the plate microwells. 92 clones were screened for each library, with crude extracts containing DesAb$_{3-9}$, DesAb$_{29-36}$ and a non-binding DesAb (DesAb-F) as controls for comparison. The results of the screening for both DesAb$_{3-9}$ pLib and DesAb$_{29-36}$ pLib are shown together for comparison in Figure 3.11.

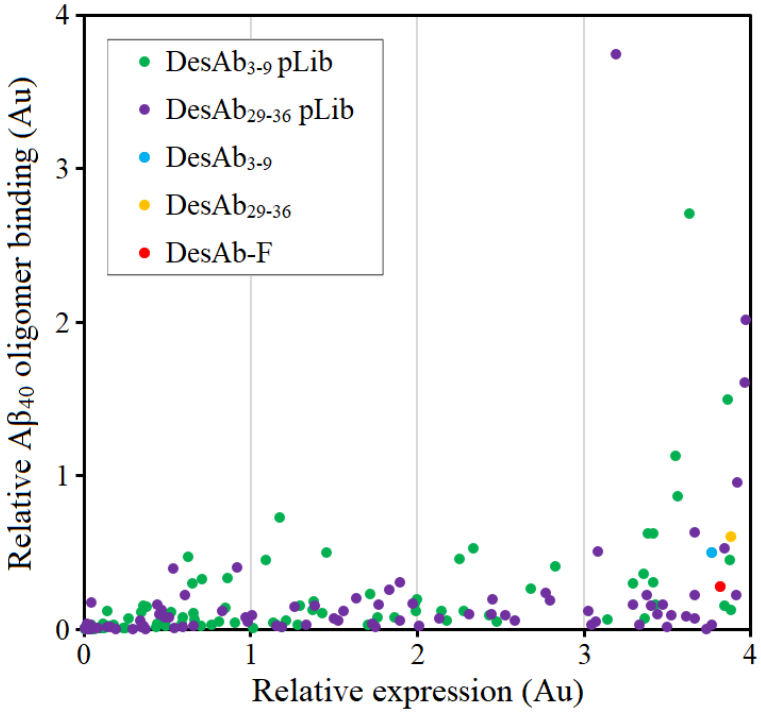

Figure 3.11. Crude extract screening of individual EvDesAbs from DesAb$_{3-9}$ pLib and DesAb$_{29-36}$ pLib, as measured by ELISA. DesAb$_{3-9}$ pLib EvDesAbs are shown in green and DesAb$_{29-36}$ pLib EvDesAbs are shown in purple. For comparison with the parental DesAbs, DesAb$_{3-9}$ is shown in blue and DesAb$_{29-36}$ is shown in orange. DesAb-F is shown in red as a negative control. Values are the measurements of the 450 nm absorbance (Au) change produced by the oxidation of TMB, which is proportional to the presence of the screened Abs.

Unlike the crude-extract ELISA screens described in Chapter 2.5.1, there was little evidence of expression enrichment during competitive selection, as ~95% of all screened variants displayed lower expression scores than $DesAb_{3-9}$ and $DesAb_{29-36}$. Also, strikingly, the vast majority of variants (91% for $DesAb_{3-9}$ pLib and 95% for $DesAb_{29-36}$ pLib) showed no improvement to binding scores, with many showing little or no $A\beta_{40}$ oligomer binding at all. Nevertheless, a number of variants from each library showed strong apparent improvements to binding scores with respect to $DesAb_{3-9}$ and $DesAb_{29-36}$ whilst retaining desirable expression levels. These clones were selected for further characterisation and sequencing analysis was performed to analyse the distributed mutations in the genes of the EvDesAbs.

3.5.2 Sequencing analysis of evolved antibody populations

DNA sequencing analysis was performed on 15 EvDesAbs from each library displaying apparent $A\beta_{40}$ oligomer binding affinity improvements, as measured during crude-extract screening. Due to the potentially complex nomenclature for naming EvDesAbs derived from ep-PCR, all variants shall henceforth be referred to by the ELISA screen microwell that they were first identified in (e.g. EvDesAb-A1). The resulting mutations are shown in Table 3.1.

Table 3.1. DesAb$_{3-9}$ and DesAb$_{29-36}$ EvDesAb mutations as revealed by DNA sequencing. Clones identities correspond to their ELISA screen microwells and those marked in bold and italics were characterised in more detail. Mutations marked in bold are conserved either within or between libraries. Mutations marked with an underline are potential 'hotspot' mutations (i.e. different mutations occurring at the same position). Mutations marked with an asterisk correspond to conserved or 'hotspot' mutations between libraries, downstream of the grafted CDR3 sequence. This is because DesAb$_{29-36}$ has a longer CDR3 loop by one residue, shifting the numbering of DesAb$_{29-36}$ residues by +1 after the CDR3 loop. Mutations marked in blue are in the CDR2 loop and mutations marked in green are in the CDR3 loop. No mutations were found in the CDR1 loop. Mutations involving a Cysteine are highlighted in red. Mutant sequences in italic mark EvDesAbs found more than once.

DesAb$_{3-9}$ pLib		DesAb$_{29-36}$ pLib	
Clone	***Mutations***	***Clone***	***Mutations***
A4	**Q13R**, **C22R**, L104R	A4	**E89G**, **D90V**, **T91I**, V121M*
A11	*Q3R*,***I34N***,***P41R***,*N55S*	B12	E1G, G8C, I29N, K65R
A5	S63R, N77S, N84I, C96S	B8	**Q14R**, R39C, A72S, S75N, R87H, C96R
A6	*Q3R*,***I34N***,***P41R***,*N55S*	C8	**E45G**, V64A, S71G, S75I, **D90V**
B11	Q3L, K30E, Q82H, **N84Y**, S85R, E89V, E108D, Q116R*, **V120E***	D2	**E1V**, Q13L, S21N, **G56S**, **D73Y**, N77I, M83K
B8	V2M, **I34N**, **P41H**, E108K	E1	Q13P, M83T, C96Y
C10	A97P	***E10***	**A98T**, **V121E***
C7	**E1K**, **P41H**, W47G, V122M*	E2	L18Q, S21I, **C22R**
D4	E6G, Q82R, **T91I**	F3	**E1V**, Y33H, I34T
E11	V2L, G9C, F27L	F5	**E1V**, I34F, **E89G**, Y94N
E5	L11P, **D73Y**, **N84Y**, **L104Q**, **W114R**	F6	R38C
F12	S25C, G42V, **E45G**, A97V, E110V, **W114R**	G10	*E45K*,***A98T***,*Q117P**,*V123E**
G10	**E1K**, D31N, **P41R**, R59H, L86M, Y94F	G11	L4P, **Q13R**, K30R, G42W, P53L, L86Q, **E89G**
G7	**E1V**, S21G, **G56S**, R59L, L106Q, **W114R**, Q116L*	G5	K43R, E46K, V48A, **D73Y**, M103W, V108G
H11	V5A, **C22R**, Y52F, V64L, S75C, **L104Q**	***H4***	*E45K*,***A98T***,*Q117P**,*V123E**

The sequences of all 30 affinity-selected variants were in-frame and devoid of premature stop codons. No 'wild-type' sequences were found, which may be testament to the ep-PCR conditions employed and the apparent reliability of the crude-extract screen. A sequence was found in each selected library occurring in more than one clone (EvDesAb-A6/EvDesAb-A11 for DesAb$_{3-9}$ and EvDesAb-G10/EvDesAb-H4 for DesAb$_{29-36}$), indicating successful sequence enrichment during affinity selection. A fairly large proportion of sequenced clones (~33%) contained mutations involving at least one Cysteine. An explanation for this may be binding selection due to a propensity to dimerise through disulphide bonds, resulting in selection based on binding avidity, rather than absolute binding affinity[231]. For this reason, further use of these clones was avoided. A noticeable difference in the mutagenesis of the CDR loops was observed between the selected libraries, with ~53% of DesAb$_{3-9}$ pLib EvDesAbs and only ~20% of DesAb$_{29-36}$ pLib EvDesAbs containing at least one mutation in the CDR2 and/or CDR3 loops. It is challenging to conclude any reasonable trends due to the small sample size, however it is

clear that the variants yielded from selection have a significantly altered mutation spectra. The analysis comparing the mutation spectra of both $DesAb_{3-9}$ pLib and $DesAb_{29-36}$ pLib, before and after competitive affinity selection against $A\beta_{40}$ oligomers is shown in Figure 3.12.

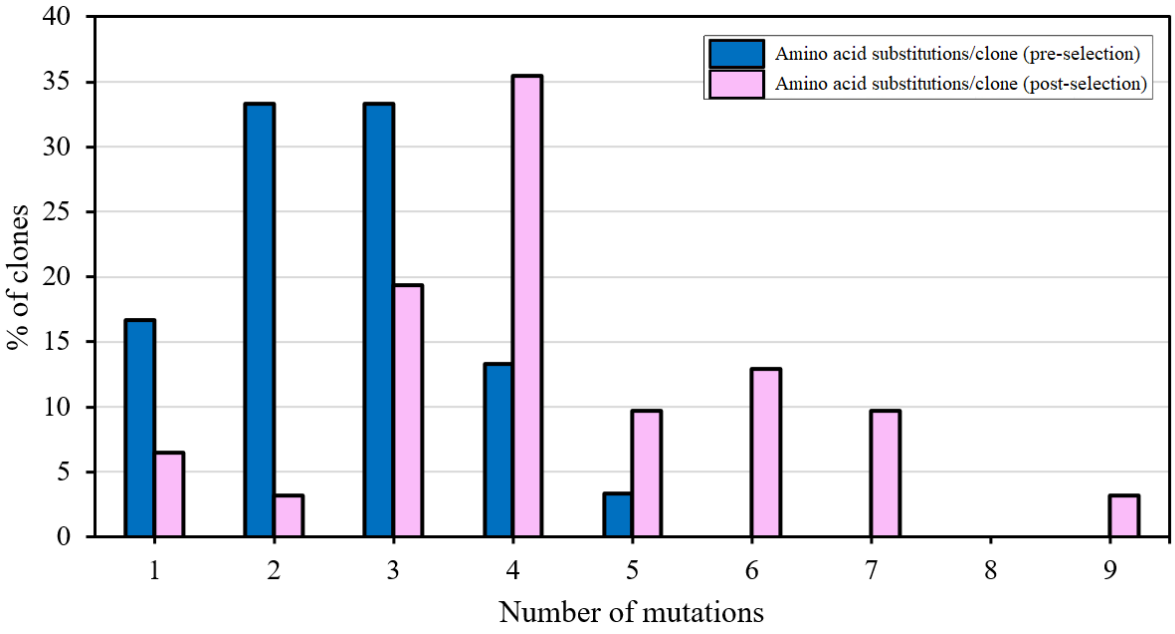

Figure 3.12. Comparison of the mutation spectra of both $DesAb_{3-9}$ pLib and $DesAb_{29-36}$ pLib, before and after affinity selection. Both datasets are of a sample size of 30 sequenced unique clones each. Shown is the percentage frequency of sequenced clones (*y*-axis) containing certain numbers of AA substitutions (*x*- axis). The mutation spectra of both $DesAb_{3-9}$ pLib and $DesAb_{29-36}$ pLib before affinity selection is shown in dark blue and the mutation spectra of both $DesAb_{3-9}$ pLib and $DesAb_{29-36}$ pLib after affinity selection is shown in pink.

The pre/post-selection mutation spectra analysis clearly shows a selection preference for variants with higher mutation frequencies (average ~4.5 mutations per selected clone). This was a concern as the average number of mutations desired in the ep-PCR was kept low to attempt to avoid the risk of introducing heavily destabilising mutations. It is also problematic when analysing variants for 'hotspot' mutations as it can be almost impossible to know which mutations are contributing to the affinity improvement without mutating them back into the parental DesAb one-by-one. Even this labour-intensive strategy can be unsuccessful as some affinity enhancing mutations may only display their effect in epistatic interactions with other mutations, requiring all combinations of these mutations to be tested[213]. Regardless of this issue, useful information may yet be acquired by analysing the nature of the occurrences of the potential 'hotspot' mutations (i.e. the frequency in which they occur and whether or not they are conserved between libraries). An analysis of the types of observed potential 'hotspot' mutations is shown in Figure 3.13.

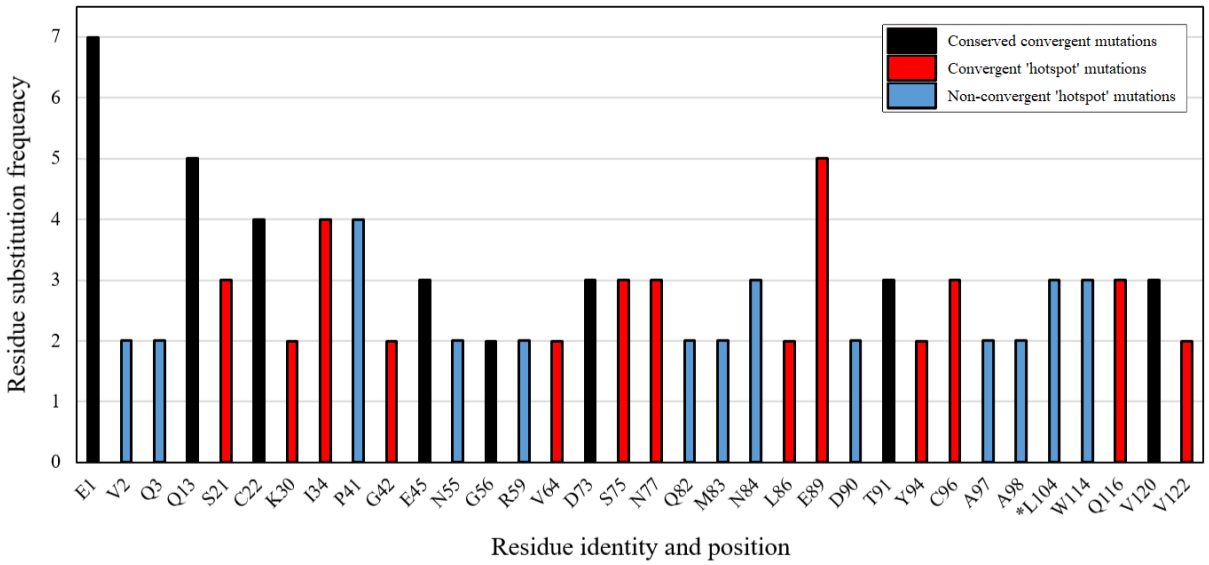

Figure 3.13. Frequency and nature of observed potential 'hotspot' mutation analysis. The mutations shown are substitutions at specific residues (*x*-axis) that occur more than once, and their total frequency (i.e. number of clones containing the mutation) is compared (*y*-axis). Mutations that are unique to each affinity-selected library are 'non-convergent' and are shown in blue. Substitutions that are observed in both libraries are grouped into 'convergent' mutations. Those that are identical (i.e. the specific residue substitution) are termed 'conserved convergent' and are shown in black. Those that are not identical (i.e. the position of the substitution is the same but the resulting residue is different) are just termed 'convergent hotspot' and are shown in red. L104 is marked with an asterisk (*) as it is unique to the grafted CDR3 loop of $DesAb_{3\text{-}9}$.

Whilst conserved mutations between affinity-selected variants are good indicators of being responsible for protein fitness improvements, ep-PCR amplification bias can lead to a significant number of conserved mutations being false-positives[245, 269]. However, amplification bias is extremely unlikely to generate conserved mutations observed between libraries generated in independent ep-PCR reactions[245]. For this reason, the conserved and convergent substitution mutations may likely contribute significantly towards the evolved protein fitness, especially when considering that both $DesAb_{3\text{-}9}$ pLib and $DesAb_{29\text{-}36}$ pLib were generated and affinity-selected under the exact same conditions. These mutations were: E1V, Q13V, C22R, E45G, G56S, D73Y, T91I and V120E. It would be extremely interesting to sequentially mutate these mutations back into the parental DesAbs to quantify their effects on Aβ oligomer binding; however, due to time constraints, this remains to be performed. The mutation E45K, which is present in EvDesAb-H4 (the $DesAb_{29\text{-}36}$ variant with the highest binding score in the crude-extract screen), has been described before in a study involving the affinity maturation of the same sdAb scaffold against Aβ[272]. E45K is a charge-reversal

mutation in the base of the β-strand immediately prior to the CDR2 that has been implicated in V_H framework stability during affinity maturation[272].

3.5.3 Expression and purification of soluble evolved antibody fragments

Following crude extract screening, the selected EvDesAbs of $DesAb_{3-9}$ and $DesAb_{29-36}$ were expressed and purified as described in Chapter 2.5.3. A representative purification comparison of a DesAb ($DesAb_{29-36}$) and one of its EvDesAbs (EvDesAb-H4) is illustrated in Figure 3.14.

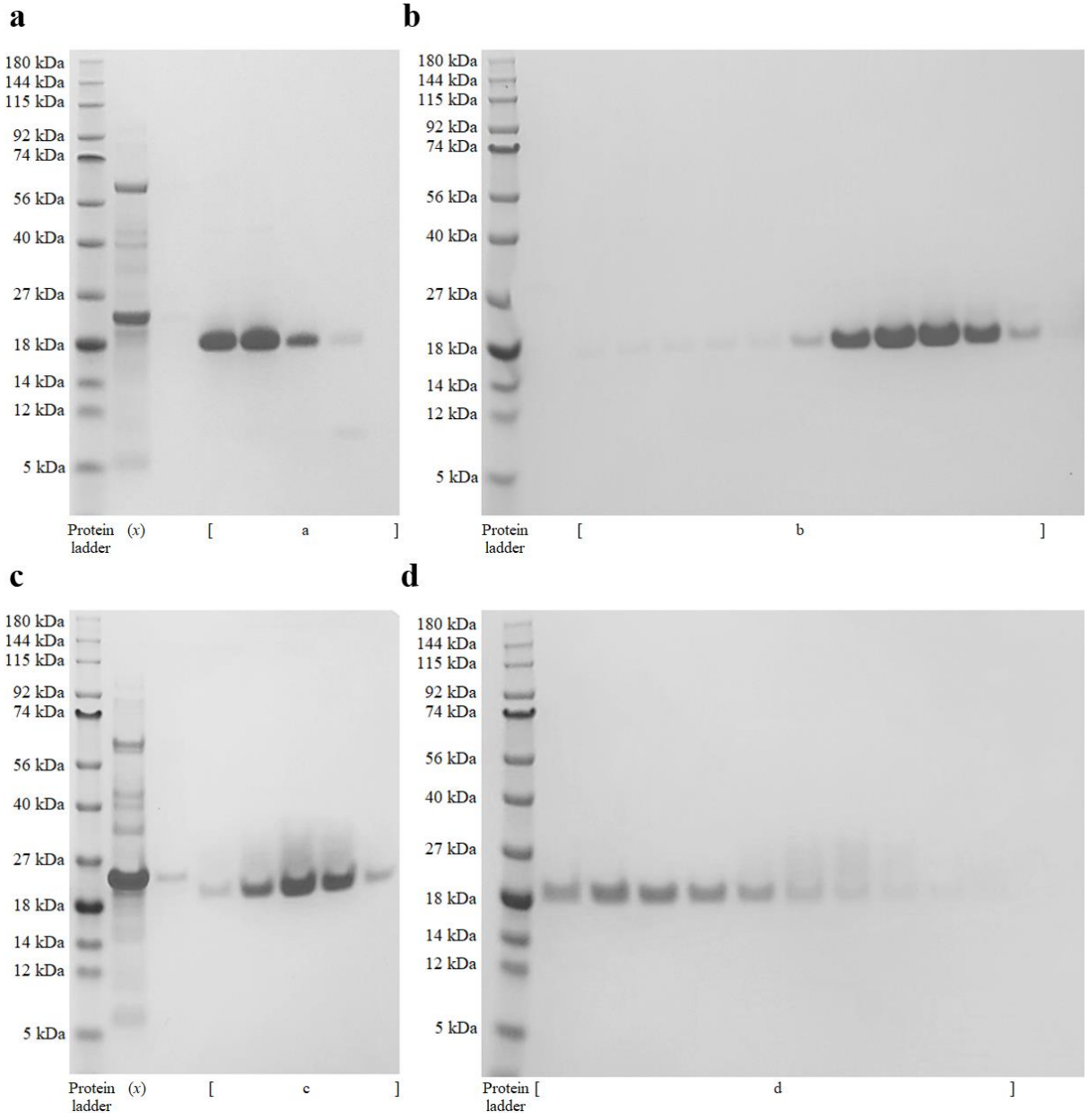

Figure 3.14. SDS PAGE analysis of the purifications of $DesAb_{29-36}$ and one of its mutants (EvDesAb-H4). a) IMAC purification of $DesAb_{29-36}$ (~18 kDa). b) SEC purification of $DesAb_{29-36}$. c) IMAC purification of EvDesAb-H4 (~18 kDa). d) SEC purification of EvDesAb-H4. (*x*) Discarded *E. coli* periplasmic extract flow-through.

Only five EvDesAbs (EvDesAbs-A6/C7/C10/E10 and H4) from both libraries expressed in yields sufficient for further characterisation (~10 mg/L of liquid culture). Concerningly, all expressed EvDesAbs displayed a similar characteristic 'smear', as shown in the representative EvDesAb-H4 IMAC and SEC purification SDS PAGE analyses in Figure 3.14. The parental DesAbs, $DesAb_{3-9}$ and $DesAb_{29-36}$, did not display this smear in either IMAC or SEC purification. The eluted EvDesAb fractions in SEC purifications were combined, excluding the later fractions (on the right hand side of Figure 3.14 (d)) containing the smeared bands, in an attempt to remove this potential contamination.

3.6 Results: $A\beta_{42}$ aggregate selectivity characterisation of evolved antibodies by ELISA

As $DesAb_{3-9}$ and $DesAb_{29-36}$ were designed and characterised against $A\beta_{42}$ and the competitive affinity-selection and crude-extract screening was performed against $A\beta_{40}$ oligomers, it was crucial to characterise whether the EvDesAbs had retained their $A\beta_{42}$ binding and aggregation inhibition activity[104]. MST was deemed unsuitable for binding characterisation due to the noise complications associated with the rapid aggregation of $A\beta_{42}$, unlike the relatively kinetically stable αSyn[273]. Due to the unstable nature of $A\beta_{42}$, a characterisation procedure with a high degree of simplicity was desired and it was decided ELISA would be the best method due to the lack of labelling requirements and its sensitivity with extremely small quantities of Ag[236]. It was decided that the binding selectivity characterisation would be performed against aggregate species extracted directly from an aggregation reaction as this would likely represent the most physiologically relevant aggregate species obtainable by *in vitro* $A\beta_{42}$ aggregation. Stabilising the $A\beta_{42}$ oligomeric species with Zn^{2+} would allow the precise control of concentration required for accurate K_D determination; however the kinetic 'trapping' of $A\beta_{42}$ oligomers may only represent a biased subset of species that cannot convert to mature amyloid fibrils (i.e. 'off-pathway' oligomers)[270, 274]. Therefore, in order to sample the maximum heterogeneous population of oligomers, samples would be taken from an *in vitro* $A\beta_{42}$ aggregation at specific time-points and coated onto the surface of ELISA microwells to compare the relative affinities of the EvDesAbs towards different aggregate species. The time-points were selected to represent stages of the aggregation where the proportions of different aggregate species would be distinctly different from one-another. The design rationale of this experiment is illustrated in Figure 3.15.

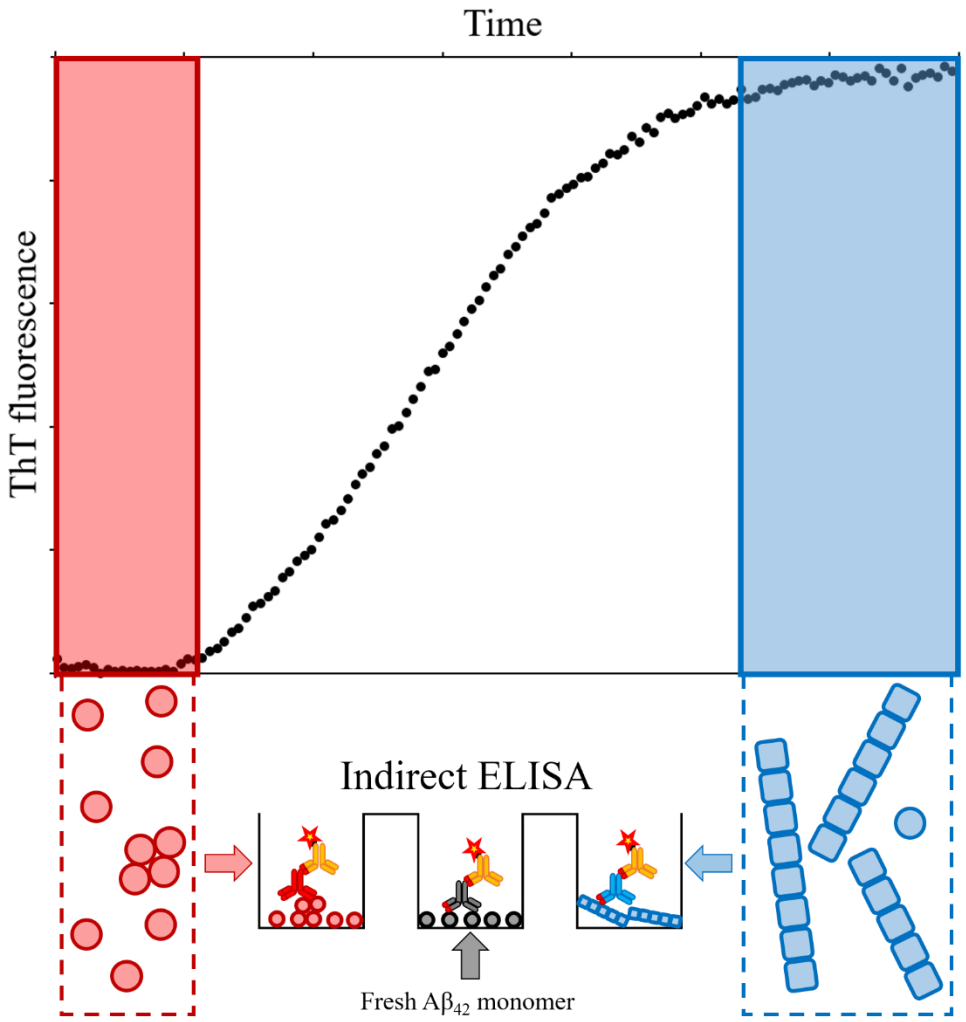

Figure 3.15. Experimental set-up for the selectivity characterisation of EvDesAbs for aggregated species extracted directly from the aggregation of Aβ42. The aggregation of Aβ42 is monitored by ThT fluorescence (top) and samples are obtained at time-points representing the highest theoretical ratio of oligomers to fibrils (lag phase, red) and the highest ratio of mature fibrils to monomers and oligomers (growth plateau, blue). The dashed boxes below show the bulk average species present in the selected time-points and are shown in the same colours. Monomers are depicted as circles, oligomers are depicted as four joined circles and fibrils are depicted as lines of rounded squares. Samples taken at the chosen aggregation time-points are immediately coated onto different microwells for indirect ELISA selectivity characterisation of the EvDesAbs (bottom centre). The binding of the EvDesAbs to the Aβ42 aggregates is compared to their binding to fresh Aβ42 monomer.

The time-point selected to maximise the yield of Aβ42 oligomers was at the end of the lag phase, before the increase in ThT fluorescence (associated with the generation of the β-sheet-rich amyloid fibrils)[79]. This time-point sample would certainly consist mostly of Aβ42 monomer, with the Aβ42 oligomeric species being heterogeneous and lowly-populated[275, 276]. For this reason, in the hypothetical case of complete oligomer binding specificity, any binding signal difference between this time point and the monomer and fibril samples would still be expected

to be small at best. The aggregation reaction, as monitored by ThT fluorescence, would not directly provide the samples for the binding ELISA, to avoid any undesired interference from ThT. It would instead provide the aggregation time-course visualisation; and a second aggregation would be performed without the use of ThT, using the calculated time-points from the first aggregation to obtain the samples for binding selectivity ELISA. The results of $A\beta_{42}$ aggregate binding selectivity ELISAs are shown for the EvDesAbs of $DesAb_{3-9}$ in Figure 3.16 and the EvDesAbs of $DesAb_{29-36}$ in Figure 3.17. In both experiments, relative comparisons were made with the parental DesAbs and a sequence-specific commercial anti-$A\beta_{42}$ Ab (6E10).

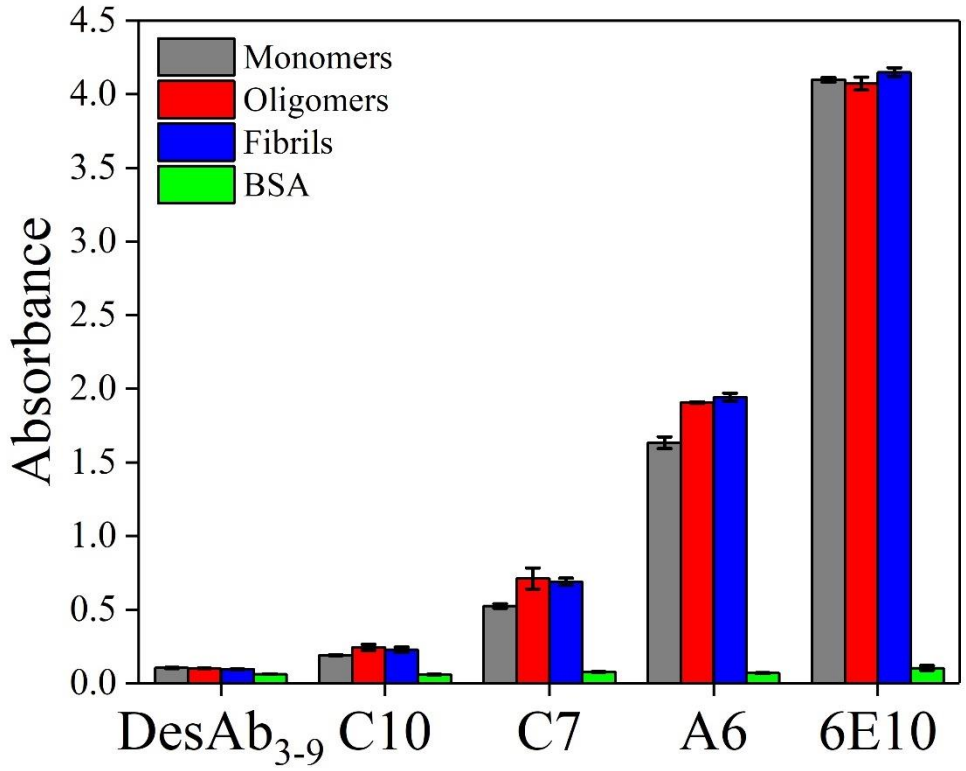

Figure 3.16. $DesAb_{3-9}$ EvDesAb binding selectivity to $A\beta_{42}$ aggregate species as measured by ELISA. Values are the measurements of the 450 nm absorbance (Au) change produced by the oxidation of TMB, which is proportional to the binding strength of the screened Abs. The relative binding affinities of EvDesAb-C10, EvDesAb-C7 and EvDesAb-A6 to $A\beta_{42}$ monomers (grey), oligomers (red), fibrils (blue) and BSA (negative control, green) are shown with comparison to the parental $DesAb_{3-9}$ and the commercial Ab 6E10. Error bars represent the standard deviation of four repeats and bars represent the mean average.

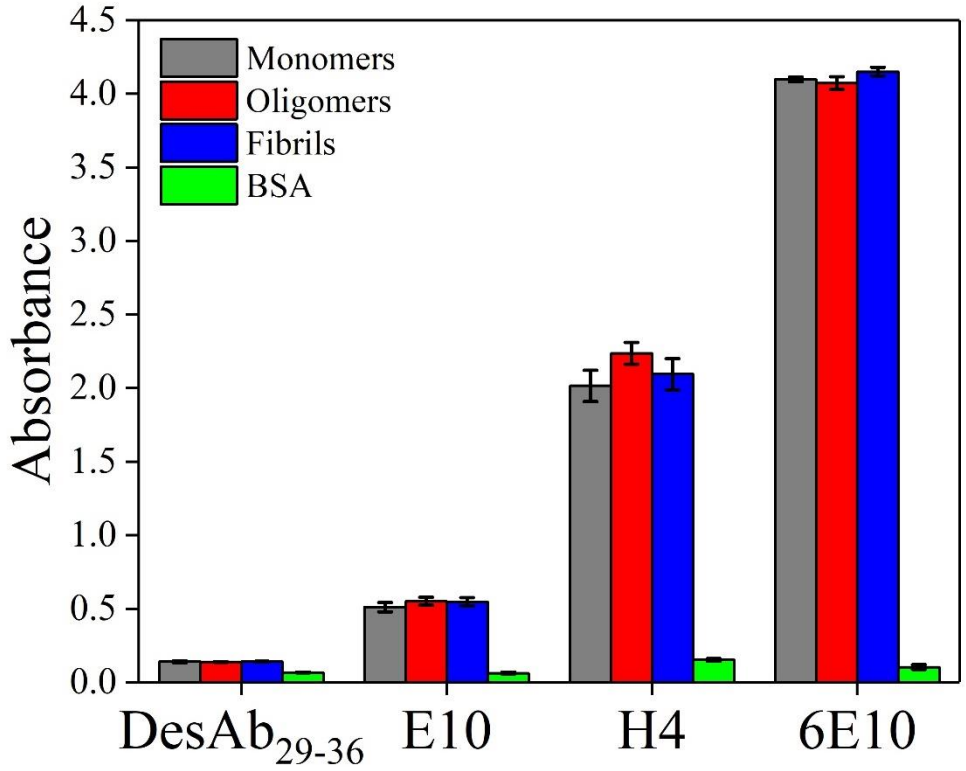

Figure 3.17. DesAb$_{29-36}$ EvDesAb binding selectivity to Aβ$_{42}$ aggregate species as measured by ELISA. Values are the measurements of the 450 nm absorbance (Au) change produced by the oxidation of TMB, which is proportional to the binding strength of the screened Abs. The relative binding affinities of EvDesAb-E10 and EvDesAb-H4 to Aβ$_{42}$ monomers (grey), oligomers (red), fibrils (blue) and BSA (negative control, green) are shown with comparison to the parental DesAb$_{29-36}$ and the commercial Ab 6E10. Error bars represent the standard deviation of four repeats and bars represent the mean average.

The results of the Aβ$_{42}$ aggregate binding selectivity ELISA showed a large difference between the average Aβ$_{42}$ binding affinities of the EvDesAbs relative to one another, their parental DesAbs and 6E10. All EvDesAbs showed improved average Aβ$_{42}$ binding affinities compared to their parental DesAbs, suggesting that affinity selection had been successful and that the use of Aβ$_{40}$ had not interfered with the selected EvDesAb's Aβ$_{42}$ binding ability. There was effectively no difference in the Aβ$_{42}$ binding selectivities for monomers, oligomers and fibrils for DesAb$_{3-9}$, DesAb$_{29-36}$ and 6E10. However, there was also little difference between the Aβ$_{42}$ binding selectivities for monomers, oligomers and fibrils for the EvDesAbs, indicating that binding specificity may be mostly sequence directed, rather than to any specific conformations. For all of the EvDesAbs of DesAb$_{3-9}$, there was a consistent (but not significant) increased binding signal to the lag-phase and growth plateau time-point samples compared to the fresh Aβ$_{42}$ monomer sample, indicating a slightly stronger binding affinity towards one or more aggregate species present in the time-point samples. EvDesAb-H4 did show a visible

preference for binding to the oligomeric time-point, however the error bars overlap with those of the fibril time-point. It should not be ignored however, due to the extremely low oligomer concentration present in the lag phase (compared to the monomer). As the total concentration of $A\beta_{42}$ was the same across all samples, and as the vast majority of species present are $A\beta_{42}$ monomers and fibrils[276], even small increases in the lag-phase time point binding signal may indicate a preference for binding to species other than the monomer. $A\beta_{42}$ fibrils are also already present in low concentrations in the lag-phase, therefore careful comparison must be made with the binding signal generated from the growth plateau time-point. In the case of EvDesAb-H4, the signal is marginally higher for the lag-phase time-point than the growth plateau time-point, indicating a small $A\beta_{42}$ oligomer binding preference over both fibrils and monomer, but far from the high degree of specificity displayed by the conformation specific Abs KW1[133] and A11[61].

3.7 Results: $A\beta_{42}$ aggregation inhibition characterisation

Following $A\beta_{42}$ aggregate selectivity characterisation of the EvDesAbs, the $A\beta_{42}$ aggregation inhibition potential of each EvDesAb was evaluated using the techniques described in Chapters 1.2.2 and 1.3.1. The aggregation of $A\beta_{42}$ was followed by the increase in ThT fluorescence over time and the resulting aggregation curves were compared to $A\beta_{42}$ aggregation curves in the presence of the EvDesAbs. For each EvDesAb, a dilution series was created and individually assayed for $A\beta_{42}$ aggregation inhibition to observe any dose-dependent effects of each EvDesAb upon $A\beta_{42}$ aggregation. Any deviations from the reaction profile of $A\beta_{42}$ (without EvDesAb) were analysed with a kinetic model[85] to ascertain which aggregation mechanisms are most affected by the presence of each EvDesAb. To identify and compare the inhibition of the k_n and k_2 microscopic nucleation rates for each EvDesAb, the changes in the global parameters k_+k_n and k_+k_2 were calculated by fitting the aggregation curves using the integrated kinetic laws described in Chapter 5.9. The k_n and k_2 microscopic nucleation rates can be calculated by decoupling the global parameters k_+k_n and k_+k_2 from the elongation rate (k_+) through analysing the effect of the EvDesAbs on $A\beta_{42}$ aggregation in the presence of pre-formed aggregates, known as ‘seeding’. Unfortunately, this could not be performed due to time constraints. Instead, comparisons were made between the calculated global parameters k_+k_n and k_+k_2 of the EvDesAbs and their parental DesAbs. Of the characterised EvDesAbs described so far, only EvDesAb-C10, EvDesAb-H4 and EvDesAb-E10 displayed dose-dependent $A\beta_{42}$

aggregation inhibition. The Aβ$_{42}$ aggregation inhibition curves of EvDesAb-C10, EvDesAb-H4 and EvDesAb-E10 are shown in Figure 3.18 and the comparisons of the calculated global parameters k_+k_n and k_+k_2 of the EvDesAbs with their parental DesAbs are shown in Figure 3.19 and 3.20.

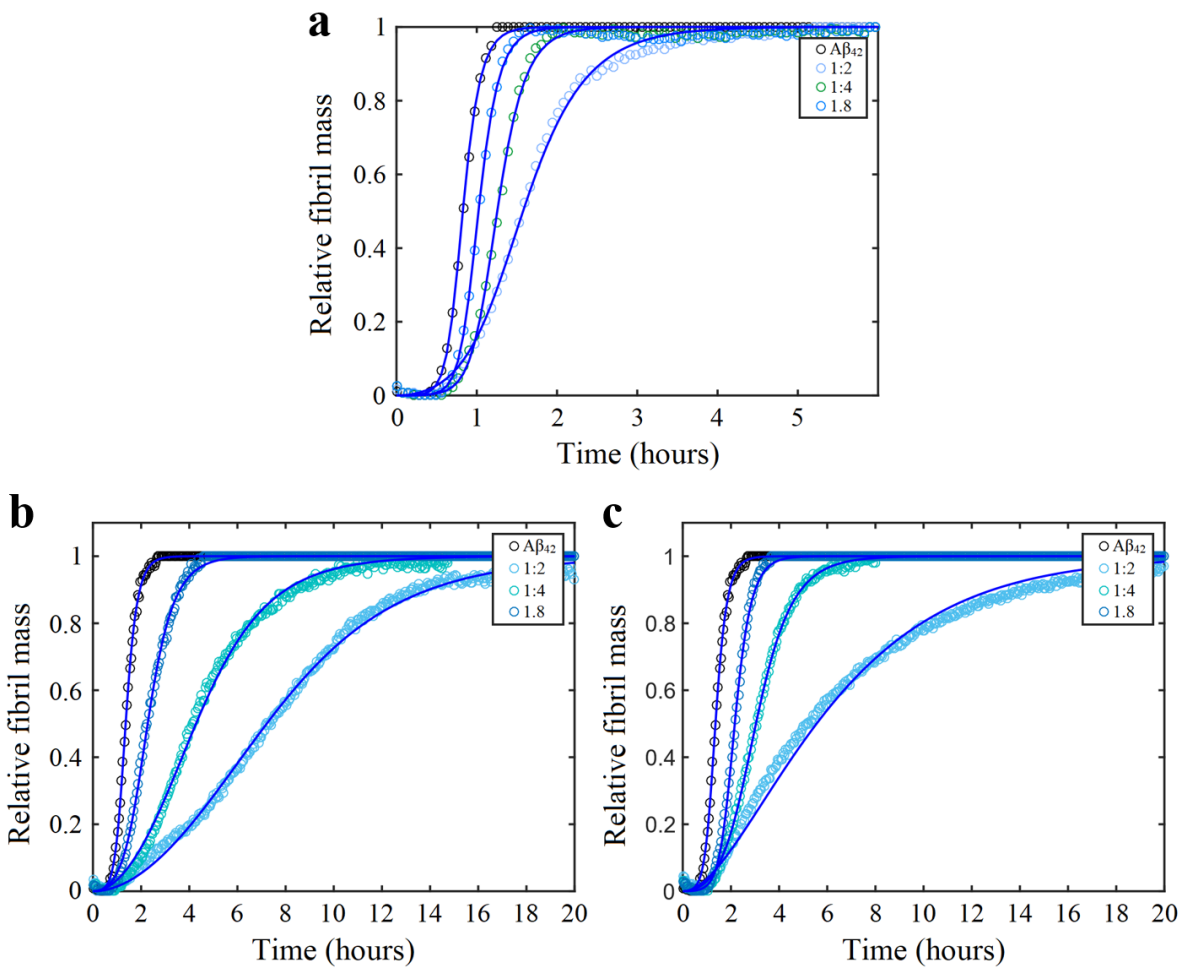

Figure 3.18. Aβ$_{42}$ aggregation curves for the EvDesAbs showing dose-dependent inhibition. Each aggregation curve was normalised to the maximum ThT fluorescence signal of the growth plateau phase, which yields each curve as a fraction of fibril mass (*y*-axis). The Aβ$_{42}$ aggregation inhibition, as followed by ThT fluorescence over time (*x*-axis) of EvDesAb-C10 (a), EvDesAb-H4 (b) and EvDesAb-E10 (c) are shown for comparison. Solutions containing 2 μM Aβ$_{42}$ were incubated in the presence of increasing concentrations of EvDesAb (shown as the molar ratio of EvDesAb to Aβ$_{42}$). The aggregation of Aβ$_{42}$ in the absence of EvDesAb is also shown for comparison in black. Blue continuous lines represent the fits of the data using the integrated kinetic laws for Aβ$_{42}$ aggregation. The data shown are the mean average of three independent experiments.

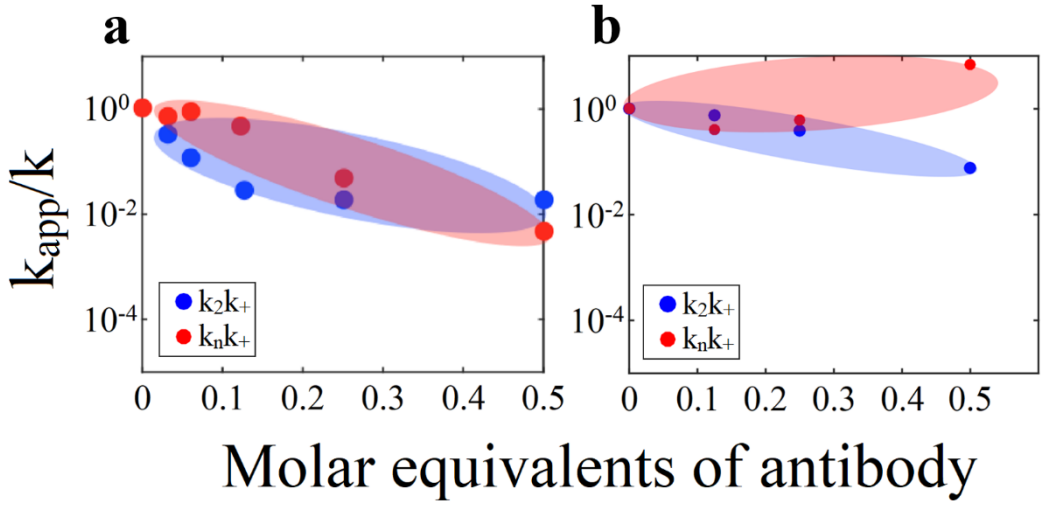

Figure 3.19. Comparison of the effect of DesAb$_{3\text{-}9}$ and EvDesAb-C10 on the global parameters k_+k_n and k_+k_2 of Aβ$_{42}$ aggregation. Shown are the decreases of the global parameters k_+k_n (red) and k_+k_2 (blue) as the direct result of Aβ$_{42}$ aggregation inhibition (*y*-axis), evaluated from the fits as a function of the relative DesAb/EvDesAb concentration to Aβ$_{42}$ monomer (*x*-axis). a) DesAb$_{3\text{-}9}$. b) EvDesAb-C10. The global parameters k_+k_n and k_+k_2 plot for DesAb$_{3\text{-}9}$ was reproduced with permission from reference [104].

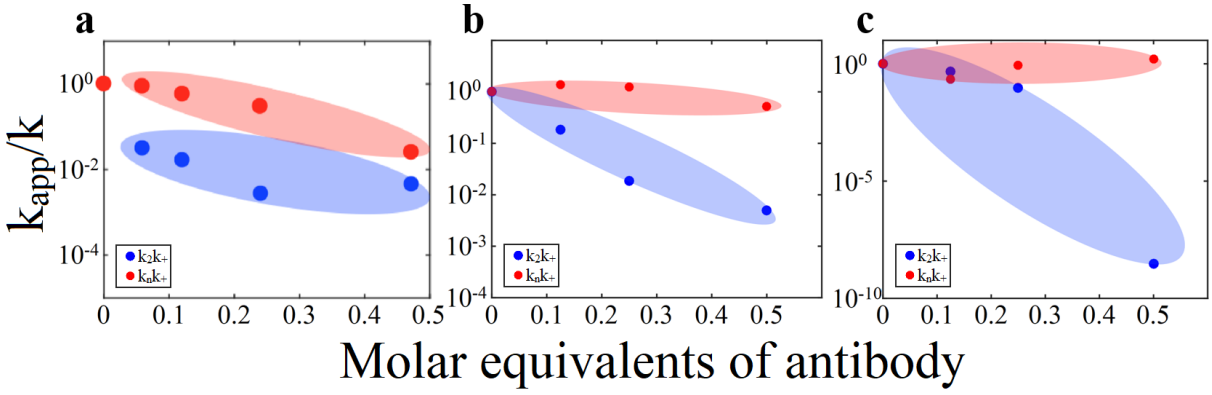

Figure 3.20. Comparison of the effect of DesAb$_{29\text{-}36}$, EvDesAb-H4 and EvDesAb-E10 on the global parameters k_+k_n and k_+k_2 of Aβ$_{42}$ aggregation. Shown are the decreases of the global parameters k_+k_n (red) and k_+k_2 (blue) as the direct result of Aβ$_{42}$ aggregation inhibition (*y*-axis), evaluated from the fits as a function of the relative DesAb/EvDesAb concentration to Aβ$_{42}$ monomer (*x*-axis). a) DesAb$_{29\text{-}36}$. b) EvDesAb-H4. c) EvDesAb-E10. The global parameters k_+k_n and k_+k_2 plot for DesAb$_{29\text{-}36}$ was reproduced with permission from reference [104].

A visible difference can be seen in the trends for the global parameters k_+k_n and k_+k_2 when comparing the EvDesAbs to their parental DesAbs. EvDesAb-C10 shows an increase for both k_+k_n and k_+k_2 with respect to DesAb$_{3\text{-}9}$, whilst increasing the discrepancy between them with a slight preference for k_+k_2 inhibition. EvDesAb-H4 and EvDesAb-E10 show a large selectivity increase for k_+k_2 inhibition, with respect to DesAb$_{29\text{-}36}$. EvDesAb-H4 had similar k_+k_2 to

$DesAb_{29-36}$, but an almost total loss of k_+k_n inhibition. The apparent loss of k_+k_n inhibition was also observed for EvDesAb-E10, with a significant increase in k_+k_2 inhibition, clearly visible at the 0.5 molar equivalence to $A\beta_{42}$.

3.8 Results: Stability characterisation by circular dichroism spectroscopy

3.8.1 Evolved designed antibody structure characterisation

The characterisation of the effect of evolution on the secondary and tertiary structures on the EvDesAbs of $DesAb_{3-9}$ and $DesAb_{29-36}$ was performed by CD, using the same methods described in Chapter 2.7.1. To characterise any changes in EvDesAb secondary structure, the CD spectra was recorded between 200-250 nm for each EvDesAb and its parental DesAb for comparison. The analysis of the EvDesAb secondary structure comparisons are shown in Figure 3.21 and Figure 3.22.

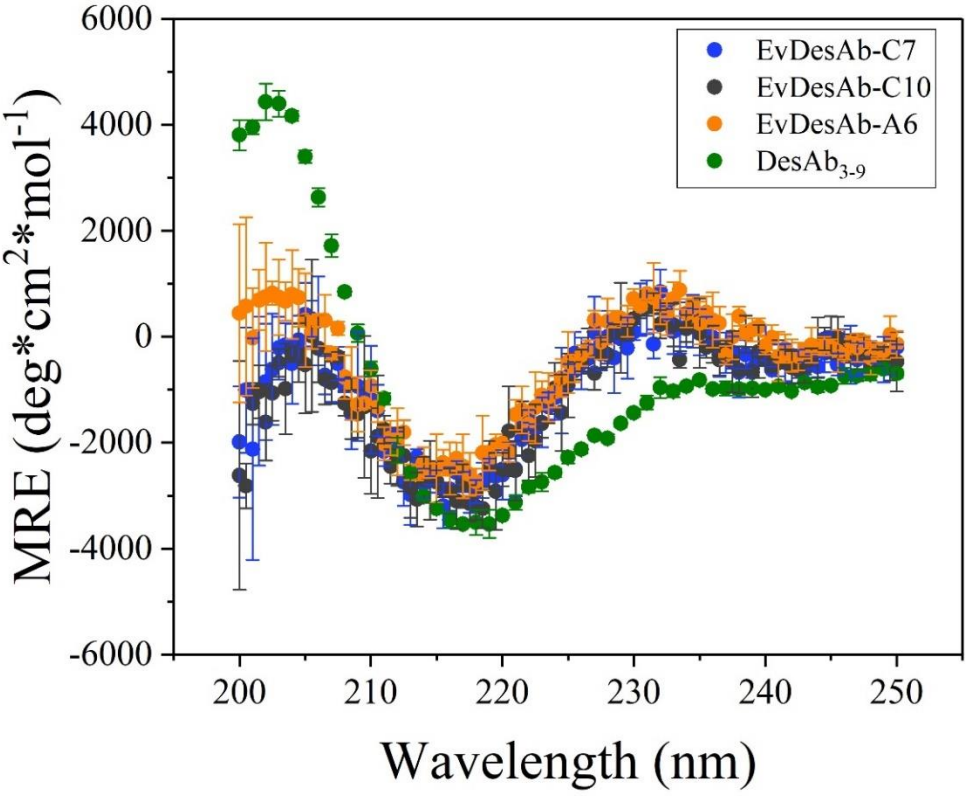

Figure 3.21. Analysis of $DesAb_{3-9}$ and its EvDesAbs with highest binding affinity as measured by CD in the far-UV region. Secondary structure analysis for all Abs are in terms of mean residue ellipticity (MRE) at a given wavelength. $DesAb_{3-9}$ (dark green), EvDesAb-C7 (blue), EvDesAb-C10 (dark grey) and EvDesAb-A6 (orange) are shown for comparison. The data is shown as the mean average and error bars represent the standard deviation of three independent experiments.

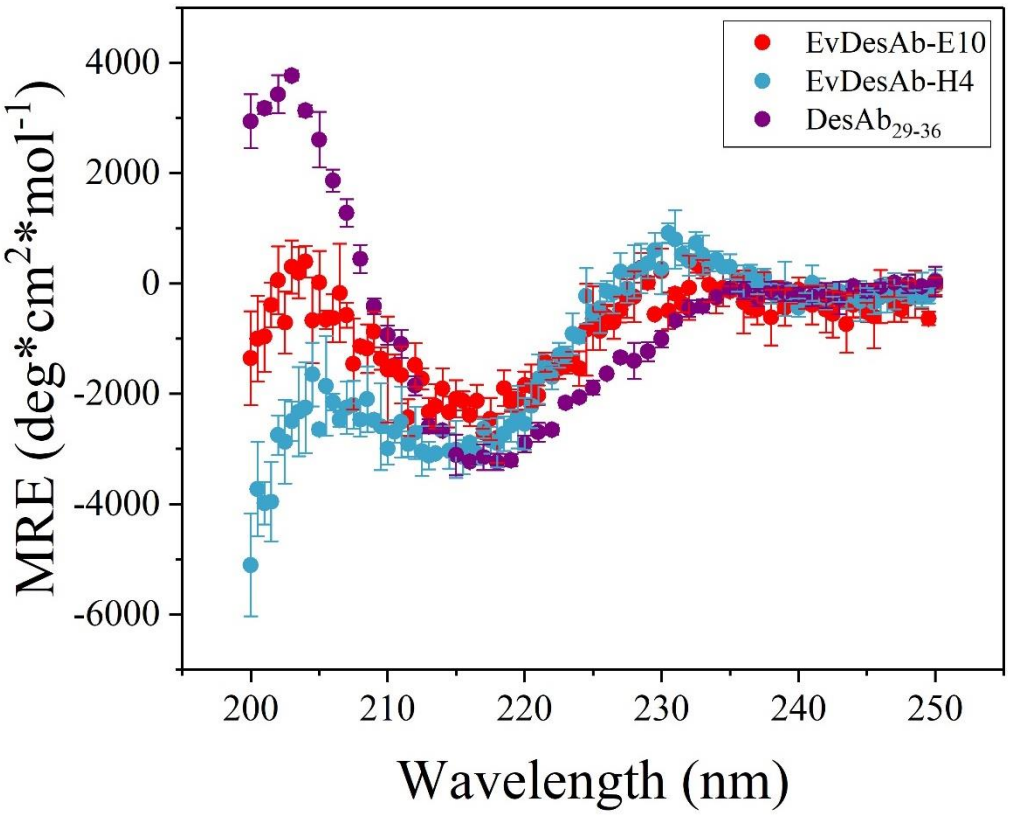

Figure 3.22. Analysis of DesAb$_{29-36}$ and its EvDesAbs with highest binding affinity as measured by CD in the far-UV region. Secondary structure analysis for all Abs are in terms of mean residue ellipticity (MRE) at a given wavelength. DesAb$_{29-36}$ (purple), EvDesAb-E10 (red) and EvDesAb-H4 (pale blue) are shown for comparison. The data is shown as the mean average and error bars represent the standard deviation of three independent experiments.

All EvDesAbs of both DesAb$_{3-9}$ and DesAb$_{29-36}$ display similar changes to the secondary structure content with respect to their parental DesAbs. A general decrease in the MRE from 200-215 nm and an increase between 220-235 nm indicates a shift in the proportion of β-sheet content towards random coil, indicating that the EvDesAbs are partially unfolded with respect to their parental DesAbs. This difference is clearly observed with EvDesAb-C7, EvDesAb-C10 and EvDesAb-H4, which have a drastically reduced MRE between 200-205 nm. It was imperative to assess the effect of this potential partial unfolding on the tertiary structure stabilities of the EvDesAbs.

3.8.2 Evolved designed antibody stability characterisation.

CD was used again to assess the thermal stability of the EvDesAbs by following the MRE signal generated at 207 nm across a temperature gradient to determine their melting temperatures (T_m). The comparison of the thermal denaturation curves of $DesAb_{3-9}$ and its EvDesAbs is shown in Figure 3.23 and their calculated melting temperatures (T_m) are shown in Table 3.2.

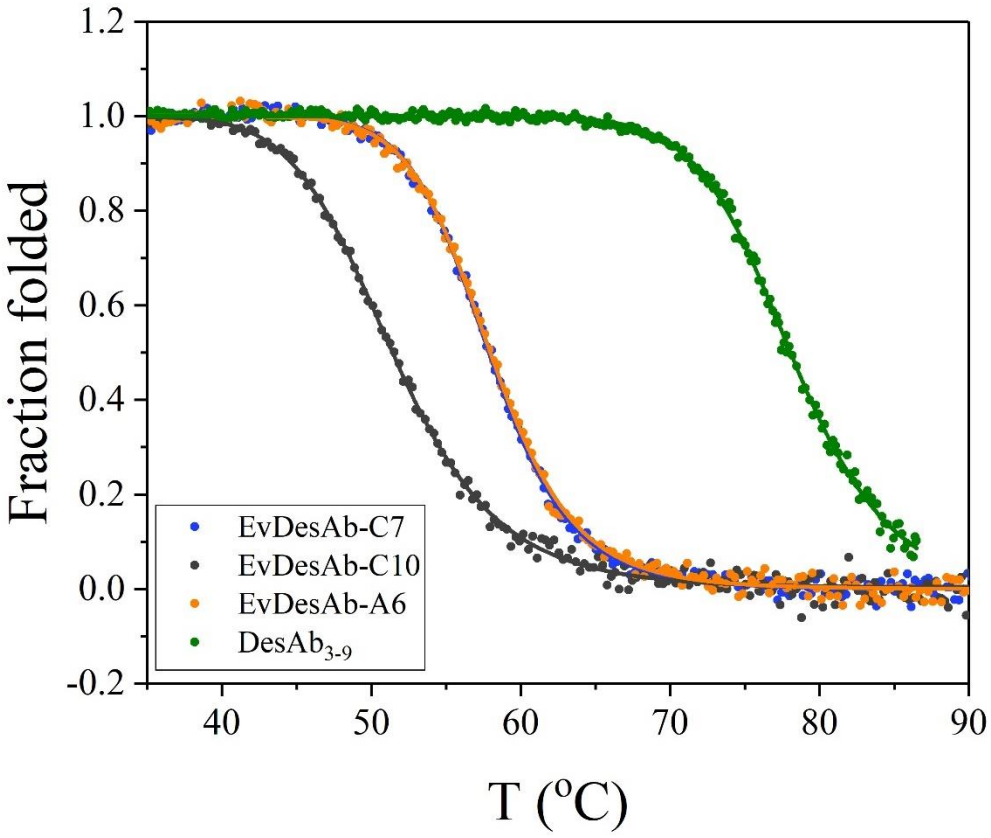

Figure 3.23. Comparison of the thermal denaturation curves of $DesAb_{3-9}$ and its EvDesAbs as monitored in the far-UV region (207 nm) by CD. The thermal denaturation curves of $DesAb_{3-9}$ (dark green), EvDesAb-C7 (dark blue), EvDesAb-C10 (dark grey) and EvDesAb-A6 (orange) are shown as the folded fraction with their two-state model fittings. Values shown the mean averages of three independent experiments.

Table 3.2. Calculated melting temperatures (T_m) for $DesAb_{3-9}$ and its EvDesAbs.

Antibody	T_m (°C)
$DesAb_{3-9}$	78.1 ± 0.3
EvDesAb-A6	58.0 ± 0.1
EvDesAb-C7	57.9 ± 0.1
EvDesAb-C10	51.4 ± 0.1

The thermal denaturation curves for $DesAb_{3-9}$ and its EvDesAbs showed a substantial decrease in the melting temperatures of EvDesAb-A6 (20.1 ºC), EvDesAb-C7 (20.2 ºC) and EvDesAb-C10 (26.7 ºC). These large decreases in melting temperature suggest that at least some the selected mutations have a largely destabilising effect on the sdAb framework. The comparison of the thermal denaturation curves of $DesAb_{29-36}$ and its EvDesAbs is shown in Figure 3.24 and their calculated melting temperatures (T_m) are shown in Table 3.3.

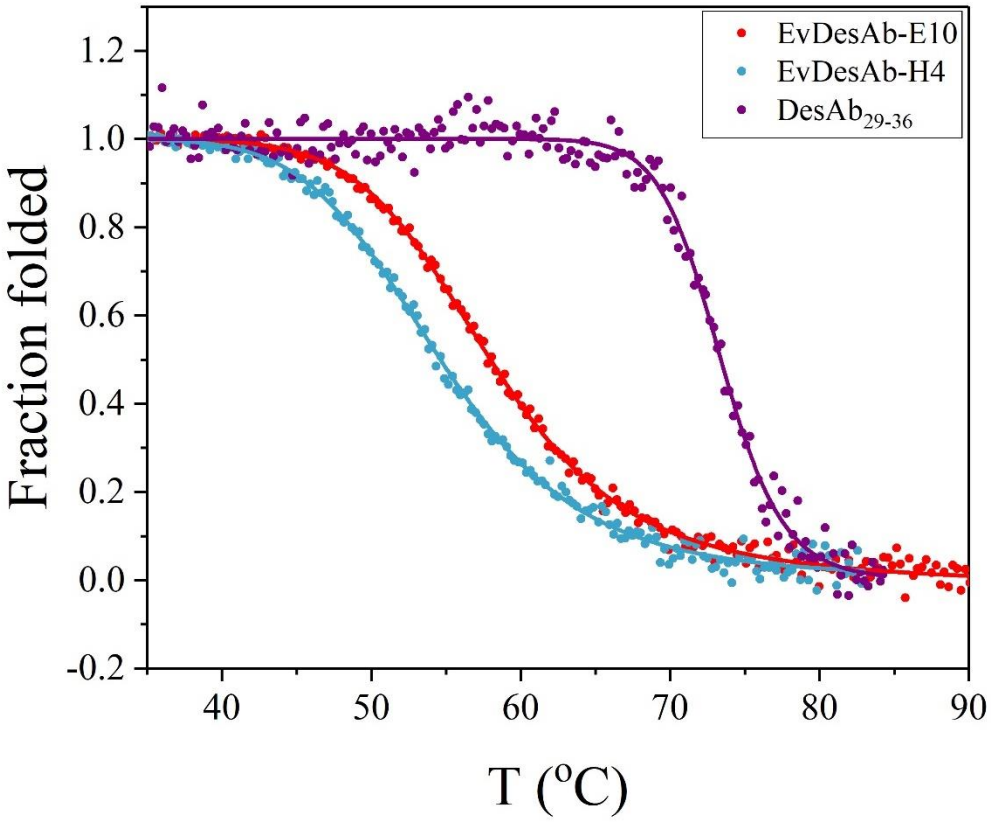

Figure 3.24. Comparison of the thermal denaturation curves of $DesAb_{29-36}$ and its EvDesAbs as monitored in the far-UV region (207 nm) by CD. The thermal denaturation curves of $DesAb_{29-36}$ (purple), EvDesAb-E10 (red) and EvDesAb-H4 (pale blue) are shown as the folded fraction with their two-state model fittings. Values shown the mean averages of three independent experiments.

Table 3.2. Calculated melting temperatures (T_m) for $DesAb_{29-36}$ and its EvDesAbs.

Antibody	T_m (ºC)
$DesAb_{29-36}$	73.4 ± 0.3
EvDesAb-E10	58.0 ± 0.1
EvDesAb-H4	54.6 ± 0.2

The thermal denaturation curves for $DesAb_{29-36}$ and its EvDesAbs also a showed substantial decrease in the melting temperatures for EvDesAb-E10 (15.4 ºC) and EvDesAb-H4 (18.8 ºC).

3.9 Results: Thermal stability selection with Protein A

As all the characterised EvDesAbs yielded by competitive affinity selection showed changes to the secondary structure content and large losses in thermodynamic stability, it was hypothesised that the combination of the observed high mutation frequency selection and the aggregation-prone nature of $A\beta_{40}$ had selected for highly destabilising mutations, potentially promoting the co-aggregation of the evolved sdAbs with $A\beta_{40}$. An attempt was made to rectify this potential detrimental fitness-selection by exploiting the heat-resistance of bacteriophage[229, 277, 278] and the exquisite selectivity of Protein A for folded Abs[250-252, 279]. Protein A can be used to select for thermally-stable Abs by subjecting the Ab-displaying phage to a high-temperature and then selecting for stable and/or reversibly folding EvDesAbs by binding to Protein A. The latter point is of much importance as none of the characterised selected EvDesAbs displayed reversible thermal denaturation. Heat-induced unfolding should, in theory also select for aggregation-resistant EvDesAbs as transient heating induces aggregation of misfolded proteins, which are subsequently lost from selection with Protein A[279]. It was decided to perform thermal stability selection with Protein A on the selected $DesAb_{3\text{-}9}$ and $DesAb_{29\text{-}36}$ libraries resulting from the 5^{th} round of competitive affinity selection. The temperature chosen for thermal stability selection was 60 ºC as this was deemed to be enough to induce the unfolding of non-desirable, irreversibly unfolding EvDesAbs and also because phage infectivity is mostly retained at this temperature. A comparison of the output phages resulting from room-temperature selection and selection at high-temperature is shown in Figure 3.25.

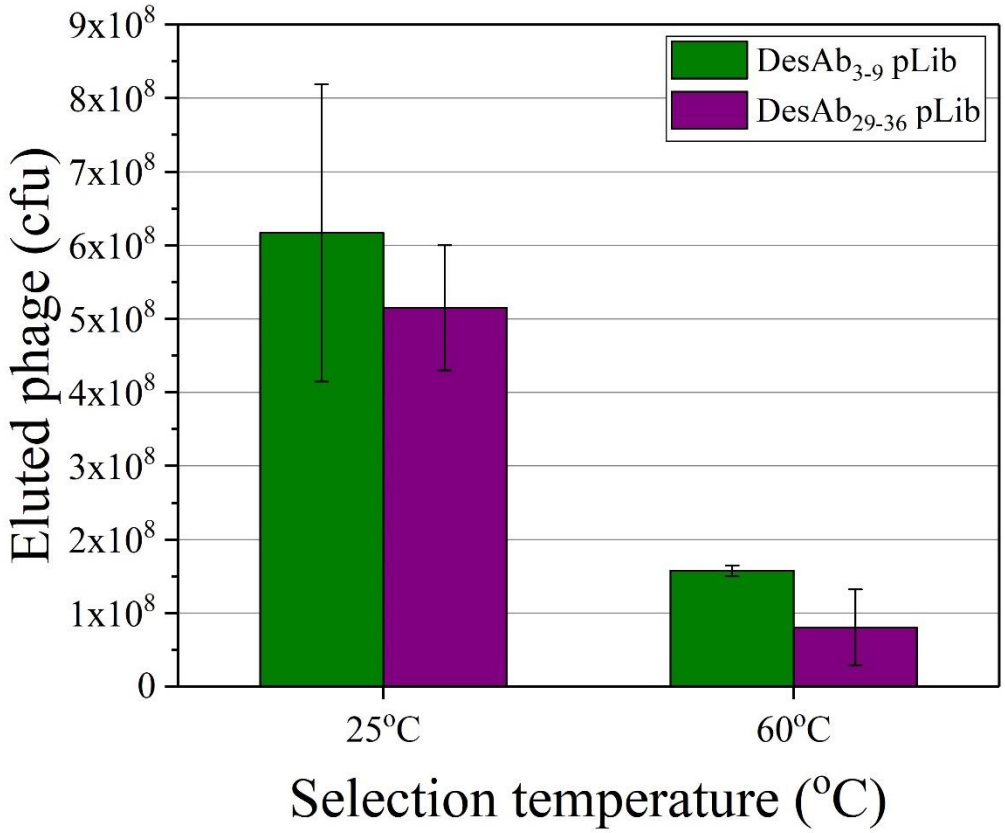

Figure 3.25. Comparison of the effect of temperature pre-treatment on the output phage titres of DesAb$_{3-9}$ pLib and DesAb$_{29-36}$ pLib selected by binding to Protein A. The output phage titres for DesAb$_{3-9}$ (dark green) and DesAb$_{29-36}$ (purple) are shown for both 25 ºC and 60 ºC pre-treatment. Bars represent the mean average and error bars represent the standard deviation of three repeat measurements.

The effect of thermal pre-treatment at 60 ºC on the DesAb$_{3-9}$ and DesAb$_{29-36}$ library phage recovery with Protein A was clearly observed, with a ~3.9-fold loss in library population for DesAb$_{3-9}$ pLib and a ~6.4-fold loss for DesAb$_{29-36}$ pLib, with comparison to Protein A selection at 25 ºC. This decrease does suggest that the majority of the both library members suffer poor thermal stability and/or irreversible unfolding, and DesAb$_{3-9}$ pLib likely contains a higher proportion of poorly stable EvDesAbs. These data do not reveal the actual diversity percentage loss resulting from thermal treatment due to the different expression levels for each clone, however it can be assumed that substantial diversity restriction had indeed occurred.

3.10 Results: Crude extract screening for thermal stability-selected antibodies against $A\beta_{40}$ oligomers

3.10.1 EvDesAb-expressing cell-lysate screening via ELISA

Crude-extract EvDesAb screening of the 60 ºC thermally-selected libraries for binding to $A\beta_{40}$ oligomers was performed using the same methodology as described in Chapter 2.5.1, with Zn^{2+}-stabilised $A\beta_{40}$ oligomers used again as target Ag. 92 clones were screened from each library, with crude extracts containing $DesAb_{3\text{-}9}$, $DesAb_{29\text{-}36}$ and a non-binding DesAb (DesAb-F) as controls for comparison. The results of the screening for both $DesAb_{3\text{-}9}$ pLib and $DesAb_{29\text{-}36}$ pLib are shown together for comparison in Figure 3.26.

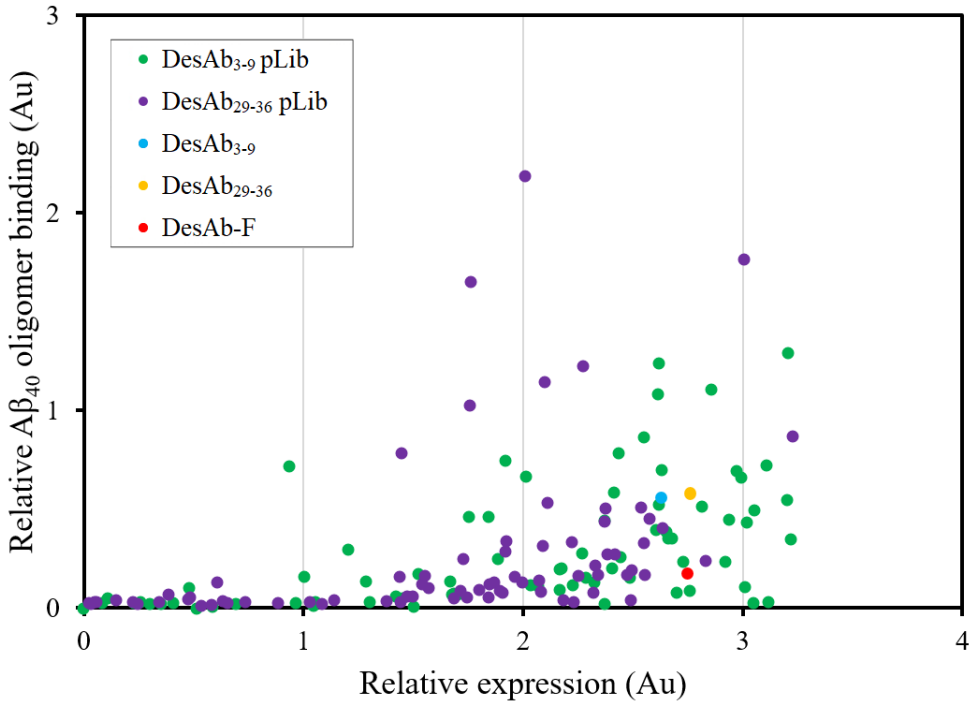

Figure 3.26. Crude extract screening of individual EvDesAbs from $DesAb_{3\text{-}9}$ pLib and $DesAb_{29\text{-}36}$ pLib after stability selection with Protein A, as measured by ELISA. $DesAb_{3\text{-}9}$ pLib EvDesAbs are shown in green and $DesAb_{29\text{-}36}$ pLib EvDesAbs are shown in purple. For comparison with the parental DesAbs, $DesAb_{3\text{-}9}$ is shown in blue and $DesAb_{29\text{-}36}$ is shown in orange. DesAb-F is shown in red as a negative control. Values are the measurements of the 450 nm absorbance (Au) change produced by the oxidation of TMB, which is proportional to the presence of the screened Abs.

Unlike the crude-extract ELISA screens described in Chapter 3.5.1, a slightly higher proportion of screened EvDesAbs (15.2% for $DesAb_{3\text{-}9}$ pLib and 8.7% for $DesAb_{29\text{-}36}$ pLib) displayed

improved binding scores with respect to their parental DesAbs. Also, the proportion of EvDesAbs with increased expression scores increased for $DesAb_{3-9}$ pLib from 4.3% to 22.8%, as a result of thermal stability selection. This indicates that significant expression selection occurred for $DesAb_{3-9}$ pLib, whilst $DesAb_{29-36}$ pLib appeared to be largely unaffected. 3 EvDesAbs from each library with improved binding scores were selected for further characterisation and their mutation distributions are shown in Table 3.3.

Table 3.3. Selected $DesAb_{3-9}$ and $DesAb_{29-36}$ EvDesAb mutations as revealed by DNA sequencing. Clones identities correspond to their ELISA screen microwells. Mutations marked in bold are conserved either within or between libraries. Mutations marked with an underline are potential 'hotspot' mutations (i.e. different mutations occurring at the same position). Mutations marked with an asterisk correspond to conserved or 'hotspot' mutations between libraries, downstream of the grafted CDR3 sequence. This is because $DesAb_{29-36}$ has a longer CDR3 loop by one residue, shifting the numbering of $DesAb_{29-36}$ residues by +1 after the CDR3 loop. Mutations marked in green are in the CDR3 loop. No mutations were found in the CDR1 or CDR2 loops. Mutations involving a Cysteine are highlighted in red.

DesAb3-9		**DesAb29-36**	
Clone	***Mutations***	***Clone***	***Mutations***
A4	T32K, **P41H**, **E89D**, E109V, **V120M**	***B11***	E1A, W47L, **W115R**, G118A, V123A*
C3	A23G, **P41S**, V48M, **S63R**	***F9***	**S25C**, **Y33H**, **E109K***
D2	**E1G**, V12E, S25R, **F27L**, **N84Y**, **T91I**	***D4***	A98S, **V123E***

The mutations for the selected EvDesAbs were analysed and classified with comparison to the analysis in Chapter 3.5.2. Unfortunately, a larger scale DNA sequencing analysis for the stability-selected EvDesAbs was not possible due to time constraints. Once again, the average mutation frequency was higher than the un-selected ep-PCR library at ~4.2 mutations per 'improved clone'.

3.10.2 Expression and purification of soluble evolved antibody fragments

Following crude extract screening, the selected EvDesAbs of $DesAb_{3-9}$ and $DesAb_{29-36}$ were expressed and purified as described in Chapter 2.5.3. A representative purification comparison of a DesAb ($DesAb_{29-36}$) and one of its thermal stability-selected EvDesAbs (EvDesAb-B11) is illustrated in Figure 3.27.

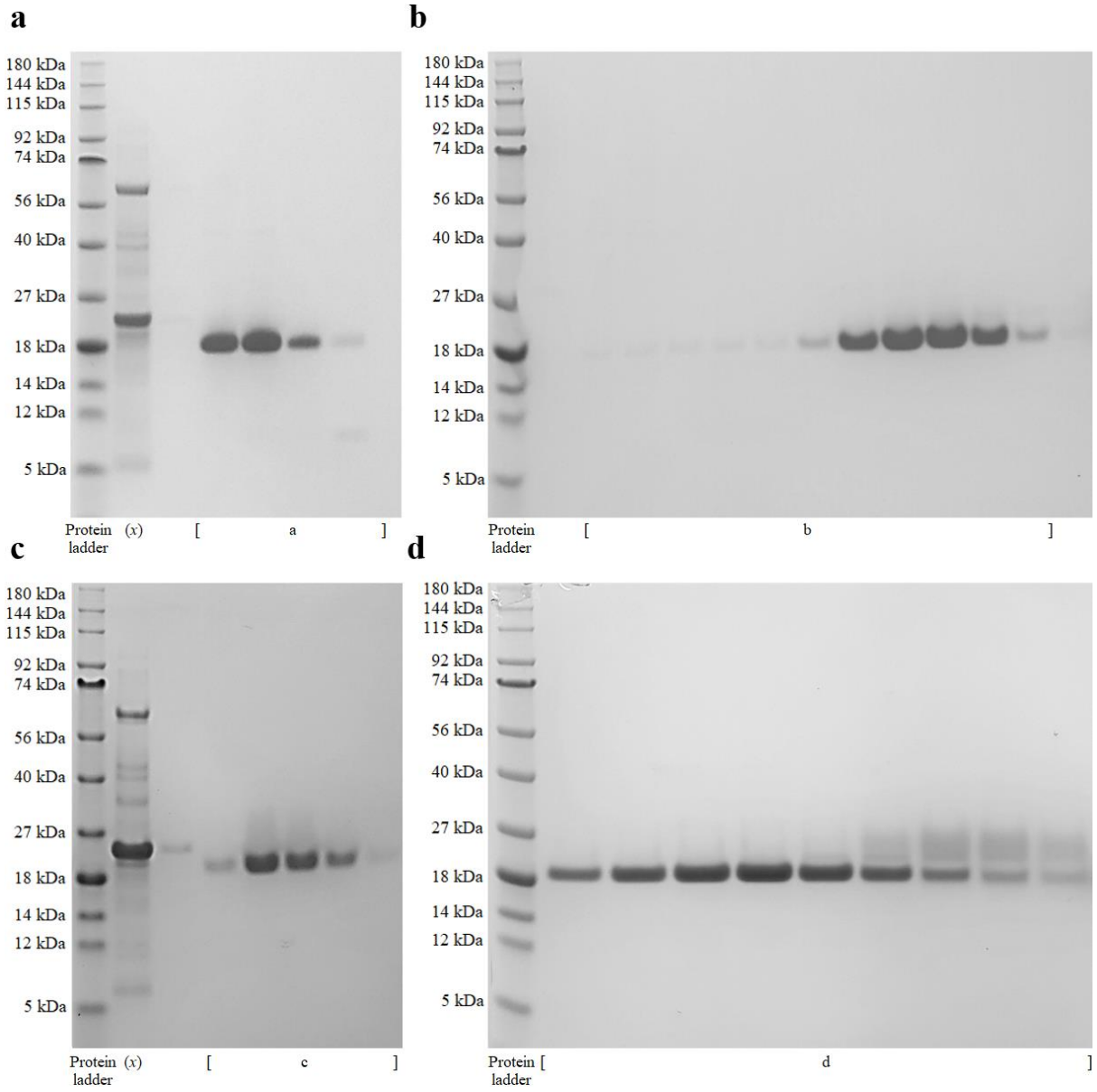

Figure 3.27. SDS PAGE analysis of the purifications of DesAb$_{29-36}$ and one of its thermal stability-selected mutants (EvDesAb-B11). a) IMAC purification of DesAb$_{29-36}$ (~18 kDa). b) SEC purification of DesAb$_{29-36}$. c) IMAC purification of EvDesAb-B11 (~18 kDa). d) SEC purification of EvDesAb-B11. (*x*) Discarded *E. coli* periplasmic extract flow-through.

Again, all expressed EvDesAbs from thermal stability selection displayed the same similar characteristic 'smear' observed in Chapter 3.5.3, as shown in the representative EvDesAb-B11 IMAC and SEC purification SDS PAGE analyses in Figure 3.27. The eluted EvDesAb fractions in SEC purifications were combined, excluding the later fractions (on the right hand side of Figure 3.27 (d)) containing the smeared bands, in an attempt to remove this potential contamination.

3.11 Results: Aβ$_{42}$ aggregate selectivity characterisation of thermal stability-selected antibodies by ELISA

The Aβ$_{42}$ aggregate selectivity characterisation of the thermal stability-selected EvDesAbs of DesAb$_{3-9}$ and DesAb$_{29-36}$ was performed using the same ELISA experiment described in Chapter 3.6. The results of Aβ$_{42}$ aggregate binding selectivity ELISAs are shown for the EvDesAbs of DesAb$_{3-9}$ in Figure 3.28 and the EvDesAbs of DesAb$_{29-36}$ in Figure 3.29. In both experiments, relative comparisons were made with the parental DesAbs and a sequence-specific commercial anti-Aβ$_{42}$ Ab (6E10).

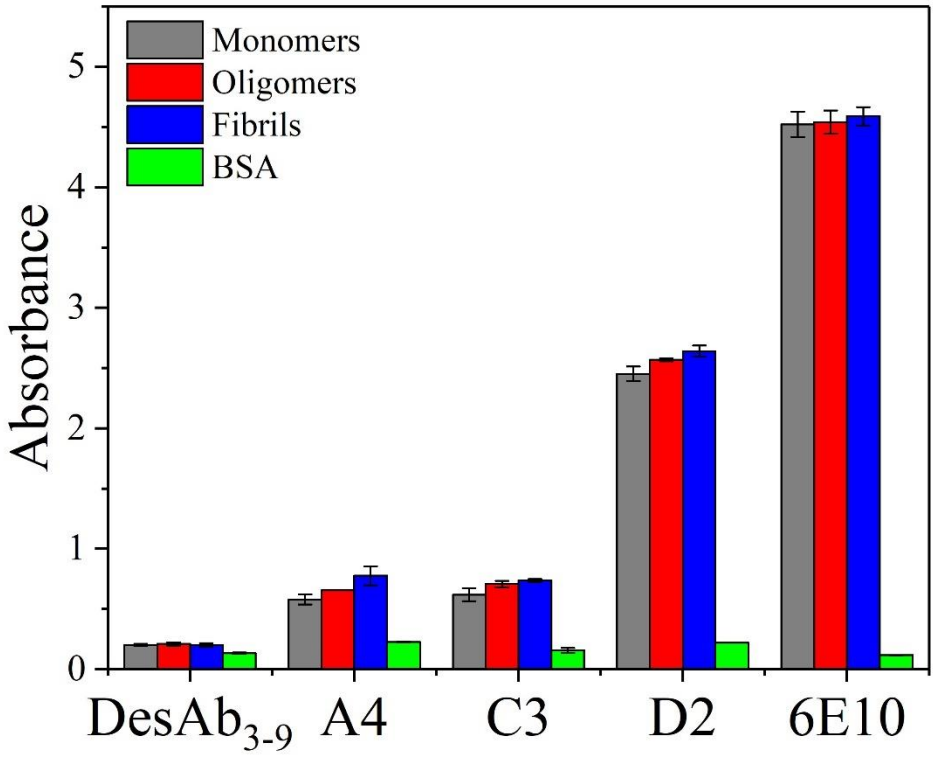

Figure 3.28. DesAb$_{3-9}$ EvDesAb binding selectivity to Aβ$_{42}$ aggregate species as measured by ELISA. Values are the measurements of the 450 nm absorbance (Au) change produced by the oxidation of TMB, which is proportional to the binding strength of the screened Abs. The relative binding affinities of EvDesAb-A4, EvDesAb-C3 and EvDesAb-D2 to Aβ$_{42}$ monomers (grey), oligomers (red), fibrils (blue) and BSA (negative control, green) are shown with comparison to the parental DesAb$_{3-9}$ and the commercial Ab 6E10. Error bars represent the standard deviation of four repeats and bars represent the mean average.

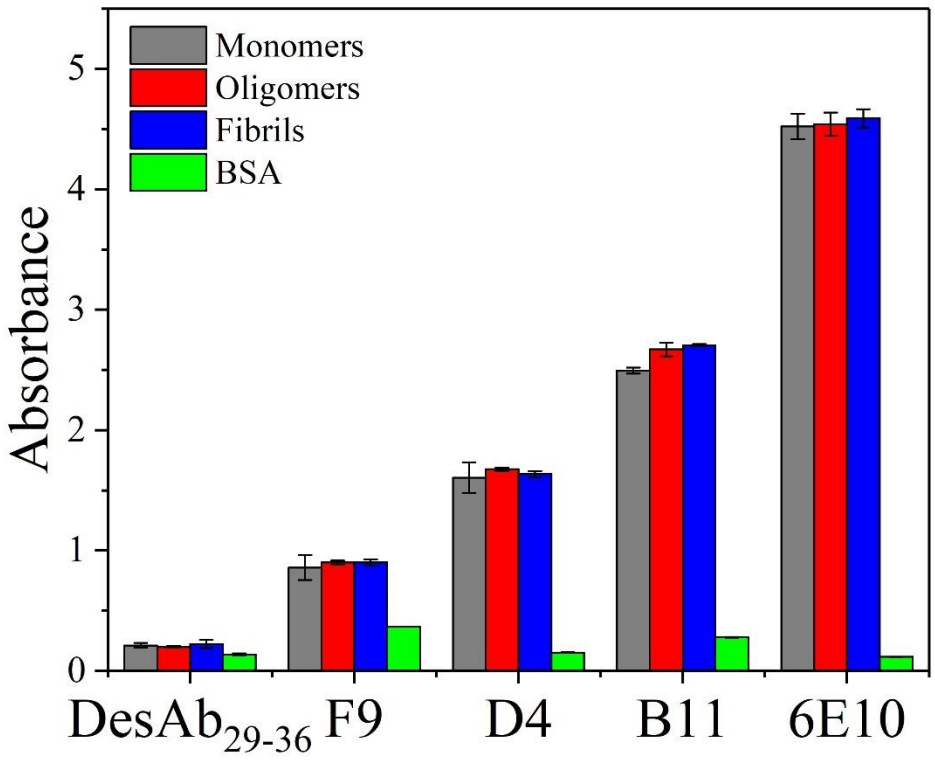

Figure 3.29. DesAb$_{29\text{-}36}$ EvDesAb binding selectivity to Aβ$_{42}$ aggregate species as measured by ELISA. Values are the measurements of the 450 nm absorbance (Au) change produced by the oxidation of TMB, which is proportional to the binding strength of the screened Abs. The relative binding affinities of EvDesAb-F9, EvDesAb-D4 and EvDesAb-B11 to Aβ$_{42}$ monomers (grey), oligomers (red), fibrils (blue) and BSA (negative control, green) are shown with comparison to the parental DesAb$_{29\text{-}36}$ and the commercial Ab 6E10. Error bars represent the standard deviation of four repeats and bars represent the mean average.

Again, the results of the Aβ$_{42}$ aggregate binding selectivity ELISA showed a large difference between the average Aβ$_{42}$ binding affinities of the EvDesAbs relative to one another, their parental DesAbs and 6E10. All selected EvDesAbs once again showed improvements in average Aβ$_{42}$ binding affinities compared to their parental DesAbs, suggesting that thermal stability-selection had retained some Aβ-binding EvDesAbs even with its risk of selecting rapidly propagating non-binding EvDesAbs. Again however, there was little difference between the Aβ$_{42}$ binding selectivities for monomers, oligomers and fibrils for the EvDesAbs, indicating that conformation-specificity remains elusive. For all EvDesAbs, with the exception of EvDesAb-F9 and EvDesAb-D4, there was a consistent (but not significant) increased binding signal to the lag-phase and growth plateau time-point samples compared to the fresh Aβ$_{42}$ monomer sample, indicating a slightly stronger binding affinity towards one or more aggregate species present in the time-point samples. As the maximum signal for these EvDesAbs belonged to the growth plateau time-point, it can be concluded that each EvDesAb preferentially binds to the dominant fibrillar aggregates present. EvDesAb-F9 and EvDesAb-

D4 showed a more even binding to all samples, like 6E10, indicating a lack of any conformational binding preference. There was a clearly visible increase in the BSA binding signal for EvDesAb-A4, EvDesAb-D2, EvDesAb-F9 and EvDesAb-B11; comparable to the $A\beta_{42}$ binding signals of $DesAb_{3\text{-}9}$ and $DesAb_{29\text{-}36}$. This implies an increase in EvDesAb cross-reactivity towards non-Aβ proteins.

3.12 Results: $A\beta_{42}$ aggregation inhibition characterisation

Following $A\beta_{42}$ aggregate selectivity characterisation of the thermal stability-selected EvDesAbs, the $A\beta_{42}$ aggregation inhibition potential of each EvDesAb was evaluated using the techniques described in Chapters 1.2.2, 1.3.1 and 3.7. Of the characterised thermal stability-selected EvDesAbs, only EvDesAb-B11 showed a dose-dependent inhibition of $A\beta_{42}$ aggregation. The $A\beta_{42}$ aggregation inhibition curves of EvDesAb-B11 are shown in Figure 3.30 and the comparisons of the calculated global parameters k_+k_n and k_+k_2 of the EvDesAb-B11 with its parental $DesAb_{29\text{-}36}$ are shown in Figure 3.31.

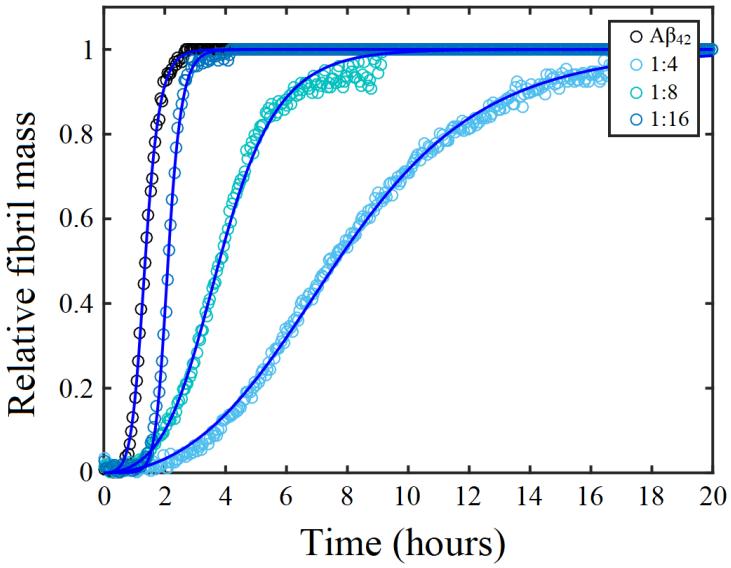

Figure 3.30. $A\beta_{42}$ aggregation curves for the EvDesAb-B11. Each aggregation curve was normalised to the maximum ThT fluorescence signal of the growth plateau phase, which yields each curve as a fraction of fibril mass (*y*-axis). The $A\beta_{42}$ aggregation inhibition was followed by the change in ThT fluorescence over time (*x*-axis). Solutions containing 2 μM $A\beta_{42}$ were incubated in the presence of increasing concentrations of EvDesAb-B11 (shown as the molar ratio of EvDesAb-B11 to $A\beta_{42}$). The 1:2 ratio of EvDesAb-B11 to $A\beta_{42}$ is not shown as it did not reach the growth plateau, and thus could not be normalised. The aggregation of $A\beta_{42}$ in the absence of EvDesAb-B11 is also shown for comparison in black. Blue continuous lines represent the fits of the data using the integrated kinetic laws for $A\beta_{42}$ aggregation. The data shown are the mean average of three independent experiments.

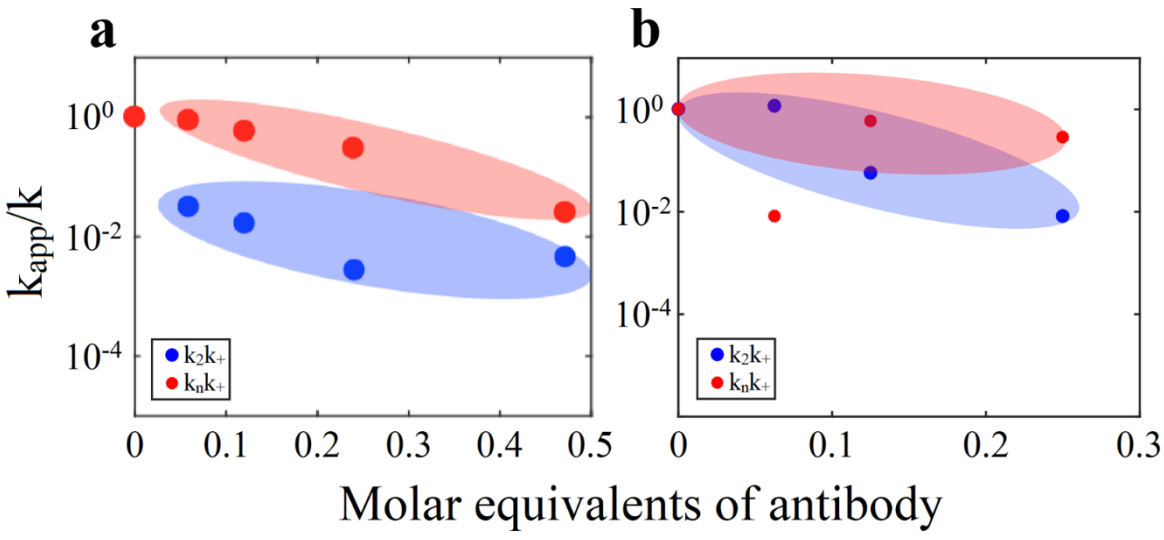

Figure 3.31. Comparison of the effect of DesAb$_{29-36}$ and EvDesAb-B11 on the global parameters k_+k_n and k_+k_2 of Aβ$_{42}$ aggregation. Shown are the decreases of the global parameters k_+k_n (red) and k_+k_2 (blue) as the direct result of Aβ$_{42}$ aggregation inhibition (*y*-axis), evaluated from the fits as a function of the relative DesAb/EvDesAb concentration to Aβ$_{42}$ monomer (*x*-axis). a) DesAb$_{29-36}$. b) EvDesAb-B11. The global parameters k_+k_n and k_+k_2 plot for DesAb$_{3-9}$ was reproduced with permission from reference [104].

The Aβ$_{42}$ aggregation curves for EvDesAb showed it to be the most potent inhibitor described so far, with comparable generation of relative fibril mass at 1:4 molar equivalence to the 1:2 molar equivalences of EvDesAb-H4 and EvDesAb-E10. Unfortunately, due to the inability to fit the 1:2 (0.5) molar equivalence of EvDesAb-B11 due to its high inhibition potency, an accurate comparison between the global parameters k_+k_n and k_+k_2 is unlikely to be possible. From the available global parameters k_+k_n and k_+k_2 for EvDesAb-B11, it appears that k_+k_n is somewhat unchanged (if the low concentration outlier is not taken into consideration), whilst k_+k_2 appears to increase slightly. This indicates a loss in selectivity for any specific microscopic nucleation inhibition rate for EvDesAb-B11. Had the 0.5 molar equivalence been able to be fitted, a more reliable conclusion could be made.

3.13 Results: Stability characterisation by circular dichroism spectroscopy

3.13.1 Evolved designed antibody structure characterisation

The characterisation of the effect of evolution on the secondary and tertiary structures on the thermal stability-selected EvDesAbs of $DesAb_{3-9}$ and $DesAb_{29-36}$ was performed by CD, again using the same methods described in Chapter 2.7.1. To characterise any changes in EvDesAb secondary structure, the CD spectra was recorded between 200-250 nm for each EvDesAb and its parental DesAb for comparison. The analysis of the EvDesAb secondary structure comparisons are shown in Figure 3.32 and Figure 3.33.

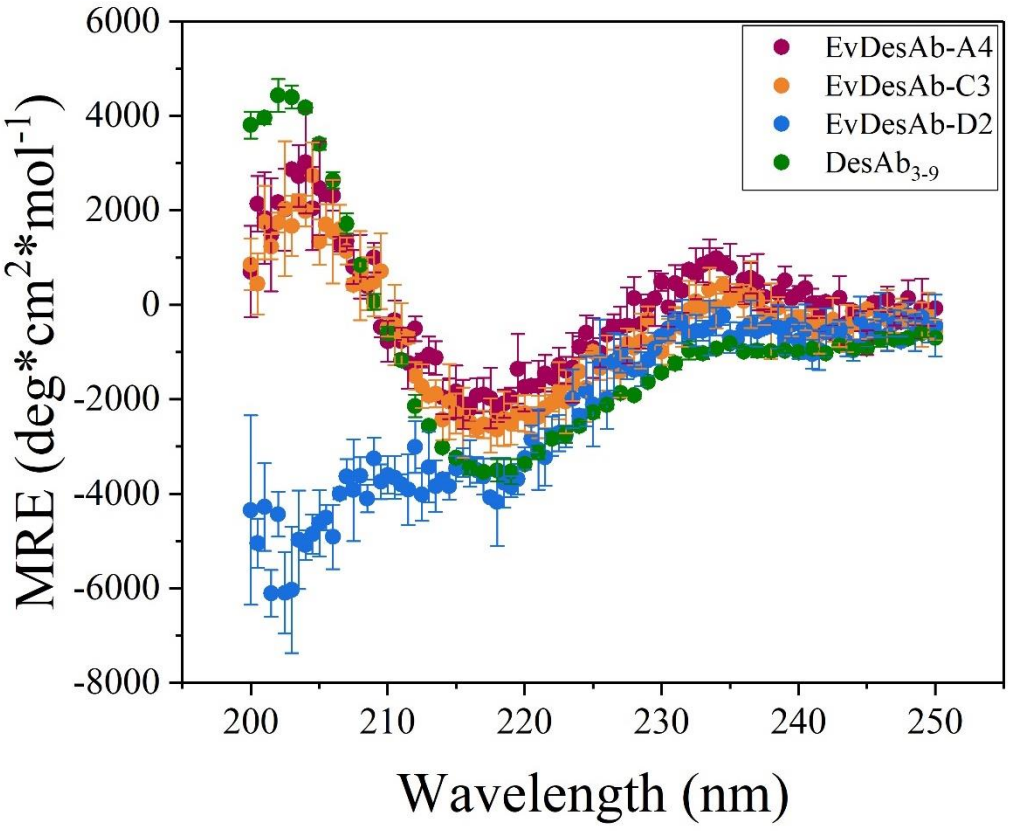

Figure 3.32. Analysis of $DesAb_{3-9}$ and its thermal stability-selected EvDesAbs with highest binding affinity as measured by CD in the far-UV region. Secondary structure analysis for all Abs are in terms of mean residue ellipticity (MRE) at a given wavelength. $DesAb_{3-9}$ (dark green), EvDesAb-A4 (maroon), EvDesAb-C3 (orange) and EvDesAb-D2 (blue) are shown for comparison. The data is shown as the mean average and error bars represent the standard deviation of three independent experiments.

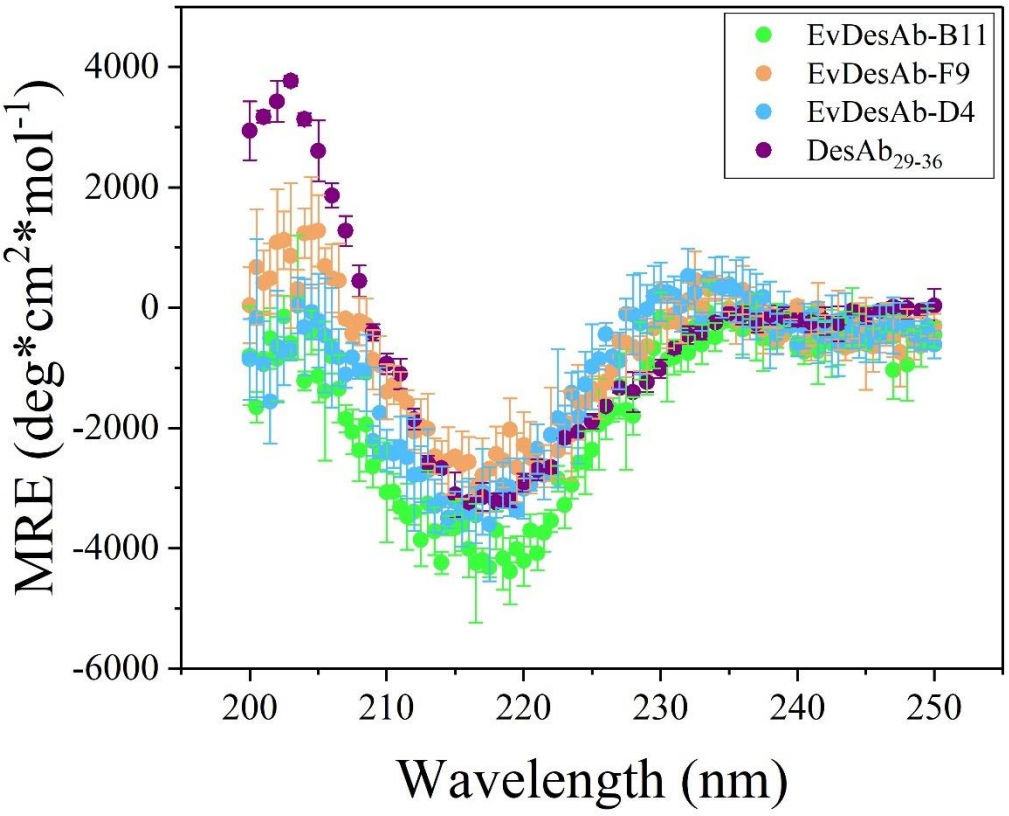

Figure 3.33. Analysis of DesAb$_{29-36}$ and its thermal stability-selected EvDesAbs with highest binding affinity as measured by CD in the far-UV region. Secondary structure analysis for all Abs are in terms of mean residue ellipticity (MRE) at a given wavelength. DesAb$_{29-36}$ (purple), EvDesAb-B11 (green), EvDesAb-F9 (orange) and EvDesAb-D4 (pale blue) are shown for comparison. The data is shown as the mean average and error bars represent the standard deviation of three independent experiments.

All EvDesAbs of both DesAb$_{3-9}$ and DesAb$_{29-36}$ display similar changes to the secondary structure as the EvDesAbs analysed in Chapter 3.8.1, with general decreases in the MRE from 200-215 nm and increases between 220-235 nm. This suggested that the EvDesAbs are again partially unfolded with respect to their parental DesAbs. This difference is clearly observed with EvDesAb-D2 which has such a drastically reduced MRE between 200-215 nm, that it is likely entirely random coil and almost completely unfolded. For the other EvDesAbs, it was again crucial to assess the effect of the potential partial unfolding on their tertiary structure stabilities.

3.13.2 Evolved designed antibody stability characterisation.

CD was used once again to assess the thermal stability of the heat treatment-selected EvDesAbs by following the MRE signal generated at 207 nm across a temperature gradient to determine

their melting temperatures (T_m). The comparison of the thermal denaturation curves of $DesAb_{3-9}$ and its thermal stability-selected EvDesAbs is shown in Figure 3.34 and their calculated melting temperatures (T_m) are shown in Table 3.4.

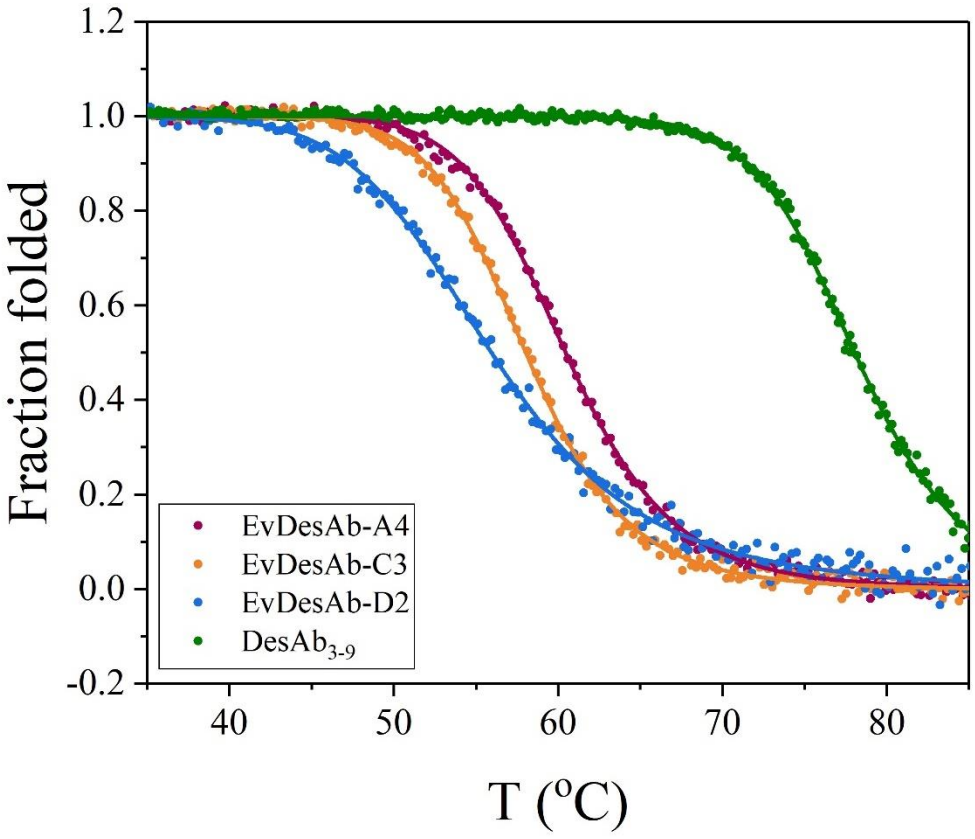

Figure 3.34. Comparison of the thermal denaturation curves of $DesAb_{3-9}$ and its thermal stability-selected EvDesAbs as monitored in the far-UV region (207 nm) by CD. The thermal denaturation curves of $DesAb_{3-9}$ (dark green), EvDesAb-A4 (maroon), EvDesAb-C3 (orange) and EvDesAb-D2 (blue) are shown as the folded fraction with their two-state model fittings. Values shown the mean averages of three independent experiments.

Table 3.4. Calculated melting temperatures (T_m) for $DesAb_{3-9}$ and its thermal stability-selected EvDesAbs.

Antibody	T_m (°C)
$DesAb_{3-9}$	78.1 ± 0.3
EvDesAb-A4	60.5 ± 0.1
EvDesAb-C3	58.0 ± 0.1
EvDesAb-D2	56.0 ± 0.2

The thermal denaturation curves for $DesAb_{3-9}$ and its EvDesAbs again showed a substantial decrease in the melting temperatures of EvDesAb-A4 (17.6 °C), EvDesAb-C3 (20.1 °C) and EvDesAb-D2 (22.1 °C). The comparison of the thermal denaturation curves of $DesAb_{29-36}$ and

its thermal stability-selected EvDesAbs is shown in Figure 3.35 and their calculated melting temperatures (T_m) are shown in Table 3.5.

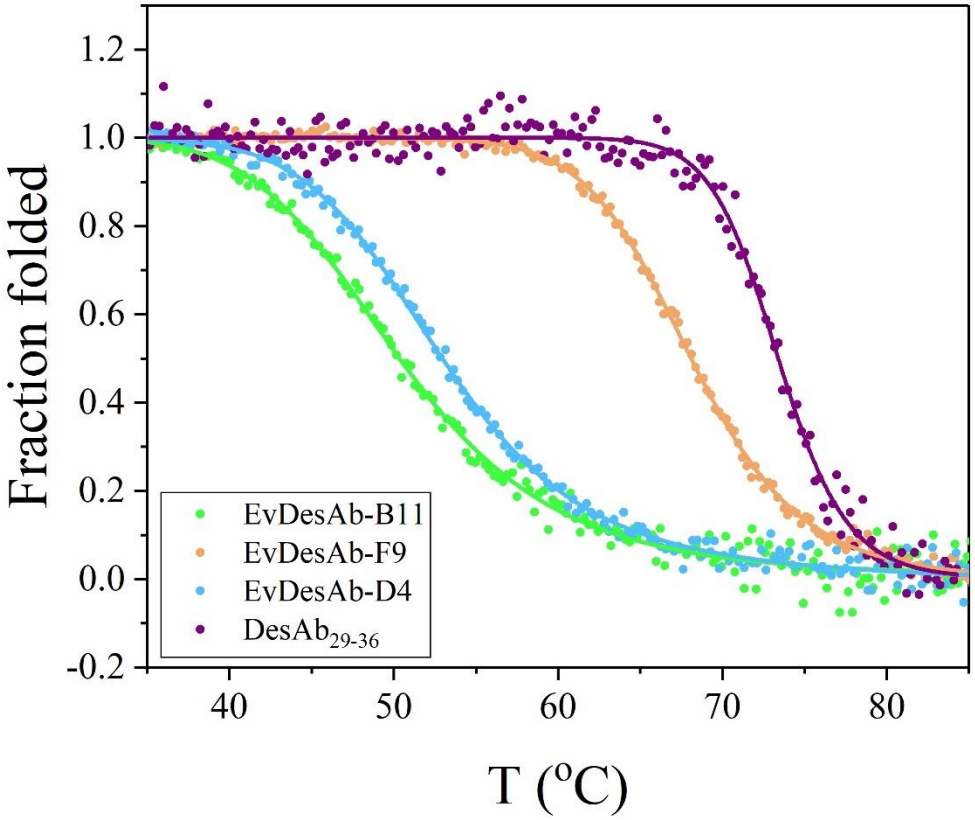

Figure 3.35. Comparison of the thermal denaturation curves of DesAb$_{29-36}$ and its thermal stability-selected EvDesAbs as monitored in the far-UV region (207 nm) by CD. The thermal denaturation curves of DesAb$_{29-36}$ (purple), EvDesAb-B11 (green), EvDesAb-F9 (orange) and EvDesAb-D4 (pale blue) are shown as the folded fraction with their two-state model fittings. Values shown the mean averages of three independent experiments.

Table 3.5. Calculated melting temperatures (T_m) for DesAb$_{29-36}$ and its thermal stability-selected EvDesAbs.

Antibody	T_m (ºC)
DesAb$_{29-36}$	73.4 ± 0.3
EvDesAb-F9	68.1 ± 0.1
EvDesAb-D4	53.0 ± 0.1
EvDesAb-B11	50.3 ± 0.2

The thermal denaturation curves for DesAb$_{29-36}$ and its thermal stability-selected EvDesAbs again also showed a substantial decrease in the melting temperatures for EvDesAb-D4 (20.4 ºC) and EvDesAb-B11 (23.1 ºC). The thermal stability loss for EvDesAb-F9 (5.3 ºC) was far less, and given that it was the weakest Aβ$_{42}$ binder in the ELISA characterisation for the EvDesAbs of DesAb$_{29-36}$, this suggests that Aβ binding affinity is correlated with thermal

stability loss, under these evolution conditions. In fact, this trade-off trend is observed for all characterised EvDesAbs described in this chapter, with the exceptions of EvDesAb-A6 and EvDesAb-C10.

3.14 Conclusion

In this chapter we explored the use of directed evolution of Modular-designed Abs to modify their selectivity towards Aβ, in an effort to alter the binding affinities towards different forms of the peptide and, as a result, alter its aggregation inhibition profile by selectively targeting specific microscopic nucleation events. Instead of engineering $DesAb_{3\text{-}9}$ and $DesAb_{29\text{-}36}$ for absolute binding affinity improvements, altering the presentation of the rationally designed CDR3 loop was favoured in an attempt to drive selection towards variants with more conformational specificity than linear sequence specificity. Due to the challenging nature of predicting which residue sites would give rise to CDR3 conformational changes upon mutation, ep-PCR whole-protein scanning mutagenesis was used to identify these positions by mutating the V_H framework region at random. The DesAb variants were then displayed on bacteriophage and subjected to competitive affinity selection, using Zn^{2+} stabilised $A\beta_{40}$ oligomers as a 'conformational' selection and $A\beta_{40}$ monomers as a negative 'sequence' selection. This experiment was designed enrich the phage libraries for Aβ conformations present in certain types of oligomers and not in the monomeric form, to ascertain how such a selection would affect the specificity and aggregation inhibition profiles of DesAbs with already significant theoretical oligomer reduction. What was found was that, whilst significant improvements to the binding to Aβ were observed (as determined by ELISA), no clear specificity towards any species present in the aggregation of $A\beta_{42}$ could been found in any of the characterised EvDesAbs. This improvement towards Aβ binding did not correlate to the inhibition of $A\beta_{42}$ aggregation, with <40% of characterised EvDesAbs showing dose-dependent inhibition. Of the four EvDesAbs showing $A\beta_{42}$ aggregation inhibition, three showed the desired divergence in the global rate parameters k_+k_n and k_+k_2 that was hypothesised to be a result of competitive affinity selection. This positive result was not without disadvantage, as a serious trade-off occurred with each improved binder showing substantial losses in thermal stability and changes to the β-sheet content of the framework region. Efforts to alleviate these issues with thermal pre-treatment selection by binding to Protein A were unsuccessful, suggesting that the choices of diversification and selection strategies may be inherently flawed.

Chapter 4: Discussion and future work

The overarching aim of the work described in this thesis was to explore the protein-engineering potential of Abs rationally designed by Modular. At the start of this work, the Cascade and CamSol methods that form the basis of Modular had only recently been described[176, 195] and required further validation as an applicable technique for generating useful artificial PPIs. Naturally, a key desirable application of Modular is the engineering of Ab binding interactions and for rational design to offer a genuinely competitive alternative to the already powerful established methods of Ab discovery, the Abs yielded by rational design must be engineerable to the standards required for typical Ab applications. As mentioned in Chapter 1.4.1, it is very common for Ab leads to be subjected to *in vitro* affinity maturation in order to obtain the binding affinities desired for therapeutic/diagnostic applications[166, 167]. For this reason, directed evolution was used as the protein-engineering technique of choice, not only because of the immense throughput offered but because it the most standardised practice of achieving *in vitro* affinity maturation[196-198, 201, 203]. By applying directed evolution to the DesAbs yielded my Modular, we sought to use the advantages of the throughput offered to improve the 'fitness' of the DesAbs to maximise their potential as tools for research, whilst simultaneously demonstrating that Modular offers a novel approach to targeting pre-selected poorly-immunogenic epitopes, which can be extremely challenging via classical methods[36, 176].

Since the start of this work, the disordered epitope pre-selection potential of Modular was put to effective use in another study which showed the importance of epitope targeting on protein aggregation[104]. As the field of neurodegenerative disorders research is facing an overhaul in the perception of effective treatment towards preventative intervention[141], therapeutics targeting the modulation of pathological protein aggregation require careful understanding of the precise mechanisms they affect, in order to ensure maximum reduction of pathological aggregate generation with the minimum amount of disruption to healthy cellular processes[85, 104, 137]. The DesAbs generated using Modular to target epitopes across the majority of the length of $A\beta_{42}$ offered a fascinating insight into which regions could potentially be targets for the design of therapeutics aiming to inhibit specific microscopic nucleation events and modulate the entire aggregation pathway towards a reduced disease pathology. $DesAb_{3-9}$ and $DesAb_{29-36}$ showed not only a large reduction in the theoretical concentrations of $A\beta_{42}$ oligomers when used as aggregation inhibitors, but also selective inhibition of primary and

secondary nucleation rather than fibril elongation. These DesAbs represented attractive starting points for further microscopic event inhibition selectivity and this work aimed to further improve their selectivity by decreasing their primary nucleation inhibition and increasing their secondary nucleation inhibition or simply increasing the difference between the two. This use of Abs to act as neutralising agents of specific microscopic protein nucleation has recently been described with the use of phage display selection, coupled with kinetic screening, to identify desirable aggregation inhibitors[137]. This study involved the use of a commercial synthetic scFv naïve library (Tomlinson I + J) and acted as inspiration for the use of directed evolution and affinity selection once again, in order to modify the neutralising abilities of Modular DesAbs towards their target protein/peptide aggregation and attempt to demonstrate their ability to be comparable with Ab leads discovered through classical methods.

In Chapter 2, the results of the *in vitro* affinity maturation of DesAb-F were presented as evidence that Abs rationally designed through the use of Modular yield engineerable 'hits' that can be subjected to the typical development strategies required for generating 'leads'. DesAb-F was chosen for this study as it represented the unique method of targeting a pre-selected epitope and offering the low resource-intensive Ab discovery offered by Modular. It was also chosen as, at the time, it was the most characterised DesAb generated by Modular rational design[176]. The development of DesAb-F to improve its weak binding affinity would have provided good evidence that DesAbs are comparable to hits from classical Ab discovery, however it was crucial that their key advantage over immunisation/naïve library selection of being able to target a predetermined disordered epitope was retained in the engineered variants. With this in mind, it was necessary to implement an identical evolution of a control Ab to show that the affinity maturation of a non-designed Ab would not reach the same level of improvement. This hypothesis was realised when it was observed that the identical evolution of DesAb-IAPP yielded EvDesAbs of weaker average binding affinities towards αSyn and divergent CDR2 residue characteristics to the EvDesAbs of DesAb-F. The EvDesAbs of both DesAb-F and DesAb-IAPP displayed minimal changes to the β-sheet content of their sdAb framework regions, suggesting that focussed mutagenesis on the CDR2 loop is highly tolerated and that the EvDesAb folding is largely the same as the parental DesAbs. However, all EvDesAbs showed some form of loss of thermal stability, although the average losses for the EvDesAbs of DesAb-F (~5.5 ºC) was less pronounced than those for the EvDesAbs of DesAb-IAPP (~13.6 ºC). This may have likely been the result of the difference between the polar/charged CDR2 residue enrichment for DesAb-F pLib and the non-polar/amphipathic

residue enrichment for DesAb-IAPP pLib. The exposed non-polar/amphipathic residues in the CDR2 loops of the DesAb-IAPP EvDesAbs would certainly negatively affect their solubility and it would be interesting to characterise their effects using solubility measurements such as PEG precipitation[280]. If possible, obtaining X-ray crystal structures would allow the structural visualisation of the sdAb frameworks and the identification of any tertiary structure changes induced by the mutations.

The choice of the conservative DNA library design strategy was reflective of the desire to retain the pre-selected epitope of DesAb-F and for this 'pilot' study this decision appeared to pay off as, whilst the affinity improvements of the resulting EvDesAbs was modest at best, the pre-selected epitope was retained in each of the variants as indicated in the binding affinity comparisons with the Proline-disrupted epitope variant of αSyn. The possibility still remains that the evolved CDR2 loops of the EvDesAbs could be separately binding to another epitope of αSyn due to its inherent flexibility, which may not be implausible as the polar/charged residue-enriched CDR2 loops complement binding towards the acidic C-terminus of αSyn more than the highly hydrophobic predetermined epitope (VVTGVTAV). This phenomenon may be observed through the use of heteronuclear single quantum coherence (HSQC) spectroscopy by comparing the spectra of unbound and EvDesAb-bound ^{15}N-labelled αSyn and analysing broadening or chemical shift perturbations of resonances of residues outside of positions 70-77. Nonetheless, the encouraging results of the Proline-disrupted epitope binding experiments suggest that less conservative diversification strategies may be employed to further increase the binding affinity potential of Modular DesAbs without loss of the predetermined epitope. Exploring more CDR chemical space through the use of an increased number of simultaneous focussed residue randomisation will likely increase the binding affinities towards the low-nanomolar range desirable for therapeutic and diagnostic applications. An attractive strategy may be the randomisation of the residues flanking the grafted peptide in the CDR3 loop of DesAb-F, which is a method that has been shown to be reliable for conformational epitopes[179]. For example, randomisation of two residues on either side of the complementary peptide may increase the length of the β-sheet-like binding interaction without too much risk of losing the selected epitope. The current method of CDR2 evolution may also be improved upon as, whilst the CDR2 loop of DesAb-F is in relatively close proximity to the grafted complementary peptide, it is much more restricted in its flexibility. It may be desirable to extend the 6-residue CDR2 loop to allow the flexibility required for both CDR2 and CDR3 loops to bind a linear epitope in a parallel manner. As the

optimal size of the extension is unknown, the length and residue content could be simultaneously randomised. It would be interesting to establish a DesAb-F library with 4 randomised residues in the CDR2 loop and also a randomised length (~6-9 residues).

The determination of EvDesAb binding affinities to αSyn using MST proved to be straightforward, however it only allowed the determination of the K_D and not the kinetic rates k_{on} and k_{off}. These kinetic rates would have been useful to obtain to allow feedback and optimisation of future affinity selection conditions (such as the competitive affinity selection described in Chapter 3). These kinetic rates could be readily obtained through the use of real-time immobilisation binding measurements such as surface plasmon resonance (SPR) and biolayer interferometry (BLI). These methods are also suitable for binding affinity measurements against fibrillar aggregates[137], which would also be interesting to characterise as DesAb-F showed sub-stoichiometric inhibition of αSyn fibril elongation, indicating fibril binding activity. For this reason, the inhibition of the seeded aggregation of αSyn using the EvDesAbs generated in this work should also be compared to that of DesAb-F to determine the effect (if any) of improved affinity against the NAC region on the formation of αSyn amyloid fibrils. Finally, it may prove very useful to perform high-throughput sequencing of the libraries obtained after each round of biopanning to provide binding selection residue evolution data as feedback for the optimisation of the Cascade method for complementary peptide design.

In Chapter 3, the results of the evolutions of $DesAb_{3-9}$ and $DesAb_{29-36}$ to alter their selectivities against Aβ aggregates and/or $Aβ_{42}$ aggregation inhibition was presented. As mentioned previously, the decision to implement random mutations into the sdAb framework of $DesAb_{3-9}$ and $DesAb_{29-36}$ was made with the goal of changing the conformation of their rationally designed CDR3 loops to promote their presentation towards preferential binding to conformational epitopes present in kinetically trapped Aβ oligomers, rather than to the free monomer. It was hoped that selection using $Aβ_{40}$ oligomers would translate to increased interactions of the resulting EvDesAbs with the oligomers formed during the *in vitro* aggregation of $Aβ_{42}$. It was also hypothesised that this selection strategy would also generate EvDesAbs with improved $Aβ_{42}$ secondary nucleation inhibition and reduced primary nucleation inhibition, due to the implementation of a competitive affinity selection with $Aβ_{42}$ monomer to remove EvDesAbs with high monomer binding affinities and strong primary nucleation inhibition[133, 137]. Whilst the results of the $Aβ_{42}$ aggregate selectivity ELISAs showed a generally large increase in $Aβ_{42}$ binding affinity for every EvDesAb selected from

the crude-extract ELISA screens, there were no significantly clear preferences for binding to $A\beta_{42}$ monomers or fibrils. Identifying EvDesAbs with $A\beta_{42}$ oligomer binding specificity using the employed method of sampling an *in vitro* $A\beta_{42}$ aggregation was certainly far from optimal due to the heterogeneous aggregate populations present, however it did appear to show that the EvDesAb's apparent lack of selectivity between the monomer and fibrillar species indicates that their binding is largely sequence-specific. That being said, with the exceptions of EvDesAb-E10, EvDesAb-F9 and EvDesAb-D4, some preferential binding was observed for aggregate-containing samples for every EvDesAb. Given that the $DesAb_{3-9}$ and $DesAb_{29-36}$ showed almost no preference for any aggregate-containing samples, this suggests that binding to certain conformations present in $A\beta_{42}$ aggregates was slightly enhanced by the selection strategy.

The most promising results of this study was found in the $A\beta_{42}$ aggregation inhibition characterisation of the EvDesAbs showing dose-dependent activity. Three out of the four characterised EvDesAbs showed an increase in the relative difference of the global parameters k_+k_n and k_+k_2, with each becoming more selective for apparent secondary nucleation inhibition through the loss of apparent primary nucleation inhibition. Notably, EvDesAb-E10 showed a very large increase in apparent secondary nucleation inhibition alongside a loss of apparent primary nucleation inhibition. These results suggest that affinity maturation with the use of competitive affinity selection is a viable strategy for altering the microscopic nucleation inhibition specificity of Ab/protein-based aggregation inhibitors. The theory behind this methodology has been proven before for the isolation of Abs with specific inhibition of certain microscopic nucleation events from naïve libraries[137], however to the best of our knowledge this study is the first description of the use of affinity maturation to alter and increase the microscopic nucleation inhibition specificity of an Ab inhibitor of aggregation. Be that as it may, it would be imperative to perform seeded aggregation experiments to evaluate any $A\beta_{42}$ elongation inhibition activity for EvDesAb-C10, EvDesAb-H4 and EvDesAb-E10 to decouple the global parameters k_+k_n and k_+k_2 to calculate the actual primary and secondary nucleation rates and accurately evaluate the extent to which the selectivities changed by.

This study also highlighted the risks and limitations of affinity maturation with ep-PCR against aggregation-prone proteins as all selected EvDesAbs were marred by large thermal stability trade-offs. These troublesome findings were likely reflective of the combination of both the diversification and competitive affinity selection strategies. This hypothesis has been proven

before in a study that used ep-PCR to introduce mutations in random locations into the same sdAb scaffold used in this study for selection against $A\beta_{42}$ using yeast display[281]. The evolved Abs also suffered large thermal stability losses and changes to the framework β-sheet content and it was proposed that affinity maturation in the presence of soluble $A\beta_{42}$ may create an additional misfolding/co-aggregation selection pressure. Their elegant solution to this was the use of a Protein A co-selection, involving Ab-yeast display against $A\beta_{42}$ and Protein A labelled with a reporter that could isolate individual cells displaying Abs that both bind $A\beta_{42}$ and remain folded[281]. Such a solution could be implemented for the ep-PCR libraries generated for this study, however it is still likely that desirable EvDesAbs could still be isolated from the selections employed here. The crude-extract screens simply ranked the EvDesAbs on their relative binding affinities and expression levels but not their folding stability. The use of HRP-conjugated Protein A could, in theory, be used as a reporter on heat pre-treated cell-lysates instead of the HRP-conjugated anti-His Ab. This would give an additional sdAb folding read-out to the binding affinity ranking and possibly save time and resources wasted by characterising poor-stability EvDesAbs post-purification. It is likely that this oversight may have been responsible for the isolation of EvDesAbs with poor thermal stability after thermal stability-selection with Protein A as these candidates were screened based on their binding affinities alone. As the vast majority of characterised EvDesAbs displayed severely compromised thermal stability and were chosen from the screen as the variants with highest relative binding affinity, it is possible that in this particular case the increases in binding affinity are inversely correlated with thermal stability. With this hypothesis, it would have been desirable to characterise the EvDesAbs with weaker relative $A\beta_{42}$ binding affinities in an attempt to obtain variants with the least amount of compromised traits and the use of HRP-conjugated Protein A would greatly assist in this identification process.

There are measures that could be taken to mitigate the misfolding/co-aggregation selection pressure by altering the design of the DNA libraries and the affinity selection strategy. An issue with the ep-PCR strategy was that every residue of the sdAb had an equal chance of mutagenesis, including the most conserved residues. Employing a 'semi-rational' diversification by restricting the mutagenesis to non-conserved residues only, identified by human V_H multiple sequence alignments would not only reduce the chances of stability losses, but would also result in smaller libraries[282, 283], increasing the diversity coverage of phage display. The competitive affinity selection carried with it inherent risk due to the heterogeneous mixture of $A\beta_{40}$ oligomers and monomers. Efforts were made to reduce the aggregation of these

species though short incubation times and low concentrations, however this could not completely rule out ongoing aggregation, especially with oligomeric 'seeds' present. This aggregation risk could have been further minimised with the use of sequential affinity selection, whereby Streptavidin bead-captured biotinylated $A\beta_{40}$ monomer could have been incubated with the Ab-phage first to remove the strong monomer-binding variants, and the unbound phage could have then been introduced to the biotinylated $A\beta_{40}$ oligomers and selected, avoiding a heterogeneous $A\beta_{40}$ mixture. This strategy was initially considered, however it is extremely challenging to control the effective solution concentration of competitor with the use of pre-captured $A\beta_{40}$ monomer. Nevertheless, the merits of sequential selection using negligibly aggregating homogeneous target proteins probably outweigh any aforementioned competitor concentration issues if less unstable EvDesAbs are enriched.

The mutations found in the $A\beta_{42}$ aggregation-inhibiting EvDesAbs give some insight into the structural change enrichment patterns and are shown in Figure 4.1. All four EvDesAbs contained at least one mutation in the stem of the grafted CDR3 loop and three EvDesAbs (EvDesAb-H4, EvDesAb-E10 and EvDesAb-B11) contained a Glutamic acid substitution of one of the highly conserved C-terminal Valines (V120/V122). Both conserved C-terminal Valines are buried in the β-sheet core of the V_H framework and likely act as hydrophobic 'clamps', assisting with the final fold of the V_H fragment. The substitution of Valine to glutamic acid not only represents a hydrophobic to charged side chain conversion, but also an increase in side chain size and steric hindrance, both highly disfavoured characteristics for protein core localisation. This repeated observation, alongside the changes of secondary structure content from β-sheet to random coil, gave rise to the hypothesis that the final C-terminal β-sheet fold, which immediately follows and creates the CDR3 loop, underwent a drastic conformational change and potentially its folding could be entirely inhibited. This hypothesis is supported by the fact that of the twelve identified mutations in the $A\beta_{42}$ aggregation-inhibiting EvDesAbs, nine (75%) are contained within the stems of the CDR3 loop and the C-terminus. Of these nine mutations, five are hydrophobic to hydrophilic substitutions and visa versa; and the CDR3 stem mutation of EvDesAb-C10 (A97P) is located in the β-sheet immediately preceding the CDR3 loop. As Proline disfavours the formation of secondary structure[256], it is probable that the V_H framework folding around the CDR3 loop is highly disrupted in EvDesAb-C10. Any significant changes in CDR3 presentation and even the hypothetical complete release of the C-terminus from the V_H framework could be identified with the use of proteinase K degradation coupled with AA analysis of the resulting digested peptide sequences.

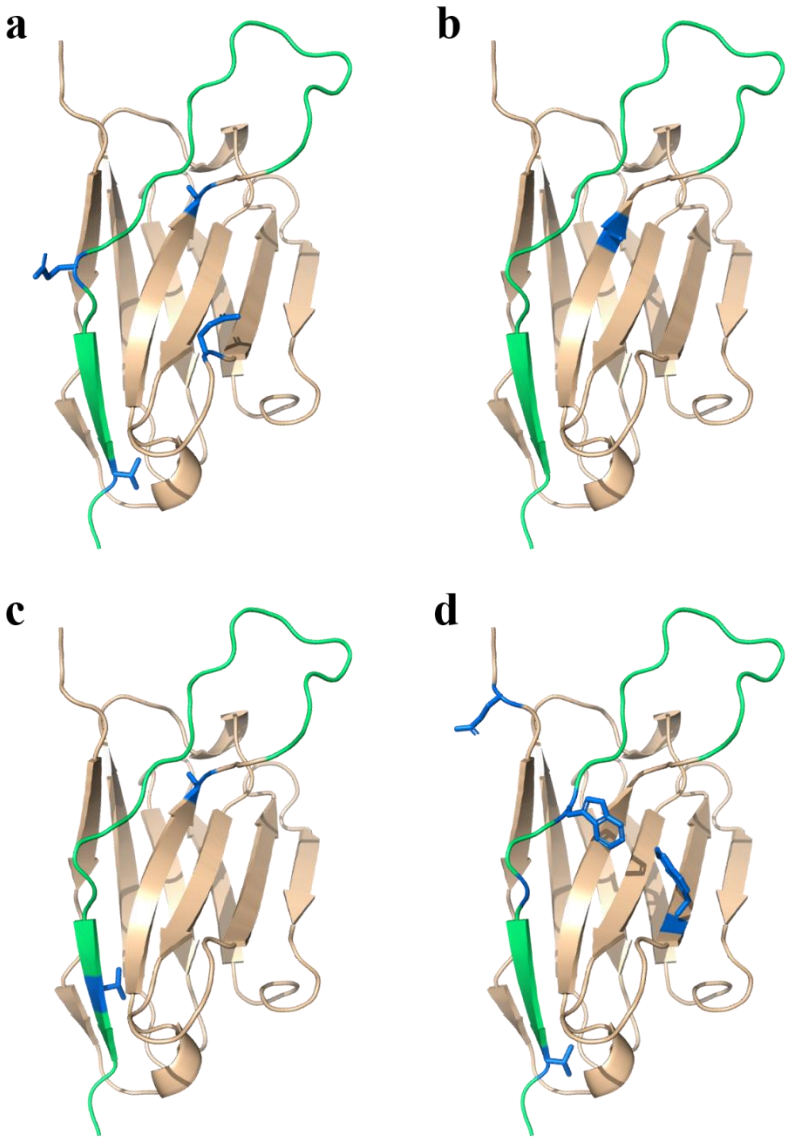

Figure 4.1. Residue substitution locations of the selected EvDesAbs displaying Aβ$_{42}$ aggregation inhibition activity. The CDR3 loops and the following C-terminus is shown in green for each EvDesAb. The mutations are shown with side chains (original residues) in blue and the rest of the sdAb structure is shown in tan. a) EvDesAb-H4. b) EvDesAb-C10. c) EvDesAb-E10. d) EvDesAb-B11. The majority of mutations localise around the C-terminus and stems of the CDR3 loop. The mutations were modelled upon the X-ray crystal structure of DesAb-F, which was provided by P. Sormanni and F. A. Aprile and produced using PyMOL (PyMOL, Molecular Graphics System, Version 2.2.0, Schrödinger, LLC).

The results described in this thesis indeed demonstrate that the DesAbs generated by Modular rational design can be subjected to protein engineering to improve their characteristics and that they represent viable starting points for developing novel research tools. The majority of the limitations presented are likely due to the design and implementation of the directed evolution engineering strategies. These can be readily altered and rapidly performed if further functional improvements are required.

Chapter 5: Materials and methods

5.1 DNA library construction

5.1.1 Choice of phage display phagemid

The phage-display phagemid used for this study was the pMESy4 phagemid (4513 bp; Genbank KF415192), which was developed for the monovalent phage display of camelid nanobodies[158]. The vector map and sequence information are shown in Figure 5.1.

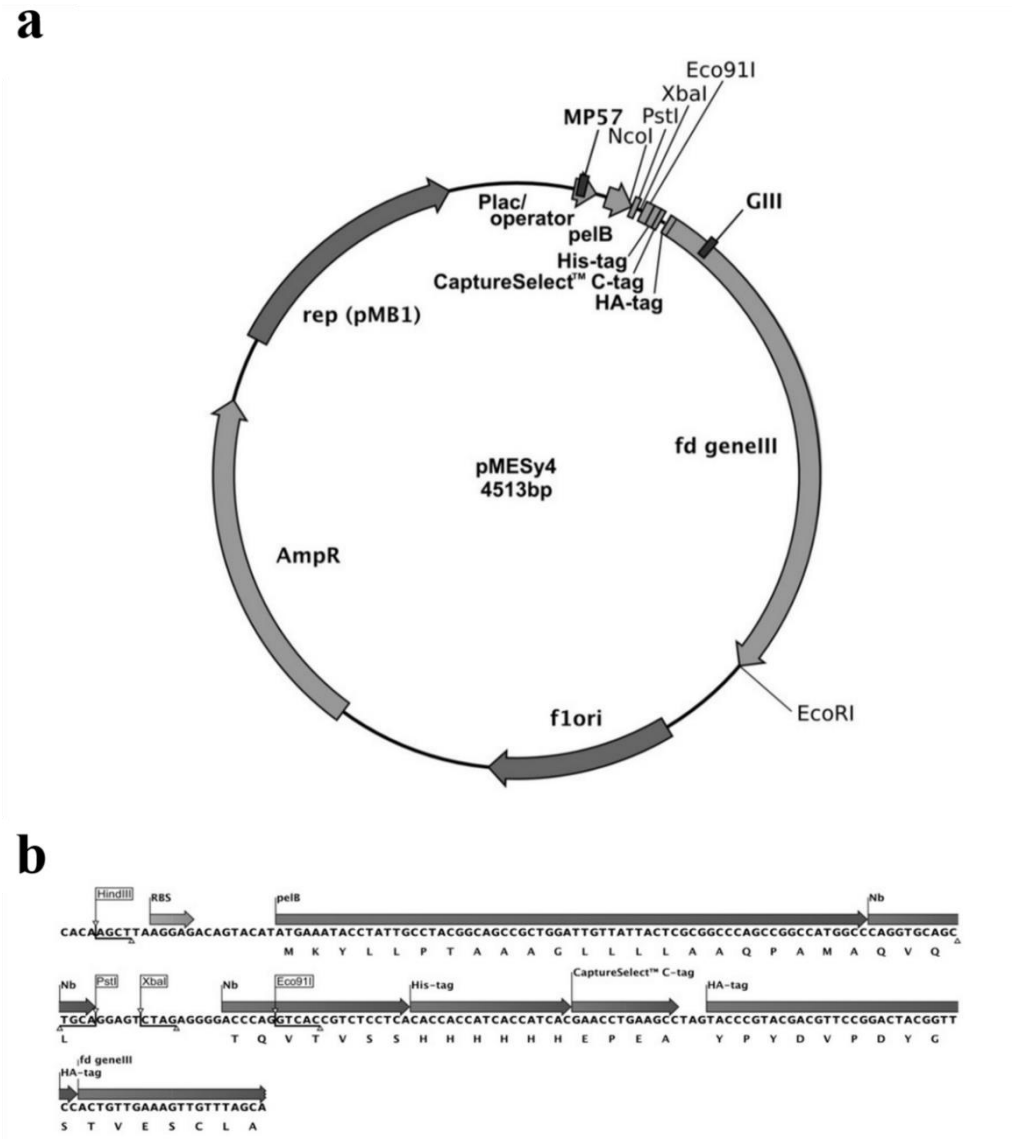

Figure 5.1. a) pMESy4 phage display vector map. b) Sequence information for the pMESy4 MCS. Figure adapted with permission from reference [158].

pMESy4 encodes a PelB leader sequence on the N-terminus of the sdAb, which facilitates secretion of the sdAb-pIII fusion to the periplasm of *E. coli* (where phage particles are assembled). The encoded linker that separates the sdAb from the pIII protein includes a His-tag (6x polyhistidine), CaptureSelect™ C-tag and HA-tag (hemagglutinin tag). An amber stop-codon is located between the C-tag and HA-tag for expression of soluble sdAb fragments (post phage-display). Other genes encoded are the pIII protein, the *lac* promoter/operator, β-lactamase (ampicillin resistance) and pMB1 and f1 origins of replication[158].

5.1.2 Cloning of single-domain antibodies into pMESy4

sdAbs DesAb-F and DesAb-IAPP were obtained in expression vector pET17-b. They also had PelB leader sequences and His-tags and could therefore be easily cloned into pMESy4. Unique restriction sites NcoI (PelB) and SpeI (TAG stop codon) were chosen for the cloning and were both introduced into the DesAb antibodies.

Oligonucleotides:

pET17-b NcoI-For: 5'-CAACCAGCCATGGCGATGTC-3’

pET17-b SpeI-Rev: 5'-ATCTGCTCGAACTAGTGATGGTG-3’

PCR conditions: 30 seconds initial denaturing (98 ºC), 10 seconds denaturing (98 ºC), 30 seconds annealing (52 ºC), 60 seconds elongation (72 ºC) for 35 cycles with a final extension of 7 minutes (72 ºC). Each reaction (50 µL) contained 5x Phusion HF Buffer (10 µL), 10 mM dNTPs (1 µL), 100 µM forward primer (0.25 µL), 100 µM reverse primer (0.25 µL), 50 ng/µL DesAb template DNA (0.2 µL), ddmQ H_2O (38.3 µL) and Phusion High-fidelity Polymerase (0.5 µL).

Template DNA digestion was then performed by adding dpnI (1 µL) to the reaction and incubating at 37 ºC for 1 hour. The DNA was purified using a PCR clean-up kit (QIAGEN) as per the QIAGEN clean-up protocol. The DNA was eluted in 30 µL sterile ddmQ H_2O and the DNA concentration was measured using a NanoDrop 2000 (Thermo Scientific).

pMESy4 already contains the NcoI restriction site in the PelB leader sequence so only SpeI was introduced.

Oligonucleotides:

pMESy4 SpeI-For: 5'-CGAACCTGAAGACTAGTACCCGTAC-3’

pMESy4 SpeI-Rev: 5'-TGATGGTGATGGTGGTGACTGGAG-3’

PCR conditions: 30 seconds initial denaturing (98 ^{o}C), 10 seconds denaturing (98 ^{o}C), 30 seconds annealing (55 ^{o}C), 5 minutes elongation (72 ^{o}C) for 32 cycles with a final extension of 7 minutes (72 ^{o}C). Each reaction (50 μL) contained 5x Phusion HF Buffer (10 μL), 10 mM dNTPs (1 μL), 100 μM forward primer (0.25 μL), 100 μM reverse primer (0.25 μL), 100 ng/μL pMESy4 template DNA (0.1 μL), ddmQ H_2O (38.4 μL) and Phusion High-fidelity Polymerase (0.5 μL).

Template DNA digestion was then performed by adding dpnI (1 μL) to the reaction and incubating at 37 ^{o}C for 1 hour. The DNA was purified using a PCR clean-up kit (QIAGEN) as per the QIAGEN clean-up protocol.

Self-circularisation was performed on pMESy4+SpeI using T4 ligase (1 μL) at 22 ^{o}C for 10 minutes and subsequently transformed into XL10-Gold cells (Agilent) as per the Agilent heat-shock transformation protocol. Cells were plated on LB-Agar supplemented with 100 μg/mL ampicillin and incubated overnight at 37 ^{o}C. Colonies were then picked and used to inoculate 2xYT media (5 mL) supplemented with 100 μg/mL ampicillin and the cultures were incubated overnight at 37 ^{o}C with shaking (200 rpm). The cultures were then centrifuged (4,700 rpm) for 5 minutes and DNA was purified from the pellet using a miniprep kit (QIAGEN) as per the QIAGEN miniprep protocol. The DNA was eluted in 30 μL sterile ddmQ H_2O and the DNA concentration was measured using a NanoDrop 2000 (Thermo Scientific). 100 ng/μL DNA (10 μL) was sent for Sanger sequencing (Department of Biochemistry, University of Cambridge).

Restriction digestion with NcoI and SpeI (New England Biolabs/NEB) was performed on pMESy4+SpeI and DesAb-F/DesAb-IAPP genes overnight at 16 ^{o}C using the volumes of material shown in Table 5.1.

Table 5.1. Restriction digest recipe for pMESy4+SpeI and the PCR products of the NcoI and SpeI insertion into the DesAb genes.

Restriction Digestion			
pMESy4+SpeI		DesAb gene	
DNA (627 ng/µL)	1.6 µL	DNA (115 ng/µl)	8.7 µL
10x NEB Buffer	5 µL	10x NEB Buffer	5 µL
SpeI	1 µL	SpeI	1 µL
NcoI	1 µL	NcoI	1 µL
ddmQ H_2O	41.4 µL	ddmQ H_2O	34.3 µL

The resulting digests were purified using agarose gel electrophoresis (1% Agarose) and gel extraction (QIAGEN) as per the QIAGEN gel-extraction protocol. All DNA was eluted in 30 µL sterile ddmQ H_2O and DesAb (insert) + pMESy4 (vector) ligation was performed at 22 ^oC for 15 minutes using the material shown in Table 5.2.

Table 5.2. Ligation recipe for the insertion of the DesAb-F and DesAb-IAPP genes into pMESy4.

Ligation	
pMESy4 digest (6 ng/µL)	16 µL
DesAb Gene digest (11 ng/µL)	1 µL
10x T4 Buffer	2 µL
T4 Ligase	1 µL

5 µL of the ligation products were used to transform XL10-Gold cells (Agilent) as per the Agilent heat-shock transformation protocol. Cells were plated on LB-Agar supplemented with 100 µg/mL ampicillin and incubated overnight at 37 ^oC. Colonies were then picked and used to inoculate 2xYT media (5 mL) supplemented with 100 µg/mL ampicillin and the cultures were incubated overnight at 37 ^oC with shaking (200 rpm). The cultures were then centrifuged (4,700 rpm) for 5 minutes and DNA was purified from the pellet using a miniprep kit (QIAGEN) as per the QIAGEN miniprep protocol. The DNA was eluted in 30 µL sterile ddmQ H_2O and the DNA concentration was measured using a NanoDrop 2000 (Thermo Scientific). 100 ng/µL DNA (10 µL) was sent for Sanger sequencing (Department of Biochemistry, University of Cambridge).

5.1.3 Saturation mutagenesis of the CDR2 loop with a two-step inverse-PCR

Firstly, a PCR was performed to introduce a -2 base frameshift into the CDR2 loop of the antibody so that any failed mutagenesis from the library construction would not be translated during phage-display.

Oligonucleotides:

CDR2 Frameshift-For 5'-GAGGGCTATACGCGTTATGC-3' (5'-Phosphorylated)

CDR2 Frameshift-Rev 5'-TAACATAAATGCTAGCCACCCATTC-3' (5'-Phosphorylated)

PCR conditions: 30 seconds initial denaturing (98 ^{o}C), 10 seconds denaturing (98 ^{o}C), 30 seconds annealing (55 ^{o}C), 5 minutes elongation (72 ^{o}C) for 34 cycles with a final extension of 7 minutes (72 ^{o}C). Each reaction (50 µL) contained 5x Phusion HF Buffer (10 µL), 10 mM dNTPs (1 µL), 100 µM forward primer (0.25 µL), 100 µM reverse primer (0.25 µL), 500 ng/µL sdAb-gIII template DNA (0.02 µL), ddmQ H_2O (37.98 µL) and Phusion High-fidelity Polymerase (0.5 µL).

Digestion, PCR clean-up, self-circularisation, transformation, mini-culture DNA purification and sequencing were performed as described in Chapter 5.1.2.

Secondly, trial PCRs of both the mutagenic and amplification steps were performed using a gradient annealing temperature. Annealing temperatures for saturation mutagenesis, 77.8 ^{o}C, 75.5 ^{o}C, 72.8 ^{o}C, 70.8 ^{o}C, 69.2 ^{o}C, 68.0 ^{o}C. Annealing temperatures for amplification, 70 ^{o}C, 68.2 ^{o}C, 66.5 ^{o}C, 63.2 ^{o}C, 59.1 ^{o}C, 56.1 ^{o}C.

Oligonucleotides (Mutagenic PCR):

pLib-For: 5'-
GAAGAATGGGTGGCTAGCATTTATNNKNNKNNKGGCTATACCCGTTATGCGG
ATAGCGTG-3' (5'-Phosphorylated)

pLib-Rev: 5'-GCCTTTCCCGGGTGCACGACGCACCCAGCCAATATATGTGTCC-3' (5'-Phosphorylated)

Oligonucleotides (Amplification PCR):

Amplification-For: 5'-GAAGAATGGGTGGCTAGCATT-3' (5'-Phosphorylated)

Amplification-Rev: 5'-GCCTTTCCCGGGTGCACG-3' (5'-Phosphorylated)

PCR conditions: 30 seconds initial denaturing (98 °C), 10 seconds denaturing (98 °C), 30 seconds annealing (78-68 °C for mutagenesis and 70-55 °C for amplification), 5 minutes elongation (72 °C) for 35 cycles with a final extension of 7 minutes (72 °C). Each reaction (50 µL) contained 5x Phusion HF Buffer (10 µL), 10 mM dNTPs (1 µL), 100 µM forward primer (0.25 µL), 100 µM reverse primer (0.25 µL), 500 ng/µL frameshift sdAb-gIII template DNA (0.02 µL), ddmQ H_2O (37.98 µL) and Phusion High-fidelity Polymerase (0.5 µL).

Template DNA digestion was then performed by adding dpnI (1 µL) to the reaction and incubating at 37 °C for 1 hour. The DNA was analysed using agarose gel electrophoresis (1% Agarose). Annealing temperatures chosen for library generation were 70.8 °C (Mutagenic PCR) and 59.1 °C (Amplification PCR).

The DNA library (pLib DesAb-F & pLib DesAb-IAPP) construction was then performed firstly using the pLib mutagenic oligonucleotides.

Mutagenic PCR conditions: 30 seconds initial denaturing (98 °C), 10 seconds denaturing (98 °C), 30 seconds annealing (70.8 °C), 5 minutes elongation (72 °C) for 5 cycles with a final extension of 7 minutes (72 °C). Each reaction (50 µL) contained 5x Phusion HF Buffer (10 µL), 10 mM dNTPs (1 µL), 100 µM forward primer (0.25 µL), 100 µM reverse primer (0.25 µL), 50 ng/µL frameshift sdAb-gIII template DNA (0.2 µl), ddmQ H_2O (37.8 µL) and Phusion High-fidelity Polymerase (0.5 µL).

Template DNA digestion was then performed by adding dpnI (1 µL) to the reaction and incubating at 37 °C for 1 hour. The PCR product was purified using a PCR clean-up kit (QIAGEN) as per the QIAGEN clean-up protocol and eluted in 30 µL sterile ddmQ H_2O. The PCR product was then immediately amplified using the non-mutagenic amplification oligonucleotides.

Amplification PCR conditions: 30 seconds initial denaturing (98 °C), 10 seconds denaturing (98 °C), 30 seconds annealing (59.1 °C), 5 minutes elongation (72 °C) for 45 cycles with a final extension of 7 minutes (72 °C). Each reaction (50 µL) contained 5x Phusion HF Buffer (10 µL), 10 mM dNTPs (1 µL), 100 µM forward primer (0.25 µL), 100 µM reverse primer (0.25 µL), pLib PCR Product (15 µL), ddmQ H_2O (23 µL) and Phusion High-fidelity Polymerase (0.5 µL).

The PCR products (pLib) were purified using agarose gel electrophoresis (1% Agarose) and gel extraction (QIAGEN) as per the QIAGEN gel-extraction protocol. All DNA was eluted in

30 µL sterile ddmQ H_2O and self-circularization ligation was performed at 22 °C for 60 minutes using T4 ligase.

5.1.4 CDR3 replacement for changing target antigen

For replacing the CDR3 loop of DesAb-F in pMESy4 to those of $DesAb_{3-9}$ and $DesAb_{29-36}$, two separate inverse-PCRs with the following overhang oligonucleotides was performed.

Oligonucleotides:

$DesAb_{3-9}$ CDR3-For 5'-TGCGCGAGGAAGAGGCGGCCGC-3' (5'-Phosphorylated)

$DesAb_{3-9}$ CDR3-Rev 5'-GGGTCAGGGTTTCATGAGATCCCGCTGCGCAAT-3' (5'-Phosphorylated)

$DesAb_{29-36}$ CDR3-For 5'-GCGACCGTGGAGGAAGAGGCGGCCGC-3' (5'-Phosphorylated)

$DesAb_{29-36}$ CDR3-Rev 5'-TTTATACATGCTGCCAGATCCCGCTGCGCAAT-3' (5'-Phosphorylated)

PCR conditions: 30 seconds initial denaturing (98 °C), 10 seconds denaturing (98 °C), 30 seconds annealing (65 °C), 5 minutes elongation (72 °C) for 34 cycles with a final extension of 7 minutes (72 °C). Each reaction (50 µL) contained 5x Phusion HF Buffer (10 µL), 10 mM dNTPs (1 µL), 100 µM forward primer (0.25 µL), 100 µM reverse primer (0.25 µL), 500 ng/µL DesAb-F-gIII template DNA (0.02 µL), ddmQ H_2O (37.98 µL) and Phusion High-fidelity Polymerase (0.5 µL).

Digestion, PCR clean-up, self-circularisation, transformation, mini-culture DNA purification and sequencing were performed as described in Chapter 5.1.2.

5.1.5 ep-PCR of $DesAb_{3-9}$ and $DesAb_{29-36}$ genes

The following ep-PCR protocol was optimised in collaboration with Kazimir Uzwyshyn-Jones, who was summer student on an internship in the Dobson/Vendruscolo group during August 2017.

ep-PCR was performed on the $DesAb_{3-9}$ and $DesAb_{29-36}$ genes in the pMESy4 phagemid using the following oligonucleotides and the GeneMorph II random mutagenesis kit (Agilent).

Oligonucleotides:

ep-PCR-For 5'-AGCCGGCCATGGCGATGTCT-3'

ep-PCR-Rev 5'-CGTCCTTATAGTCTGCAGCGGTACC-3'

ep-PCR conditions: 2 minutes initial denaturing (95 ^{o}C), 30 seconds denaturing (95 ^{o}C), 30 seconds annealing (60 ^{o}C), 1 minute elongation (72 ^{o}C) for 36 cycles with a final extension of 10 minutes (72 ^{o}C). Each reaction (50 µL) contained 10x Mutazyme II reaction Buffer (5 µL), 10 mM dNTPs (1 µL), 100 µM forward primer (0.25 µL), 100 µM reverse primer (0.25 µL), 100 ng/µL $DesAb_{3-9}$ or $DesAb_{29-36}$-gIII template DNA (0.125 µL), ddmQ H_2O (42.38 µL) and Mutazyme II DNA polymerase (1 µL).

Template DNA digestion was then performed by adding dpnI (1 µL) to the reaction and incubating at 37 ^{o}C for 1 hour. The DNA was purified using a PCR clean-up kit (QIAGEN) as per the QIAGEN clean-up protocol. Restriction digestion with NcoI and KpnI (NEB) was performed on $DesAb_{3-9}$+pMESy4, $DesAb_{29-36}$+pMESy4 and the $DesAb_{3-9}$/$DesAb_{29-36}$ ep-PCR products for 4 hours at 37 ^{o}C using the volumes of material shown in Table 5.3.

Table 5.3. Restriction digest recipe for $DesAb_{3-9}$+pMESy4, $DesAb_{29-36}$+pMESy4 and the $DesAb_{3-9}$/$DesAb_{29-36}$ ep-PCR products.

Restriction Digestion			
$DesAb_{3-9}$/$DesAb_{29-36}$+pMESy4		$DesAb_{3-9}$/$DesAb_{29-36}$ ep-PCR products	
DNA (100 ng/µL)	100 µL	DNA (500 ng/µL)	10 µL
10x NEB Buffer	25 µL	10x NEB Buffer	20 µL
KpnI	2.5 µL	KpnI	2 µL
NcoI	2.5 µL	NcoI	2 µL
ddmQ H_2O	120 µL	ddmQ H_2O	166 µL

The resulting digests were purified using agarose gel electrophoresis (1% Agarose) and gel extraction (QIAGEN) as per the QIAGEN gel-extraction protocol. All DNA was eluted in 30 µL sterile ddmQ H_2O. Alkaline phosphatase treatment of the digested $DesAb_{3-9}$+pMESy4 and $DesAb_{29-36}$+pMESy4 vectors was performed to prevent any contaminating 'wild-type' sequence ligation. Vector de-phosphorylation with FastAP (Thermo Scientific) was performed on the $DesAb_{3-9}$+pMESy4 and $DesAb_{29-36}$+pMESy4 digests for 1 hour at 37 ^oC and then for 5 minutes at 75 ^oC using the volumes of material shown in Table 5.4.

Table 5.4. $DesAb_{3-9}$+pMESy4 and $DesAb_{29-36}$+pMESy4 digest de-phosphorylation recipe.

De-phosphorylation (Alkaline phosphatase)	
$DesAb_{3-9}$+pMESy4 digest/$DesAb_{29-36}$+pMESy4 digest (100 ng/µL)	100 µL
FastAP Buffer	20 µL
ddmQ H_2O	70 µL
FastAP	10 µL

Digested $DesAb_{3-9}$ and $DesAb_{29-36}$ ep-PCR products (insert) + de-phosphorylated digested pMESy4 (vector) ligation was performed at 16 ^oC overnight using the material shown in Table 5.5.

Table 5.5. Ligation recipe for the insertion of the $DesAb_{3-9}$ and $DesAb_{29-36}$ ep-PCR products into pMESy4.

Ligation			
$DesAb_{3-9}$ pMESy4 digest (13.6 ng/µL)	29.42 µL	$DesAb_{29-36}$ pMESy4 digest (12 ng/µL)	33.33 µL
$DesAb_{3-9}$ ep-PCR product digest (23.6 ng/µL)	4.82 µL	$DesAb_{29-36}$ ep-PCR product digest (17.2 ng/µL)	6.61 µL
10x T4 Buffer	8 µL	10x T4 Buffer	8 µL
ddmQ H_20	36.16 µL	ddmQ H_20	30.46 µL
T4 Ligase	1.6 µL	T4 Ligase	1.6 µL

5.2 Bacterial library generation and diversity evaluation

5.2.1 DNA purification and TG_1 electroporation

For electroporation of TG_1 cells (Agilent), the DNA libraries required purification. The DNA was purified using a PCR clean-up kit (QIAGEN) as per the QIAGEN clean-up protocol. 1 µL Purified pLib DNA was added to 40 µL TG_1 electro-competent cells (Agilent) in a 0.1 cm Gene

Pulser®/Micropulser™ electroporation cuvette (Bio-Rad) and pulsed using the 'Ec.1' setting (1.8 kV, 5 ms). Pulsing was performed in a Bio-Rad Micropulser™ Electroporator. 960 µL pre-warmed (37 °C) SOC media (Thermo Scientific) was then added and the cells were incubated for one hour with shaking (37 °C). The cells were then plated on 25x25 cm LB-agar plates supplemented with ampicillin (100 µg/mL) and glucose (2% w/v) and incubated overnight at 37 °C. After colonies were picked and sequenced (described in Chapter 5.2.2), 40 mL LB-media was poured on top of the 25x25 cm LB-agar plates and incubated at room temperature for 30 minutes with gentle shaking (50 rpm). The colonies were scraped from the plate using a sterile spatula to re-suspend the cells and the cell-suspensions were centrifuged for 10 minutes (3,200 xg). The supernatants were discarded and the cell pellets was re-suspended in 5 mL 2xYT media. Sterile glycerol was added to a final concentration of 40% and the bacterial libraries were aliquoted, flash-frozen in liquid nitrogen and stored (-80 °C).

5.2.2 Bacterial library DNA sequencing to determine diversity and quality

Colony-PCRs were performed to amplify the sdAb-gIII gene variants from fifty colonies per library to assess diversity and quality. Before the library was harvested from the TYE agar plates (Chapter 5.2.1), colonies were picked from the TG_1 library plates and diluted separately into 10 µL ddmQ H_2O.

Oligonucleotides[158]:

MP57: 5′-TTATGCTTCCGGCTCGTATG-3′

GIII: 5′-CCACAGACAGCCCTCATAG-3′

Colony PCR conditions: 1 minute initial denaturing (98 °C), 10 seconds denaturing (98 °C), 30 seconds annealing (60 °C), 1 minute elongation (72 °C) for 32 cycles with a final extension of 7 minutes (72 °C). Each reaction (50 µL) contained 5x Phusion HF Buffer (10 µL), 10 mM dNTPs (1 µL), 100 µM MP57 primer (0.25 µL), 100 µM GIII primer (0.25 µL), colony solution (1 µL), ddmQ H_2O (37 µL) and Phusion High-fidelity Polymerase (0.5 µL).

The PCR products (x50) were purified using a PCR clean-up kit (QIAGEN) as per the QIAGEN clean-up protocol and eluted in 50 µL sterile ddmQ H_2O. The DNA concentration was measured using a NanoDrop 2000 (Thermo Scientific). 100 ng/µL DNA (10 µL) was submitted for Sanger sequencing (Department of Biochemistry, University of Cambridge)

5.3 Experimental preparation for phage-display

5.3.1 α-Synuclein single-labelling with biotin

αSyn mutant A140C was purified using a modified protocol as described before[284]. αSyn A140C was expressed BL21-Gold *E. coli* (Agilent) following transformation with plasmid pT7-7 encoding the mutant. The cells were induced with IPTG (1 mM) in LB-media containing ampicillin (100 μg/mL) and incubated overnight (28 ºC/180 rpm). The cells were then harvested by centrifugation for 45 minutes (5,000 rpm) and the pellets were washed by re-suspension in 30 mL/L culture PBS (pH 7.4). The washed cells were centrifuged once again for 60 minutes (4,000 rpm) and the pellets were re-suspended in 20 mL/L culture lysis buffer (10 mM Tris, 0.2 mM EDTA, 1 mM PMSF, 1 mM DTT). Sonication was performed to lyse the cells for 5 minutes (15 seconds pulse/45 seconds pause) and the supernatant was collected by centrifugation for 30 minutes (13,500 rpm). The supernatant was heated to 85 ºC for 20 minutes and centrifuged for 20 minutes (13,500 rpm). Streptomycin sulphate was added to the supernatant to give a concentration of 10 mg/mL and the mixture was incubated at 4 ºC for 15 minutes on a roller. The supernatant was collect by centrifugation for 30 minutes (13,500 rpm) and ammonium sulphate was added to a concentration of 360 mg/mL and the mixture was incubated at 4 ºC for 30 minutes on a roller. The precipitate was collected by a final centrifugation for 30 minutes (13,500 rpm) and re-suspended in 40 mL buffer (25 mM Tris, 1 mM DTT, pH 7.7). Dialysis in a 5000 MWCO membrane was carried out overnight in 3x1 L 25 mM Tris, 1 mM DTT, pH 7.7 and the protein was then purified using Anion-exchange chromatography (HiLoad 26/600 Superdex 200 pg). Elution was performed using 25 mM Tris, 1.5 M NaCl, 1 mM DTT, pH 7.7 at a gradient of 600 mL of 0%-100% elution buffer. αSyn A140C was confirmed by SDS-PAGE in the presence of sample reducing agent. An additional purification by SEC (HiLoad 26/600 Superdex 200 pg) was carried out and αSyn A140C was eluted in PBS with 1 mM DTT (pH 7.4). Protein identity was confirmed by SDS-PAGE and MALDI mass-spectroscopy. αSyn A140C concentration was calculated using the absorbance at 275 nm using the extinction coefficient (5600 M^{-1} cm^{-1})[284].

350 mM αSyn A140C (2 mL) was dialysed against 2x4 L 25 mM HEPES, pH 7.0 in 10,000 MWCO Slide-A-Lyzer® mini dialysis units (Thermo Scientific) overnight at 4 ºC. Post-dialysis, 1.5 mL protein was recovered and 77.5 μL 25 mM HEPES, 60 mM Pierce™ TCEP-HCl, pH 7.0 was added and allowed to incubate for 20 minutes at room temperature.

Confirmation of disulphide reduction was checked using SDS-PAGE. 2.8 mg EZ-link™ Maleimide-$(PEG)_2$-Biotin in 25 mM HEPES, pH 7.0 was then added and the labelling reaction was carried out overnight at 4 ºC with stirring. The biotinylated αSyn A140C was dialysed in 2x4 L ddmQ H_2O overnight at 4 ºC. 10 µL was sent for MALDI mass-spectroscopy analysis (Department of Biochemistry, University of Cambridge). The dialysed biotinylated αSyn was flash-frozen and lyophilised. Before use, biotinylated αSyn was purified from the unlabelled αSyn A140C using Pierce® monomeric Avidin agarose (Thermo scientific) using the Thermo Scientific affinity purification protocol.

5.3.2 $A\beta_{40}$ labelling with biotin

As mentioned in Chapter 3.31, $A\beta_{40}$ was provided as the recombinantly expressed variant, containing an additional N-terminal Methionine, by the Centre for Misfolding Diseases (CMD), University of Cambridge. Expression and purification of the recombinant $a\beta_{40}$ was carried out as previously described for $A\beta_{42}$[98]. Briefly, $A\beta_{40}$ or $A\beta_{42}$ was expressed in BL21-Gold (DE3) *E. coli* (Stratagene, La Jolla, CA) and purified by sonicating the bacterial cells, dissolving the inclusion bodies in urea (8 M) and performing ion exchange in batch mode on diethylaminoethyl cellulose resin. The fractions were lyophilised and further purified using a Superdex 75HR 26/60 column (GE Healthcare, Chicago, IL). Fractions were analysed using SDS-PAGE for the presence of the desired product. The fractions containing the recombinant protein were combined, frozen using liquid nitrogen, lyophilised in either sodium phosphate buffer (20 mM, pH 8.0) for preparing $A\beta_{40}$ or $A\beta_{42}$ monomers or ammonium acetate (50 mM, pH 8.5) for producing $A\beta_{40}$ oligomers[270], and stored at -80 ºC.

Before use in any experiment (labelling, ELISA, aggregations etc.), $A\beta_{40}$ or $A\beta_{42}$ required denaturing to the monomeric form on the same day. $A\beta_{40}$ or $A\beta_{42}$ was denatured using 6 M guanidinium HCL (20 mM sodium phosphate buffer, 0.2 mM EDTA, pH 8.0) for 3 hours at 0 ºC, injected onto a Superdex 75 10/300 GL column (GE Healthcare, Chicago, IL) and eluted in 20 mM sodium phosphate buffer, 0.2 mM EDTA, pH 8.0. $A\beta_{40}$ or $A\beta_{42}$ peptide concentration was determined from the absorbance of the integrated peak area using ε_{280} = 1,490 L mol^{-1} cm^{-1}.

For $A\beta_{40}$ labelling with biotin, a 1:2 ratio of $A\beta_{40}$ to (+)-Biotin N-hydroxysuccinimide ester was formulated in 20 mM sodium phosphate buffer pH 7.4. The solution was stirred for 1 hour at 25 ºC before being flash-frozen in liquid nitrogen and lyophilised. The labelled $A\beta_{40}$

monomer was denatured using 6 M guanidinium HCL (20 mM sodium phosphate buffer, 0.2 mM EDTA, pH 8.0) for 3 hours at 0 ºC, injected onto a Superdex 75 10/300 GL column (GE Healthcare, Chicago, IL) and eluted in 50 mM ammonium acetate, pH 8.5. LC-MS was performed on a sample to confirm biotin labelling and the remaining labelled $A\beta_{40}$ monomer was flash-frozen in liquid nitrogen and lyophilised.

5.3.3 $A\beta_{40}$ oligomer preparation

0.5 mg labelled or unlabelled lyophilised $A\beta_{40}$ was re-suspended in 300 µL 100% HFIP and incubated for overnight at 4 ºC. The solvent was gently evaporated under a flow of nitrogen and the dried peptide was re-suspended in 50 µL DMSO before being sonicated for 2x10 minutes at 25 ºC. For biotinylated $A\beta_{40}$ oligomer generation, a 1:10 ratio of biotinylated $A\beta_{40}$ to unlabelled $A\beta_{40}$ in DMSO was mixed. The $A\beta_{40}$ peptide in DMSO was then diluted in 20 mM sodium phosphate buffer, 200 µM $ZnCl_2$, pH 6.9, to a final concentration of $A\beta_{40}$ of 100 µM. The mixture was incubated at 20 ºC for 20 hours in a final volume of 550 µL and centrifuged at 15,000 xg for 15 minutes at 20 ºC. The $A\beta_{40}$ oligomer pellet was re-suspended in PBS and the concentration of the oligomers was determined by measuring the absorbance at 280 nm using the theoretical molar extinction coefficient ε_{280} = 1490 $L\ mol^{-1}\ cm^{-1}$[270].

5.3.4 $A\beta_{40}$ ANS and turbidimetry analysis

For the comparison of biotinylated $A\beta_{40}$ oligomers to unlabelled $A\beta_{40}$ oligomers by ANS binding, 40 µM (monomer equivalents) aliquots of both types pre-prepared $A\beta_{40}$ oligomers were added separately to solutions of ANS in 20 mM phosphate buffer at pH 6.9 to obtain a 3-fold excess of dye. The emission spectra (excitation at 380 nm) were recorded at 37 ºC using a plate reader (BMG Labtech, Aylesbury, UK). Biotinylated $A\beta_{40}$ oligomer and unlabelled $A\beta_{40}$ oligomer turbidity measurements were performed using 40 µM oligomers in 20 mM phosphate buffer at pH 6.9. The absorbance spectra were recorded at 37 ºC between 350-650 nm using a plate reader (BMG Labtech, Aylesbury, UK)[270].

5.3.5 Atomic force microscopy

AFM was performed on freshly cleaved, positively functionalized mica substrates. The functionalization was performed by incubating the substrates for 1 minute with 10 μL of a 0.5% v/v (3-aminopropyl)triethoxysilane (APTES) solution in water, rinsing with 3x1 mL of water and drying under a gentle flow of nitrogen. Before deposition onto the substrate, the biotinylated $A\beta_{40}$ oligomer or unlabelled $A\beta_{40}$ oligomer preparations were diluted 10 times in water. 10 μL aliquots of each diluted sample were deposited on the functionalized mica at 25 ºC, incubated for 10 minutes, rinsed with 1 mL water and then dried under a gentle nitrogen flow. AFM maps were generated by means of a JPK nanowizard2 system (JPK Instruments, Berlin, Germany) operating in tapping mode and equipped with a silicon tip (mmasch, 2 N m^{-1}) with a nominal radius of 10 nm. Image flattening and analysis was performed by SPIP software (Image Metrology, Hørsholm, Denmark)[270].

5.3.6 VCSM13 helper-phage propagation

A colony from a fresh TG_1 streak plate was used to inoculate 5 mL 2xYT-media and the culture was grown to OD_{600} = 0.5 at 37 ºC (250 rpm). A dilution series of VCSM13 Interference-Resistant Helper Phage (Agilent) was created by mixing 10 μL phage with 90 μL PBS and using 10 μL of each dilution to create a 10x dilution series from (10^{-3} to 10^{-13}). 10 μL of each dilution was added to individual 200 μL TG_1 cell cultures and incubated for 30 minutes at 37 ºC. Pipette tips were discarded after every dilution due to the 'stickiness' of phage particles. 3 mL of melted H-Top agar was added to each phage/bacteria culture and each mixture was poured onto LB-Agar plates (no antibiotic) and incubated overnight at 37 ºC.

A phage plaque was picked from a plate containing 10^5 plaques and was used to infect a 5 mL TG_1 culture, grown to OD_{600} = 0.5 and the culture was incubated for 2 hours at 37 ºC (250 rpm). The infected culture was then used to inoculate 250 mL 2xYT media which was then incubated for another 2 hours at 37 ºC (250 rpm). Kanamycin was then added to a concentration of 50 μg/mL and the culture was incubated overnight at 37 ºC (250 rpm). The culture was centrifuged for 10 minutes (3,200 xg) and ¼ volume of 20% PEG 6000, 2.5 M NaCl was added to the supernatant to precipitate the phage. After incubating on ice for one hour, the precipitate was collected by centrifugation for 30 minutes (3,200 xg) and re-suspended in 5 mL PBS. The solution was centrifuged again for 10 minutes (3,200 xg) and ¼ volume of 20% PEG 6000, 2.5

M NaCl was added to the supernatant. The precipitate was collected again via centrifugation for 30 minutes (3,200 xg) and re-suspended in 1 mL PBS. Residual cells were removed by filtering the mixture with a 0.45 μm filter. Glycerol was added to the phage to a concentration of 20% and the phage was aliquoted, flash-frozen in liquid nitrogen and stored (-80 ^{o}C).

To calculate the phage titres for use in phage display library infection, a dilution series of this helper-phage stock was made (see above) and used to infect 200 μL TG_1 cultures. After 30 minutes incubation at 37 ^{o}C the cultures were 'spotted' using 5 μL droplets onto an LB-Agar plate supplemented with kanamycin (50 μg/mL) and the plate was incubated overnight at 37 ^{o}C[226].

5.4 Phage display

5.4.1 Library expression and phage packaging

A TG_1 library glycerol stock was thawed and 100 μL was used to inoculate 50 mL 2xYT-GA medium (2xYT supplemented with 2% w/v glucose and 100 μg/mL ampicillin). The culture was incubated at 37 ^{o}C (250 rpm) until the OD_{600} ~ 0.5 and then $5x10^{12}$ cfu VCSM13 helper phage from the prepared stock (Chapter 5.3.4) was added. The infected culture was then incubated at 37 ^{o}C for 30 minutes, followed by incubation at 37 ^{o}C for another 30 minutes with shaking (250 rpm). The cells were then harvested by centrifugation for 10 minutes (3,200 xg) and the pellet was aspirated to remove as much glucose as possible. The pellet was the re-suspended in 1 mL 2xYT-AK medium (2xYT supplemented with 100 μg/mL ampicillin and 50 μg/mL Kanamycin) and the suspension was used to inoculate 50 mL 2xYT-AK medium. The infected cell media was incubated overnight at 30 ^{o}C with shaking (250 rpm)[158].

5.4.2 sdAb-displaying phage purification

The infected TG_1 library culture (Chapter 5.4.1) was centrifuged for 15 minutes (3,200 xg) and 10 mL 20% PEG, 2.5 M NaCl was added to 40 mL supernatant and the mixture was incubated on ice for 30 minutes with gentle shaking (100 rpm). The precipitate was collected by centrifugation for 10 minutes (3,200 xg) and re-suspended in 1 mL PBS. The mixture was centrifuged for 1 minute (20,000 xg) and the pellet was discarded. 250 μL 20% PEG, 2.5 M

NaCl was added to re-precipitate the phage and the mixture was incubated on ice for 10 minutes before being centrifuged for 15 minutes (20,000 xg). The supernatant was discarded and the pellet was re-suspended in 1 mL PBS-T (0.05% Tween® 20, 2% BSA) (0 ºC) and the suspension was centrifuged for 1 minute to remove the last traces of bacteria (20,000 xg). Negative selection of the library was performed to minimise background binding by incubating the purified phage with M-280 streptavidin-coated magnetic beads (Invitrogen). 50 µL streptavidin beads were added to the phage solution and incubated for 30 minutes at room temperature on a roller. The beads were collected using a magnetic field and discarded. A dilution series of the pre-incubated phage was made and used to infect TG_1 cultures (see Chapter 5.3.4) and was 'spotted' on TYE-Agar plates and incubated overnight at 37 ºC. The remaining purified phage were stored overnight at 4 ºC[158].

5.4.3 Confirmation of single-domain antibody display with protein A/enriching for folded antibodies

A biopanning cycle was performed using Pierce™ protein A magnetic beads (Thermo Scientific) to enrich the library for correctly folded sdAbs. A negative control was also performed using streptavidin beads to calculate the number of folded antibodies in the library. The biopanning procedure was performed with no Ag present. The capturing of sdAb-phage and washings was performed using 5x PBS-T (1 mL, 0.05% Tween® 20) and then 5x PBS (1 mL). Elution, phage 'titering' and library recovery were also performed as described in Chapter 5.4.4. For the enrichment for thermally stable EvDesAbs, $1x10^{11}$ library phage were heated to 60 ºC for 1 hour before capture with the protein A magnetic beads.

5.4.4 Affinity selection against α-Synuclein monomer

$1x10^{11}$ pre-incubated library phage (Chapter 5.4.2) was mixed with 1 µM biotinylated A140C αSyn in PBS-T (0.05% Tween® 20, 2% w/v BSA) to a final volume of 1 mL and incubated for 2 hours at 25 ºC. 50 µL streptavidin-beads were added and capturing was performed by incubation for 30 minutes at 25 ºC on a rolling platform. A negative control was implemented to assess the level of background binders was identical in set-up except with the omission of antigen (biotinylated αSyn A140C).

The beads were then collected with a magnetic field and the solution was discarded. The beads were then stringently washed using different wash buffers by suspending the beads in wash buffer (1 mL) for 90 seconds and then collecting the beads in the magnetic field and discarding the wash buffer. Washing steps/buffers were: 5xPBS-T (0.05% Tween® 20), 5xPBS. After washing, captured antibody-phage were eluted by adding 500 µL Trypsin in PBS (10 µg/mL) and incubating at 37 °C for 30 minutes. The beads were collected using the magnetic field and discarded. A 10^{-2} to 10^{-11} dilution series of the eluted phage was made in triplicate and used to infect TG_1 cultures at OD_{600} = 0.5 (see Chapter 5.3.4) and was spotted on a 25x25 cm TYE-Agar plate and incubated overnight at 37 °C. The remaining eluted phage was then rescued by infecting a 20 mL TG_1 cell culture at OD_{600} = 0.5 and incubating at 37 °C for 30 minutes, followed by incubation at 37 °C for another 30 minutes with shaking (250 rpm). The infected cells were harvested by centrifugation for 10 minutes (3,200 xg), re-suspended in 1 mL 2xYT media, plated on a 25x25 cm TYE-Agar plate and incubated overnight at 37 °C. Glycerol stocks of the post-selection library were created as described in Chapter 5.2.1 and used for further rounds of biopanning as described in Chapter 5.4.1. The following rounds were repeated with decreasing volumes of antigen and capture beads. 100 nM biotinylated A140C αSyn was used for round 2 and 10 nM biotinylated A140C αSyn was used for round 3. 5 µL NeutrAvidin-beads were used in round 2 and 0.5 µL streptavidin-beads was used in round 3. The blocking agent, 2% w/v BSA in PBS-T (0.05% Tween® 20), was alternated with 2% w/v skimmed milk in PBS-T (0.05% Tween® 20) between rounds.

5.4.5 Competitive affinity selection between $A\beta_{40}$ oligomers and monomers

Competitive affinity selection against biotinylated $A\beta_{40}$ oligomers and unlabelled $A\beta_{40}$ monomers was performed using the same protocol as described in Chapter 5.4.4, with a few alterations. After the 2 hour incubation of $1x10^{11}$ pre-incubated library phage with biotinylated $A\beta_{40}$ oligomers, unlabelled $A\beta_{40}$ monomers were added to the mixture and incubated at room temperature under quiescent conditions for 30 minutes. Capture using streptavidin or NeutrAvidin-coated magnetic beads, washing, elution and library recovery was performed under the same conditions as described in Chapter 5.4.4. The volume of capture beads (50 µL) was not decreased between biopanning rounds, but alternating between streptavidin or NeutrAvidin-coated magnetic beads was still performed. Rounds one and two were selections against 5 µM biotinylated $A\beta_{40}$ oligomers and 1 nM $A\beta_{40}$ monomers. Round three was a

selection against 500 nM biotinylated $A\beta_{40}$ oligomers and 10 nM $A\beta_{40}$ monomers, round four was a selection against 50 nM biotinylated $A\beta_{40}$ oligomers and 100 nM $A\beta_{40}$ monomers and round five was a selection against 5 nM biotinylated $A\beta_{40}$ oligomers and 1 μM $A\beta_{40}$ monomers.

5.5 Screening for evolved antibodies

5.5.1 EvDesAb-expressing crude-extract preparation

The following screening protocols were optimised in collaboration with Robert I. Horne, who was a Part III Chemistry undergraduate student at the University of Cambridge from October 2017 to May 2018. Robert was also responsible for the characterisation of EvDesAb-RHR.

Colonies picked from the 25x25 cm TYE-Agar plate from a final round off affinity selection were inoculated separately into 100 μL 2xYT-GA media supplemented with 20% glycerol (final concentration), contained in a sterile 96-well microplate. These 'master' plates were sealed with gas-permeable plate film and incubated at 37 ºC, 500 rpm on a plate shaker overnight and stored at -80 ºC. 150 μL of 2xYT-GA was added to all but one well of a fresh sterile 96-well 'growth' microplate. Ampicillin was not used in one well as this would contain fresh TG_1 cells lacking a plasmid with the ampicillin resistance gene as the cell-lysate only control. This well was filled with 150 μL of 2xYT supplemented with 2% w/v glucose only. Bacteria were transferred by scraping cells from the frozen master plate wells to the growth plates and the control TG_1 cells were added to the control well from a freshly streaked plate without antibiotic. Other wells were reserved for the TG_1 cells expressing the control DesAbs such as DesAb-F and DesAb-IAPP for the αSyn binding screens and $DesAb_{3\text{-}9}$ and $DesAb_{29\text{-}36}$ for the $A\beta_{40}$ oligomer binding screens. The plates were then were sealed with gas-permeable plate film and incubated on a plate shaker (37 ºC, 700 rpm, overnight).

A fresh sterile 96-well 'induction' microplate was set-up using the same solutions and layout as a growth plate. Bacteria from the incubated growth plate (10 μL per well) was then transferred to the induction plate. The induction plate was sealed with gas-permeable plate film and incubated on a plate shaker (37 ºC, 700 rpm, 3 hours). IPTG (10 mM, 17.8 μL per well) was then added and the plate was incubated overnight on a plate shaker (30 ºC, 700 rpm). The induction plate was centrifuged (4 ºC, 4,000 rpm, 15 minutes) and the supernatant was discarded. The cells were lysed by incubating the plate at -20 ºC for 30 minutes. The plate was

thawed at room temperature for 30 minutes and the pellet in each well was then re-suspended in 170 µL PBS-T (0.05% Tween® 20). The plate was placed on a plate shaker (20 ºC, 700 rpm, 30 minutes) before centrifuging (20 °C, 4,000 rpm, 15 minutes). 150 µL of the supernatant was collected and 50 µL was used for each type of ELISA (expression, binding and background).

5.5.2 Expression screening by direct ELISA.

50 µL of crude-extract was coated onto the wells of a Nunc™ Microwell™ 96-well microplate (ELISA plate) and incubated for 2 hours on a plate shaker (20 ºC, 100 rpm). The ELISA plate wells were then washed three times with PBS-T (3 x 200 µL, 0.05% Tween® 20) and then blocked with BSA in PBS-T (300 µL, 3% w/v BSA, 0.05% Tween® 20). The plates were then incubated overnight on a plate shaker (4 ºC, 100 rpm). The ELISA plate wells were then washed three times with PBS-T (3 x 200 µL, 0.05% Tween® 20), and a HRP-conjugated anti-His antibody (Abcam, ab1187) was added to the wells in PBS-T (50 µL per well, 10,000-fold dilution, 0.1% BSA, 0.05% Tween® 20). The plate was incubated for 2 hours on a plate shaker (25 ºC, 400 rpm). The plate wells were washed 5 times with PBS-T (5 x 200 µL, 0.05% Tween® 20) and 5 times with PBS (5 x 200 µL) before addition of TMB solution (50 µL per well). The plate was left at room temperature until the desired blue colour developed before stopping the reaction with addition of 2 M H_2SO_4 (50 µL per well). The absorbance at 450 nm for each well was measured using a plate reader (BMG Labtech, Aylesbury, UK).

5.5.3 Binding screening by indirect ELISA

50 µL of Ag (either 2 µM αSyn or 5 µM $A\beta_{40}$ oligomers) was coated onto the wells of an ELISA plate and incubated for 2 hours on a plate shaker (20 ºC, 100 rpm). The ELISA plate wells were then washed three times with PBS-T (3 x 200 µL, 0.05% Tween® 20) and then blocked with BSA in PBS-T (300 µL, 3% w/v BSA, 0.05% Tween® 20). The plates were then incubated overnight on a plate shaker (4 ºC, 100 rpm). The ELISA plate wells were then washed three times with PBS-T (3 x 200 µL, 0.05% Tween® 20) and 50 µL of crude-extract (Chapter 5.5.1) was added to the wells. The plate was incubated for 2 hours on a plate shaker (25 ºC, 400 rpm), washed five times with PBS-T (5 x 200 µL, 0.05% Tween® 20), and a HRP-conjugated anti-His antibody (Abcam, ab1187) was added to the wells in PBS-T (50 µL per well, 10,000-fold dilution, 0.1% BSA, 0.05% Tween® 20). The plate was incubated for 2 hours

on a plate shaker (25 ºC, 400 rpm). The plate wells were washed 5 times with PBS-T (5 x 200 µL, 0.05% Tween® 20) and 5 times with PBS (5 x 200 µL) before addition of TMB solution (50 µL per well). The plate was left at room temperature until the desired blue colour developed before stopping the reaction with addition of 2 M H_2SO_4 (50 µL per well). The absorbance at 450 nm for each well was measured using a plate reader (BMG Labtech, Aylesbury, UK).

5.5.4 Cross-reactivity screening by indirect ELISA

A TG_1 colony from a fresh streak plate was used to inoculate 5 mL 2xYT (no antibiotic) and the culture was incubated overnight (37 ºC, 200 rpm). The culture was centrifuged for 5 minutes (4700 rpm) and the pellet was re-suspended in 20 mL PBS. The suspension was sonicated for 5 minutes, centrifuged for 15 minutes (4,700 rpm) and the pellet was re-suspended in 5 mL PBS. The suspension was passed through a 0.22 µm filter and 0.2 g Streptomycin sulphate was added to precipitate the DNA and the mixture was incubated for 30 minutes on a rolling platform (4 ºC). The cell-lysate was centrifuged for 15 minutes (4 ºC, 4,700 rpm) and the supernatant was passed through a 0.22 µm filter.

50 µL of cell-lysate was coated onto the wells of an ELISA plate and incubated for 2 hours on a plate shaker (20 ºC, 100 rpm). The ELISA plate wells were then washed three times with PBS-T (3 x 200 µL, 0.05% Tween® 20) and then blocked with BSA in PBS-T (300 µL, 3% w/v BSA, 0.05% Tween® 20). The plates were then incubated overnight on a plate shaker (4 ºC, 100 rpm). The ELISA plate wells were then washed three times with PBS-T (3 x 200 µL, 0.05% Tween® 20) and 50 µL of crude-extract (Chapter 5.5.1) was added to the wells. The plate was incubated for 2 hours on a plate shaker (25 ºC, 400 rpm), washed five times with PBS-T (5 x 200 µL, 0.05% Tween® 20), and a HRP-conjugated anti-His antibody (Abcam, ab1187) was added to the wells in PBS-T (50 µL per well, 10,000-fold dilution, 0.1% BSA, 0.05% Tween® 20). The plate was incubated for 2 hours on a plate shaker (25 ºC, 400 rpm). The plate wells were washed 5 times with PBS-T (5 x 200 µL, 0.05% Tween® 20) and 5 times with PBS (5 x 200 µL) before addition of TMB solution (50 µL per well). The plate was left at room temperature until the desired blue colour developed before stopping the reaction with addition of 2 M H_2SO_4 (50 µL per well). The absorbance at 450 nm for each well was measured using a plate reader (BMG Labtech, Aylesbury, UK).

5.5.5 Expression and purification of soluble single-domain antibodies

A single clone was scraped from a master plate well and inoculated into 10 mL of 2xYT-GA and incubated overnight (37 ºC, 200 rpm). The plasmid was prepared from the TG_1 culture using a miniprep kit (QIAGEN) as per the QIAGEN miniprep protocol. The purified plasmid was transformed into WK.6 *E. coli* via heat-shock and the cells were plated on LB-Agar supplemented with ampicillin (100 μg/mL) and incubated overnight (37 ºC). A single colony was inoculated 10 mL of 2xYT-GA supplemented with 1 mM $MgCl_2$ and the culture was grown overnight (37 ºC, 200 rpm). 330 mL of Terrific broth (TB), supplemented with ampicillin (100 μg/mL), glucose (0.1% w/v) and 1 mM $MgCl_2$, was inoculated with 3 mL of the overnight culture. The culture was incubated (37 ºC, 180 rpm) until it reached an OD_{600} of 0.5-0.8. sdAb expression was induced with 1 mM IPTG (final concentration) and incubated overnight (28 ºC, 170 rpm). The cells were harvested by centrifugation for 15 minutes (4 ºC, 9,000 xg). The cell pellet of 1 L of culture was re-suspended in 15 mL of ice-cold TES buffer (200 mM Tris, 0.5 mM EDTA, 500 mM sucrose) and incubated for 1 hour (0 ºC) on an orbital shaking platform (100 rpm). 30 mL of TES/4 buffer (50 mM Tris, 0.125 mM EDTA, 125 mM sucrose) was added to the re-suspended pellet, which was then incubated for 45 minutes (0 ºC) on an orbital shaking platform (100 rpm). The suspension was centrifuged for 30 minutes (4 ºC ,10,000 xg) and the supernatant was recovered as the periplasmic extract. The His-tagged sdAbs were purified from the periplasmic extract using HisPur™ Ni-NTA Resin IMAC according to the Thermo Scientific™ protocol before subsequent further purification using SEC on a HiLoad® 16/600 Superdex® 75 column.

5.6 Binding affinity characterisation by MST

5.6.1 Single-labelling of α-Synuclein N122C with Alexa488-Maleimide

αSyn mutant N122C was purified using the modified protocol as described in Chapter 5.3.1[284]. Immediately before labelling with A488-Maleimide, the DTT was removed with the use of small-scale SEC involving Sephadex® G-25 gel filtration with de-gassed PBS. 100 μM αSyn N122C in PBS (1 mL) was mixed with a 10-fold excess of A488-Maleimide in DMSO and the mixture was incubated in the dark overnight at 4 ºC on a rolling platform. The excess labelling

reagent was removed using Sephadex® G-25 gel filtration and the labelling was confirmed using LC-MS.

5.6.2 Binding affinity characterisation by MST.

Purified Abs in 50 mM Tris-HCl, 150 mM NaCl, pH 7.4 were concentrated using 3K Ultracel® Amicon® Ultra-15 centrifugal filters to ~200-300 μM final concentration. Both αSyn N122C-A488 (150 nM, 0.15% Tween® 20, 50 mM Tris-HCl, 150 mM NaCl, pH 7.4) and concentrated Ab was then centrifuged (15,000 rpm, 4 ºC, 15 min) to remove aggregates. A 1:1 dilution series of the Ab was performed into 50 mM Tris-HCl, 150 mM NaCl, pH 7.4 to yield 16 dilutions. 150 nM αSyn N122C-A488 (10 μL) was then added to each antibody dilution (20 μL) to give a constant final αSyn N122C-A488 concentration of 50 nM (0.05% Tween® 20, 50 mM Tris-HCl, 150 mM NaCl, pH 7.4). After binding equilibration by incubation in the dark at room temperature (2 hours), the dilution series was subjected to MST assays in standard-treated capillaries on a Nanotemper Monolith NT.115 system. The optimised settings used for each assay were 50% LED power (blue), 80% MST power, 5 s fluorescence before MST activation, 20 s MST activation, 5 s fluorescence after MST activation, and a 25 s delay between runs at a temperature of 22 ºC. A capillary scan of each sample was taken of each sample prior to testing to ensure that the fluorescent label was at a consistent concentration and to ensure that no sticking to the capillary occurred. Fluorophore photobleaching was also taken into account and any runs that showed excessive photobleaching were discounted.

All data analysis was performed using the Monolith® NT.115 instrument software. Before normalisation of the binding curves to fraction bound (FB), measured fluorescence values are displayed as normalised fluorescence (F_{norm}) which relates to the fluorescence values prior (F_0) to and after (F_1) IR laser activation. F_{norm} is given by the equations

$$F_{norm} = \frac{F_1}{F_0} \quad \text{(Eq. 5.1)}$$

$$F_{norm} = (1\text{-}FB)F_{norm}^{(Ag)} + (FB)F_{norm}^{(AbAg)} \quad \text{(Eq. 5.2)}$$

where the latter equation describes the contribution of the bound and unbound state of a fluorescent ‘antigen’ (Ag) to the F_{norm} signal. $F(Ag)_{norm}$ is the contribution of the unbound fluorescent Ag molecule, $F(AbAg)_{norm}$ is the contribution of the complex of the fluorescent Ag

molecule and its interacting antibody 'ligand' (Ab), and FB is the fraction of fluorescent molecules that formed the complex. Upon binding of an Ab to the fluorescent target Ag, changes in the MST signal are quantified based on the altered MST signal of the AbAg complex. By analysing a dilution series with an increasing Ab concentration and constant fluorescent Ag concentration, this change in MST signal, expressed as ΔF_{norm}, can be used to calculate changes in the fraction of bound molecules to derive their K_D. An illustration of the determination of F_0 and F_1 from a typical laser-induced thermophoresis effect on the fluorescence is shown in Figure 5.2.

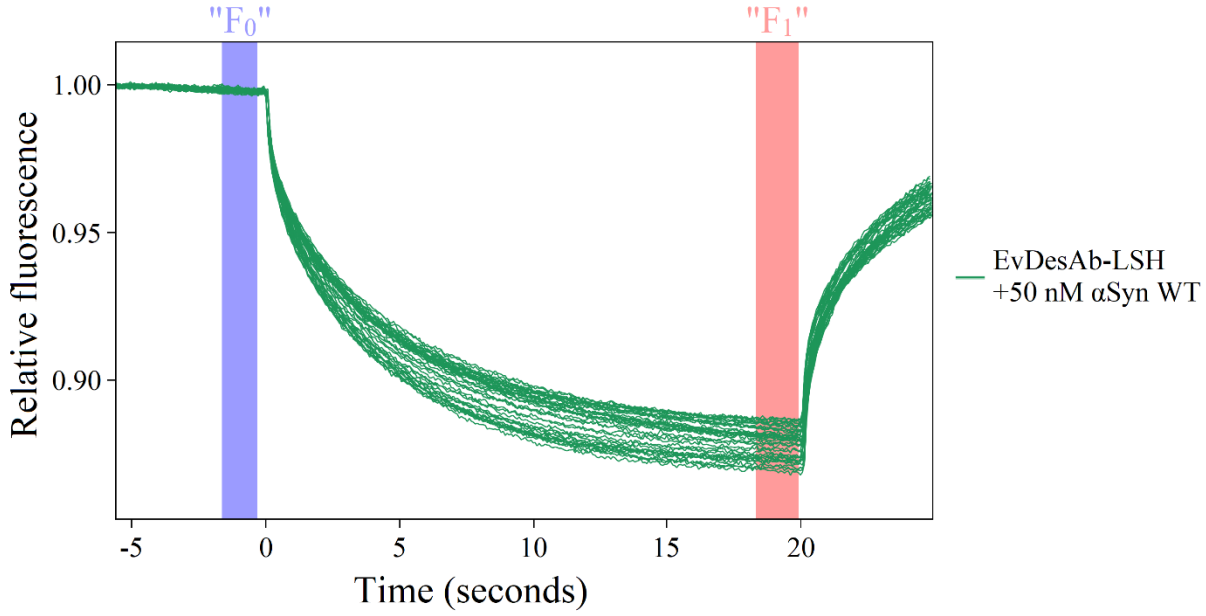

Figure 5.2. Raw MST trace for EvDesAb-LSH binding to 50 nM αSyn WT (A488). Initially (-5 to 0 seconds), the molecules are homogeneously distributed and a constant 'initial fluorescence' is detected. F_0 is calculated from this region. After activation of the IR laser, a drop in fluorescence is observed, which corresponds to the thermophoretic movement of the fluorescent molecules out of the heated sample volume. F_1 can be calculated anywhere in this region, however it is preferable to calculate it later in the thermophoresis duration as this frequently results in higher signal/noise ratios. After deactivation of the IR laser, a fluorescence increase occurs, caused by the diffusion of molecules back towards the vacated region, due to a decrease in sample temperature. The MST signal of a fluorescent molecule (αSyn WT (A488)) changes upon binding to a non-fluorescent ligand (EvDesAb-LSH), resulting in different traces.

The K_D can be obtained by fitting a dose-response curve to a plot of Fraction bound (FB) against fluorescent Ag concentration (see Chapter 2.6.2 and Chapter 2.6.4). K_D is calculated from the equation

$$FB=\frac{[AbAg]}{[Ag]}=\frac{[Ab]+[Ag]+K_D-\sqrt{([Ab]+[Ag]+K_D)^2-4[Ab][Ag]}}{2[Ag]} \quad \text{(Eq. 5.3)}$$

where [Ag] is the concentration of free fluorescent antigen, [Ab] is the concentration of free antibody and [AbAg] is the concentration of the complex of Ab and Ag. The concentration of fluorescent antigen [Ag] is kept constant during the experiments and the concentration of antibody [Ab] is varied in a dilution series. The signal obtained in the measurement directly corresponds to the fraction of fluorescent molecules (FB), which can be easily fitted with the derived equation to obtain the K_D of the interaction.

5.6.3 Proline insertion into position 73 of α-Synuclein N122C and single labelling with Alexa488-Maleimide

Inverse-PCR with the use of 5'-phosphorylated oligonucleotides was used to insert a proline into position 73 of αSyn N122C, contained in the pT7-7 vector (provided by the Centre of Misfolding Diseases (CMD), University of Cambridge).

Oligonucleotides:

73P-For 5'- CCGGTGACAGCAGTAGCCCAGAAGACAGTG-3' (5'-phosphorylated)

73P-Rev 5'- ACCCGTCACCACTGCTCCTCCAACATTTGTCAC-3' (5'-phosphorylated)

PCR conditions: 30 seconds initial denaturing (98 °C), 10 seconds denaturing (98 °C), 30 seconds annealing (60 °C), 5 minutes elongation (72 °C) for 35 cycles with a final extension of 7 minutes (72 °C). Each reaction (50 µL) contained 5x Phusion HF Buffer (10 µL), 10 mM dNTPs (1 µL), 100 µM forward primer (0.25 µL), 100 µM reverse primer (0.25 µL), 100 ng/µL αSyn N122C template DNA (0.02 µL), ddmQ H_2O (37.98 µL) and Phusion High-fidelity Polymerase (0.5 µL).

Digestion, PCR clean-up, self-circularisation, transformation, mini-culture DNA purification and sequencing were performed as described in Chapter 5.1.2. αSyn 73P+N122C was purified using the modified protocol as described in Chapter 5.3.1[284]. Single labelling of αSyn 73P+N122C with A488-Maleimide was also performed using the same protocol described in Chapter 5.6.1.

5.7 Circular dichroism spectroscopy

CD spectroscopy was performed on a Jasco J-810 spectropolarimeter (JASO Ltd., Great Dunmow, UK), equipped with a Peltier holder. Far-UV data were measured in a 0.1 cm path-length cuvette with a protein concentration of 6 µM in PBS and the scans were recorded between 200 and 250 nm at 25 ºC. Scans were recorded at 50 nm min^{-1} with a 1 nm band width and a 4 s response time. The mean residue ellipticity (MRE) was calculated as described in reference [261]. In brief, the MRE at a certain wavelength (λ) is calculated as

$$MRE = MRW \times \frac{\theta_\lambda}{10} \times d \times c \quad \text{(Eq. 5.4)}$$

where MRW is the mean residue weight, θ_λ is the observed ellipticity (degrees) at wavelength λ, d is the path length (cm), and c is the concentration (g/mL). The MRW is calculated as

$$MRW = \frac{M}{N - 1} \quad \text{(Eq. 5.5)}$$

where M is the molecular mass of the protein (in Da) and N is its number of AAs.

Far-UV thermal denaturation was monitored at 207 nm. During thermal denaturation, the temperature was increased from 25 to 95 ˚C at a rate of 0.5 ˚C min^{-1}. Data points were acquired every 0.1 ºC with a bandwidth of 1 nm. Ellipticity values were normalised to the fraction of unfolded protein (F_u) using

$$F_u = \frac{\theta - \theta_U}{\theta_N - \theta_U} \quad \text{(Eq. 5.6)}$$

where Θ is the observed ellipticity, Θ_N is the native ellipticity and Θ_U is the unfolded ellipticity. Θ_N and Θ_U were extrapolated from pre- and post-transition baselines at the relative temperature. Experimental data were fitted with a sigmoidal expression, using OriginPro 9.1 (OriginLab Corporation) where T_m is defined as the temperature where the fraction of unfolded protein is 0.5. This method is described in detail in reference [285].

5.8 Aβ42 binding selectivity characterisation by ELISA

A 3 μM $A\beta_{42}$ aggregation, followed by ThT fluorescence, was performed as described in Chapter 5.8. The lag phase and growth plateau phase time points were calculated from the ThT fluorescence read-out and a second 3 μM $A\beta_{42}$ aggregation was performed under identical conditions without ThT. At each calculated time-point, samples were taken from the aggregation reaction and chilled to 0 ºC. A 1:1 dilution of each time-point was made with 20 mM sodium phosphate buffer, 0.2 mM EDTA, pH 7.4 to give a final concentration of 1.5 μM $A\beta_{42}$ (as a function of the original monomer concentration). 40 μL of each diluted time-point and 40 μL fresh $A\beta_{42}$ monomer (1.5 μM) was coated onto separate wells of an ELISA plate and incubated for 1 hour under quiescent conditions (4 ºC). The ELISA plate wells were then washed three times with PBS (3 x 200 μL) and then blocked with BSA in PBS-T (300 μL, 3% w/v BSA, 0.05% Tween® 20). The plates were then incubated overnight under quiescent conditions (4 ºC). The ELISA plate wells were then washed three times with PBS (3 x 200 μL) and 50 μL of purified DesAb/EvDesAb in PBS-T (2 μM, 0.05% Tween® 20, Chapter 5.5.5) was added to the wells. The plate was incubated for 2 hours on a plate shaker (room temperature, 400 rpm), washed five times with PBS-T (5 x 200 μL, 0.05% Tween® 20), and a HRP-conjugated anti-His antibody (Abcam, ab1187) was added to the wells in PBS-T (50 μL per well, 10,000-fold dilution, 0.1% BSA, 0.05% Tween® 20). The plate was incubated for 2 hours on a plate shaker (room temperature, 400 rpm). The plate wells were washed 5 times with PBS-T (5 x 200 μL, 0.05% Tween® 20) and 5 times with PBS (5 x 200 μL) before addition of TMB solution (50 μL per well). The plate was left at room temperature until the desired blue colour developed before stopping the reaction with addition of 2 M H_2SO_4 (50 μL per well). The absorbance at 450 nm for each well was measured using a plate reader (BMG Labtech, Aylesbury, UK).

5.9 Aβ$_{42}$ aggregation inhibition and kinetics analysis

Monomeric Aβ$_{42}$ was freshly purified from lyophilised powder as described in Chapter 5.3.2 and stored at 0 ºC in protein low-binding test tubes. Monomeric Aβ$_{42}$ and DesAb/EvDesAb variants were used to create solutions at a final Aβ$_{42}$ concentration of 2 μM and different DesAb/EvDesAb concentrations in 20 mM sodium phosphate buffer (pH 8.0), 0.2 mM EDTA, supplemented with 6 μM ThT[87]. Each sample (90 μL) was then added into different wells of a 96-well half-area clear-bottom black polystyrene PEG-coated plate (Corning). After sealing the plate, aggregation assays were performed at 37 ºC under quiescent conditions using a CLARIOstar plate reader (BMG Labtech). The ThT fluorescence was measured through the bottom of the plate every minute, using an excitation filter of 440 nm and an emission filter of 480 nm.

The time evolution of the total fibril mass concentration, $M(t)$, in the absence of seeds is described by the integrated rate law

$$\frac{M(t)}{M(\infty)} = 1 - \left(\frac{B_+ + C_+}{B_+ + C_+ e^{kt}} \frac{B_- + C_+ e^{kt}}{B_- + C_+} \right)^{\frac{k_\infty^2}{k\tilde{k}_\infty}} e^{-k_\infty t} \quad \text{(Eq. 5.7)}$$

where the kinetic parameters $B_\pm$, $C_\pm$, k, k_∞, $\tilde{k}_\infty$ are described in detail in reference [286] and are the functions of the two combinations of the microscopic rate constants k_+k_n and k_+k_2. The inhibition of the microscopic events by the DesAbs/EvDesAbs were identified by applying equation 5.7 to describe the aggregation profiles in Chapters 3.7 and 3.12 and comparing the generated microscopic rate constants k_+k_n and k_+k_2[85, 104, 286]. All aggregation curve fitting, kinetic analyses and the resulting data visualisation was performed using MATLAB® (MathWorks).

5.10 Analysis and analytical equipment

5.10.1 SDS-PAGE

Confirmation of all protein sizes was carried out using pre-cast Novex® NuPAGE® SDS-PAGE gels (Thermo Scientific) with the appropriate standard protein ladders and using NuPAGE® MES SDS running buffer (20x, Thermo Scientific). Electrophoresis was performed at constant voltage 200V for 35 minutes. Photos were taken and analysed using GelDocXR software.

5.10.2 Agarose gel electrophoresis

DNA was analysed and extracted using agarose gels cast by hand. All gels were 1% agarose in this study and were constructed by mixing 0.28 g Agarose in 30 mL TAE buffer (40 mM Tris Acetate, 1 mM EDTA, pH 8.3) and microwaving the solution to boiling until the agarose was dissolved. 3 μL GelRed^{TM} stain (Biotium) was added and the gel was poured into the casting vessel and allowed to solidify (~45 minutes). Electrophoresis was performed at 80 V, constant current, 45-60 minutes. Photos were taken and analysed using GelDocXR software.

5.10.3 NanoDrop 2000

All DNA concentrations and quality were measured at 260/280 nm using a NanoDrop 2000 (Thermo Scientific).

5.10.4 Cary 400 UV-Vis spectrophotometer

All protein concentrations were measured at 275 nm using a Cary 400 UV-Vis spectrophotometer (Varian).

5.10.5 Sanger sequencing

All DNA sequences were analysed by the laboratory of John Lester in the DNA sequencing facility at the Department of Biochemistry (University of Cambridge). The custom primer MP57 was used for all sequencing reactions involving the pMESy4 phagemid. Sequencing data was analysed using FinchTV software. All sequencing was done with the 'MP57' primer.

5.10.6 MALDI mass-spectroscopy

The biotinylation reaction of αSyn A140C was confirmed by analysis carried out in the PNAC facility of the Department of Biochemistry (University of Cambridge) by Dr. Len Packman.

5.10.7 LC-MS mass-spectroscopy

Conformation of EvDesAb molecular weights, biotinylation of $A\beta_{40}$ and A488 labelling of αSyn N122C/73P+N122C was performed on a Synapt/Xevo LC-MS instrument, located in the mass spectrometry laboratory (B101) in the Department of Chemistry (University of Cambridge)

5.11 Other materials

Primers for PCR were designed and ordered from Sigma-Aldrich and research enzymes were purchased from Agilent, Thermo Scientific and NEB. Vectors, constructs and cell stocks were also provided by the Dobson and Vendruscolo groups from previous research. Media and buffers were created using commercially-available stock chemicals. All work with GM organisms was performed in a Class-II safety cabinet (phage) or next to a blue Bunsen flame (*E. coli*). All work with bacteria (except during incubation or storage) and proteins was performed at, or as close to 0 ºC as possible. All laboratory work was personally carried out in Labs 289C (CBC), 290, MPACC (Chemistry of health building), 1st floor lab (Chemistry of

health building) and UB7 (Unilever building) in the Department of Chemistry of the University of Cambridge.

5.11.1 Common solution recipes

LB-Media: 1% (w/v) Tryptone, 0.5% (w/v) yeast extract, 1% (w/v) NaCl, pH 7.0. All LB-media was autoclaved at 121 ºC for 15 minutes.

2xYT media: 1.6% (w/v) Tryptone, 1% (w/v) yeast extract, 0.5% (w/v) NaCl, pH 7.0. All 2xYT-media was autoclaved at 121 ºC for 15 minutes.

LB-Agar: 1.5% Agar (w/v) in LB-media, pH 7.0. All LB-Agar was autoclaved at 121 ºC for 15 minutes and poured into plate at <45 ºC.

H-Top Agar: 0.75% Agar (w/v) in LB-media, pH 7.0. All H-Top-Agar was autoclaved at 121 ºC for 15 minutes and poured into plate at <35 ºC.

PBS: 1x PBS tablet (Gibco) per 500 mL ddmQ H_2O to yield 10 mM Phosphate, 140 mM NaCl, 2.7 mM KCl, pH 7.4.

PBS-T (PBS-Tween): 0.05% (v/v) Tween® 20 in PBS.

Chapter 6: Bibliography

1. Elvin, J.G., R.G. Couston, and C.F. van der Walle, *Therapeutic antibodies: market considerations, disease targets and bioprocessing.* Int J Pharm, 2013. **440**(1): p. 83-98.
2. LeBien, T.W. and T.F. Tedder, *B lymphocytes: how they develop and function.* Blood, 2008. **112**(5): p. 1570-80.
3. Oo, C. and S.S. Kalbag, *Leveraging the attributes of biologics and small molecules, and releasing the bottlenecks: a new wave of revolution in drug development.* Expert Rev Clin Pharmacol, 2016. **9**(6): p. 747-9.
4. Saper, C.B., *A guide to the perplexed on the specificity of antibodies.* J Histochem Cytochem, 2009. **57**(1): p. 1-5.
5. Peng, H.P., et al., *Origins of specificity and affinity in antibody-protein interactions.* Proc Natl Acad Sci U S A, 2014. **111**(26): p. E2656-65.
6. Yu, J., et al., *Mutation-specific antibodies for the detection of EGFR mutations in non-small-cell lung cancer.* Clin Cancer Res, 2009. **15**(9): p. 3023-8.
7. Esplin, E.D., L. Oei, and M.P. Snyder, *Personalized sequencing and the future of medicine: discovery, diagnosis and defeat of disease.* Pharmacogenomics, 2014. **15**(14): p. 1771-1790.
8. Siddiqui, M.Z., *Monoclonal antibodies as diagnostics; an appraisal.* Indian J Pharm Sci, 2010. **72**(1): p. 12-7.
9. Liu, J.K., *The history of monoclonal antibody development - Progress, remaining challenges and future innovations.* Ann Med Surg (Lond), 2014. **3**(4): p. 113-6.
10. Kaplon, H. and J.M. Reichert, *Antibodies to watch in 2019.* MAbs, 2019. **11**(2): p. 219-238.
11. Ecker, D.M., S.D. Jones, and H.L. Levine, *The therapeutic monoclonal antibody market.* MAbs, 2015. **7**(1): p. 9-14.
12. Shaughnessy, A.F., *Monoclonal antibodies: magic bullets with a hefty price tag.* BMJ, 2012. **345**: p. e8346.
13. Ryman, J.T. and B. Meibohm, *Pharmacokinetics of Monoclonal Antibodies.* CPT Pharmacometrics Syst Pharmacol, 2017. **6**(9): p. 576-588.
14. Perchiacca, J.M. and P.M. Tessier, *Engineering aggregation-resistant antibodies.* Annu Rev Chem Biomol Eng, 2012. **3**: p. 263-86.
15. Pendley, C., A. Schantz, and C. Wagner, *Immunogenicity of therapeutic monoclonal antibodies.* Curr Opin Mol Ther, 2003. **5**(2): p. 172-9.
16. Pineda, C., et al., *Assessing the Immunogenicity of Biopharmaceuticals.* BioDrugs, 2016. **30**(3): p. 195-206.
17. Catapano, A.L. and N. Papadopoulos, *The safety of therapeutic monoclonal antibodies: implications for cardiovascular disease and targeting the PCSK9 pathway.* Atherosclerosis, 2013. **228**(1): p. 18-28.
18. Lonberg, N., *Fully human antibodies from transgenic mouse and phage display platforms.* Curr Opin Immunol, 2008. **20**(4): p. 450-9.
19. Gebauer, M. and A. Skerra, *Engineered protein scaffolds as next-generation antibody therapeutics.* Curr Opin Chem Biol, 2009. **13**(3): p. 245-55.
20. Simeon, R. and Z. Chen, *In vitro-engineered non-antibody protein therapeutics.* Protein Cell, 2018. **9**(1): p. 3-14.
21. Yu, X., et al., *Beyond Antibodies as Binding Partners: The Role of Antibody Mimetics in Bioanalysis.* Annu Rev Anal Chem (Palo Alto Calif), 2017. **10**(1): p. 293-320.

22. Rhodes, C.A. and D. Pei, *Bicyclic Peptides as Next-Generation Therapeutics.* Chemistry, 2017. **23**(52): p. 12690-12703.
23. Winau, F., O. Westphal, and R. Winau, *Paul Ehrlich--in search of the magic bullet.* Microbes Infect, 2004. **6**(8): p. 786-9.
24. Woof, J.M. and D.R. Burton, *Human antibody-Fc receptor interactions illuminated by crystal structures.* Nat Rev Immunol, 2004. **4**(2): p. 89-99.
25. Sela-Culang, I., V. Kunik, and Y. Ofran, *The structural basis of antibody-antigen recognition.* Front Immunol, 2013. **4**: p. 302.
26. Tonegawa, S., *Somatic generation of antibody diversity.* Nature, 1983. **302**(5909): p. 575-81.
27. Wilson, P.C., et al., *Somatic hypermutation introduces insertions and deletions into immunoglobulin V genes.* J Exp Med, 1998. **187**(1): p. 59-70.
28. Market, E. and F.N. Papavasiliou, *V(D)J recombination and the evolution of the adaptive immune system.* PLoS Biol, 2003. **1**(1): p. E16.
29. Harris, L.J., et al., *Refined structure of an intact IgG2a monoclonal antibody.* Biochemistry, 1997. **36**(7): p. 1581-97.
30. Heyman, B., *Complement and Fc-receptors in regulation of the antibody response.* Immunol Lett, 1996. **54**(2-3): p. 195-9.
31. Mattu, T.S., et al., *The glycosylation and structure of human serum IgA1, Fab, and Fc regions and the role of N-glycosylation on Fcalpha receptor interactions.* J Biol Chem, 1998. **273**(4): p. 2260-72.
32. Jennewein, M.F. and G. Alter, *The Immunoregulatory Roles of Antibody Glycosylation.* Trends Immunol, 2017. **38**(5): p. 358-372.
33. Li, Y., et al., *Mechanism of neutralization by the broadly neutralizing HIV-1 monoclonal antibody VRC01.* J Virol, 2011. **85**(17): p. 8954-67.
34. Fabrizio, K., et al., *Aggregation of Streptococcus pneumoniae by a pneumococcal capsular polysaccharide-specific human monoclonal IgM correlates with antibody efficacy in vivo.* Clin Vaccine Immunol, 2010. **17**(5): p. 713-21.
35. Holliger, P. and P.J. Hudson, *Engineered antibody fragments and the rise of single domains.* Nat Biotechnol, 2005. **23**(9): p. 1126-36.
36. Sormanni, P., F.A. Aprile, and M. Vendruscolo, *Third generation antibody discovery methods: in silico rational design.* Chem Soc Rev, 2018. **47**(24): p. 9137-9157.
37. Ransohoff, R.M., et al., *Neuroinflammation: Ways in Which the Immune System Affects the Brain.* Neurotherapeutics, 2015. **12**(4): p. 896-909.
38. Dong, Y., et al., *Drug Development for Alzheimer's Disease: Microglia Induced Neuroinflammation as a Target?* Int J Mol Sci, 2019. **20**(3).
39. Fuller, J.P., et al., *Comparing the efficacy and neuroinflammatory potential of three anti-abeta antibodies.* Acta Neuropathol, 2015. **130**(5): p. 699-711.
40. MacRaild, C.A., et al., *Antibody Recognition of Disordered Antigens.* Structure, 2016. **24**(1): p. 148-157.
41. Uversky, V.N., *Unusual biophysics of intrinsically disordered proteins.* Biochim Biophys Acta, 2013. **1834**(5): p. 932-51.
42. Dunker, A.K., et al., *Intrinsic disorder and protein function.* Biochemistry, 2002. **41**(21): p. 6573-82.
43. Tompa, P., *Intrinsically disordered proteins: a 10-year recap.* Trends Biochem Sci, 2012. **37**(12): p. 509-16.
44. Meszaros, B., I. Simon, and Z. Dosztanyi, *The expanding view of protein-protein interactions: complexes involving intrinsically disordered proteins.* Phys Biol, 2011. **8**(3): p. 035003.

45. Berggard, T., S. Linse, and P. James, *Methods for the detection and analysis of protein-protein interactions.* Proteomics, 2007. **7**(16): p. 2833-42.
46. Uversky, V.N., C.J. Oldfield, and A.K. Dunker, *Intrinsically disordered proteins in human diseases: introducing the D2 concept.* Annu Rev Biophys, 2008. **37**: p. 215-46.
47. Hipp, M.S., S.H. Park, and F.U. Hartl, *Proteostasis impairment in protein-misfolding and -aggregation diseases.* Trends Cell Biol, 2014. **24**(9): p. 506-14.
48. Dobson, C.M., *Protein folding and misfolding.* Nature, 2003. **426**(6968): p. 884-90.
49. Knowles, T.P., M. Vendruscolo, and C.M. Dobson, *The amyloid state and its association with protein misfolding diseases.* Nat Rev Mol Cell Biol, 2014. **15**(6): p. 384-96.
50. Chiti, F. and C.M. Dobson, *Protein misfolding, functional amyloid, and human disease.* Annu Rev Biochem, 2006. **75**: p. 333-66.
51. Tyedmers, J., A. Mogk, and B. Bukau, *Cellular strategies for controlling protein aggregation.* Nat Rev Mol Cell Biol, 2010. **11**(11): p. 777-88.
52. Morley, J.F., et al., *The threshold for polyglutamine-expansion protein aggregation and cellular toxicity is dynamic and influenced by aging in Caenorhabditis elegans.* Proc Natl Acad Sci U S A, 2002. **99**(16): p. 10417-22.
53. Scheife, R.T., et al., *Impact of Parkinson's disease and its pharmacologic treatment on quality of life and economic outcomes.* Am J Health Syst Pharm, 2000. **57**(10): p. 953-62.
54. Brookmeyer, R., S. Gray, and C. Kawas, *Projections of Alzheimer's disease in the United States and the public health impact of delaying disease onset.* Am J Public Health, 1998. **88**(9): p. 1337-42.
55. Gething, M.J. and J. Sambrook, *Protein folding in the cell.* Nature, 1992. **355**(6355): p. 33-45.
56. Roberts, C.J., *Non-native protein aggregation kinetics.* Biotechnol Bioeng, 2007. **98**(5): p. 927-38.
57. Yoshimura, Y., et al., *Distinguishing crystal-like amyloid fibrils and glass-like amorphous aggregates from their kinetics of formation.* Proc Natl Acad Sci U S A, 2012. **109**(36): p. 14446-51.
58. Lambert, M.P., et al., *Diffusible, nonfibrillar ligands derived from Abeta1-42 are potent central nervous system neurotoxins.* Proc Natl Acad Sci U S A, 1998. **95**(11): p. 6448-53.
59. Cline, E.N., et al., *The Amyloid-beta Oligomer Hypothesis: Beginning of the Third Decade.* J Alzheimers Dis, 2018. **64**(s1): p. S567-S610.
60. Bucciantini, M., et al., *Inherent toxicity of aggregates implies a common mechanism for protein misfolding diseases.* Nature, 2002. **416**(6880): p. 507-11.
61. Kayed, R., et al., *Common structure of soluble amyloid oligomers implies common mechanism of pathogenesis.* Science, 2003. **300**(5618): p. 486-9.
62. Haass, C. and D.J. Selkoe, *Soluble protein oligomers in neurodegeneration: lessons from the Alzheimer's amyloid beta-peptide.* Nat Rev Mol Cell Biol, 2007. **8**(2): p. 101-12.
63. Cremades, N., et al., *Direct observation of the interconversion of normal and toxic forms of alpha-synuclein.* Cell, 2012. **149**(5): p. 1048-59.
64. Lesne, S., et al., *A specific amyloid-beta protein assembly in the brain impairs memory.* Nature, 2006. **440**(7082): p. 352-7.
65. Benilova, I., E. Karran, and B. De Strooper, *The toxic Abeta oligomer and Alzheimer's disease: an emperor in need of clothes.* Nat Neurosci, 2012. **15**(3): p. 349-57.

66. Janson, J., et al., *The mechanism of islet amyloid polypeptide toxicity is membrane disruption by intermediate-sized toxic amyloid particles.* Diabetes, 1999. **48**(3): p. 491-8.
67. Sousa, M.M. and M.J. Saraiva, *Neurodegeneration in familial amyloid polyneuropathy: from pathology to molecular signaling.* Prog Neurobiol, 2003. **71**(5): p. 385-400.
68. Merlini, G. and V. Bellotti, *Molecular mechanisms of amyloidosis.* N Engl J Med, 2003. **349**(6): p. 583-96.
69. Rahimi, F., A. Shanmugam, and G. Bitan, *Structure-function relationships of pre-fibrillar protein assemblies in Alzheimer's disease and related disorders.* Curr Alzheimer Res, 2008. **5**(3): p. 319-41.
70. Cookson, M.R. and M. van der Brug, *Cell systems and the toxic mechanism(s) of alpha-synuclein.* Exp Neurol, 2008. **209**(1): p. 5-11.
71. Onuchic, J.N., Z. Luthey-Schulten, and P.G. Wolynes, *Theory of protein folding: the energy landscape perspective.* Annu Rev Phys Chem, 1997. **48**: p. 545-600.
72. Vendruscolo, M. and C.M. Dobson, *Towards complete descriptions of the free-energy landscapes of proteins.* Philos Trans A Math Phys Eng Sci, 2005. **363**(1827): p. 433-52.
73. Hartl, F.U., A. Bracher, and M. Hayer-Hartl, *Molecular chaperones in protein folding and proteostasis.* Nature, 2011. **475**(7356): p. 324-32.
74. Buell, A.K., et al., *Detailed analysis of the energy barriers for amyloid fibril growth.* Angew Chem Int Ed Engl, 2012. **51**(21): p. 5247-51.
75. Sipe, J.D. and A.S. Cohen, *Review: history of the amyloid fibril.* J Struct Biol, 2000. **130**(2-3): p. 88-98.
76. Fandrich, M., *On the structural definition of amyloid fibrils and other polypeptide aggregates.* Cell Mol Life Sci, 2007. **64**(16): p. 2066-78.
77. Dobson, C.M., *Protein misfolding, evolution and disease.* Trends Biochem Sci, 1999. **24**(9): p. 329-32.
78. Vassar, P.S. and C.F. Culling, *Fluorescent stains, with special reference to amyloid and connective tissues.* Arch Pathol, 1959. **68**: p. 487-98.
79. Khurana, R., et al., *Mechanism of thioflavin T binding to amyloid fibrils.* J Struct Biol, 2005. **151**(3): p. 229-38.
80. Fitzpatrick, A.W., et al., *Atomic structure and hierarchical assembly of a cross-beta amyloid fibril.* Proc Natl Acad Sci U S A, 2013. **110**(14): p. 5468-73.
81. Fandrich, M. and C.M. Dobson, *The behaviour of polyamino acids reveals an inverse side chain effect in amyloid structure formation.* EMBO J, 2002. **21**(21): p. 5682-90.
82. Cohen, S.I., et al., *Nucleated polymerization with secondary pathways. I. Time evolution of the principal moments.* J Chem Phys, 2011. **135**(6): p. 065105.
83. Cohen, S.I., et al., *Nucleated polymerization with secondary pathways. II. Determination of self-consistent solutions to growth processes described by non-linear master equations.* J Chem Phys, 2011. **135**(6): p. 065106.
84. Cohen, S.I., et al., *Nucleated polymerization with secondary pathways. III. Equilibrium behavior and oligomer populations.* J Chem Phys, 2011. **135**(6): p. 065107.
85. Arosio, P., et al., *Chemical kinetics for drug discovery to combat protein aggregation diseases.* Trends Pharmacol Sci, 2014. **35**(3): p. 127-35.
86. Knowles, T.P., et al., *An analytical solution to the kinetics of breakable filament assembly.* Science, 2009. **326**(5959): p. 1533-7.
87. Cohen, S.I., et al., *Proliferation of amyloid-beta42 aggregates occurs through a secondary nucleation mechanism.* Proc Natl Acad Sci U S A, 2013. **110**(24): p. 9758-63.

88. Cohen, S.I., et al., *From macroscopic measurements to microscopic mechanisms of protein aggregation.* J Mol Biol, 2012. **421**(2-3): p. 160-71.
89. Cohen, S.I.A., et al., *Distinct thermodynamic signatures of oligomer generation in the aggregation of the amyloid-beta peptide.* Nat Chem, 2018. **10**(5): p. 523-531.
90. Shammas, S.L., et al., *A mechanistic model of tau amyloid aggregation based on direct observation of oligomers.* Nat Commun, 2015. **6**: p. 7025.
91. Kundel, F., et al., *Measurement of Tau Filament Fragmentation Provides Insights into Prion-like Spreading.* ACS Chem Neurosci, 2018. **9**(6): p. 1276-1282.
92. Kjaergaard, M., et al., *Oligomer Diversity during the Aggregation of the Repeat Region of Tau.* ACS Chem Neurosci, 2018. **9**(12): p. 3060-3071.
93. Iljina, M., et al., *Kinetic model of the aggregation of alpha-synuclein provides insights into prion-like spreading.* Proc Natl Acad Sci U S A, 2016. **113**(9): p. E1206-15.
94. Brown, J.W.P., et al., *Kinetic barriers to alpha-synuclein protofilament formation and conversion into mature fibrils.* Chem Commun (Camb), 2018. **54**(56): p. 7854-7857.
95. Padrick, S.B. and A.D. Miranker, *Islet amyloid: phase partitioning and secondary nucleation are central to the mechanism of fibrillogenesis.* Biochemistry, 2002. **41**(14): p. 4694-703.
96. Pithadia, A., et al., *Inhibition of IAPP Aggregation and Toxicity by Natural Products and Derivatives.* J Diabetes Res, 2016. **2016**: p. 2046327.
97. Habchi, J., et al., *An anticancer drug suppresses the primary nucleation reaction that initiates the production of the toxic Abeta42 aggregates linked with Alzheimer's disease.* Sci Adv, 2016. **2**(2): p. e1501244.
98. Habchi, J., et al., *Systematic development of small molecules to inhibit specific microscopic steps of Abeta42 aggregation in Alzheimer's disease.* Proc Natl Acad Sci U S A, 2017. **114**(2): p. E200-E208.
99. Perni, M., et al., *A natural product inhibits the initiation of alpha-synuclein aggregation and suppresses its toxicity.* Proc Natl Acad Sci U S A, 2017. **114**(6): p. E1009-E1017.
100. Perni, M., et al., *Multistep Inhibition of alpha-Synuclein Aggregation and Toxicity in Vitro and in Vivo by Trodusquemine.* ACS Chem Biol, 2018. **13**(8): p. 2308-2319.
101. Chia, S., et al., *SAR by kinetics for drug discovery in protein misfolding diseases.* Proc Natl Acad Sci U S A, 2018. **115**(41): p. 10245-10250.
102. De Genst, E., et al., *A nanobody binding to non-amyloidogenic regions of the protein human lysozyme enhances partial unfolding but inhibits amyloid fibril formation.* J Phys Chem B, 2013. **117**(42): p. 13245-13258.
103. Iljina, M., et al., *Nanobodies raised against monomeric a-synuclein inhibit fibril formation and destabilize toxic oligomeric species.* BMC Biol, 2017. **15**(1): p. 57.
104. Aprile, F.A., et al., *Selective targeting of primary and secondary nucleation pathways in Abeta42 aggregation using a rational antibody scanning method.* Sci Adv, 2017. **3**(6): p. e1700488.
105. Narayan, P., et al., *The extracellular chaperone clusterin sequesters oligomeric forms of the amyloid-beta(1-40) peptide.* Nat Struct Mol Biol, 2011. **19**(1): p. 79-83.
106. Rocca, W.A., *The burden of Parkinson's disease: a worldwide perspective.* Lancet Neurol, 2018. **17**(11): p. 928-929.
107. Rowley, W.R., et al., *Diabetes 2030: Insights from Yesterday, Today, and Future Trends.* Popul Health Manag, 2017. **20**(1): p. 6-12.
108. Xing, Y., et al., *Lysophosphatidylcholine modulates the aggregation of human islet amyloid polypeptide.* Phys Chem Chem Phys, 2017. **19**(45): p. 30627-30635.
109. Paulsson, J.F. and G.T. Westermark, *Aberrant processing of human proislet amyloid polypeptide results in increased amyloid formation.* Diabetes, 2005. **54**(7): p. 2117-25.
110. Burns, A. and S. Iliffe, *Alzheimer's disease.* BMJ, 2009. **338**: p. b158.

111. Ballard, C., et al., *Alzheimer's disease.* Lancet, 2011. **377**(9770): p. 1019-31.
112. Hardy, J. and D. Allsop, *Amyloid deposition as the central event in the aetiology of Alzheimer's disease.* Trends Pharmacol Sci, 1991. **12**(10): p. 383-8.
113. Goedert, M., M.G. Spillantini, and R.A. Crowther, *Tau proteins and neurofibrillary degeneration.* Brain Pathol, 1991. **1**(4): p. 279-86.
114. Priller, C., et al., *Synapse formation and function is modulated by the amyloid precursor protein.* J Neurosci, 2006. **26**(27): p. 7212-21.
115. Olsson, F., et al., *Characterization of intermediate steps in amyloid beta (Abeta) production under near-native conditions.* J Biol Chem, 2014. **289**(3): p. 1540-50.
116. Zhao, L.N., et al., *The toxicity of amyloid beta oligomers.* Int J Mol Sci, 2012. **13**(6): p. 7303-27.
117. Vivekanandan, S., et al., *A partially folded structure of amyloid-beta(1-40) in an aqueous environment.* Biochem Biophys Res Commun, 2011. **411**(2): p. 312-6.
118. Colvin, M.T., et al., *Atomic Resolution Structure of Monomorphic Abeta42 Amyloid Fibrils.* J Am Chem Soc, 2016. **138**(30): p. 9663-74.
119. Larsen, K.E., et al., *Alpha-synuclein overexpression in PC12 and chromaffin cells impairs catecholamine release by interfering with a late step in exocytosis.* J Neurosci, 2006. **26**(46): p. 11915-22.
120. Scott, D. and S. Roy, *alpha-Synuclein inhibits intersynaptic vesicle mobility and maintains recycling-pool homeostasis.* J Neurosci, 2012. **32**(30): p. 10129-35.
121. Sun, J., et al., *Functional cooperation of alpha-synuclein and VAMP2 in synaptic vesicle recycling.* Proc Natl Acad Sci U S A, 2019. **116**(23): p. 11113-11115.
122. Spillantini, M.G., et al., *Alpha-synuclein in Lewy bodies.* Nature, 1997. **388**(6645): p. 839-40.
123. Spillantini, M.G., et al., *alpha-Synuclein in filamentous inclusions of Lewy bodies from Parkinson's disease and dementia with lewy bodies.* Proc Natl Acad Sci U S A, 1998. **95**(11): p. 6469-73.
124. Mezey, E., et al., *Alpha synuclein in neurodegenerative disorders: murderer or accomplice?* Nat Med, 1998. **4**(7): p. 755-7.
125. Sveinbjornsdottir, S., *The clinical symptoms of Parkinson's disease.* J Neurochem, 2016. **139 Suppl 1**: p. 318-324.
126. Clayton, D.F. and J.M. George, *The synucleins: a family of proteins involved in synaptic function, plasticity, neurodegeneration and disease.* Trends Neurosci, 1998. **21**(6): p. 249-54.
127. Ueda, K., et al., *Molecular cloning of cDNA encoding an unrecognized component of amyloid in Alzheimer disease.* Proc Natl Acad Sci U S A, 1993. **90**(23): p. 11282-6.
128. Ulmer, T.S., et al., *Structure and dynamics of micelle-bound human alpha-synuclein.* J Biol Chem, 2005. **280**(10): p. 9595-603.
129. Li, B., et al., *Cryo-EM of full-length alpha-synuclein reveals fibril polymorphs with a common structural kernel.* Nat Commun, 2018. **9**(1): p. 3609.
130. Patrias, L.M., et al., *Specific antibodies to soluble alpha-synuclein conformations in intravenous immunoglobulin preparations.* Clin Exp Immunol, 2010. **161**(3): p. 527-35.
131. Gustafsson, G., et al., *Alpha-synuclein oligomer-selective antibodies reduce intracellular accumulation and mitochondrial impairment in alpha-synuclein exposed astrocytes.* J Neuroinflammation, 2017. **14**(1): p. 241.
132. Covell, D.J., et al., *Novel conformation-selective alpha-synuclein antibodies raised against different in vitro fibril forms show distinct patterns of Lewy pathology in Parkinson's disease.* Neuropathol Appl Neurobiol, 2017. **43**(7): p. 604-620.

133. Morgado, I., et al., *Molecular basis of beta-amyloid oligomer recognition with a conformational antibody fragment.* Proc Natl Acad Sci U S A, 2012. **109**(31): p. 12503-8.
134. Droste, P., et al., *Structural differences of amyloid-beta fibrils revealed by antibodies from phage display.* BMC Biotechnol, 2015. **15**: p. 57.
135. Chukwu, J.E., et al., *Tau Antibody Structure Reveals a Molecular Switch Defining a Pathological Conformation of the Tau Protein.* Sci Rep, 2018. **8**(1): p. 6209.
136. De Genst, E., A. Messer, and C.M. Dobson, *Antibodies and protein misfolding: From structural research tools to therapeutic strategies.* Biochim Biophys Acta, 2014. **1844**(11): p. 1907-1919.
137. Munke, A., et al., *Phage display and kinetic selection of antibodies that specifically inhibit amyloid self-replication.* Proc Natl Acad Sci U S A, 2017. **114**(25): p. 6444-6449.
138. Linse, S., *Monomer-dependent secondary nucleation in amyloid formation.* Biophys Rev, 2017. **9**(4): p. 329-338.
139. Meisl, G., et al., *Molecular mechanisms of protein aggregation from global fitting of kinetic models.* Nat Protoc, 2016. **11**(2): p. 252-72.
140. Crespi, G.A., et al., *Molecular basis for mid-region amyloid-beta capture by leading Alzheimer's disease immunotherapies.* Sci Rep, 2015. **5**: p. 9649.
141. Toyn, J., *What lessons can be learned from failed Alzheimer's disease trials?* Expert Rev Clin Pharmacol, 2015. **8**(3): p. 267-9.
142. van Dyck, C.H., *Anti-Amyloid-beta Monoclonal Antibodies for Alzheimer's Disease: Pitfalls and Promise.* Biol Psychiatry, 2018. **83**(4): p. 311-319.
143. Mehta, D., et al., *Why do trials for Alzheimer's disease drugs keep failing? A discontinued drug perspective for 2010-2015.* Expert Opin Investig Drugs, 2017. **26**(6): p. 735-739.
144. Abbott, A. and E. Dolgin, *Failed Alzheimer's trial does not kill leading theory of disease.* Nature, 2016. **540**(7631): p. 15-16.
145. DeMattos, R.B., et al., *Peripheral anti-A beta antibody alters CNS and plasma A beta clearance and decreases brain A beta burden in a mouse model of Alzheimer's disease.* Proc Natl Acad Sci U S A, 2001. **98**(15): p. 8850-5.
146. Yang, T., et al., *Target engagement in an alzheimer trial: Crenezumab lowers amyloid beta oligomers in cerebrospinal fluid.* Ann Neurol, 2019. **86**(2): p. 215-224.
147. Sevigny, J., et al., *The antibody aducanumab reduces Abeta plaques in Alzheimer's disease.* Nature, 2016. **537**(7618): p. 50-6.
148. Zhao, J., R. Nussinov, and B. Ma, *Mechanisms of recognition of amyloid-beta (Abeta) monomer, oligomer, and fibril by homologous antibodies.* J Biol Chem, 2017. **292**(44): p. 18325-18343.
149. Arndt, J.W., et al., *Structural and kinetic basis for the selectivity of aducanumab for aggregated forms of amyloid-beta.* Sci Rep, 2018. **8**(1): p. 6412.
150. Mullard, A., *Pfizer exits neuroscience.* Nat Rev Drug Discov, 2018. **17**(2): p. 86.
151. Folch, J., et al., *Current Research Therapeutic Strategies for Alzheimer's Disease Treatment.* Neural Plast, 2016. **2016**: p. 8501693.
152. Li, R., et al., *Early Detection of Alzheimer's Disease Using Non-invasive Near-Infrared Spectroscopy.* Front Aging Neurosci, 2018. **10**: p. 366.
153. Zheng, T., et al., *Antibody selection using clonal cocultivation of Escherichia coli and eukaryotic cells in miniecosystems.* Proc Natl Acad Sci U S A, 2018. **115**(27): p. E6145-E6151.
154. Chiu, M.L. and G.L. Gilliland, *Engineering antibody therapeutics.* Curr Opin Struct Biol, 2016. **38**: p. 163-73.

155. Roberts, R.W., *Totally in vitro protein selection using mRNA-protein fusions and ribosome display.* Curr Opin Chem Biol, 1999. **3**(3): p. 268-73.
156. Milstein, C., *The hybridoma revolution: an offshoot of basic research.* Bioessays, 1999. **21**(11): p. 966-73.
157. Jijakli, K., et al., *The in vitro selection world.* Methods, 2016. **106**: p. 3-13.
158. Pardon, E., et al., *A general protocol for the generation of Nanobodies for structural biology.* Nat Protoc, 2014. **9**(3): p. 674-93.
159. Hoogenboom, H.R. and G. Winter, *By-passing immunisation. Human antibodies from synthetic repertoires of germline VH gene segments rearranged in vitro.* J Mol Biol, 1992. **227**(2): p. 381-8.
160. Ponsel, D., et al., *High affinity, developability and functional size: the holy grail of combinatorial antibody library generation.* Molecules, 2011. **16**(5): p. 3675-700.
161. Winter, G., et al., *Making antibodies by phage display technology.* Annu Rev Immunol, 1994. **12**: p. 433-55.
162. Knappik, A., et al., *Fully synthetic human combinatorial antibody libraries (HuCAL) based on modular consensus frameworks and CDRs randomized with trinucleotides.* J Mol Biol, 2000. **296**(1): p. 57-86.
163. Spencer, S., et al., *Solubility evaluation of murine hybridoma antibodies.* MAbs, 2012. **4**(3): p. 319-25.
164. Safdari, Y., et al., *Antibody humanization methods - a review and update.* Biotechnol Genet Eng Rev, 2013. **29**: p. 175-86.
165. Wu, H., et al., *Humanization of a murine monoclonal antibody by simultaneous optimization of framework and CDR residues.* J Mol Biol, 1999. **294**(1): p. 151-62.
166. Lim, C.C., Y.S. Choong, and T.S. Lim, *Cognizance of Molecular Methods for the Generation of Mutagenic Phage Display Antibody Libraries for Affinity Maturation.* Int J Mol Sci, 2019. **20**(8).
167. Smith, K.A., et al., *Demystified...recombinant antibodies.* J Clin Pathol, 2004. **57**(9): p. 912-7.
168. Fischman, S. and Y. Ofran, *Computational design of antibodies.* Curr Opin Struct Biol, 2018. **51**: p. 156-162.
169. Nimrod, G., et al., *Computational Design of Epitope-Specific Functional Antibodies.* Cell Rep, 2018. **25**(8): p. 2121-2131 e5.
170. Baran, D., et al., *Principles for computational design of binding antibodies.* Proc Natl Acad Sci U S A, 2017. **114**(41): p. 10900-10905.
171. Sevy, A.M. and J. Meiler, *Antibodies: Computer-Aided Prediction of Structure and Design of Function.* Microbiol Spectr, 2014. **2**(6).
172. Pantazes, R.J. and C.D. Maranas, *OptCDR: a general computational method for the design of antibody complementarity determining regions for targeted epitope binding.* Protein Eng Des Sel, 2010. **23**(11): p. 849-58.
173. Li, T., R.J. Pantazes, and C.D. Maranas, *OptMAVEn--a new framework for the de novo design of antibody variable region models targeting specific antigen epitopes.* PLoS One, 2014. **9**(8): p. e105954.
174. Lapidoth, G.D., et al., *AbDesign: An algorithm for combinatorial backbone design guided by natural conformations and sequences.* Proteins, 2015. **83**(8): p. 1385-406.
175. Adolf-Bryfogle, J., et al., *RosettaAntibodyDesign (RAbD): A general framework for computational antibody design.* PLoS Comput Biol, 2018. **14**(4): p. e1006112.
176. Sormanni, P., F.A. Aprile, and M. Vendruscolo, *Rational design of antibodies targeting specific epitopes within intrinsically disordered proteins.* Proc Natl Acad Sci U S A, 2015. **112**(32): p. 9902-7.

177. Robinson, L.N., et al., *Structure-Guided Design of an Anti-dengue Antibody Directed to a Non-immunodominant Epitope.* Cell, 2015. **162**(3): p. 493-504.
178. Wang, H.W., et al., *Prediction of B-cell linear epitopes with a combination of support vector machine classification and amino acid propensity identification.* J Biomed Biotechnol, 2011. **2011**: p. 432830.
179. Barbas, C.F., 3rd, L.R. Languino, and J.W. Smith, *High-affinity self-reactive human antibodies by design and selection: targeting the integrin ligand binding site.* Proc Natl Acad Sci U S A, 1993. **90**(21): p. 10003-7.
180. Smith, J.W., et al., *Building synthetic antibodies as adhesive ligands for integrins.* J Biol Chem, 1994. **269**(52): p. 32788-95.
181. Perchiacca, J.M., C.C. Lee, and P.M. Tessier, *Optimal charged mutations in the complementarity-determining regions that prevent domain antibody aggregation are dependent on the antibody scaffold.* Protein Eng Des Sel, 2014. **27**(2): p. 29-39.
182. Perchiacca, J.M., et al., *Structure-based design of conformation- and sequence-specific antibodies against amyloid beta.* Proc Natl Acad Sci U S A, 2012. **109**(1): p. 84-9.
183. Hattori, T., et al., *High affinity anti-inorganic material antibody generation by integrating graft and evolution technologies: potential of antibodies as biointerface molecules.* J Biol Chem, 2010. **285**(10): p. 7784-93.
184. Ward, E.S., et al., *Binding activities of a repertoire of single immunoglobulin variable domains secreted from Escherichia coli.* Nature, 1989. **341**(6242): p. 544-6.
185. Hamers-Casterman, C., et al., *Naturally occurring antibodies devoid of light chains.* Nature, 1993. **363**(6428): p. 446-8.
186. Dottorini, T., et al., *Crystal structure of a human VH: requirements for maintaining a monomeric fragment.* Biochemistry, 2004. **43**(3): p. 622-8.
187. Jespers, L., et al., *Crystal structure of HEL4, a soluble, refoldable human V(H) single domain with a germ-line scaffold.* J Mol Biol, 2004. **337**(4): p. 893-903.
188. Kijanka, M., et al., *Nanobody-based cancer therapy of solid tumors.* Nanomedicine (Lond), 2015. **10**(1): p. 161-74.
189. Duggan, S., *Caplacizumab: First Global Approval.* Drugs, 2018. **78**(15): p. 1639-1642.
190. Bencurova, E., et al., *A rapid and simple pipeline for synthesis of mRNA-ribosome-V(H)H complexes used in single-domain antibody ribosome display.* Mol Biosyst, 2015. **11**(6): p. 1515-24.
191. Arbabi-Ghahroudi, M., *Camelid Single-Domain Antibodies: Historical Perspective and Future Outlook.* Front Immunol, 2017. **8**: p. 1589.
192. Muyldermans, S., *Single domain camel antibodies: current status.* J Biotechnol, 2001. **74**(4): p. 277-302.
193. Gainkam, L.O., et al., *Localization, mechanism and reduction of renal retention of technetium-99m labeled epidermal growth factor receptor-specific nanobody in mice.* Contrast Media Mol Imaging, 2011. **6**(2): p. 85-92.
194. Roopenian, D.C. and S. Akilesh, *FcRn: the neonatal Fc receptor comes of age.* Nat Rev Immunol, 2007. **7**(9): p. 715-25.
195. Sormanni, P., F.A. Aprile, and M. Vendruscolo, *The CamSol method of rational design of protein mutants with enhanced solubility.* J Mol Biol, 2015. **427**(2): p. 478-90.
196. Gram, H., et al., *In vitro selection and affinity maturation of antibodies from a naive combinatorial immunoglobulin library.* Proc Natl Acad Sci U S A, 1992. **89**(8): p. 3576-80.
197. Rajpal, A., et al., *A general method for greatly improving the affinity of antibodies by using combinatorial libraries.* Proc Natl Acad Sci U S A, 2005. **102**(24): p. 8466-71.
198. Packer, M.S. and D.R. Liu, *Methods for the directed evolution of proteins.* Nat Rev Genet, 2015. **16**(7): p. 379-94.

199. Eylenstein, R., et al., *Molecular basis of in vitro affinity maturation and functional evolution of a neutralizing anti-human GM-CSF antibody.* MAbs, 2016. **8**(1): p. 176-86.
200. Tiller, K.E., et al., *Facile Affinity Maturation of Antibody Variable Domains Using Natural Diversity Mutagenesis.* Front Immunol, 2017. **8**: p. 986.
201. Tabasinezhad, M., et al., *Trends in therapeutic antibody affinity maturation: From in-vitro towards next-generation sequencing approaches.* Immunol Lett, 2019. **212**: p. 106-113.
202. Childs, L.M., E.B. Baskerville, and S. Cobey, *Trade-offs in antibody repertoires to complex antigens.* Philos Trans R Soc Lond B Biol Sci, 2015. **370**(1676).
203. Clementi, N., et al., *Phage display-based strategies for cloning and optimization of monoclonal antibodies directed against human pathogens.* Int J Mol Sci, 2012. **13**(7): p. 8273-92.
204. Arnold, F.H., *Directed Evolution: Bringing New Chemistry to Life.* Angew Chem Int Ed Engl, 2018. **57**(16): p. 4143-4148.
205. McIsaac, R.S., et al., *Directed evolution of a far-red fluorescent rhodopsin.* Proc Natl Acad Sci U S A, 2014. **111**(36): p. 13034-9.
206. Jespers, L.S., et al., *Guiding the selection of human antibodies from phage display repertoires to a single epitope of an antigen.* Biotechnology (N Y), 1994. **12**(9): p. 899-903.
207. Williams, G.J., A.S. Nelson, and A. Berry, *Directed evolution of enzymes for biocatalysis and the life sciences.* Cell Mol Life Sci, 2004. **61**(24): p. 3034-46.
208. Carr, R., et al., *Directed evolution of an amine oxidase for the preparative deracemisation of cyclic secondary amines.* Chembiochem, 2005. **6**(4): p. 637-9.
209. Prasad, S., M. Bocola, and M.T. Reetz, *Revisiting the lipase from Pseudomonas aeruginosa: directed evolution of substrate acceptance and enantioselectivity using iterative saturation mutagenesis.* Chemphyschem, 2011. **12**(8): p. 1550-7.
210. Becker, S., et al., *Single-cell high-throughput screening to identify enantioselective hydrolytic enzymes.* Angew Chem Int Ed Engl, 2008. **47**(27): p. 5085-8.
211. Giver, L., et al., *Directed evolution of a thermostable esterase.* Proc Natl Acad Sci U S A, 1998. **95**(22): p. 12809-13.
212. Doerner, A., et al., *Therapeutic antibody engineering by high efficiency cell screening.* FEBS Lett, 2014. **588**(2): p. 278-87.
213. Currin, A., et al., *Synthetic biology for the directed evolution of protein biocatalysts: navigating sequence space intelligently.* Chem Soc Rev, 2015. **44**(5): p. 1172-239.
214. Reetz, M.T. and J.D. Carballeira, *Iterative saturation mutagenesis (ISM) for rapid directed evolution of functional enzymes.* Nat Protoc, 2007. **2**(4): p. 891-903.
215. Borrebaeck, C.A. and M. Ohlin, *Antibody evolution beyond Nature.* Nat Biotechnol, 2002. **20**(12): p. 1189-90.
216. Kille, S., et al., *Reducing codon redundancy and screening effort of combinatorial protein libraries created by saturation mutagenesis.* ACS Synth Biol, 2013. **2**(2): p. 83-92.
217. Ashraf, M., et al., *ProxiMAX randomization: a new technology for non-degenerate saturation mutagenesis of contiguous codons.* Biochem Soc Trans, 2013. **41**(5): p. 1189-94.
218. Lindner, T., et al., *DNA libraries for the construction of phage libraries: statistical and structural requirements and synthetic methods.* Molecules, 2011. **16**(2): p. 1625-41.
219. Dabney, J. and M. Meyer, *Length and GC-biases during sequencing library amplification: a comparison of various polymerase-buffer systems with ancient and modern DNA sequencing libraries.* Biotechniques, 2012. **52**(2): p. 87-94.

220. Aird, D., et al., *Analyzing and minimizing PCR amplification bias in Illumina sequencing libraries.* Genome Biol, 2011. **12**(2): p. R18.
221. Williams, E.M., J.N. Copp, and D.F. Ackerley, *Site-saturation mutagenesis by overlap extension PCR.* Methods Mol Biol, 2014. **1179**: p. 83-101.
222. Sidhu, S.S., et al., *Phage display for selection of novel binding peptides.* Methods Enzymol, 2000. **328**: p. 333-63.
223. Jain, P.C. and R. Varadarajan, *A rapid, efficient, and economical inverse polymerase chain reaction-based method for generating a site saturation mutant library.* Anal Biochem, 2014. **449**: p. 90-8.
224. Wu, C.H., et al., *Advancement and applications of peptide phage display technology in biomedical science.* J Biomed Sci, 2016. **23**: p. 8.
225. Schmitz, U., et al., *Phage display: a molecular tool for the generation of antibodies--a review.* Placenta, 2000. **21 Suppl A**: p. S106-12.
226. Lee, C.M., et al., *Selection of human antibody fragments by phage display.* Nat Protoc, 2007. **2**(11): p. 3001-8.
227. Smith, G.P., *Filamentous fusion phage: novel expression vectors that display cloned antigens on the virion surface.* Science, 1985. **228**(4705): p. 1315-7.
228. Rickert, K.W., et al., *Combining phage display with de novo protein sequencing for reverse engineering of monoclonal antibodies.* MAbs, 2016. **8**(3): p. 501-12.
229. Enever, C., M. Pupecka-Swider, and A. Sepp, *Stress selections on domain antibodies: 'what doesn't kill you makes you stronger'.* Protein Eng Des Sel, 2015. **28**(3): p. 59-66.
230. Ehrlich, G.K., W. Berthold, and P. Bailon, *Phage display technology. Affinity selection by biopanning.* Methods Mol Biol, 2000. **147**: p. 195-208.
231. Clackson, T. and H.B. Lowman, *Phage display : a practical approach*. 2004, Oxford: Oxford University Press. xxiv, 332 p. 61-83.
232. Kontermann, R., S. Dübel, and SpringerLink (Online service), *Antibody Engineering*, in *Springer protocols*. 2010, Springer Berlin Heidelberg : Imprint: Springer,: Berlin, Heidelberg. p. 1 online resource (800p.) p. 397-409.
233. Tiller, T., *Synthetic antibodies : methods and protocols*, in *Methods in molecular biology,*. 2017, Humana Press ; Springer,: New York. p. 1 online resource (xiv, 420 p.) p. 93-119.
234. Ylera, F., et al., *Off-rate screening for selection of high-affinity anti-drug antibodies.* Anal Biochem, 2013. **441**(2): p. 208-13.
235. de la Rica, R. and M.M. Stevens, *Plasmonic ELISA for the ultrasensitive detection of disease biomarkers with the naked eye.* Nat Nanotechnol, 2012. **7**(12): p. 821-4.
236. Porstmann, T. and S.T. Kiessig, *Enzyme immunoassay techniques. An overview.* J Immunol Methods, 1992. **150**(1-2): p. 5-21.
237. Wienken, C.J., et al., *Protein-binding assays in biological liquids using microscale thermophoresis.* Nat Commun, 2010. **1**: p. 100.
238. Seidel, S.A., et al., *Label-free microscale thermophoresis discriminates sites and affinity of protein-ligand binding.* Angew Chem Int Ed Engl, 2012. **51**(42): p. 10656-9.
239. De Genst, E.J., et al., *Structure and properties of a complex of alpha-synuclein and a single-domain camelid antibody.* J Mol Biol, 2010. **402**(2): p. 326-43.
240. Perchiacca, J.M., M. Bhattacharya, and P.M. Tessier, *Mutational analysis of domain antibodies reveals aggregation hotspots within and near the complementarity determining regions.* Proteins, 2011. **79**(9): p. 2637-47.
241. Hu, J., et al., *Reducing epitope spread during affinity maturation of an anti-ganglioside GD2 antibody.* J Immunol, 2009. **183**(9): p. 5748-55.

242. Hu, D., et al., *Effective Optimization of Antibody Affinity by Phage Display Integrated with High-Throughput DNA Synthesis and Sequencing Technologies.* PLoS One, 2015. **10**(6): p. e0129125.
243. Loset, G.A., et al., *Expanding the versatility of phage display II: improved affinity selection of folded domains on protein VII and IX of the filamentous phage.* PLoS One, 2011. **6**(2): p. e17433.
244. Pai, J.C., K.C. Entzminger, and J.A. Maynard, *Restriction enzyme-free construction of random gene mutagenesis libraries in Escherichia coli.* Anal Biochem, 2012. **421**(2): p. 640-8.
245. Neylon, C., *Chemical and biochemical strategies for the randomization of protein encoding DNA sequences: library construction methods for directed evolution.* Nucleic Acids Res, 2004. **32**(4): p. 1448-59.
246. MacBeath, G. and P. Kast, *UGA read-through artifacts--when popular gene expression systems need a pATCH.* Biotechniques, 1998. **24**(5): p. 789-94.
247. Ravn, U., et al., *Deep sequencing of phage display libraries to support antibody discovery.* Methods, 2013. **60**(1): p. 99-110.
248. Barreto, K., et al., *Next-generation sequencing-guided identification and reconstruction of antibody CDR combinations from phage selection outputs.* Nucleic Acids Res, 2019. **47**(9): p. e50.
249. Dower, W.J., J.F. Miller, and C.W. Ragsdale, *High efficiency transformation of E. coli by high voltage electroporation.* Nucleic Acids Res, 1988. **16**(13): p. 6127-45.
250. Roben, P.W., A.N. Salem, and G.J. Silverman, *VH3 family antibodies bind domain D of staphylococcal protein A.* J Immunol, 1995. **154**(12): p. 6437-45.
251. Starovasnik, M.A., et al., *Antibody variable region binding by Staphylococcal protein A: thermodynamic analysis and location of the Fv binding site on E-domain.* Protein Sci, 1999. **8**(7): p. 1423-31.
252. Graille, M., et al., *Crystal structure of a Staphylococcus aureus protein A domain complexed with the Fab fragment of a human IgM antibody: structural basis for recognition of B-cell receptors and superantigen activity.* Proc Natl Acad Sci U S A, 2000. **97**(10): p. 5399-404.
253. Ledsgaard, L., et al., *Basics of Antibody Phage Display Technology.* Toxins (Basel), 2018. **10**(6).
254. Baek, H., et al., *An improved helper phage system for efficient isolation of specific antibody molecules in phage display.* Nucleic Acids Res, 2002. **30**(5): p. e18.
255. Panchuk-Voloshina, N., et al., *Alexa dyes, a series of new fluorescent dyes that yield exceptionally bright, photostable conjugates.* J Histochem Cytochem, 1999. **47**(9): p. 1179-88.
256. Camilloni, C., et al., *Determination of secondary structure populations in disordered states of proteins using nuclear magnetic resonance chemical shifts.* Biochemistry, 2012. **51**(11): p. 2224-31.
257. Tokuriki, N., et al., *How protein stability and new functions trade off.* PLoS Comput Biol, 2008. **4**(2): p. e1000002.
258. Broom, A., et al., *Computational tools help improve protein stability but with a solubility tradeoff.* J Biol Chem, 2017. **292**(35): p. 14349-14361.
259. Rabia, L.A., et al., *Understanding and overcoming trade-offs between antibody affinity, specificity, stability and solubility.* Biochem Eng J, 2018. **137**: p. 365-374.
260. Greenfield, N.J., *Using circular dichroism spectra to estimate protein secondary structure.* Nat Protoc, 2006. **1**(6): p. 2876-90.
261. Kelly, S.M., T.J. Jess, and N.C. Price, *How to study proteins by circular dichroism.* Biochim Biophys Acta, 2005. **1751**(2): p. 119-39.

262. Kayed, R., et al., *Fibril specific, conformation dependent antibodies recognize a generic epitope common to amyloid fibrils and fibrillar oligomers that is absent in prefibrillar oligomers.* Mol Neurodegener, 2007. **2**: p. 18.
263. Wacker, J., et al., *Oligomer-targeting with a conformational antibody fragment promotes toxicity in Abeta-expressing flies.* Acta Neuropathol Commun, 2014. **2**: p. 43.
264. Renaut, L., et al., *Affinity maturation of antibodies: optimized methods to generate high-quality ScFv libraries and isolate IgG candidates by high-throughput screening.* Methods Mol Biol, 2012. **907**: p. 451-61.
265. Ovchinnikov, V., et al., *Role of framework mutations and antibody flexibility in the evolution of broadly neutralizing antibodies.* Elife, 2018. **7**.
266. Unkauf, T., M. Hust, and A. Frenzel, *Antibody Affinity and Stability Maturation by Error-Prone PCR.* Methods Mol Biol, 2018. **1701**: p. 393-407.
267. Cadwell, R.C. and G.F. Joyce, *Randomization of genes by PCR mutagenesis.* PCR Methods Appl, 1992. **2**(1): p. 28-33.
268. Vanhercke, T., et al., *Reducing mutational bias in random protein libraries.* Anal Biochem, 2005. **339**(1): p. 9-14.
269. Firth, A.E. and W.M. Patrick, *Statistics of protein library construction.* Bioinformatics, 2005. **21**(15): p. 3314-5.
270. Mannini, B., et al., *Stabilization and Characterization of Cytotoxic Abeta40 Oligomers Isolated from an Aggregation Reaction in the Presence of Zinc Ions.* ACS Chem Neurosci, 2018. **9**(12): p. 2959-2971.
271. Hawe, A., M. Sutter, and W. Jiskoot, *Extrinsic fluorescent dyes as tools for protein characterization.* Pharm Res, 2008. **25**(7): p. 1487-99.
272. Julian, M.C., et al., *Efficient affinity maturation of antibody variable domains requires co-selection of compensatory mutations to maintain thermodynamic stability.* Sci Rep, 2017. **7**: p. 45259.
273. Wolff, M., et al., *Quantitative thermophoretic study of disease-related protein aggregates.* Sci Rep, 2016. **6**: p. 22829.
274. Bemporad, F. and F. Chiti, *Protein misfolded oligomers: experimental approaches, mechanism of formation, and structure-toxicity relationships.* Chem Biol, 2012. **19**(3): p. 315-27.
275. Orte, A., et al., *Direct characterization of amyloidogenic oligomers by single-molecule fluorescence.* Proc Natl Acad Sci U S A, 2008. **105**(38): p. 14424-9.
276. Arosio, P., T.P. Knowles, and S. Linse, *On the lag phase in amyloid fibril formation.* Phys Chem Chem Phys, 2015. **17**(12): p. 7606-18.
277. Jung, S., A. Honegger, and A. Pluckthun, *Selection for improved protein stability by phage display.* J Mol Biol, 1999. **294**(1): p. 163-80.
278. Pershad, K. and B.K. Kay, *Generating thermal stable variants of protein domains through phage display.* Methods, 2013. **60**(1): p. 38-45.
279. Jespers, L., et al., *Aggregation-resistant domain antibodies selected on phage by heat denaturation.* Nat Biotechnol, 2004. **22**(9): p. 1161-5.
280. Li, L., A. Kantor, and N. Warne, *Application of a PEG precipitation method for solubility screening: a tool for developing high protein concentration formulations.* Protein Sci, 2013. **22**(8): p. 1118-23.
281. Julian, M.C., et al., *Co-evolution of affinity and stability of grafted amyloid-motif domain antibodies.* Protein Eng Des Sel, 2015. **28**(10): p. 339-50.
282. Jochens, H. and U.T. Bornscheuer, *Natural diversity to guide focused directed evolution.* Chembiochem, 2010. **11**(13): p. 1861-6.

283. Jochens, H., D. Aerts, and U.T. Bornscheuer, *Thermostabilization of an esterase by alignment-guided focussed directed evolution.* Protein Eng Des Sel, 2010. **23**(12): p. 903-9.
284. Hoyer, W., et al., *Dependence of alpha-synuclein aggregate morphology on solution conditions.* J Mol Biol, 2002. **322**(2): p. 383-93.
285. Hagan, C.L., et al., *A non-natural variant of human lysozyme (I59T) mimics the in vitro behaviour of the I56T variant that is responsible for a form of familial amyloidosis.* Protein Eng Des Sel, 2010. **23**(7): p. 499-506.
286. Cohen, S.I.A., et al., *A molecular chaperone breaks the catalytic cycle that generates toxic Abeta oligomers.* Nat Struct Mol Biol, 2015. **22**(3): p. 207-213.